N°: 42046

THESE DE DOCTORAT

NUMERICAL MODELLING AND SMALL SCALE TESTING OF FIRE PERFORMANCES FOR HALOGEN-FREE CABLE

Présentée et soutenue publiquement à

L'UNIVERSITE LILLE1 SCIENCES ET TECHNOLOGIES

Pour obtenir le grade de

DOCTEUR

Spécialité: Molécules et Matière Condensée

Par

Bertrand Girardin

Ingénieur diplômé de l'Ecole Nationale Supérieure de Chimie de Lille

Thèse dirigée par

Prof. Sophie Duquesne et Prof. Serge Bourbigot

Soutenue le 31 Mai 2016 devant la Commission d'Examen composée de :

Prof. Gaëlle Fontaine	ENSCL	Présidente de Jury
Prof. Alexis Coppalle	INSA Rouen	Rapporteur
Prof. Patrick van Hees	Lund University	Rapporteur
Dr. Eric Guillaume	Efectis Group	Examinateur
Prof. Sophie Duquesne	ENSCL	Directrice de thèse
Prof. Serge Bourbigot	ENSCL	Co-directeur de thèse

Acknowledgement

First, I would like to thank Prof. Alexandre Legris, head of the UMET laboratory, and Prof. Serge Bourbigot, head of the team ISP-R2F (Reaction and Resistance to Fire) for giving me the opportunity to join their labs, work on this project and achieve this PhD in excellent job conditions. I extend my thanks to Mr. Bernard Fontaine, head of the Ecole Nationale Supérieure de Chimie de Lille (ENSCL), where the laboratory is located.

I would like to thank my supervisors, Sophie, Serge and Gaëlle who gave me the possibility to work with them and to pass my PhD thesis in the R_2Fire lab. Working with them was a great pleasure throughout the whole project. Their encouragement and faith in me helped me to progress. I appreciated their scientific knowledge and their availability, whenever it was needed.

I am very grateful to Prof. Patrick van Hees, to Prof Alexis Coppalle and to Dr. Eric Guillaume who accepted to take their time, to bring their expertise as reviewers of this work and to be part of the jury.

I would like to acknowledge all the industrial and academicals partners of the DEROCA project. In particular, I would also like to thank Michael Försth and Petra Andersson from SP Fire Research who invited me several times in Sweden and made me discover cable testing (and Sweden). I would also like to thanks Dr. Lydie Delineau from Leoni Stüder for giving me the opportunity to work with her cables and sharing the data. I would never be able to develop my test without them.

I also sincerely thank all current and former members of the R2F team for all the moments we shared in easy-going atmosphere. First, thanks to those who left before me but brought me a real pleasure to work in the beginning of this PhD: Bastien, Carmen, Marianne, Marion, Antoine, Caroline, Nico Renaud, Gwen, Trang and Francis. Thanks to all the lab's permanent members: Gaëlle, Sophie, Serge, Fabienne, Mathilde, Michel, Maude, Charaf', Catherine, Severine, and particular, to Pierre for his good mood, his remarkable laugh and his help in everything in the lab; and to Brigitte, who for all the orders I improperly completed and she corrected. Thanks also to Agnès, Anil, Audrey, Ben, Benjamin, Hirak, JoJo, Johnathan, Mathieu, Nico, Nittaya, Pauline, Rège, Tchoubi, Sawsen and Tatenda.

Finally, I would like to thank my friends and everyone who bore with me outside of the lab and especially Audrey for her patience and her love.

Table of contents

Table of contents

List of abbreviations

ATH	Aluminum trihydroxide
CMF	Critical Mass Flux for ignition
CPR	Construction Products Regulation
CLS	Classical Least Square-
DoE	Design of Experiments
(m)DSC	(modulated) Differential Scanning Calorimetry
EHC	Effective Heat of Combustion
EVA	Ethylene vinyl acetate
FIGRA	Fire Growth Rate
FIPEC	Fire Performance of Electric Cables
FTIR	Fourier-Transform Infrared microscopy
FS	Flame Spread
HFFR	Halogen-Free Flame Retardant
HRR	Heat Release Rate
LOI	Limiting Oxygen Index
MCC	Microscale Combustion Calorimeter
MDH	Magnesium dihydroxide
(o)MMT	(organo-modified) Montmorillonite
(CA)MLC	(Controlled Atmosphere) Mass Loss Calorimeter
MLR	Mass Loss Rate
NC	Nanoclays (Cloisite 30B^{TM})
PCS	Pouvoir Calorifique Supérieur

(LD)PE	(Low Density) Polyethylene
pMLR	Peak of Mass Loss Rate
pHRR	Peak of Heat Release Rate
Py-GC/MS	Pyrolysis-Gas Chromatography-Mass Spectrometry
SBI	Single Burning Item
STA	Simultaneous Thermal Analysis
TGA	Thermogravimetric analysis
THR	Total Heat Relapsed
TTI	Time to Ignition
TTF	Time to Flameout
VA	Vinyl Acetate
VAC	Vinyl Acetate Content

Nomenclature

	General parameters		
t	Time	x	Depth
T	Temperature	m	Mass
P	Pressure	N_r	Number of decomposition reaction
N_g	Number of gaseous component	R	Ideal gas constant (8.314 J/mol/K)
c_0	Speed of light in vacuum ($2.997\ 10^8$ m/s)	h_0	Planck constant ($6.626\ 10^{-34}$ m².kg/s)
k_B	Boltzmann constant ($1.381\ 10^{-23}$ m²/kg/s²/K)		
	Optical properties		
M_λ	Black body excitance	I	Irradiance
α	Reflectivity	A	Absorption coefficient
ε	Emissivity	T	Transmittance
λ	Wavelength	R	Reflectance
d	Thickness		
	Kinetics parameters		
$\dot{r}_r$	Reaction rate of reaction *r*	n	Order of reaction
A_r	Pre-exponential factor of reaction *r*	ν_r^i	Stoichiometric coefficient of component *i* in reaction *r*
E_r	Activation energy of reaction *r*	α	Conversion degree
β	Heating rate		
	Thermo-physical properties		
Cp	Heat capacity	ρ	Density
k	Thermal conductivity	H_r	Enthalpy of reaction *r*
$D_{gas\ i}$	Mass transfer coefficient of component *i*	Φ	Porosity
K_g	Permeability	μ_g	Dynamic viscosity

GENERAL INTRODUCTION

Fire has an important place as hazards in the industry, public transport and building facilities because it can lead to loss of lives and goods. Given the number and extent potentially flammable materials encountered in everyday life, fire safety is of main concern and remains a current issue. In order to reduce the cost of fire both in terms of human death but also economical loss, national and international regulators have developed fire standards at which end products need to comply before selling. Those standards ensure people that end products used in our everyday life reach a certain level of fire resistance and/or fire protection.

Among those products, cables are a major concern for fire safety. Indeed, cables are used to transmit energy and/or data and an ever-growing amount of them are installed to connect rooms and floors in buildings. Low up to medium voltage cables, phone and LAN cables are then part of all residential, industrial or public building. Independently from the conductors (mainly conductive copper wires), these cables generally contain polymer-insulation, jacket/sheathing or bedding. All types of cables can then produce a significant quantity of fuel that can contribute to fire and also to its propagation. Indeed, as they need to pass through fire doors and are frequently located in horizontal and vertical ducting, they have a significant potential to increase the fire hazard in a building as they contribute to the spread of fires. Thus, they need to pass tests that are generally based on real-scale fire scenario. These tests are large-scale tests and require a large amount of cables to be tested and even if they ensure good fire performances of the cables, they can be an issue in the development of new and more efficient cables.

With the new harmonized European classification system in place for building products such as cables and pipe insulation, all European end-users of flame retarded products seek to comply with these standards. It is therefore of great importance to be able to predict the fire performance of end-products based on small scale tests in the development phase, as it would be far too costly and time consuming to make full end-products during this stage of a product development. The prediction of large scale results can be achieved by finding correlation between large, intermediate and small scale tests. This showed to be effective when correlating the Room Corner Test to the Small Burning Item test. Few studies were conducted on how to predict full scale behavior of products based on small scale experiments. These studies include ConeTools, developed by SP Fire Research, where SBI and Room-Corner test results are predicted based on cone calorimeter test results for building materials [1]. First steps towards extending the ConeTools to include cable testing apparatus were made, but the model needs further refinement in order to be considered as a complete tool for developing flame retarded products.

Another way to predict the large scale test and support materials development is to develop numerical models that can predict small to large scale tests results using different material properties as inputs data. Sensitivity analysis can then be performed in order to find the relative importance of one parameters against the others and thus gives clues for further material development. The development of computational tools focused on the modelling of the gas phase processes such as turbulence, combustion and flames. In particular, the Fire Dynamics Simulator (FDS) was developed and validated for scenario where the gas phase action dominates (such as plumes or compartment fires for example). However, a large variety of models for the condensed phase action have been developed for the last decade (FDS pyrolysis sub-model [2], Gpyro [3], ThermaKin [4] and Pyropolis [5] for example). Despite those developments, pyrolysis models are yet seldom applied to complex objects or to formulated materials. For instance, numerous studies previously conducted successfully modelled mass loss and heat release histories of charring and non-charring polymers undergoing an external heat flux. This work is thus focused on the development of a pyrolysis model and a small scale test applicable to cables. In particular, typical formulations of polyolefin-based materials were examined, namely, an ethylene-vinyl acetate (EVA) flame retarded by a combination of mineral fillers with and without synergists.

This PhD thesis is divided into five different chapters. The first chapter gives a general background about EVA and the fire retardancy of EVA materials. The different types of flame retardants commonly used with EVA are investigated. Then, an overview of pyrolysis modelling from the physical explanation to mathematical expressions is presented. The last section of this chapter gives information about the pyrolytic decomposition of EVA and EVA formulated with aluminum trihydroxide (ATH). EVA nanocomposites and their decomposition are also investigated since nanoparticles are often used as synergists in polyolefin based cables.

The second chapter presents the materials and methods used in this study. The polymer and the flame retardant additives are described as well as the materials preparation techniques. Then, the methods used for the characterization of the thermo-physical properties of the materials are explained. Finally, tests to evaluate these properties as well as the fire behavior of the materials and their thermal stabilities are also depicted.

Chapter three is dedicated to the investigation of the pyrolytic decomposition of EVA/ATH materials as well as the characterization of their thermo-physical properties as a function of temperature. The objectives of this chapter are to understand how our materials decompose and to determine suitable inputs data for modelling purposes which would be consistent with the decomposition pathways.

In chapter four, the decomposition of EVA/ATH and EVA/ATH/nanoclays (NC) is numerically simulated. The inputs determined in chapter three are first validated using gasification experiments. Then, mass loss cone results are simulated.

The last chapter presents the development of a novel small scale test for the study of the fire performance of cables. Indeed, the fire performances of cables are generally carried out using large scale fire tests that are difficult to numerically simulate. Thus, a small scale test was developed in this PhD work with a clear link to large scale test fire scenario. The bench-scale test was then be applied for material screening.

At the end of this work, a general conclusion is given and a proposal for future work on this topic is suggested.

CHAPTER I. STATE OF THE ART

In this chapter, the fire retardancy of ethylene vinyl acetate (EVA) will be discussed with a specific emphasis on mineral fillers and their synergists. Moreover, the fundamentals of 1D pyrolysis modelling will be presented from the simplest model to the more generalized one. At the end of the chapter, the decomposition of EVA composites as well as some of their thermo-physical properties of interest for modelling will be presented.

I.1. FLAME RETARDANCY OF EVA COPOLYMER

I.1.1. WHAT IS EVA?

Ethylene vinyl acetate (EVA) is a copolymer made through the copolymerization of ethylene and vinyl acetate (VA). Its structure is presented in **Figure 1**.

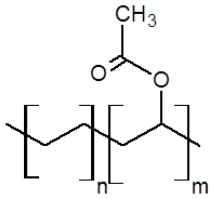

Figure 1: Structure of EVA copolymer

The copolymerization of EVA was first reported in 1938 [6] and was described by Perrin in 1940 [7]. Since that date, a lot of patents concerning the polymerization of EVA can be found in the literature [8–11]. Generally, EVA is obtained via radical copolymerization of ethylene and vinyl acetate (**Figure 2**). The polymerization is initiated chemically (by *e.g.* azocompounds) or using high energy radiation. The reaction can be carried out in every ratio of the co-monomers as the reactivity ratios are close to one [12]. Therefore, a random distribution of the co-monomers in the chain is achieved. One occurring problem of the polymerization reaction is the low water solubility of ethylene (3.5 mg/100 mL at 17 °C). Vinyl acetate on the contrary has a better one (2 g/100 mL at 20 °C). Another solvent than water is therefore necessary for the polymerization reaction of EVA. Toluene, benzene, heptane or *tert*-butanol are often used as solvents. Commonly the polymerization reaction is catalyzed using *e.g.* trialkylaluminum-Lewis base and peroxide mixture [13] or a ternary catalyst consisting of equimolar amounts of $AlEt_3$, $ZnCl_2$ and CCl_4 [14].

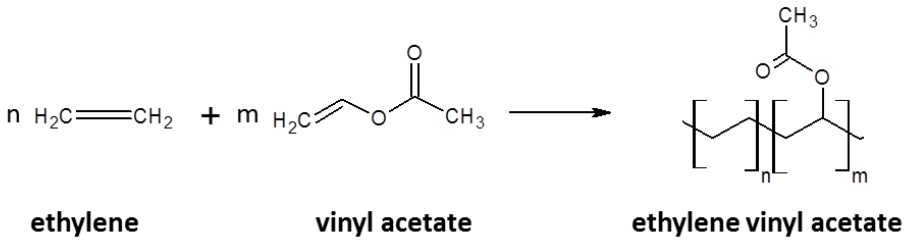

Figure 2: Copolymerization of ethylene and vinyl acetate

As a consequence, the physical properties of EVA copolymer depend on the VA content in the material as summarized in **Table 1** [15,16]. Transparency, flexibility, density, glass transition temperature, weather resistance, stickiness and filler acceptance of EVA materials increase with increasing VA content. On the other side, hardness, stiffness, melting point, chemical stability, yield stress, and crystallinity decrease with increasing VA content. Depending on the ethylene/vinyl acetate ratio, EVA copolymers can exhibit elastomeric or thermoplastic properties. Between 0-40 wt% and 80-100 wt% of VA content, EVA copolymers are semi-crystalline thermoplastics whereas they are rubber-like elastomeric polymers in between.

Table 1: Change of physical properties with increasing VA content in EVA

Increase	Decrease
Transparence	Hardness
Glass transition temperature	Stiffness
Flexibility	Melting point
Density	Chemical stability
Weather resistance	Yield stress
Stickiness	Stability of shape in warmth
Polarity	Crystallinity

I.1.2. LIMITATION ON THE USE OF EVA

As described in the previous section, due to their broad range of properties, EVA can be used in various applications by tuning its vinyl acetate content. For instance, due to their high filler acceptance, they can be used in cables and wires, inks or compounding for toys or automotive industries. EVA materials are also used for hot melt adhesives or packaging films and coatings.

For some of their applications, EVA-based materials have to comply with several standards, such as mechanical tests, chemical tests (ageing, non-migration of chemicals, *etc.*) and also flammability tests. For instance, for the toys industry, EVA copolymers can be used to produce foams for cuddly toys and have to comply with European standards EN 71-2. In that case, the test is carried out in a specified flammability chamber after preconditioning the specimen. A small gas flame is applied to the sample for a specified period of time. Upon removal of the flame, the burning duration is recorded. When required,

the flame spread is determined by measuring the time for the flames to spread over a known distance. Samples burning faster than 30 mm/s fail, while those with a burning rate between 10 and 30 mm/s must display the following warning: “Warning! Keep away from fire”. Similarly, materials used in the automotive industry have to comply with fire standards. For instance, materials used for the interior of various vehicles, from classical automotive to tractors for agriculture or forestry have to comply with ISO 3795 [17]. In another case, EVA based cables (and more generally, polyolefin based cables) need also to comply with fire safety regulation standard. More specifically, European regulation has recently included cables in the Construction Product Regulation (CPR). The objective is to get a harmonization of national fire tests for buildings products at the European level in order to facilitate their transportation, their development and the commercialization of new products in Europe.

Cables have thus to comply with the European Standard EN 13501 [18]. This standard gives guidance on the tests to be performed to get the classification (Euroclass). For Euroclass A_{ca}, the EN ISO 1716 [19] test have to be passed and cables have to exhibit a gross heat of combustion lower than 2.0 MJ/kg. Euroclass $B1_{ca}$ to D_{ca} can be obtained by passing the EN 60332-1 [20] and the EN 50399 [21] tests. Euroclass E_{ca} is obtained if the damaged length at the EN 60332-1 [20] is lower than 425 mm and the cable is thus classified F_{ca} if any of these criteria are met. Note that for Euroclasses $B1_{ca}$ to D_{ca}, additional test for acidity have to be performed and other considerations such as smoke production, flaming droplets are also studied. The EN 50399 (**Figure 3**) is a large-scale test method where several cables are mounted on a ladder and impacted by a 20.5 kW (or 30 kW if classification $B1_{ca}$ is required) methane burner for 20 min. The heat release rate (HRR) is monitored along with the smoke production rate as well as the final damaged length. The EN/IEC 60332-1 (**Figure 3**) is a small scale test method where a 1 kW burner tilted at 45 ° is applied for 30 to 120 s on a 500 mm cable depending on its diameter. The final damaged length is noted after flameout of the cable.

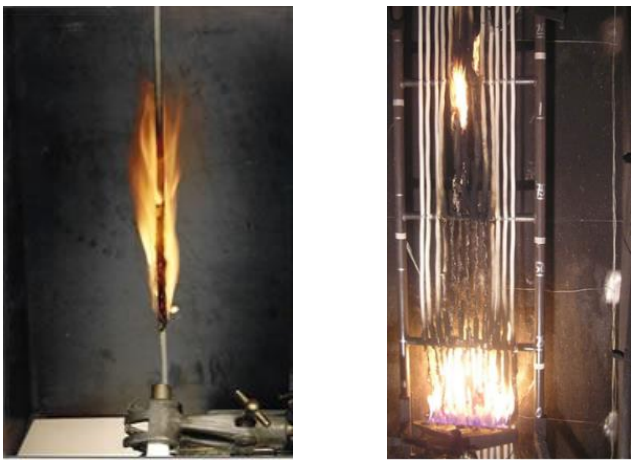

Figure 3: Cables tested in EN 50399 apparatus (right) and cable tested according to EN 60332-1-2 test (left)

I.1.3. HOW TO FLAME RETARD EVA?

I.1.3.a. Flammability of EVA copolymers

In order to comply with the previously described standards, EVA based materials have to be flame retarded. Indeed, due to its organic nature, EVA is a flammable material. The flammability of EVA copolymers is linked to its vinyl acetate content (VAC). Indeed, the higher the VAC, the higher the Limiting Oxygen Index (LOI) of the EVA and the lower the heat of combustion (**Figure 4**).

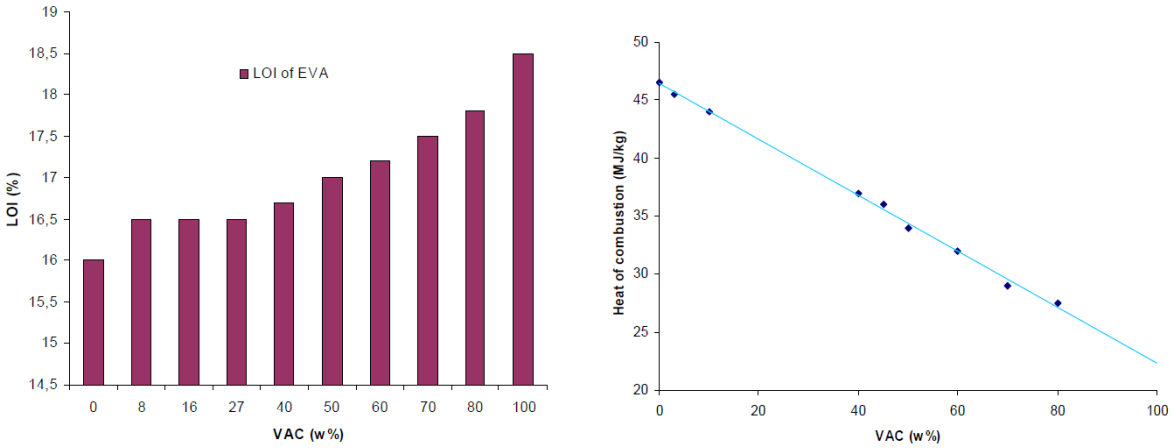

Figure 4: Influence of vinyl-acetate content on the LOI value (left) and heat of combustion (right) of EVA copolymers [22]

These improvements are not really significant since values remain poor *i.e.* from 16 to 18.5 vol%. On the opposite, the heat of combustion of EVA varies from 46 MJ/kg for low VAC values to around 30 MJ/kg for EVA containing more than 60 wt% of VA (**Figure 4**). For any VAC value, the UL-94V rating of EVA is HB. Those results however show that virgin polymer is considered as highly flammable and needs to be flame retarded to comply with legal fire requirements.

I.1.3.b. Mode of action of fire retardants

To improve the flame retardancy of EVA, flame retardant additives are usually added to the virgin matrix. The effectiveness of these additives depends on the fire scenario of the considered tests. For instance, additives promoting dripping can be very effective for getting a V2 classification in UL-94V test but will have a limited impact in cone calorimeter experiments. On the opposite, gas phase additives will be extremely effective to reach high LOI values.

Flame retardant additives can have a physical and/or a chemical mode of action in the gas and/or condensed phase. The physical action takes place by cooling and/or dilution of fuels and/or formation of a protective layer. In that cases, there are no or low interactions between the polymer and the additives. In the first case, materials are protected through endothermic decomposition of the fire retardant additives (generally dehydration) leading to a limitation of the temperature increase. The protection by dilution takes place through the addition of compounds releasing inert gases (such as water or carbon dioxide) when decomposing. Thus, these additives dilute the fuel in the gaseous phase. Finally, a protective layer of low conductivity can be formed when materials are exposed to an external heat flux. This layer protects the materials by reducing the net heat flux and the mass transfer inside the materials.

Materials can also be flame retarded though a chemical mode of action. In the condensed phase, such additive can catalyze the formation of carbonaceous residue (charring) on the polymer surface limiting the volatilization of the fuel and also limiting oxygen diffusion inside the materials. This char insulates the underneath polymer from the external heat. On the opposite, condensed phase additives can also accelerate the polymer decomposition and induce the flowing of the polymer. The burning materials can thus be removed from the flaming region and the combustion process is then stopped. In the gas phase, flame-retardants producing radicals can poison the flame by interfering with the radical mechanisms of the combustion process. Consequently, the exothermic processes occurring in the flame are limited and the system cools down, reducing the release of flammable gases.

I.1.3.c. Use of mineral fillers

Among the various approaches that were developed to flame retard materials, first attempts consisted in the use of halogenated flame retardants either grafted onto the copolymer chain [23,24] or added during the processing of the materials. Some studies focused on the fire retardancy of EVA using halogenated additives [25,26]. However, there is a growing demand led by industrial sector for non-halogenated flame-retardants due to possible effects on health and environment of some of these additives.

Due to their low cost and high level of flame retardancy, mineral fillers appear as an interesting and extensively studied alternative. The major mineral fillers are aluminum tri-hydroxide (ATH), magnesium di-hydroxide (MDH) and less frequently hydromagnesite ($Mg_5(CO_3)_4(OH)_2.H_2O$) or boemhite AlOOH [27–30]. It is noteworthy that a number of other alternatives were investigated but no records were found on their use at a large scale or their commercialization are subjected to confidentiality causes.

The mode of action of mineral fillers is based on the endothermic release of inert gases (water in the case of metal hydroxides or carbon dioxide for metal carbonates such as hydromagnesite) and the formation of a protective layer at the surface of the material [31]. For example, ATH and MDH decompose endothermically between 200-220 °C and 300-350 °C respectively, while releasing water and forming alumina (or aluminum oxide Al_2O_3) or magnesium oxide as shown in ***Eq. 1*** and ***Eq. 2***.

$$2\ Al(OH)_3 \rightarrow Al_2O_3 + 3\ H_2O \qquad \textbf{\textit{Eq. 1}}$$

$$Mg(OH)_2 \rightarrow MgO + H_2O \qquad \textbf{\textit{Eq. 2}}$$

The endothermic decomposition of mineral fillers slows down the diffusion of heat into the material and thus helps to decrease the temperature of the material. The rate of polymer decomposition decreases and possibly leads to delay the ignition. Moreover, the release of inert gases can dilute the fuel in the flame. Finally, the oxide layer formed during the decomposition of the mineral filler can act as a physical and insulative protective layer.

I.1.3.d. Other flame retardants

Other types of flame retardants were also proposed to flame retard EVA. Phosphorus based flame retardants such as red phosphorus [32,33], phosphates, polyphosphates, phosphonates and phosphinates [34] can be used in many polymers. Concerning EVA, ammonium polyphosphate exhibits low compatibility with EVA leading to limited industrial applications. Even if phosphorus additives can inhibit ignition and reduce smoke production, they can also present ageing issues and can be water sensitive. They are therefore not considered as a principal flame retardant for cables materials. Nonetheless, they can be used as synergists or co-additives with other flame-retardants. For example, Cérin *et al.* [35,36] showed that a combination of ATH and organic phosphinate (Exolit^{TM} OP1230) at a ratio 2:1 in a 60 wt% VA containing EVA led to the formation of alumino-phosphate compounds that exhibit a higher barrier effect than the aluminum oxide obtained with ATH alone.

Nitrogen based flame retardants are melamine-based compounds such as pure melamine, organic and inorganic melamine salts and melamine condensation products (melam, melon and melem). Few works report the use of nitrogen containing flame-retardants in EVA. Zilberman *et al.* [37] showed that the incorporation of 60 wt% melamine into EVA led to comparable fire retardant properties in terms of pHRR as the virgin polymer demonstrating their poor efficiency. Nonetheless, synergistic effect of melamine salts (melamine borate and phosphate) when combined with ATH were found by Hoffendahl *et al.* [38]. Regarding insulator or cable formulation, no reports of nitrogen additives flame-retardants were found in the literature.

Up to now, ATH is the best-selling mineral filler and the most used flame retardant in EVA. The main reasons for its wide use are its low cost, its flame retardant efficiency and its “environment friendly” behavior. However, for achieving good fire performances high loadings are generally required (60-70 wt%). Those high loadings can have a large impact on mechanical performances [27,39]. Moreover, the viscosity of the formulation is increasing while increasing ATH content and processability can thus be tricky, especially for cables. Synergistic compounds, such a zinc borates [40,41], silicon compounds [42–46], carbon nanotubes (CNT) [47] or nano-clays [48–54] were proposed to improve the properties of EVA/ATH formulations. The synergism between mineral hydroxide and nanoparticle is discussed in the following section.

I.1.4. NANOCOMPOSITES AS FLAME RETARDANT AND SYNERGISTS

The incorporation of nanoparticles into polymers attracted much interest in the last ten years. Indeed, apart from providing fire properties to the materials, the low loadings of nanoparticles achieved do not modify the other properties or even enhance some of them (such as the mechanical properties [55,56]). A wide range of nanoparticles was incorporated in EVA: layered or fibrous silicates, layered double hydroxides, polyhedral oligomeric silsesquioxanes and carbon nanotubes. The following section will emphasize on nanoclays and more specifically on montmorillonite (MMT) as it exhibits good fire performance in EVA [51,57] and shows synergistic effect with mineral fillers [50,52–54,58–60], especially for the cable application [59,60].

Nanoclays and in particular montmorillonite are widely used in polymers because they improve their flammability properties. They are layered silicates (phyllosilicates), which gives them the possibility to develop particular morphologies. MMT is an aluminum hydrosilicate, in which the proportion of silicic acid to alumina is about 4:1. The individual layers feature a total of three layers. As shown in **Figure 5**, the two outer layers are silica sheets, composed of SiO_4 tetrahedra. They envelope a central sheet of aluminum ions, with the result that each aluminum cation is surrounded in octahedral form by oxygen atoms of the silicate groups.

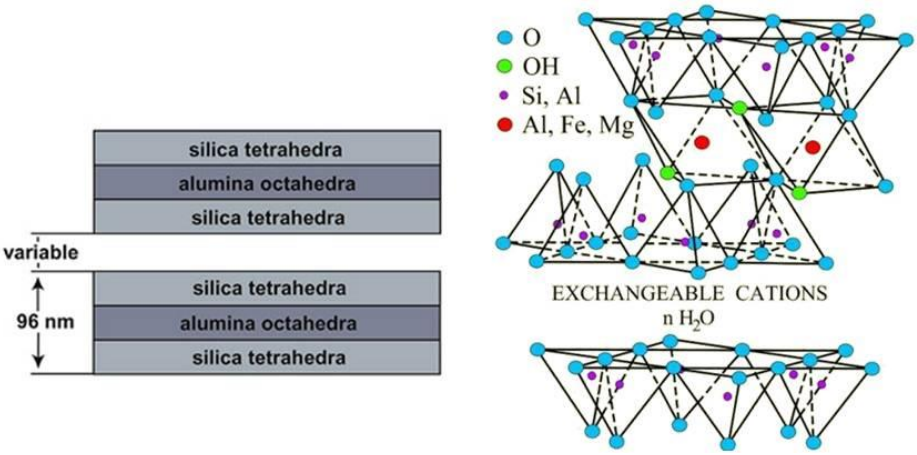

Figure 5: Montmorillonite structure [61]

When added into polymer, three categories of montmorillonite composites are generally distinguished (**Figure 6**):

(a) micro-composites: there is no penetration of the polymer into the clay lamellae

(b) intercalated composites: the insertion of polymer into the clay structure occurs so as to increase the spacing between platelets in a regular fashion

(c) exfoliated composites: the individual clay layers are dispersed as single platelets into a continuous polymer matrix.

The main parameter responsible for the dispersion quality in the composites is the compatibility of the nanofillers with the polymer matrix. Therefore, to improve the dispersion of the nano-additives, it is important to increase this compatibility by modifying the filler or the matrix. According to Duquesne *et al.* [57], the modification of the surfactant of the clay layers is an efficient way to increase MMT dispersion and thus thermal and flame retardant properties of EVA.

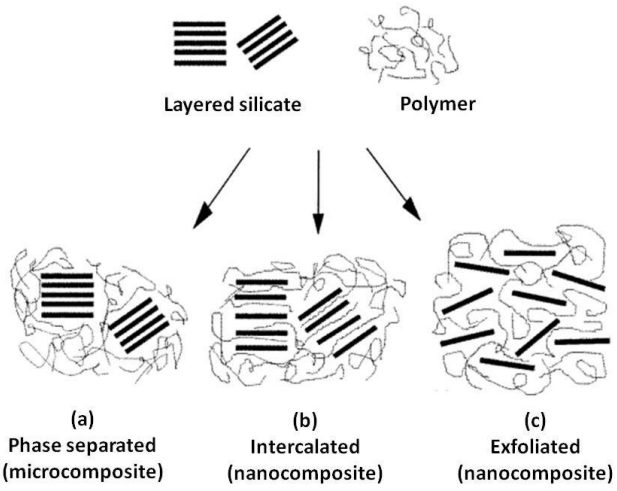

Figure 6: Scheme of different types of composites arising from the interaction between layered silicates and polymer [57]

According to Gilman *et al.* [62], the flame retardant mechanism of clay based nanocomposites is linked to the formation of carbonaceous silicate char on the surface during burning. Two hypotheses can explain how MMT-rich char surface is produced [63]. There is an assumption that the MMT is precipitated during pyrolysis as a result of progressive gasification of the polymer, but another approach suggested a

migration of MMT during and after decomposition of the nanocomposites structure due to the lower surface energy of MMT [64]. This layer insulates the underlying material and slows down the mass loss rate of decomposition products. Recently Leszczynska *et al.* [65] studied the mechanism that controls thermal stability of polymer/MMT nanocomposites. According to these authors, there are several factors influencing the thermal stability, among which:

-A labyrinth effect induced by intercalated or exfoliated structure of MMT, which limits oxygen diffusion inside the nanocomposites samples.

- A steric effect, due to the interactions between the polar MMT layers and the polymer matrix thus limiting the polymer chain motion.

- A barrier effect, which protects the bulk of sample from heat, decreases the rate of mass loss during thermal degradation of polymer nanocomposites and generates more intensive char formation on the surface.

- A catalytic effect of the clay effectively promoting char-forming reactions.

I.1.5. CONCLUSION ABOUT FIRE RETARDANCY OF EVA

As seen in the section of this chapter, EVA is a flammable polymer that needs to be formulated and fire retarded before using it. Even if other flame retardant can be used, ATH is among the most commonly used for EVA. Synergists such as nanoparticles (mainly nanoclays) can be used to further improve the fire performances of the materials.

In this section, it was also emphasize that materials have to comply several large-scale fire tests before being launched in the market. This can be a limitation for the development of new and efficient materials. One way to go further regarding this limit consists in the modelling of the fire behavior of the material including pyrolysis modelling. This will thus be detailed in the following part.

I.2. PYROLYSIS MODELLING OF POLYMERS

The use of numerical models in fire protection engineering is widespread. Partially because of the increase of computer power, fire modelling reached the point that fire development can actually be predicted. These predictions and models involve the coupling of a gas phase model that include heat transfer, fluid dynamics and combustion with a condensed-phase model that simulate the heating and pyrolysis of the condensed phase fuel.

Nowadays even if numerical models of the development of fires are more reported in the literature, the predictive capabilities for condensed phase phenomena are more limited compared to these of gas phase phenomena. Indeed, the Navier-Stokes equation governs fire induced gas fluid flow and huge progresses were made in turbulence modelling and numerical methods. Non-premixed combustion models were also developed, and combustion is now understood in terms of elementary reactions for simple fuels such as methane or dihydrogen [66,67]. A wide variety of solid fuels can be found in fires such as wood, fiber reinforced composites, thermoplastics, thermosets. However, all of them exhibit different behaviors when undergoing fire or heat including charring, non-charring, dripping, delamination or smoldering for example.

The biggest challenges of pyrolysis modelling for application in real-world fires is thus to (1) set down the governing equations representative of the phenomena involved when a material decomposes; (2) to make enough simplifications keeping real and representative physics and (3) to characterize the inputs data from bench scale experiments. The following part of this chapter is thus dedicated to the explanation of the equations governing the decomposition of solid materials before presenting some models in the next sections.

I.2.1. BASIC OF PYROLYSIS MODELLING

Pyrolysis refers to the thermal decomposition of a material caused by its heating in inert atmosphere. In case of fire, as the flame consumes the oxygen from the air, the material is assumed to be in anaerobic/pyrolytic conditions. Pyrolysis is a complicated phenomenon, which is a combination of the following interactive and inter-dependent processes:

- Heat transfer through the materials
- Thermal decomposition that produces combustible or non-combustible pyrolyzates
- Mass transfer of pyrolyzates out of the decomposing material

I.2.1.a. Use of empirical models

A way to perform pyrolysis modelling is to use empirical solutions. This approach analytically solves only the heat transfer of pyrolyzate materials at the pre-ignition stage assuming that materials are inert and semi-infinite or lumped. Instead of solving the thermal decomposition and mass transport equations, empirical models are using data from bench or small-scale test in order to simulate large-scale test results.

For instance, the mass loss rate of heat release rate is extracted from cone calorimeter studies at a given irradiance. Then the same material in a large-scale test model is assumed to release heat (or loose mass) with the previously determined rate. The main limitations of this approach can be described as follows: (1) the data extracted from the bench-scale testing have to be representative of the heat flux or fire scenario of the modelled test; (2) the heat transfer still needs to be solved at the pre-ignition stage; (3) the ignition is modelled using a single parameter (generally ignition temperature T_{ig} at surface). In this type of model, surface temperature of a material is solved based on the 1D transient heat conduction equation. The rate of surface-temperature increase is dependent upon the thermal inertia ($k/\rho.Cp$) of the material. The thermal inertia of a material is the ratio between the thermal conductivity (k), and the specific heat capacity ($\rho.Cp$) where ρ is the density and Cp the heat capacity of the material. The material is assumed to ignite when its surface temperature reaches a material-dependent value (T_{ig}).

A way to determine such ignition temperature criterion was proposed by Quintiere and Harkleroad [68] when studying thermally thick materials such as wood slabs. The method is described in ASTM E1321 [69]. The first step of the method consists of conducting ignition tests using cone calorimeter, mass loss cone or Lateral Ignition and Flame spread Test (L.I.F.T.) apparatus for instance. Times-to-ignition are obtained at heat-flux levels in descending order at intervals of 5 kW/m^2 to 10 kW/m^2. Once the critical heat flux ($\dot{q}''_{cr}$) is known, T_{ig} can be calculated from a heat balance at the surface (see **Eq. 3**) after very long exposure, since heat conduction into the specimen then becomes negligible.

$$\varepsilon\dot{q}''_{cr} = h_c\left(T_{ig} - T_\infty\right) + \varepsilon\sigma\left(T_{ig}^4 - T_\infty^4\right) \qquad \textit{Eq. 3}$$

A similar empirical approach was proposed by Janssens [70,71] to estimate critical heat flux and ignition temperature. Calorimetric experiments have also to be performed at different incident heat flux. Instead of determining experimentally the critical heat flux for ignition, it was defined as the intercept with the abscissa of the plot of $t_{ig}^{-0.55}$ versus the incident heat flux $\dot{q}''_e$. Indeed, Janssens' extensive numerical calculations showed that the following expression (**Eq. 4**) is suitable for correlating piloted ignition data of thermally thick solids. Then T_{ig} is calculated as in the approach of Quintiere using **Eq. 3**.

$$\dot{q}''_e = \dot{q}''_{cr}\left[1 + 0.73\left(\frac{k\rho Cp}{h_{ig}^2 t_{ig}}\right)^{0.55}\right] \qquad \textit{Eq. 4}$$

Contrary to ignition temperature, critical heat flux for ignition is assumed not to be a material-dependent property. Indeed, it depends on the convection environment. For instance Dientenberger [72] obtained critical heat flux of 14.3 kW/m² and 18.8 kW/m² for conditioned redwood respectively on cone calorimeter and L.I.F.T. apparatus. Note that these methods can also provide information about the thermal inertia of the material. However, the validity of the determined thermal parameters is questioning because of the temperature changes in the material and because of the decomposition of the material.

Since ignition temperature or critical heat flux for ignition are measured or estimated by the methods described above, they can be used as inputs for further pyrolysis modelling. The evolution of temperature have thus to be numerically solved using **Eq. 5** in the case of the simplest heat transfer model. When the temperature is higher than T_{ig}, then the material is assumed to release heat according to a prescribed heat release curve extracted from calorimetry experiments. The heat release rate is thus not correlated to the mass loss rate, as it is not solve. This approach is very convenient as it is easy to implement and requires few inputs and limited effort of characterization.

$$\rho Cp\frac{\partial T}{\partial t} = \frac{\partial\left(k\frac{\partial T}{\partial x}\right)}{\partial x} \qquad \textit{Eq. 5}$$

The determination of T_{ig} can be questionable and the relevance of the approach is restricted to the choice of the right heat release curve to implement in the model. Indeed, the HRR behavior depends on the tested material but also on the incident heat flux and on the thickness of the sample [73]. Thus, it is important to implement in such model, a heat release rate curve of the material with a thickness close to the one of the final application and using an incident heat flux representative of the test or fire scenario that is modelled.

Comprehensive pyrolysis models considering the heat transfer, the thermal decomposition of the material and the gas transport are assumed to be more precise as all phenomena are analytically solved. The next part of this chapter will thus presents such models.

I.2.1.b. Comprehensive models

The most complex approach available to describe the fire behavior of materials consists to directly solve the heat transfer, the thermal decomposition and the mass transport using conservation equations. In this approach, heat transfer is modelled using conservation of energy. Thermal decomposition is modelled using conservation of mass by defining a finite reaction rate through kinetic modelling. This approach can also be used for mass transfer effects through simplified or general Darcy law. Numerical calculations are conducted using finite difference, finite element or integral formats to determine mass loss and temperature profiles from the heat-exposed front surface to unexposed back surface with respect to increasing time. Due to the nature of this problem, mass and heat transfer equations are coupled together and no analytical solution exists. Therefore, a numerical solution must be sought.

This three dimensional transient problem can generally be simplified to a one dimensional (1D) problem, lowering the computational power required to solve this system of equations. **Figure 7** shows the physical situation involved in 1D pyrolysis modelling. δ is the thickness of the initial polymer.

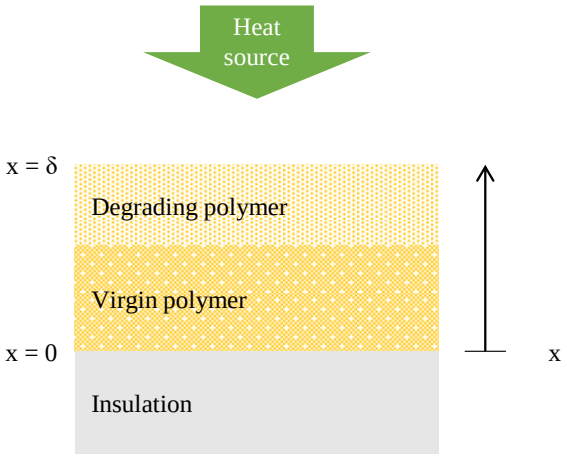

Figure 7: Scheme and geometry of physical model

In most cases, the final thickness can be assumed to be similar to the initial thickness but in the case of intumescent system or ablative material, the computational domain have to be respectively extended or restricted as a function of time. In such cases, the assumption that the volume change of a cell is negligible (Δx = constant) is not valid and further mathematical development are needed.

Even if all comprehensive models differ in their complexity, they all are based on energy and mass conservation equations as described in **Eq. 6** and **Eq. 7**. In these equations, ρ is the density, *Cp* the heat capacity, *k* the thermal conductivity, A_r, the pre-exponential factor, E_r the activation energy and *m* the mass. The differences between all existing models are then based on the way the inputs are implemented in the model: 1st order or 2nd order polynomials, raw data as a function of temperature or constant parameters but also on the phenomena that are consider in the models. As an example, models can consider or not in-depth absorption of heat inside the materials by Beer-Lambert law. Authors have then to choose to simplify or not their model in regards of the importance of these phenomenon according to them.

$$\rho Cp\frac{\partial T}{\partial t} = \frac{\partial\left(k\frac{\partial T}{\partial x}\right)}{\partial x} + \text{other process (reaction, in depth absorption etc.)} \qquad \textit{Eq. 6}$$

$$\frac{\partial m_i}{\partial t} = \upsilon_r^i A_r \exp\left(\frac{-E_r}{RT}\right) f(m_{reactant}) - \text{diffusion (for gas only)} \qquad \textit{Eq. 7}$$

To solve these systems of equations, the decomposition of a material is assumed to be irreversible and produce either another solid specie (or even liquid if considering the melting of the materials), a gas or a mixture of both as defined by **Eq. 8**. By using Arrhenius law, it is possible to define the rate of decomposition $\dot{r}_r$ as a function of kinetic parameters of reaction *r*, activation energy (E_r) and pre-exponential factor (A_r) and kinetic model $f(m_A)$ as shown in **Eq. 9**. The rate of formation of solid specie (noted B_{solid} in **Eq. 8**) is defined by **Eq. 10** while and the rate of decomposition of the initial specie A_{solid} is expressed in **Eq. 9**. It can be noted that the solid B_{solid} can then react himself to give further solid or liquid and gaseous products or remain as the final residue of the material. The conservation of gaseous species can be expressed with the rate of formation of this species and additional terms for the diffusion can also be considered.

$$A_{solid\ or\ liquid} \rightarrow \upsilon_s B_{solid\ or\ liquid} + \upsilon_g C_{gas} \qquad \textit{Eq. 8}$$

$$\frac{dm_A}{dt} = -A_r \exp\left(\frac{-E_r}{RT}\right) f(m_A) \qquad \textit{Eq. 9}$$

$$\frac{dm_B}{dt} = \upsilon_s A_r \exp\left(\frac{-E_r}{RT}\right) f(m_A) \qquad \textit{Eq. 10}$$

The definition of the kinetic model does not follow any universal rule except the search for the best quality of fit between experimental and simulated data. Because of the complexity of the process of decomposition, it is impossible to find an accurate equation to describe all types of thermal decomposition, especially in the case of complex decomposition pathways and varying kinetics [74].

Indeed, the thermal decomposition of a solid is followed by the emission of gaseous products through heterogeneous reactions. It can thus characterized by nucleation or diffusion mechanism and thus by various kinetic model f(m). A non-exhaustive list of common kinetic models is reported in **Table 2.**

Table 2: Common kinetics decomposition functions used in the field of polymer decomposition

Reaction rate expression	Reaction type
$\dot{r_r} = A_r \exp\left(\frac{-E_r}{RT}\right).{m_A}^n$	n^{th} order reaction
$\dot{r_r} = A_r \exp\left(\frac{-E_r}{RT}\right).{m_A}^n.(1 + K_{cat}.m_X)$	n^{th} order reaction with autocatalysis of specie X
$\dot{r_r} = A_r \exp\left(\frac{-E_r}{RT}\right).n.m_A.[-\ln(m_A)]^{\frac{n-1}{n}}$	n^{th} dimensional nucleation according to Avrami-Erofeev
$\dot{r_r} = A_r \exp\left(\frac{-E_r}{RT}\right).\frac{0.5}{m_B}$	one dimensional diffusion
$\dot{r_r} = -A_r \exp\left(\frac{-E_r}{RT}\right).\frac{1}{\ln(m_A)}$	two dimensional diffusion
$\dot{r_r} = A_r \exp\left(\frac{-E_r}{RT}\right).m_A.m_B$	Prout-Tompkins equation

I.2.2. THE SIMPLE MODEL: HEAT TRANSFER COUPLED WITH KINETICS AND ENTHALPIES OF DECOMPOSITION

As described in the previous section, partial differential equations of mass and heat transfer must be solved to model the heat release rate or mass loss rate observed in fire tests. These equations must accurately depict the pyrolysis reactions and the temperature profiles.

In one of the first model, published by Bamford *et al.* in 1946 [75], dealing with pyrolysis modelling and dedicated to wood, only heat conduction inside a material, release/absorption of energy by chemical reaction (**Eq. 11**) and kinetics of decomposition of the material were implemented (**Eq. 12**) [75]. In these equations, k, ρ and Cp are respectively thermal conductivity, density and heat capacity. H_r is heat released when a volatile product is formed (so the heat of decomposition).

$$\rho Cp \frac{\partial T}{\partial t} = \frac{\partial\left(k \frac{\partial T}{\partial x}\right)}{\partial x} - H_r \frac{\partial m}{\partial t} \qquad \textit{Eq. 11}$$

$$\dot{r_r} = \frac{\partial m}{\partial t} = -A_r . \exp\left(\frac{-E_r}{RT}\right) . m. \qquad \textit{Eq. 12}$$

In order to finalize the model, the boundaries conditions have to be expressed as in **Eq. 13**. In this equation, H(T) represents the total transfer coefficient at the surface, T_f represents the flame temperature, T the surface temperature, ε the emissivity of the flame, σ the Stefan's constant ($5.67\ 10^{-8}$ W/m²/K⁴) and *h* is a constant associated to a convective heat transfer coefficient. $h(T_f - T)$ represents the convection term, $\sigma\varepsilon T_f^4$ represents the radiation from the flame and $-\sigma T^4$ represents the radiation loss from the surface assuming that wood radiates as a black body.

$$H(T) = h(T_f - T) + \sigma\left(\varepsilon T_f^4 - T^4\right) \qquad \textit{Eq. 13}$$

Note that in [75], the inputs parameters (Cp, k, ρ *etc.*) were taken as constant values and were obtained from the literature available at that time. The kinetic parameters (E_r and A_r) were also estimated. It was shown that ever if the model was relatively simple, the calculated temperature at the center of the considered wood slab fits the experimental data. As shown in **Figure 8**, a good agreement is observed in the case of the 2 cm slab but the model under-predicts the temperature for all the duration of the experiment in the case of 4 cm slab. Interestingly, even if the simulated temperature curve is shifted in the case of 4 cm slab, the evolution of the temperature follows the same trend as the experimental data.

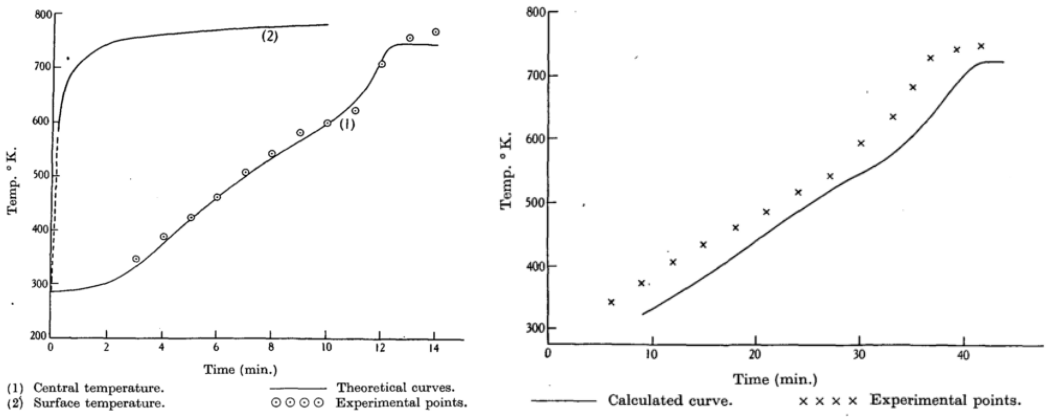

Figure 8: Comparison between calculated and experimental time-temperature curves for 2 cm slab (left) and 4 cm slab (right) [75]

Based on these results, the authors decided to investigate the release of gases when wood decomposes. It was found that a good criteria to describe the spontaneous ignition of wood slabs (with thicknesses ranging from 1 to 4 cm), was to assume that ignition occurs when the rate of gases release gets higher

than 2.5 10^{-4} g/cm²/s. Indeed the times to auto-ignition as well as burning duration were in good agreement with the experimental data using this criterion. Nonetheless, it should be noted that this criterion is more difficult to apply when the rate of gases release becomes higher than 2.5 10^{-4} g/cm²/s several times for a same sample as shown in **Figure 9**. Indeed, it would mean that flame should be observed, then extinguishes and the material would ignite again later (C in **Figure 9**). In practice, flickering flame were observed between A and B and steady flames appeared after C. This could validate that the auto-ignition or apparition of flames can be estimated by mean of empirical critical rate of gases release.

This study showed that a basic model, considering only heat conduction with absorption or release of energy by chemical reaction coupled with a mass balance equation can provide an efficient way to estimate the temperature and/or mass loss rate profiles.

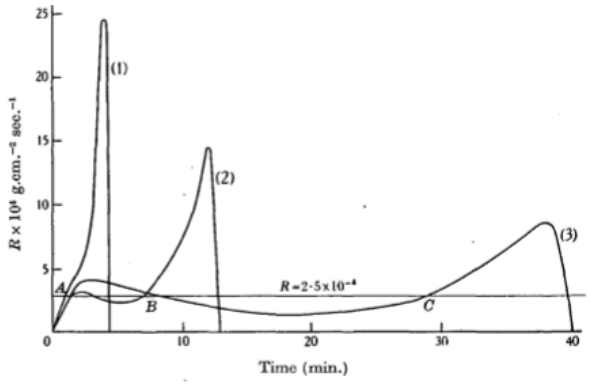

Figure 9: Rate of evolution of gases of woods sheets impacted by a flame. Curves (1) for 1 cm thick; (2) for 2 cm thick; (3) 4 cm thick sheets [75]

This study was based on simple characterization of the inputs data and empirical characterization of the boundaries conditions. It is thus expected that approaches that are more complex would be able to exhibit better prediction by considering more phenomena. Indeed, few studies use models solving so few phenomena. For instance, gas diffusion can play a role both in terms of energy balance and delay the mass release. Thus, models that are more complex were developed considering the diffusion of decomposition products. Moreover, in-depth absorption of the external heat source inside the materials in the heat balance and the diffusion of the gases out of the material in the mass balance are also widely considered in pyrolysis models.

I.2.3. A MORE COMPLEX APPROACH: GAS DIFFUSION AND HEAT IN-DEPTH ABSORPTION

A more complex approach when dealing with the pyrolysis of solid materials is to consider the gas diffusion inside the materials. Indeed, several models improved the approach previously described by taking into account the heat required to heat up the gases from ambient temperature to the temperature of the media in which the gas diffuses. This is represented by the term $-\sum_{g}^{gases} \dot{m}_{g}^{''}.\frac{d\left(\int_{0}^{T} Cp_g dT\right)}{dx}$ in **Eq. 14**. Note that this implies the fact that the heat transfer between the diffusing gases and the media *i.e.* the decomposed material is instantaneous. Another way to improve the model presented in **I.2.2** is to take into account the in-depth radiation of the incident heat flux. This implies that the heat source heats up the material via radiative transfer. This corresponds to $\frac{\partial \dot{q}_{rad}^{''}}{\partial x}$ in **Eq. 14**, where $\dot{q}_{rad}^{''}$ is defined in **Eq. 15**. It corresponds to a standard Beer Lambert law where the absorbed radiation decreases exponentially with the distance to the impacted surface. Note that no studies were found in the literature where the in-depth absorption coefficient A was measured for a material as a function of temperature and decomposition state. Indeed, the absorption of heat can change greatly depending on the temperature but also on the nature of specie, that absorbs the incident heat flux.

$$\rho Cp\frac{\partial T}{\partial t} = \frac{\partial\left(k\frac{\partial T}{\partial x}\right)}{\partial x} + \sum_{r}^{reac}(\dot{r}_r.Hr) - \sum_{g}^{gases}\dot{m}_{g}^{''}.\frac{\partial\left(\int_{0}^{T} Cp_g dT\right)}{\partial x} + \varepsilon\frac{\partial \dot{q}_{rad}^{''}}{\partial x} \qquad \textit{Eq. 14}$$

$$\dot{q}_{rad}^{''} = \dot{q}_{e}^{''}.\exp(-A.x) \qquad \textit{Eq. 15}$$

Taking into account the diffusion of the gases in the heat balance equation means that when evolving from the decomposing material, gases can absorb energy and remove it from the material as they are evolved from the surface. This part is thus directly proportional to the heat capacity of the gases Cp_g and to the mass flux of the decomposition gases $\dot{m}_{g}^{''}$, which is defined in **Eq. 16** and **Eq. 17**. Note that in this framework, mass flux is defined according to Fick law. A more complex approach would be to use Darcy law and to measure permeability or porosity of the materials as a function of temperature and decomposition state (pristine material, molten material, fully charred materials *etc.*). This approach will be presented in part **I.2.4**. The variation of mass of gaseous species varies as a function of reaction rate $\dot{r}_r$ and stoichiometric coefficient ν_r^g but also with the mass flux gradient $-\frac{\partial \dot{m}_{g}^{''}}{\partial x}$ as defined by the Fick law. Depending of mass transport coefficient D_g (or mass diffusivity) as defined in **Eq. 16**, the gases will evolve at different rates.

$$\dot{m}''_g = -D_g \frac{\partial m_g}{\partial x} \qquad \textit{Eq. 16}$$

$$\frac{\partial m_g}{\partial t} = \nu_r^g . \dot{r}_r - \frac{\partial \dot{m}''_g}{\partial x} \qquad \textit{Eq. 17}$$

The reaction rate $\dot{r}_r$ is expressed as a function of Arrhenius parameters: activation energy E_r and pre-exponential factor A_r. Note that **Eq. 18** presents the reaction rate of a first-order reaction but other reaction model can be used as already seen in **Table 2** (p.21).

$$\dot{r}_r = A_r . \exp\left(\frac{-E_r}{RT}\right) . m \qquad \textit{Eq. 18}$$

Regarding the boundaries conditions, two scenarios have to be considered. The first one, when no ignition occurs, can be used for the modelling of gasification experiments or before ignition in standard cone calorimetry experiments (**Eq. 19)**. In this case, the net heat flux at the surface impacted by the incident heat flux takes into account the part of the incident heat flux which is reflected and thus, only $\varepsilon \dot{q}''_e$ really impacts the surface. Then the surrounding air can cool the material surface. This is expressed by the term $h_c(T_{surface} - T_\infty)$ in **Eq. 19**. This convective cooling is directly proportional to the temperature difference between the surface and the surrounding air (which is assumed to be at T_∞, and generally set at 300 K). The convective heat transfer coefficient h_c is generally taken between 8 and 12 W/m^2/K as determined by several studies [76]. The material can also be cooled as the surface can re-emit heat. This is transcribed by the term $\varepsilon\sigma\left(T_{surface}^4 - T_\infty^4\right)$ in **Eq. 19**. The radiative cooling is then directly proportional to the emissivity of the material ε, as proposed by Stefan–Boltzmann law, and to the difference between the fourth power of the surface and ambient temperatures.

$$-\frac{\partial\left(k\frac{\partial T}{\partial x}\right)}{\partial x}_{x=\delta} = -\varepsilon \dot{q}''_e + h_c(T_{surface} - T_\infty) + \varepsilon\sigma\left(T_{surface}^4 - T_\infty^4\right) \qquad \textit{Eq. 19}$$

The other scenario to be considered for the boundaries conditions is the presence of a flame on the top of the surface impacted by the incident heat flux. It has to be noted that no common condition can be found in the literature regarding how to translate the presence of a flame into a boundary condition. It can be translated by one or several of the following methods applicable to **Eq. 19**: (1) removing the convective heat transfer, (2) adding an external heat flux from the flame or flame feedback [3,5,77] or (3) using a flame temperature T_{flame} in the convective and radiation terms.

Note that the change of the non-flaming condition to flaming boundaries conditions is generally triggered as the mass flow of pyrolyzates at the surface reaches a value higher than a critical mass flux for ignition [4,78]. It is interesting to note that this parameter is an empirical parameters that can be used to fit the time to ignition. It was already used in [79] for instance. The approach is similar to the one presented by

Bamford [75] in **I.2.2** (p.21). The value may also vary depending on the experimental conditions (rate of extraction of the pyrolyzates in a hood, presence of an igniter or study of self-ignition *etc.*).

$$-\frac{\partial\left(k\frac{\partial T}{\partial x}\right)}{\partial x}_{x=\delta} = -\varepsilon\left(\dot{q}_e^{"} + \dot{q}_{flame}^{"}\right) + \varepsilon\sigma\left(T_{surface}^4 - T_\infty^4\right) \qquad \textit{Eq. 20}$$

The boundary conditions for the mass transfer are not dependent on the presence or not of a flame above the exposed surface. The mass flux of component *i* at the surface $\dot{m}_g^{"S}$ is either a linear combination (as proposed in **Eq. 21)** or an exponential relation (as proposed in **Eq. 22)** of the mass of gas *i* at the surface m_i^S. The choice of one or the other condition is possible in the model, and the coefficient a_i and b_i are arbitrary values. The primary function of the linear expression is to remove or introduce gases from or to a pyrolyzing material. The exponential expression can be employed to simulate a surface reaction (such as oxidation) or dripping [4].

$$\dot{m}_g^{"S} = a_i . m_i^S - b_i \qquad \textit{Eq. 21}$$

$$\dot{m}_g^{"S} = a_i . \exp\left(\frac{-b_i}{RT^S}\right) \qquad \textit{Eq. 22}$$

The model described above was developed at the Federal Aviation Administration (FAA) and used in the frame of ThermaKin software [4]. It was successfully used to model both charring and non-charring polymers as well as corrugated cardboard and multiple floor covering in gasification experiments and standard cone calorimeter experiments [78,80–84]. In particular, cone calorimeter experiments were predicted for various polymers (High Density Polyethylene, High Impact Polystyrene or Poly(methyl methacrylate)) at various thicknesses (3, 7.7 and 9.4 mm) and various incident heat flux (25, 50 and 75 kW/m²). Nonetheless, the accuracy of the model was dependent of the conditions and varied from excellent (**Figure 10.a**) to poor (**Figure 10.b**). Indeed, for the latter case, even if the general trend of the curve is consistent with the experimental curve, the curve is shifted of around 900 s to higher times, suggesting that the quality of the inputs parameters is questionable. This also shows that even if it is possible to have a good fit between experimental and simulated data for given experimental conditions, the modelling of several and various conditions (different heat fluxes and several thicknesses) can be more difficult to achieve.

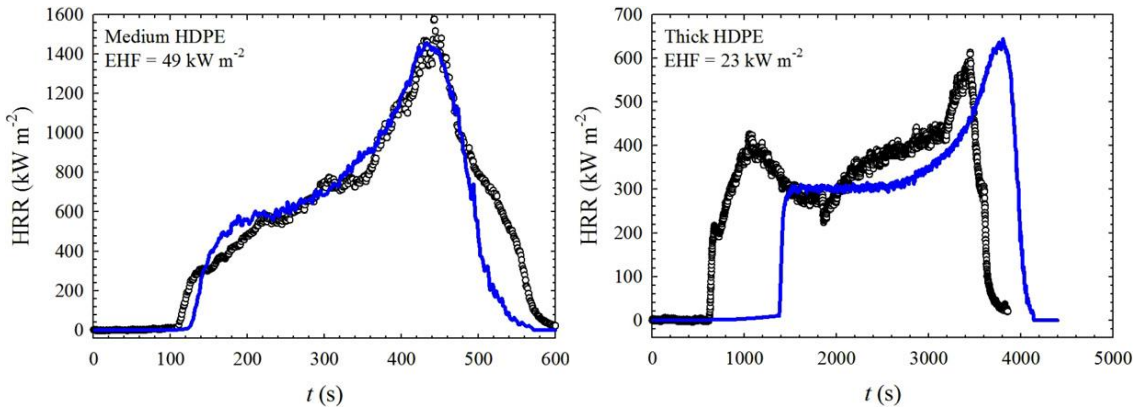

Figure 10: Predicted and experimental HRR curves for 3.3 mm thick HDPE at 49 kW/m² (a) and 9.7 mm thick HDPE at 23 kW/m² (b) [81]

In addition, ThermaKin was also used for the prediction of the combustion of low density polyethylene (LDPE), alone and in combination with carbon black or graphite [85]. Both neat polymer, neat additives and composites were first characterized and simulations were then performed for neat polymer and 10 wt% containing formulation as presented in **Figure 11**. These simulations permitted to understand and to quantify the influence of each physical property (density, heat capacity *etc.*) on the fire performance (time to ignition and peak of heat release rate). Indeed, it was shown that the heat capacity and the density of the neat polymer and of either carbon black composite or graphite composite clearly affect the time to ignition. Similarly, it was found that the composites exhibit different reflectivity, this parameter being responsible of the higher time to ignition of some carbon filled LDPE. This emphasizes the use of the numerical models in the development and the in comprehension of the impact of additives on the fire performances of polymers.

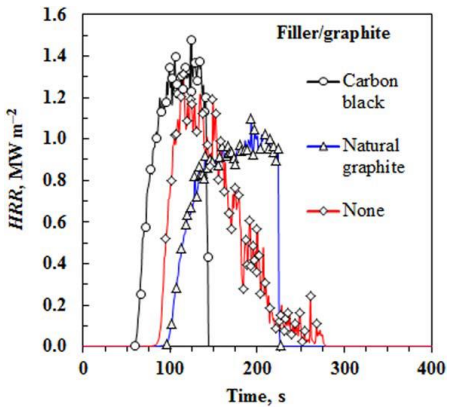

Figure 11: Predicted HRR curves for carbon containing LDPE according to ThermaKin [85]

When simulating gasification experiments in inert atmosphere, there is no need of numerical parameters describing ignition and flaming such as critical mass flux for ignition or additional heat flux from the flame. The modelling of gasification experiments was thus used to validate the characterization of thermal conductivities and heat capacities of various polymers using a controlled-atmosphere pyrolysis apparatus [80,86]. The model is able to predict well the temperature profiles and mass loss rate histories of materials (Acrylonitrile Butadiene Styrene (ABS), Polyetherimide, Polyethylene terephthalate and a thermoplastic Acrylic-Polyvinyl-chloride) under several conditions. For example, the temperature at the backside of a plaque and the mass loss rate history obtained for an ABS at incident heat flux from 30 to 70 kW/m² are presented in **Figure 12** and shows a very good agreement between experimental and simulated results.

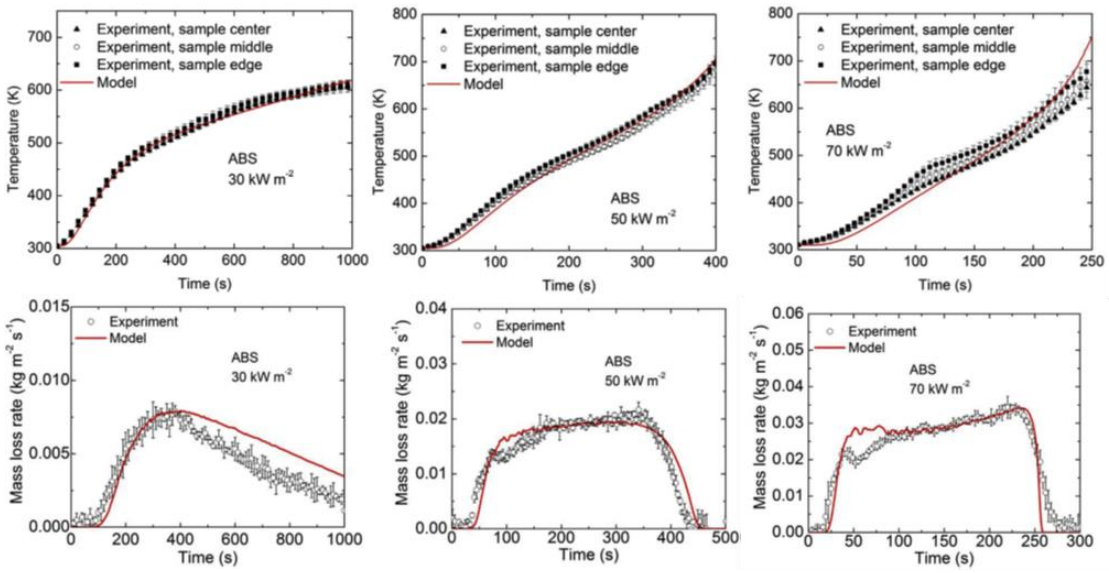

Figure 12: Experimental and predicted temperature profile and mass loss rate curves of a 6.4 mm thick ABS plaque under various incident heat flux [80]

This section showed that a more complex model, considering mass transfer in both mass and energy balance equations improves the accuracy of the pyrolysis model compared to the approach presented in **I.2.2**. It is also more suitable for polymers or complex materials but requires the characterization or estimation of thermal parameters, optical parameters, and the determination of the kinetics of decomposition as well as empirical parameters such as critical mass flow for ignition.

However, even if this approach is satisfactory, some limits can be noticed for example considering intumescent materials. Thus, it can be noted that phenomena that are more complex can be also studied. In particular, the internal pressure and the gas diffusion inside the materials can be simulated using Darcy law. The next section of this chapter will thus be dedicated to the development of more comprehensive models and how the above mentioned phenomenon are numerically studied.

I.2.4. THE MORE FUNDAMENTAL MODEL: POROSITY, INTUMESCENCE, AND INTERNAL PRESSURE

This section emphasizes a generalized pyrolysis model able to simulate the gasification and combustion of solids materials. The model is applicable to non-charring polymers, charring polymers, intumescent materials and coatings, fiber reinforced materials and wood for instance.

First, the porosity of each condensed phase specie can be calculated by **Eq. 23** in a control volume of the computational mesh. ΔVs_i represents the volume occupied by the solid substance and ΔVg_i is the associated gas volume. Component porosity ϕ_i is considered as an intrinsic material property and the porosity of the material can be described by **Eq. 24** and is the weight average of all the individual porosities. Note that the porosities can be expressed as a function of masses and densities of each individual species as well. Depending on the rate of production or consumption of solid and gaseous components, the model is able to consider thermal shrinkage (control volume $\Delta V = \sum_i \Delta V_i$ is decreasing) or intumescence (increase of ΔV) by adapting the mesh size.

$$\phi_i = \frac{\Delta V_{g,i}}{\Delta V_i} = \frac{\Delta V_{g,i}}{\Delta V_{s,i} + \Delta V_{g,i}} = \frac{\Delta m_{g,i} / \rho_{g,i}}{\Delta m_{s,i} / \rho_{s,i} + \Delta m_{g,i} / \rho_{g,i}} \qquad \textit{Eq. 23}$$

$$\phi = \sum_i \omega_i . \phi_i \qquad \textit{Eq. 24}$$

Solid and gas phases are assumed to be in local equilibrium and therefore described by a single temperature. The energy conservation equation is solved in 1D as shown in **Eq. 25**. In this equation, ρ_s and ρ_g are the densities of the condensed and gas phase respectively and can be expressed as linear combination of mass or volumetric ratio between individual species representative of these phases. It can be the different individual gases produced by the decomposition of the material, neat polymer, char, any intermediate specie or fibers for the condensed phase for example. The main differences with the heat balance equation presented in the previous section (**Eq. 14**) is the presence of the porosity of the material in the left hand part of the equation. The model takes also into account the in-depth absorption of the incident heat flux as defined in **Eq. 26**. The reaction rate is represented through Arrhenius equation as

shown in **Eq. 27**. In this equation *m* is the mass of the materials that decomposes (the equation presents the example of a first order reaction).

$$\left((1-\phi)\rho_s Cp_s + \phi.\rho_g Cp_g\right)\frac{\partial T}{\partial t} = \frac{\partial\left(k\frac{\partial T}{\partial x}\right)}{\partial x} + \sum_r^{reac}(\dot{r}_r.Hr) - \dot{m}_g^{"}\frac{\partial(Cp_g.T)}{\partial x} + \varepsilon\frac{\partial \dot{q}_{rad}^{"}}{\partial x} \quad \textit{Eq. 25}$$

$$\dot{q}_{rad}^{"} = \dot{q}_e^{"}.\exp(-A.x) \quad \textit{Eq. 26}$$

$$\dot{r}_r = A_r.\exp\left(\frac{-E_r}{RT}\right).m \quad \textit{Eq. 27}$$

Regarding the mass conservation, different cases can be considered. For solid materials, the variation of mass versus time is proportional to rates of all reactions that either produce or consume material (**Eq. 28)**. Indeed, the stoichiometric coefficient ν_r^s can be either negative if the specie acts as a reactant in reaction *r* or positive if the material is produced.

$$\frac{\partial \rho_s}{\partial t} = \frac{1}{\Delta V}\sum_r \nu_r^s.\dot{r}_r \quad \textit{Eq. 28}$$

The mass conservation for gaseous species have also to handle the diffusion of the specie out of the material. At the opposite of the approach presented in **I.2.3**, the gas diffusion is modelled according to fluid dynamics and the Darcy law is considered instead of gas concentration gradient and the Fick law. This permits to solve the pressure field inside the material but also requires more information about the material. The mass balance equations for gaseous species is presented in **Eq. 29** and takes into account the gradient of the mass flux of the gaseous species. It represents the fact that in each cell, an equilibrium is done between what is produced in the cell of the computational system ($\frac{1}{\Delta V}\sum_j \nu_r^g.\dot{r}_r$), what comes in and what comes out ($\frac{1}{\Delta V}\frac{\partial \dot{m}_g^{"}}{\partial x}$).

$$\frac{\partial \phi \rho_g}{\partial t} = \frac{1}{\Delta V}\left(\sum_j \nu_r^g.\dot{r}_r - \frac{\partial \dot{m}_g^{"}}{\partial x}\right) \quad \textit{Eq. 29}$$

The mass flux is then defined by the Darcy law as presented in **Eq. 30**. The mass flux of gas *g* is proportional to the pressure gradient$\frac{\partial P}{\partial x}$, the density of the considered gas ρ_g, the dynamic viscosity of the gas μ_g and the permeability of the gas K_g.

$$\dot{m}_g^{"} = -\rho_g\frac{K_g}{\mu_g}\frac{\partial P}{\partial x} \quad \textit{Eq. 30}$$

Using the state equation for gases (**Eq. 31**) that links pressure (P), temperature (T), density (ρ) and molar mass of the gases (M_g) and substituting **Eq. 30** and **Eq. 31** in **Eq. 29**, **Eq. 32** is stated and that allows to solve the pressure field and the mass flow of gases inside the material.

$$P = \frac{RT}{M_g}\rho_g \qquad \textit{Eq. 31}$$

$$\frac{\partial}{\partial t}\left(\frac{M_g}{R}.\phi\frac{P}{T}\right) = \frac{1}{\Delta V}\left(\sum_j \nu_r^g.\dot{r}_r - \frac{\partial}{\partial x}\left(\frac{M_g.K_g}{R.\mu_g}.\frac{P}{T}.\frac{\partial P}{\partial x}\right)\right) \qquad \textit{Eq. 32}$$

Even if this approach is more complex and relevant as it allows to consider all the physical phenomena taking place inside the material, this is not an easy task to use these models. Indeed, it requires the characterization of several inputs data such as permeability or dynamic viscosity of the gases. These characterizations are not easy regarding the number of different state that can be encountered by the material: pristine material, molten material, delaminated material, char, *etc.* Nonetheless, a number of theoretical and empirical correlations coupling material's permeability and porosity are available in the literature. Such a coupling is not universal because it is strongly dependent on material microstructure and pore connectivity. An example of such correlation can be found in **Eq. 33** [87]. This equation is for instance used in Pyropolis model [5] and represents one kind of correlation between multiple, plane or sintered wire pores (of diameter d*).

$$K_g = \frac{d^{*2}}{122}\frac{\phi^2}{(1-\phi)^2} \qquad \textit{Eq. 33}$$

Finally, for this complex approach, the boundaries conditions have to be determined. The boundary conditions for the heat conservation are similar to the one in the previous section. Nonetheless, for mass transport, boundaries conditions have to be set at the front (**Eq. 34**) and the rear face (**Eq. 35**). They represent the fact that the rear face of a specimen in cone calorimeter is in contact with aluminum foil or insulation block, so it is impermeable to gas diffusion and the pressure gradient is thus set to 0. On the front face on the opposite, pression is set to ambient pressure.

$$P_{x=\delta} = P_\infty \qquad \textit{Eq. 34}$$

$$\left(\frac{\partial P}{\partial x}\right)_{x=0} = 0 \qquad \textit{Eq. 35}$$

Several software environment was developed using the framework of this pyrolysis model. Among them, Di Blasi [88] was able to model the pyrolysis of wood. More recently, Lautenberger *et al.* [3] developed the Gpyro software and Snegirev *et al.* [5] developed Pyropolis. Note that the main differences between

each model are mainly the way the inputs data are handled by the code: constant values, smoothed or unsmoothed curves between experimental points, n^{th} order polynomes *etc.* Gpyro was for example used for the modelling of intumescent paints as shown in **Figure 13**. This shows that it is possible to model the intumescence or any volume change as well as a temperature profile in a 1D model. Similarly, Pyropolis was able to model cone calorimeter experiments of various polymers under several external heat flux. For instance, **Figure 14** shows the experimental and predicted HRR curves under external heat fluxes lying from 24 to 73 kW/m² and thickness ranging from 3.2 to 26.5 mm (example of HIPS and PC).

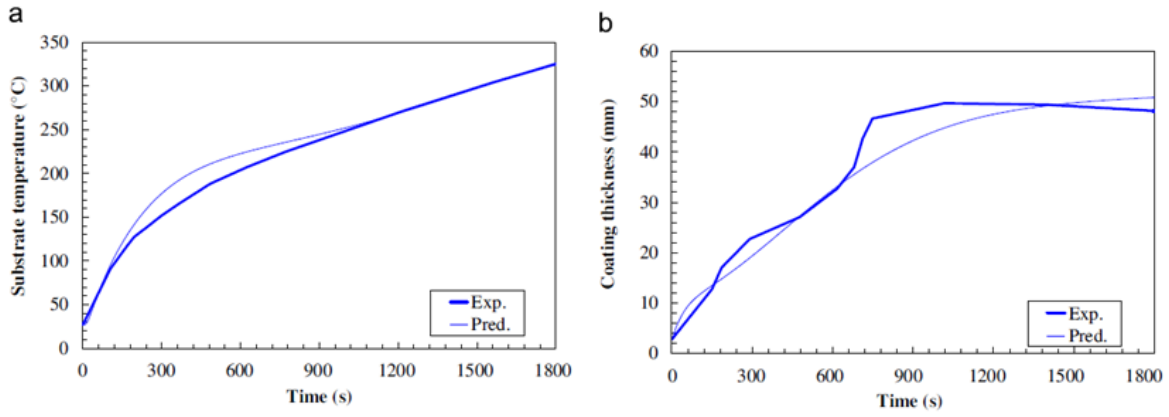

Figure 13: Experimental and predicted substrate temperature (a) and coating thickness (b) under 92 kW/m² irradiance at cone calorimeter [3,89]

One of the primary interest for the development of pyrolysis models is the possibility to predict the fire performances of a material based on small-scale characterization of material properties. Considerable efforts were made for the last decade in order to develop these models whose complexity is ever growing as it allows to consider more and more phenomena and thus improving their predictive capabilities. The accuracy and relevance of the inputs data is also of prime importance as they represent quantitatively the response of the materials to an external phenomenon. If pyrolysis models are of any help for the development of new material, it is therefore important to know what are the parameters or inputs data that governs the response of the material in a given fire scenario. To answer this question, sensitivity analyses are performed on the models. Examples of the results of such analysis are given in the following section of the chapter.

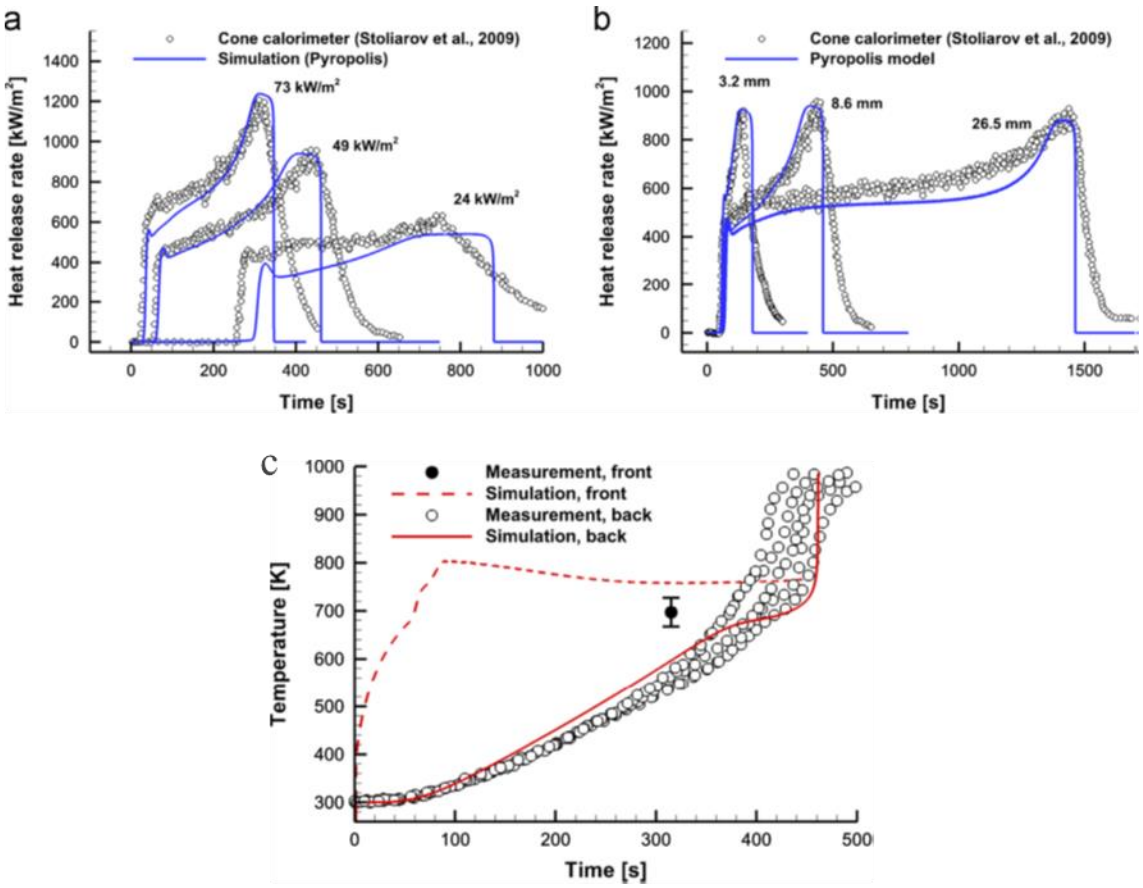

Figure 14: Measured and predicted HRR: effect of heat flux on a 8.6 mm thick PC (a); effect of PC thickness at 50 kW/m² (b); experimental and predicted surface temperature of a 8.6 mm thick HIPS sample at 50 kW/m² (c) [5]

I.2.5. SENSITIVITY OF THE PARAMETERS

Sensitivity analyses can be helpful to study the response of a model (in terms of mass loss rate, heat release rate, time to ignition, temperature *etc.*) when changing one material property but also to consider the relative importance of this parameter regarding the others.

Patel *et al.* [90] have recently published such kind of work based on an ideal material. Its properties were reported as "low", "average" or "high" values and each was associated to the lowest, highest or averaged values that can be found for thermo-physical parameters in the literature. Firstly, it is interesting to look at the reflectivity of the material. As shown in **Figure 15**, increasing the reflectivity of the material leads to higher time to ignition (TTI) and prolonged burning time as well as lower peak of heat release rate (pHRR). Indeed, the reflectivity α is linked to the emissivity of the material as $\varepsilon = 1 - \alpha$ for a grey body. As shown in the last section, the net heat flux that really impacts the surface is $\varepsilon \dot{q}''_e$. This means that the

higher the reflectivity (and so, the lower the emissivity), the lower the heat impacting the materials. **Figure 15** also presents the effect of heat of decomposition on the HRR behavior of a material. It shows that increasing the heat of decomposition will have no impact on the time to ignition but will lower the pHRR value, increase the time to pHRR as well as the total burning time.

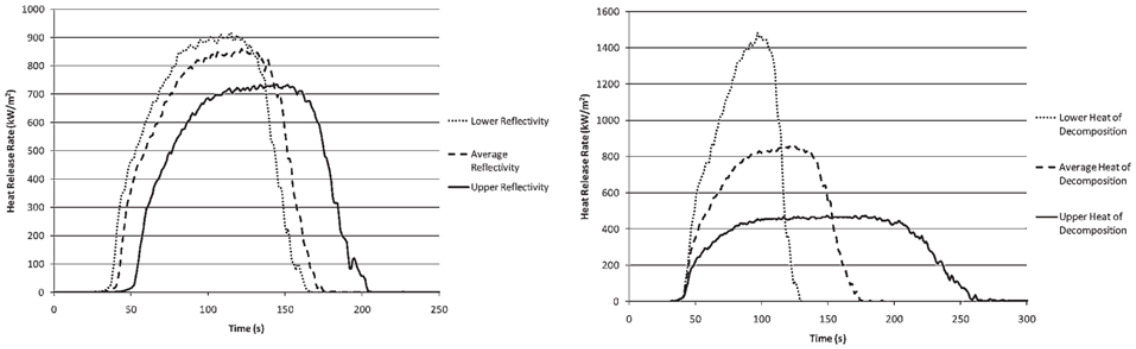

Figure 15: Impact of reflectivity and heat of decomposition on HRR curves [90]

In terms of thermo-physical properties, it is interesting to look at the thermal conductivity and heat capacity of the material. As shown in **Figure 16**, the heat capacity of the material does not play an important role on the shape of the HRR curves. Indeed, either with the low, average or high heat capacity, the only difference is that the curve is shifted to higher times when increasing the heat capacity. This can be attributed to the fact that heat capacity represents the amount of energy required to increase the temperature of 1 g of material by 1 K. Increasing this parameter then just changes the time needed for the material to reach the temperature of decomposition.

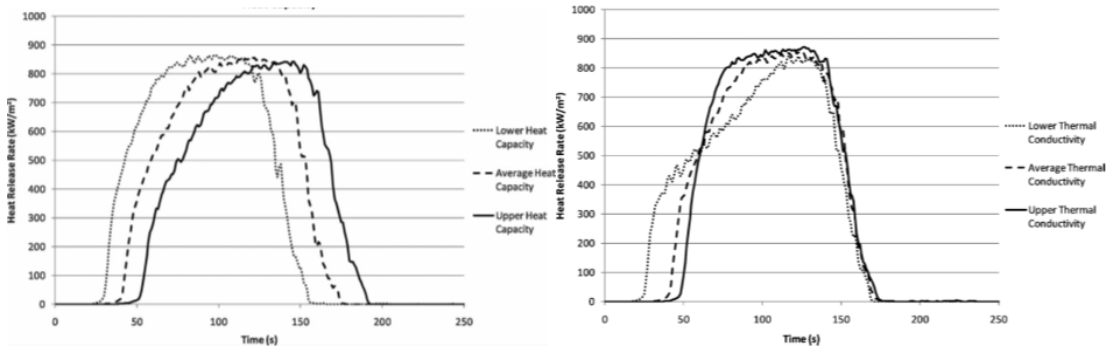

Figure 16: Impact of heat capacity and thermal conductivity on the HRR behavior [90]

On the opposite, thermal conductivity plays a more important role on the HRR behavior. Indeed, as shown in **Figure 16**, reducing the thermal conductivity leads to shorter time to ignition but it keeps the pHRR and t_{pHRR} unchanged. This can be explained by the fact that with lower conductive material, the heat is less transmitted to the thickness of the material. The temperature increase on the front face is thus more important and so the decomposition temperature is reached at shorter times. Note that these results with an ideal polymeric materials were also obtained in other studies [91,92].

I.2.6. CONCLUSION ABOUT PYROLYSIS MODEL

As shown in this section, pyrolysis is a complex phenomenon that couples heat transfer, thermal decomposition and mass diffusion. Several models that differ in their complexity were developed for the last decades. It has to be highlighted that these models are generally applied to pristine thermoplastics or thermosets (wood or composites). The different inputs that are needed for the models were also presented.

I.3. THERMAL PROPERTIES OF EVA/ATH COMPOSITES

If the fire behavior of a material has to be modelled, it is of prime interest to have information on how it behaves when heated, how it decomposes or how its thermo-physical properties changes. The next part of this chapter is thus dedicated to the thermal stability and fire retardancy of EVA and EVA/ATH composites. The impact of ATH and NC on the kinetics of decomposition and the decomposition pathway of EVA will also be presented.

I.3.1. PYROLYSIS OF EVA COPOLYMERS

The thermal decomposition of EVA is already well-reported in the literature [35,93–95]. It is shown that it depends on the atmosphere (inert or thermo-oxidative conditions). This section will nonetheless emphasize the pyrolytic decomposition of EVA as it is assumed that during the combustion and burning of materials, the oxygen is consumed by the flame so materials decompose in an inert atmosphere.

I.3.1.a. Decomposition pathways

As for the properties of EVA, the decomposition pathways and the kinetics of decomposition of these copolymers are linked to their vinyl acetate content. However, it can be noted that the pyrolytic decomposition of EVA is a two apparent steps process. The first pyrolysis step occurs between 300 and 400 °C. In this temperature range, the decomposition of the polymer starts with the cleavage of the acetate groups that present the weakest bond. Thus, the intensity of this decomposition steps is directly dependent of the vinyl acetate content as shown in **Figure 17**.

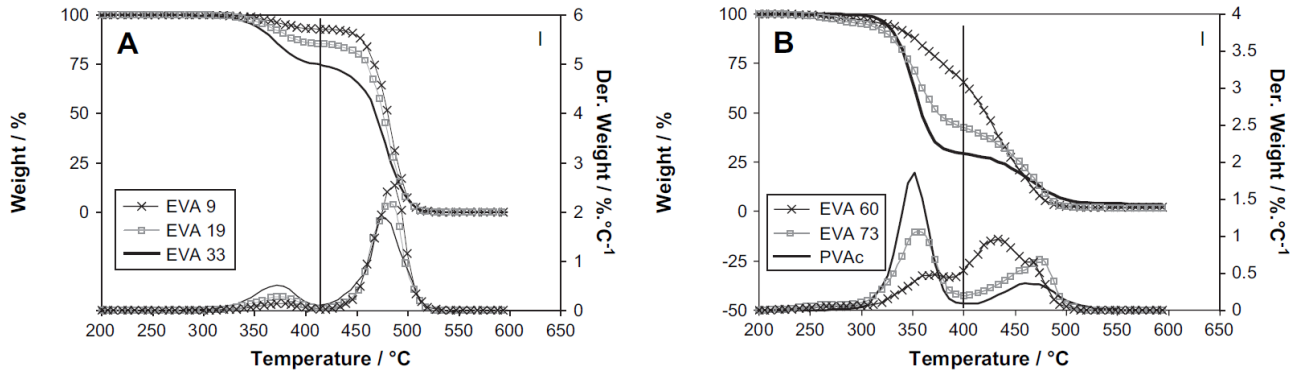

Figure 17: TGA at 20 K/min under nitrogen atmosphere of EVA with 9, 19 and 33 wt% (left) of VA and 60, 73 and 100 wt% of VA (right) [93]

This deacetylation occurs through the β-elimination of the vinyl acetate groups of the polymer [96] and leads to a polyene network and the release of acetic acid. The copolymerization of EVA leads to a random distribution of VA groups in the polymer backbone. If two or more VA units are present successively, then an autocatalytic effect can be observed as presented in **Figure 18**. The deacetylation reactions are catalyzed by the conjugation of the π-system of the double bond formed by the deacetylation of the first VA monomer [97]. The deacetylation of the second VA unit is then activated. Note that the π-system of the double bond can be deactivated if the double band becomes close to an ethylene function (instead of a vinyl acetate function). This catalytic reactions are noticeable for VA content higher than 33 wt% [93] as it becomes statistically more probable that one acetic acid group is in the vicinity of a formerly produced double bond.

At the end of the first decomposition step, a polyene network remains, which is then completely decomposed into saturated, unsaturated or aromatic compounds. This second step of decomposition

usually appears between 400 to 500 °C. It can be noted that the higher the VA content, the more important the release of aromatic structures.

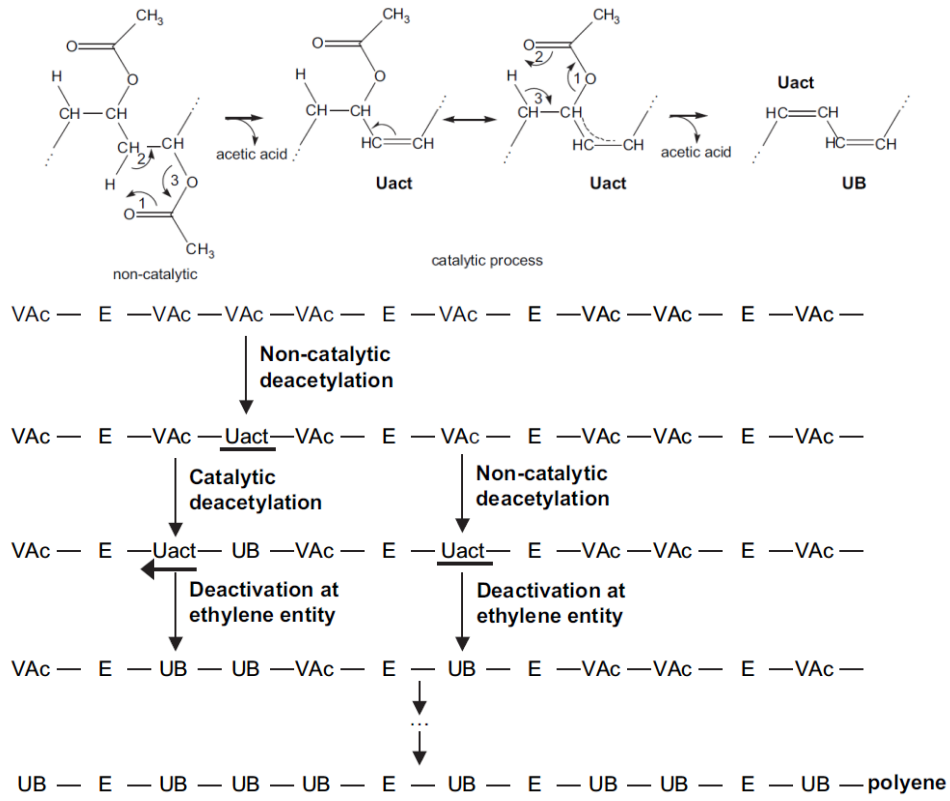

Figure 18: Schematic presentation of the deacetylation of the polymer [93]

The degradation of the polyene formed after the deacetylation was investigated by Costache and Wilkie [98,99]. Firstly, they found that the release of acetic acid is followed by a release of hydrocarbons compounds using TGA coupled with FTIR. In the case of virgin EVA, they found a release of *n*-alkanes but also of 1-alkenes. In order to go further in the investigation of the decomposition of the polyene network, they used a cold trap coupled to a GC/MS analyzer in order to identify these hydrocarbons. It was found that α,ω-dienes, 1-alkenes and *n*-alkanes were released, with a ratio between saturated and unsaturated compounds of around 27:73 and with carbon content between C_9 to C_{31}. After the deacetylation, the following decomposition pathways (**Figure 19**) can be assumed: the polyene network undergoes allylic scission producing diradicals and allylic radicals that can rearrange into more stable resonance structures and form 1-alkenes. The diradicals can undergo either hydrogen abstraction or hydrogen loss by disproponation as shown in **Figure 19**. The results of those processes are then *n*-

alkanes, 1-alkenes and α,ω-dienes. If enough instaurations are present in the polyene backbone (high VA content copolymers), it is also possible to form more complex aromatic structures.

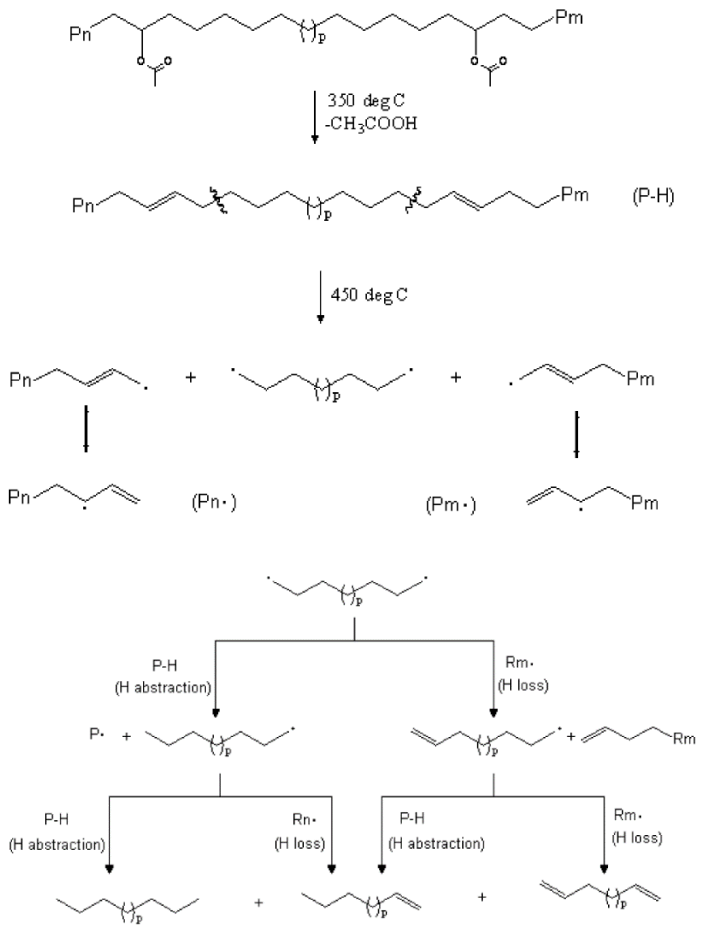

Figure 19: Thermal degradation of EVA by allylic scission of the polyene network [98]

I.3.1.b. Kinetics of decomposition of EVA copolymers

The kinetics of the deacetylation of EVA are also well described in the literature. As shown in **Table 3**, non-catalytic deacetylation of EVA exhibit higher activation energy (E_r) and pre-exponential factor ($\log A_r$) than catalytic deacetylation and similar kinetic parameters as the deactivation step. It can be noted that the deactivation process exhibits an energy of activation which seems to be independent of the VA content. On the opposite, the pre-exponential factor (also called frequency term) was increasing when decreasing VA content. This is consistent with the fact that this reaction occurs after a catalytic deacetylation and is less frequent as the VA content decreases.

On the other hand, several studies also investigated the decomposition of EVA by applying simplified kinetic model and assuming that the deacetylation is a one-step process. Specifically, Cérin *et al.* [35] studied the kinetics of decomposition of a 60 wt% VA content EVA and found similar values than those proposed for the catalytic deacetylation by Rimez *et al.* [100]. Similarly, Martin *et al.* [101] studied the deacetylation of EVA containing from 9 to 20 wt% VA with different model. Using Van Kreveln, Horrowittz-Metzger and Coats-Redfern methods, the deacetylation was found to exhibit an activation energy from 158 to 188 kJ/mol depending of the VA content and on the method used for the analysis. These results show that it is possible to simplify the decomposition pathways of EVA and to find similar kinetics parameters than when using a more complex model.

Table 3: Kinetic parameters of catalytic and non-catalytic deacetylation and the deactivation steps

Process	**E_r [kJ/mol]**	**logA_r**	**Ref**
Non-catalytic	177.5	12.7	[100]
Catalytic	163.8	11.6	[100]
Deactivation – 100-60 wt% VA	178.5	13.4-14.3	[100]
Deactivation – 9-33 wt% VA	178.5	>16	[100]
Deacetylation – vulcanized 60 wt% VA	165.7	12.12	[36]
Deacetylation – 9-20 wt% VA	158-188	N.C.	[101]

The kinetics of decomposition of the polyene network were also studied. According to Rimez *et al.*[100], the degradation of the polyene into aromatic structures exhibits an activation energy of 176.9 kJ/mol and a logA_r of 10.4. The transformation of the saturated part of the polyene into aliphatic volatiles shows a logA_r of 16.3 and an activation energy of 260.7 kJ/mol. On the other hand, Rychly *et al.* [102] found values of 264 kJ/mol which is consistent with other values found in the literature but a logA_r of 37.7 which is in disagreement with other studies. It can be noted that the kinetics associated to this decomposition step greatly vary as it is difficult to associate only one set of kinetic to a complex decomposition step as saturated and unsaturated compounds decompose.

I.3.1.c. Thermo-physical properties of EVA copolymers

The thermal properties of EVA materials are also of interest for pyrolysis models. Only few information about heat capacity and thermal conductivity of EVA can be found in the literature as most of them concern polyethylene or PE/EVA blends. Even if the properties of EVA are different from these of neat PE, it can be interesting to have information about its properties, as it is also a polyolefin. For instance, Staggs [103] investigated the thermal conductivity and heat capacity of polyethylene. It was shown that the heat capacity started around 1.5 J/g/K at ambient temperature and goes up to 3.0-4.0 J/g/K between 150 and 350 °C. The value at ambient temperature is close to this reported by Stoliarov *et al.* for EVA (1.37 J/g/K) [77]. At higher temperature the materials decomposes and no information can be obtained. The melting of the polymer was observed around 100 °C and the heat capacity could not be measured around this temperature. These observations are in agreement with other studies such as the one of Borhani Zarandi *et al.* [104] as they found a heat capacity between 3.1 and 3.8 J/g/K at 125 °C for LDPE/EVA blends (90/10 and 70/30 respectively). The same authors found a heat capacity between 2.5 and 3.5 J/g/K at 40 °C for the same LDPE/EVA blends. Note that those measurement are in agreement with the measurement made on a 42 % crystalline EVA between 80 and 300 K as a heat capacity of 3.2 to 4.0 J/g/K was found in the range 200-300 K [105].

Staggs [103] also reported the evolution of the thermal conductivity as a function of temperature for a PE. It was reported that the thermal conductivity was decreasing linearly from 0.4 at ambient temperature to 0.25 W/m/K at the melting temperature (around 100 °C) while it remained constant until the material decomposes at temperature higher than 350 °C. Those values are in agreement with those of Borhani Zarandi *et al.* [104,106] on LDPE/EVA blends as they found that the thermal conductivity of those blends ranged between 0.20 and 0.25 W/m/K. Note also that Ghose *et al.* [107] investigated the thermal conductivities of neat EVA as well as EVA/nanofillers. It was found that an EVA containing 28 wt% of vinyl acetate exhibits a thermal conductivity of 0.324 W/m/K that is in the range of the previous studies found in the literature.

As shown in this section, the pyrolysis of neat EVA is known, both in terms of decomposition pathway and kinetics. The thermo-physical properties of EVA are known or at least an expected range of values can be obtained. Indeed, as EVA is a copolymer and properties such as crystallinity or vinyl acetate content can vary greatly and are not always described, it is uneasy to found those properties. On the other hand, it is also interesting to know how the flame retardant, in our case ATH decomposes and how it can impact the decomposition pathway and kinetics of decomposition of EVA. The following section will thus be dedicated to the decomposition of ATH and EVA/ATH composites.

I.3.2. EFFECT OF ATH ON THE DECOMPOSITION OF EVA

I.3.2.a. Decomposition of ATH and its impact on EVA

The decomposition of ATH is widely reported in the literature. During its thermal decomposition, the aluminum tri-hydroxide or gibbsite ($Al(OH)_3$) turns into alumina (Al_2O_3). Some authors also suspected a first transition into boemhite (γ-AlOOH) [36]. Decomposition of ATH into alumina releases water endothermically with a heat of reaction between 1190 [108] and 1300 J/g [31,109]. This relatively high heat of reaction is one of the main mode of action of ATH as flame retardant. The release of water is also important as it can dilute the combustibles gases. Alumina can also form an insulative protective layer. Hull *et al.* [31] estimated the contribution of those different effect for various mineral fillers determining the heat absorbed due to the filler, the residue, the evolved gases, *i.e.* water or carbon dioxide and to the endothermic decomposition (**Figure 20**).

It can be noted that for the studied mineral fillers, most of the energy is absorbed by the endotherm decomposition reactions. Considering the cases of ATH and magnesium dihydoxide (MDH), the two most commonly used fillers, it can be observed that for the ATH, the heat absorbed by the condensed phase (filler) is smaller than the heat absorbed by the gas phase. In the case of MDH, the opposite is observed: the filler absorbs more energy than the gas phase.

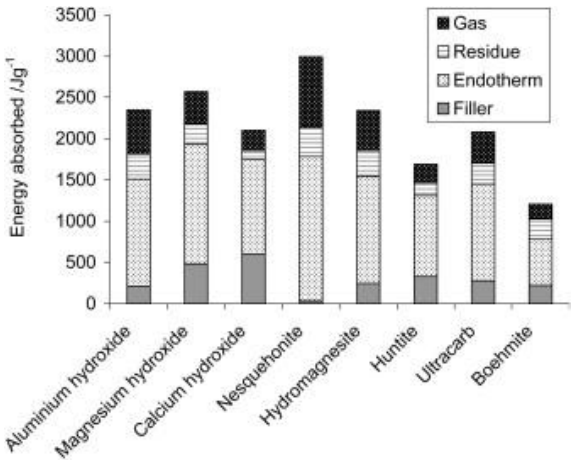

Figure 20: Estimation of heat absorbed by different fire retardant mineral fillers [31]

The decomposition of EVA can be influenced by the presence of a filler. In the case of EVA/ATH formulations, indications about a change in the decomposition pathway can be found in the literature. In particular, Witkowski *et al.* [110] found that EVA when fire retarded with mineral fillers (MDH and

ATH) releases not only acetic acid but also acetone. In the case of ATH, the release of acetone occurs together with a release of carbon dioxide and water while in the case of MDH, the same gases are released but with a delay to higher temperature for carbon dioxide. This was attributed to the fact that carbon dioxide was assumed to react with the magnesium oxide to form temperature stable magnesium carbonate which itself decompose at higher temperature [110]. This effect was not observed with ATH [38]. In both case, the production of acetone, carbon dioxide and water was attributed to the catalytic effect of mineral oxide on the transformation of carboxylic acid [111–115].

$$2\ CH_3COOH \longrightarrow CH_3COH_3 + CO_2 + H_2O \qquad \textit{Eq. 36}$$

However, we have no indications about the yield of the reaction of acetic acid into ketone or other species. The detection of acetone in typical fire scenario such as cone calorimeter was already reported by several authors [110,116] in the decomposition products of EVA/ATH or EVA/MDH. The transformation of one gas to another can play a role in the flammability of a material. Indeed, for the same amount of gases, they will not ignite in the same manner or will not release the same energy while burning. A good approximation to estimate the impact of one gas is the use of the F-number (**Eq. 37**) [117]. The F-number can be calculated with the ratio of the lower and the upper flammability limit.

$$F = 1 - \sqrt{\frac{\text{Lower flammability limit}}{\text{Upper flammability limit}}} \qquad \textit{Eq. 37}$$

For example, flammable gases with F-number values of 0.0–0.2 are classified as vaguely flammable, those of 0.2–0.4 weakly flammable, those of 0.4–0.6 normally flammable, those of 0.6–0.8 strongly flammable, and those of 0.8–1.0 highly flammable. In the case of the transformation of acetic acid into acetone, an increase of the flammability is expected as the F-number of acetone is higher than the one of acetic acid (0.552 for acetic acid versus 0.561 for acetone).

On the other hand, when the decomposition gases diffuse through the thickness of the material, they can transport energy and cool the material. This behavior is directly proportional to the heat capacity of the gases. It is noteworthy that the transformation of acetic acid into ketone would greatly influence the capacity of the gases to slow down the propagation of heat inside the material as the heat capacity of acetone is 20 % higher than the one of acetic acid [118]. However, if the transformation of acetic acid into acetone would increase the flammability of materials, this effect is seldom observed. Indeed, it can be assumed that this negative impact is compensated by the release of inert gases (water coming from the ATH dehydration) out of the material acting as a diluting agent and being part of the mode of action of this mineral filler.

It can be noted that no studies were found in the literature dealing with the modification of the last decomposition step of EVA (decomposition of the polyene) when it is flame retarded with ATH. As for the first step of decomposition, a catalytic effect of alumina could also be suspected. Indeed, mineral fillers such as zeolite (a kind of alumino-silicate) are used for the pyrolysis of biomass or polymer waste.

I.3.2.b. Kinetics of decomposition of pure ATH and ATH based formulations

More than the decomposition pathway, it is also important to know how fast the flame retarding effect delivered by ATH-based formulations occurs. The kinetics of decomposition thus need to be studied. Even if the decomposition of ATH is well known in a chemical and physical prospect, few indications about its kinetics of decomposition were found in the literature. An overview of the kinetics parameters for neat ATH or in the case of EVA/ATH materials is shown in **Table 4**.

Dembsey *et al.*[119] studied the decomposition of pure ATH, PEEK and PEEK/ATH materials at different heating rates and performed a model-free analysis. Assuming a n^{th} order reaction, an activation energy of 140.1 kJ/mol and a $\log A_r$ of 11.4 were obtained for the dehydration of ATH. On their side, Rychly *et al.* [102] found an activation energy of 112 kJ/mol associated with a $\log A_r$ of 22.8. When investigating the thermal decomposition of EVA flame retarded with ATH, Cérin *et al.* [35] found a value of 113.6 kJ/mol and a $\log A_r$ of 8.73 but associated the decomposition of the ATH to a 1^{st} order Avrami Erofeev reaction. No physical nor chemical justifications were proposed for this reaction model except that it was the best fit between experimental and simulated data. Similarly, Rychly *et al.* [102] investigated the kinetics of decomposition of ATH, PE, PE/ATH and EVA/ATH. For this latter, the results were unclear as its decomposition was associated to a three steps process and no indication were available at that time to associate an activation energy to the decomposition of ATH. The same authors found that in the case of a PE/ATH composite, the decomposition kinetics associated to ATH were decreased from 112 to 79 kJ/mol. This was assumed to be due to the interaction between ATH, PE and their decomposition products and their possible preferential recombination at the surface of the decomposed ATH.

As a conclusion, values from 140 to 80 kJ/mol can be found for the dehydration of ATH depending of the kinetic model and if pure ATH is investigated or its combination with a polymeric matrix.

Table 4: Kinetic parameters associated to the decomposition of ATH

Material	$\log A_r$	E_r [kJ/mol]	Notes	References
Pristine ATH	22.8	112	Fitted only on 10 K/min data	[102]
Neat ATH	11.4	140.1	n^{th} order reaction (n = 1.25)	[119]
PE/ATH	17	79	Average of 2.5, 5 and 10 K/min data	[102]
EVA/ATH	8.73	113.6	1^{st} order Avrami Erofeev	[36]

I.3.2.c. Thermo-physical properties of ATH or ATH based formulations

It is interesting to note that very few studies are dealing with the investigation of the thermo-physical properties of EVA/ATH. Nonetheless, some information are available about ATH alone. According to Ashton *et al.* [120], ATH exhibits a heat capacity of 1.2 J/g/K at ambient temperature. The heat capacity can go up to 1.65 J/g/K at 127 °C. Note that at the opposite of the thermal conductivity, heat capacity of a formulation can be calculated as a linear combination of both EVA and ATH, depending on the composition of the materials. Unfortunately, very few information about these properties are available either as an additive or in a formulation.

Similarly, few information can be found about the thermal conductivity of ATH alone or in formulations. Even if models [121–123] are able to predict the thermal conductivity of mixtures based on the thermal conductivities of the individual components of the formulation, it is difficult to apply them to mineral fillers or ATH based formulation. Indeed, the concentrations in ATH used in polymers to be effective are too high (>50 wt%) for these models. Moreover, information about the individual properties are needed but the thermal conductivity of ATH is nor reported as a function of temperature.

However, Hoffendahl *et al.* [38] studied the thermal conductivity of a 60 wt% vinyl acetate containing EVA flame retarded with 65 wt% of ATH in combination with melamine derivatives. It was found that the ambient temperature thermal conductivity was in the range of 0.8-0.9 W/m/K and steadily decreased to around 0.3 W/m/K in the range 350-400 °C. At temperature higher than 400 °C, the thermal conductivity of the residues formed by the decomposition of EVA/ATH systems containing or not melamine derivatives was in the range 0.2-0.32 W/m/K.

I.3.3. THERMAL DECOMPOSITION OF EVA/CLAY NANOCOMPOSITES

As for ATH, it is also of interest to know what are the effects of nanoclays on the decomposition of EVA and more precisely on EVA/ATH. However, the thermal decomposition of EVA/ATH/clay was seldom studied. Most authors dealing with the effect of nanoclays with traditional flame retardants and mineral fillers such as MDH or ATH among them are just studying mechanical or fire retardant properties and the thermal decomposition without emphasizing on decomposition pathways [56,124–126]. Very few information about the evolved species or condensed phase residue are available. Nonetheless, EVA/clay systems are more studied and the next part of this section will feature the thermal decomposition of EVA/nanoclays materials.

I.3.3.a. Impact of nanoclays on the decomposition pathway of EVA

As previously described, the first decomposition step of EVA composites is associated to the loss of acetic acid and the formation of polyene structure. According to Costache *et al.* [98], the incorporation of montmorillonite (MMT) in EVA does not change the decomposition product of the deacetylation. Nonetheless, it was found that the higher the nanoclays content, the sooner the peak of maximum mass loss rate. Moreover, the substitution of terminal –OH group from the edge of the clays by silane groups lead to an absence of this acceleration of the loss of acetic acid. Thus, it was demonstrated that the presence of free hydroxide groups and more generally acidic sites on the surface of the clay can catalyze the deacetylation. Interestingly, even if reported by different authors in the literature [51,124,127,128], no kinetic studies of this catalytic effect were performed.

As discussed previously, EVA is converted into a polyene (or more precisely, poly(ethylene-co-acetylene)) through deacetylation. This polyene undergoes further degradation to smaller molecules at higher temperature [129]. In presence of nanoclays, some differences were observed compared to neat EVA: the α,ω-diene peaks almost completely disappear and the 1-alkene peaks decrease. Interestingly, additional noise-like peaks assigned to other unsaturated structures are observed [130]. The increased production of linear saturated compounds and the decreased evolution of linear α,ω-dienes indicate that hydrogen abstraction becomes more important in the presence of clay. The overall ratio of saturated to unsaturated ratio varies from 27:73 for neat EVA to 43:57 in the presence of nanoclays. Moreover, the greater number of other unsaturated structures implies that random scission is also more extensive due to the presence of MMT.

Costache *et al.* [98] proposed that the differences in the degradation of the nanocomposites and virgin EVA may come from secondary reactions that allylic radicals can undergo [98]. In the case of EVA

nanocomposites, the nanoclays platelets can confine these radicals, so recombination reactions become much more probable than in the case of virgin copolymer leading to more complex structures. This assumption was confirmed by Beyer [59] as the chars formed in cone calorimetric experiments were studied by solid state NMR spectroscopy and it was shown that an EVA-like material is still present after 200 s of exposure of the EVA nanocomposites to the cone. On the contrary, in the case of neat EVA, the NMR peak associated to EVA-like structures disappeared after 50 s. Thus, this results support the conclusion that when incorporated in EVA, nanoclays help to contain the degrading polymer and permits recombination reactions.

We may thus conclude that the most probable decomposition reactions are radical transfer reactions with the original polymer, from which the newly formed radicals can return to the degradation cycle, undergoing additional scissions. Other reactions might also take place in the case of the nanocomposites as clay platelets can confine the radical and encouraged complex alkenes structure as shown in **Figure 21**. Cross-linked structures can undergo further scissions, leading to the formation of radical species which can either disproportionate, producing various branched trienes, or recombine, forming other cross-linked structures and/or internal olefins (**Figure 22**). Linear polymer chains that have a favorable orientation promoted by clay confinement can undergo transient cross-linking. In addition, the trienes formed can undergo Diels–Alder cycloaddition reactions leading to cyclic structures and possibly, upon hydrogen abstraction, to other unsaturated structures.

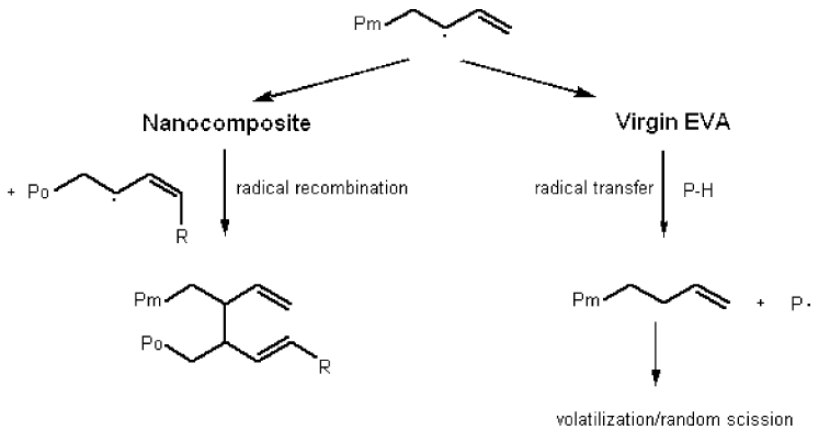

Figure 21: Possible radical recombination reactions for EVA nanocomposites [98]

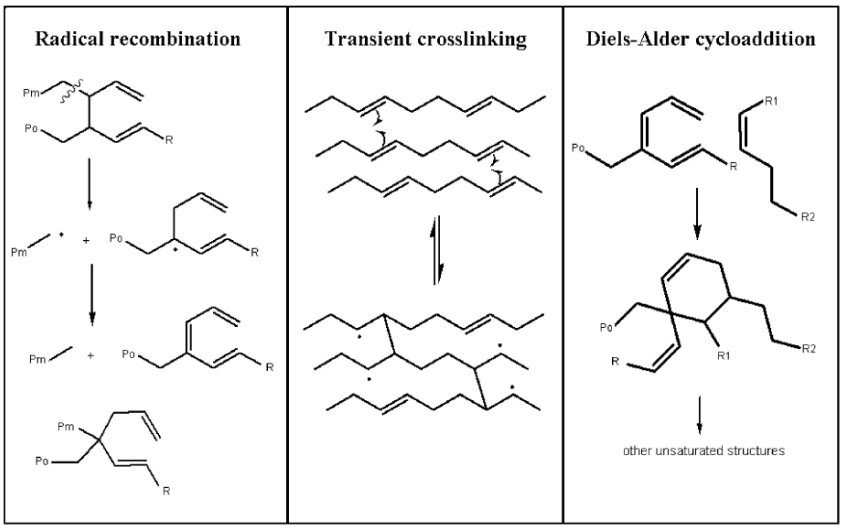

Figure 22: Secondary reactions in the thermal degradation of EVA nanocomposites. [98]

All these cross-linked shown in **Figure 22**, branched or multiple double bonds containing structures can explain the increased thermal stability of the nanocomposites observed by TGA, since more energy is required to break the additional bonds formed.

I.3.3.b. Impact of NC on the kinetics of decomposition of polymers

Even if nanoclays are widely used in EVA copolymers, limited investigations about the kinetics of decomposition of those systems and therefore the impact of the clays on the kinetics parameters were performed. Nonetheless, other polymers/montmorillonite systems were studied showing that similar catalytic or recombination reactions also apply to other polymers [130]. The impact on the kinetics of those systems, such as PA6, PP, PS or HIPS give trends on what could occur with EVA/nanoclays systems [131–135]. Therefore the next part of the section will focus on the kinetics of decomposition of PP/clay [131,134] as PP is a polyolefin.

Kumar *et al.* [131] studied the impact of 5 wt% natural montmorillonite (MMT) or montmorillonite modified with a quaternary ammonium salt (oMMT) with and without a flame retardant in PP. By studying thermogravimetric data at 10 K/min and applying different kinetic models (from simple 1st order reaction to more complex diffusion reaction and nucleation), it was found that the most probable kinetic model for PP or its composites were 1st order reactions. It was found that both activation energies and pre-exponential factors were greatly increased when MMT or oMMT were incorporated into PP. Namely, the activation energy increases from 120.7 kJ/mol for neat PP to 366.9 kJ/mol for PP/MMT and

436.6 kJ/mol for PP/oMMT system. Nonetheless, it can be noted that this apparent increase seems more likely due to the calculation process and more precisely to a "compensation effect" [135] that can be obtained when analyzing single heating rates data. These results have thus to be taken with caution.

It can be noted that an increase of the thermal stability associated to an increase of the temperature of maximum mass loss rate in TGA experiments was found in this study. This would be consistent with higher activation energy reactions. Nonetheless, Lecouvet *et al.* [134] used multiple heating rates data followed by model free analysis (Friedman method) with thermogravimetric data obtained from 1 to 20 K/min in order to study the thermal decomposition of PP alone and PP flame retarded with halloysite nanotubes (HNT) which are a kind of nanoclays. According to the authors and in accordance with other literature studies [136], the pyrolytic decomposition of PP was found to be a two-step competitive process. The first process was attributed to random chain scission of the polymer chain and to the release of radical with an activation energy of 160 kJ/mol and a frequency factor of 9.0 (**Table 5**). The same reaction for PP/HNT exhibits similar parameters as the activation energy was found to be 177 kJ/mol and a $\log A_r$ of 9.7. The second reaction was attributed to several phenomena such as end- or mid-chains β-scission, hydrogen transfer or radical recombination. It was found that the nanoclays play an important role on this step of decomposition, as the frequency factor varied from 3.9 for pristine PP to 12 for PP/HNT. The same trend was observed for the activation energy as it increased from 91.9 kJ/mol for neat PP to 198 kJ/mol for PP/HNT (**Table 5**). The higher activation energy of this reaction suggests that reactions with lower activation energy (end-chain and mid-chain β-scission, hydrogen transfer and hydrogen abstraction) could be reduced in presence of clays.

Table 5: Kinetics parameters obtained for PP and PP/HNT [134]

Polymer	$\log A_r$	E_r [kJ/mol]	Associated reaction
PP	9.0	160	Random chain scission
PP/HNT	9.7	177	
PP	3.9	91.9	End-chain / mid-chain β-scission
PP/HNT	12.2	198	radical recombination and hydrogen transfer

I.3.3.c. Impact of nano-fillers on thermo-physical properties of polymers

As for ATH based formulations, very few information about the thermal properties of nanoclays alone or in combination with a polymer can be found in the literature. One of the few example of such study would be the investigation of the thermal conductivity of EVA blended with various nanofillers [107]. Namely, an EVA with 20 to 30 wt% of Multi-Wall Carbon Nanotubes (MWCNT) or metal particles (Ni, Cu or Ag) or 20 to 50 wt% of expanded graphite (EG) were prepared and their thermal conductivities were measured. Depending on the dispersion and preparation process, some orientation effect appeared and some composites (based on MWCNT and EG mainly) exhibit a strong anisotropy in terms of thermal conductivity. For those materials, the thermal conductivity in the perpendicular direction of the orientation of the nanofillers were higher than that of the neat EVA (in the range 0.4-0.5 W/m/K versus 0.31 W/m/K for neat EVA). On the opposite, in the parallel direction of the nano-filler, the composites exhibit thermal conductivities between 2 and 5.5 W/m/K depending on the concentration and nature of the nanofillers. The materials based on metal particles exhibit isotropic thermal conductivities. In particular, they show a higher thermal conductivities compared to this of neat EVA as their conductivities were ranging between 0.49 and 0.66 W/m/K. However, it has to be noted that the fillers used in this study are sharply different to MMT and thus those results cannot be directly extrapolated to our work.

As shown in this section, the interactions of nanoclays with polymers are very complex and the decomposition products are difficult to characterize precisely. Even if the kinetics of EVA/clay systems were not studied, similar systems were investigated and it was found that the presence of nanoclays increases the activation energy of the thermal decomposition. Nonetheless, as the reactions are not well defined, the determination of the kinetics of decomposition can be uneasy. Even if the prediction of thermogravimetric results is possible with very good agreement, it is not sure that those kinetics truly represents the chemistry of the decomposition. As seen in **I.3.2** (p.41), fillers such as metal oxide can also have catalytic effects on the decomposition pathway. Moreover, no indications on ternary system such as EVA/ATH/clays were found in the literature, both in terms of decomposition pathways or in terms of kinetics.

I.4. CONCLUSION

Progress on fire processes modelling were made gradually. It expands from the late 40's and 60's with simple models to more generalized models since 2000. Furthermore, their complexity varies from semi-empirical relations based on simple heat transfer considerations to more generalized models that are supposed to consider all the phenomena occurring when a solid combustible material burns. In any cases, these models require inputs data describing the material, namely its thermo-physical properties such as heat capacity, thermal conductivity, density or gases permeability, kinetic parameters describing the decomposition of the materials, or optical properties. These inputs can be obtained by inverse methods and/or by direct measurements. **Figure 23** represents the statistics of consideration of each of these phenomenon and thus the number of studies dealing with the characterization of the inputs data required for modelling in 1D models [137]. It is obvious that most of pyrolysis models were focused on wood materials. Furthermore, studies dealing with charring or non-charring polymers are mainly focused on heat conductivity, pyrolysis (decomposition of the material and its kinetics) and gas volatiles. Few studies are looking to internal pressure, permeability or porosity. This implies that the above-described models and especially the more complex ones are not using all their features due to the lack of reliable inputs.

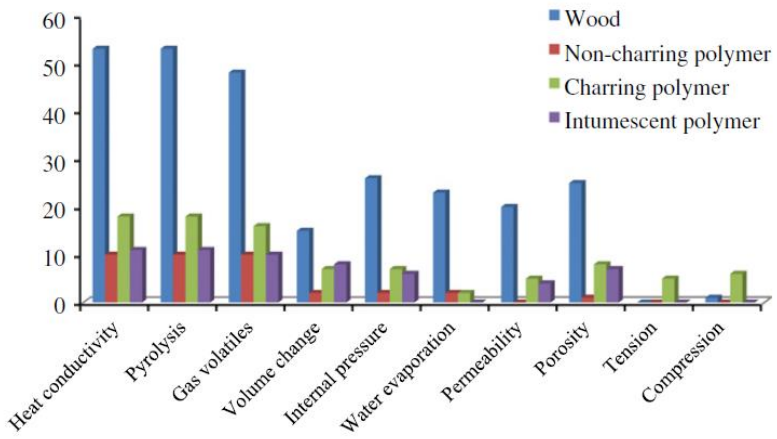

Figure 23: Statistics of considerations in previous 1D pyrolysis models [137]

To improve modelling accuracy, it is then needed to develop reliable characterization methods for the simplest parameters such as thermal conductivity, heat capacity or kinetics parameters but also for the more complex ones such as in-depth absorption coefficients. Moreover, there are few applications of

these models to flame-retarded and more generally formulated material as the interactions between an additive and the matrix are not always well understood. Indeed, even with EVA/ATH, which decomposition is quite simple and widely reported in the literature, no model was applied to this formulation. The impact of classical flame retardant such as ATH and synergist such as nanoclays were also presented in this chapter. The change on the thermal decomposition and the complexity of the phenomenon that can play a role on the fire behavior of this material were then highlighted.

Therefore, the goal of this study is the development of characterization tools of thermo-physical, optical and kinetics parameters that can be used as inputs data for further pyrolysis modelling. Analytical techniques will be applied to pristine and formulated materials. EVA, EVA/ATH and EVA/ATH/NC were chosen as there are typical materials used in the cable industry.

It was thus decided to work with EVA/ATH as it is a model material for cable sheathing. A loading of 65 wt% was used as it is the middle of the range 60-70 wt% required to pass flammability tests. Moreover, the use of nanoclays, namely organo-modified montmorillonite was also investigated as it is known to enhance the fire performances of EVA/ATH formulation [51,52] and is especially used in the cable and wire industry [138]. For this formulation, the loading of flame-retardants remain fixed at 65 wt% but 5 wt% of NC substituted to the ATH. The strategy of this work will be to assess the thermo-physical, optical and kinetic parameters of the formulations. Then, the parameters will be validated by simulating gasification experiments. Finally, standard flaming mass loss calorimeter will be also predicted. The next chapter is dedicated to the materials, the apparatus and techniques that are used in this study.

CHAPTER II. MATERIALS AND METHODS

This chapter is dedicated to the presentation of the polymer and the additives used in this study. Moreover, the preparation methods of the samples are detailed. Then, theoretical considerations about the characterization of the parameters required for pyrolysis models are described. Furthermore, test methods to investigate thermal and physical properties as well as fire retardancy of materials will be presented.

II.1. MATERIALS

This part is dedicated to the materials used in this study, *i.e.* the polymer and the fire-retardant additives. Processing of the materials is then described. In the second section, the principles of measurement of the thermo-physical properties of materials are presented. Finally, experimental details about the apparatus used in this study are presented.

II.1.1. POLYMER

The polymer used in this study is an EVATANE® 28-05 provided by Arkema, corresponding to an ethylene-vinyl acetate copolymer containing 28 wt% of vinyl acetate. Its properties are detailed in **Table 6**.

Table 6: Properties of EVATANE® 28-05

Characteristics	Value	Test method
Vinyl Acetate content	27-28 wt%	FTIR
Melt Index (190 C / 2.16 kg)	5-8 g/10min	ISO 1133 / ASTM D1238
Density (23 °C)	0.95 g/cm^3	ISO 1183
Melting Point	72 °C	ISO 11357-3
Vicat softening point (10 N)	40 °C	ISO 306 / ASTM D1525
Ring&Ball temperature	160 °C	ASTM E28 / NF EN 1238
Elongation at break	700-1000 %	ISO 527 / ASTM D638
Tensile strength at break	24 MPa	ISO 527 / ASTM D638
Hardness Shore A	80	ISO 868 / ASTM D2240

II.1.2. ADDITIVES

ATH is widely used as flame retardant for wire and cables, especially in combination with nanoclays. In this study, a high purity fine particle size precipitated ATH is used. It is an Apyral® 40CD supplied by Nabaltec AG. The nanoclays (NC) used in this study are an organo-modified montmorillonite (Cloisite 30B™) supplied by Southern Clay Product. These nanoclays are modified by methyl tallow-bis-(2-hydroxyethyl) ammonium cations (**Figure 24**). The physical properties of both additives are summarized in **Table 7**.

Table 7: Properties of Apyral® 40CD and Cloisite 30B™

Characteristics	Apyral® 40CD	Cloisite 30B™
Moisture	0.2 %	< 2 %
Loss on Ignition	34.6 wt%	30 wt%
Specific Density	2.4	1.98
D_{10}	0.6 µm	2 µm
D_{50}	1.3 µm	6 µm
D_{90}	3.2 µm	13 µm
BET	3.5 m²/g	-
Oil absorption	22 mL/100g	-

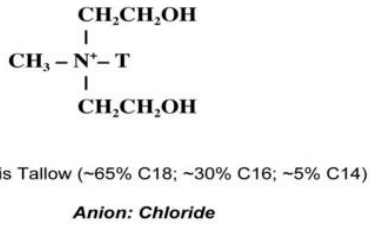

Figure 24: Chemical structure of the organo-modifier of the Cloisite 30B™

II.1.3. FORMULATIONS

Two formulations of EVA containing ATH and ATH/NC were prepared by extrusion (**Table 8**). Neat EVA was prepared in the same conditions so it has the same thermal history.

Table 8: Weight composition of materials

	EVATANE® 28-05	Apyral® 40CD	Cloisite 30B™
EVA	100	-	-
EVA/ATH	35	65	-
EVA/ATH/NC	35	60	5

The samples were prepared with a co-rotating twin screw extruder from Thermo Fisher Scientific (HAAKE Rheomix OS PTW 16 twin screw extruder) with a barrel length of 400 mm and a screw diameter of 16 mm (L/D = 25). The extruder was composed of a heated barrel divided in ten zones, in which the polymer melts. The rotational speed of the screws was set at 100 rpm. Neat EVA and 20 wt% of the flame-retardant (FR) additives (pure ATH or ATH/NC mixture with a ratio 12:1) were fed in zone 1 and the remaining 45 wt% of the flame retardants additives were delivered using volumetric feed-dosing elements in zone 5 as shown in **Figure 25**. The temperature of the first feeding zone was set at 150 °C in order to make the polymer melts. Then, the three following zones were set at 160 °C in order to disperse the FR additives within the EVA. The temperature was then increased for the next three zones to 170 °C in order to decrease the viscosity of the formulation and to promote the dispersion of the additives in the matrix. Finally, the temperature of the last zones is decreased in order to avoid a too high temperature at the end of the extrusion line with two zones set at 160 °C and the final zone set at 150 °C. This design was used in order to avoid too high torque during extrusion and to promote ATH and NC dispersion in the EVA matrix. The obtained formulations were then pelletized.

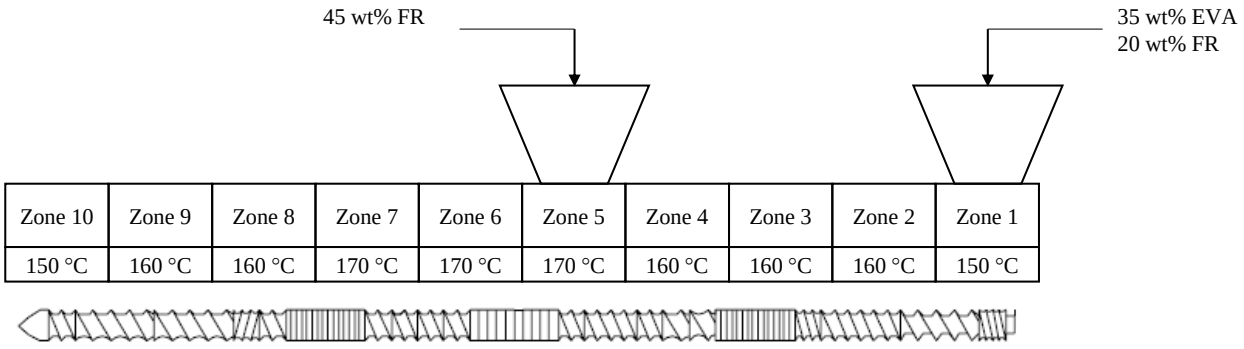

Figure 25: Extrusion process design with fed zones and temperature profile

A high-speed rotor mill (Retsch – Ultra Centrifugal Mill ZM200) was used to obtain fine powder from the formulations pellets. Before grinding, the materials were dipped in liquid nitrogen. The fed materials only remain in the grinding chamber for a very short time and so, the features of the samples were not modified (it was verified in a previous work of our lab). This powdered material will be used for further analyses including TGA, py-GC/MS or STA experiments.

Specimens for the fire testing were obtained by pressing the appropriate mass of material, previously extruded and pelletized, with a hydraulic hot press using specific molds at 170 °C and under 20 kN for 2 min and 40 kN for 8 min.

In order to characterize the dispersion of the additives (ATH and/or NC) in the EVA matrix, Transmission Electron Microscopy (TEM) and Scanning Electron Microscopy (SEM) experiments were performed. The samples were first ultra microtomed with a diamond knife on a Leica ultracut UCT microtome, at cryo temperature (-120 °C) to obtain smooth surfaces. For TEM experiments, films with a nominal thickness of 70 nm were then transferred to Cu grids of 400 meshes. Bright-field TEM images of composites were obtained at 200 kV under low dose conditions with a FEI TECNAI 62 20 microscope, using a Gatan CCD camera. TEM pictures were taken at 88 000x. SEM images were taken at various levels of magnification using a Hitachi S4700 SEM at 6 kV. It can be seen in the SEM presented in **Figure 26** that the dispersion of ATH is homogenously dispersed inside the EVA matrix. The dispersion of NC in the case of EVA/ATH/NC was determined with TEM pictures. It can be seen that the NC platelets are well individually dispersed and are exfoliated.

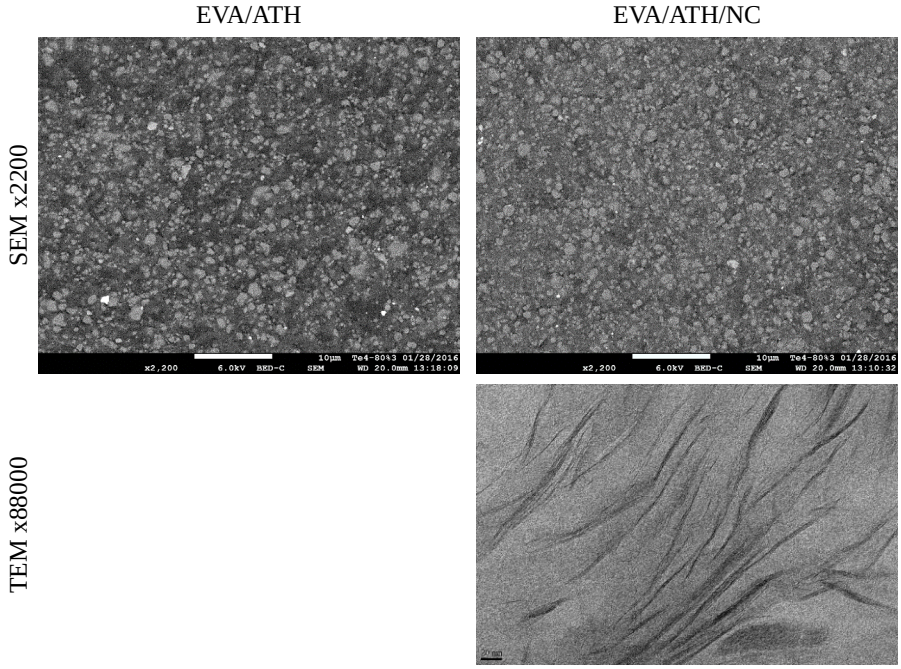

Figure 26: SEM (top) and TEM (bottom) images of EVA/ATH (left) and EVA/ATH/NC (right)

II.2. METHODS FOR THE CHARACTERIZATION OF INPUTS DATA

This section presents the theoretical considerations taken into account for the determination of the kinetics of decomposition and for the evaluation of the heat capacity, thermal conductivity and optical properties of the materials. The measurement of these properties is essential for pyrolysis models.

II.2.1. DETERMINATION OF THE KINETICS OF DECOMPOSITION

In thermal analysis, a reaction can be described with the degree of conversion α. The transformation of the TG signal (weight loss versus time *t* or temperature *T*) into the degree of conversion $\alpha(t)$ is obtained using **Eq. 38**, where $m(t_i)$ represents the mass at the initial stage, $m(t_f)$ represents the mass at the end of the experiment and m(t) the instantaneous mass at time *t*.

$$\alpha(t) = \frac{m(t_i) - m(t)}{m(t_i) - m(t_f)} \qquad \textit{Eq. 38}$$

For kinetic analysis, it is assumed that the material decomposes according to **Eq. 39.** Initial solid specie A_{solid} is assumed to decompose partly in another solid B_{solid} or liquid with a stoichiometric ratio of ν and the remaining mass $(1-\nu)$ turns into gaseous component C_{gas}. The conversion rate is expressed as $\frac{d\alpha}{dt}$ and is defined by **Eq. 40**. $k_r(T)$ is the reaction rate constant and $f(\alpha)$ represents the reaction model. $k_r(T)$ can be defined by an Arrhenius equation as defined in **Eq. 41**. In this equation, A_r and E_r are the pre-exponential factor or frequency factor and activation energy respectively associated to reaction *r*. T is the temperature (in Kelvin) and R is the ideal gas constant (8.314 J/mol/K).

$$A_{solid} \longrightarrow \nu . B_{solid} + (1-\nu) . C_{gas} \qquad \textit{Eq. 39}$$

$$\frac{d\alpha}{dt} = k_r(T) . f(\alpha) \qquad \textit{Eq. 40}$$

$$k_r(T) = A_r . e^{\frac{-E_r}{R.T}} \qquad \textit{Eq. 41}$$

For modelling purposes, it is important to be able to determine the kinetic parameters (activation energy and pre-exponential factor) of the decomposition of a material but also the reaction model ($f(\alpha)$). This latter can play an important role on the above mentioned values. Several methods for the determination of both kinetic model and kinetic parameters can be used. First, it is possible to analyse TG data from

single or multiple curves. Another difference can be on the type of TG data used for the kinetic analysis: linearly dynamic heating ramps, isothermal conditions and/or modulated heating ramps.

An example of single TG curve analysis can be found in [139–142] and the determination of activation energy and pre-exponential factor can be obtained through **Eq. 42** and **Eq. 43**. In these equations, MLR_{max} represents the mass loss rate value taken at the corresponding MLR peak that occurs at temperature T_{max}, *e* is the base of the natural logarithm (2.718), θ is the residual mass fraction, β is the heating ramp and m_{init} is the initial mass of reactant. Note that this analysis can be done for multiple steps reaction. The values of T_{max} and MLR_{max} of each steps can be recorded and each of them can be used for this analysis. One limitation is that this technique is applicable if and only if the reactions are well separated and not overlapping. Note also that this analysis is model-dependent as it implies first order reaction.

$$E_r = \frac{eRT_{max}^2 \frac{MLR_{max}}{m_{init}}}{(1-\theta).\beta} \qquad \textit{Eq. 42}$$

$$A_r = \frac{eMLR_{max}}{(1-\theta)m_{init}} e^{\frac{E_r}{RT_{max}}} \qquad \textit{Eq. 43}$$

On the other hand, Criado *et al.* [143] showed that a single TG curve recorded with a heating rate of 10 K/min, for which the reaction type is based on the two-dimensional nucleation reaction, can be fitted almost congruently with a first-order decomposition reaction and with a three-dimensional Jander's-type diffusion with the same kinetic parameters (**Figure 27**).

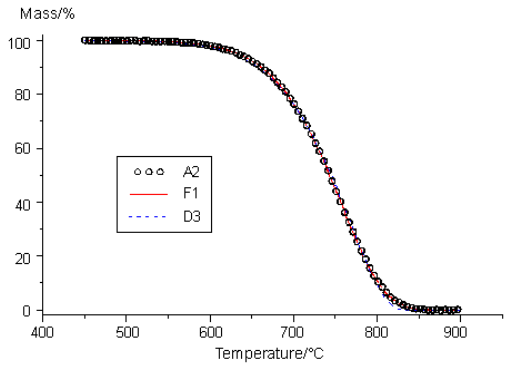

Figure 27: Fit of a single TG data at 10 K/min, simulated with reaction type of 2D nucleation type (A2), first order reaction (F1) and 3D Jander's type diffusion (D3) [143]

If one curve can be predicted using reaction models representing opposed physical phenomena (nucleation, diffusion *etc.*), it is thus obvious that single TG curve analysis does not provide enough information about the reaction. Similarly, in order to model the various heating conditions met in fires, various heating conditions have to be considered when analysing the kinetic of decomposition of materials. This lead to the conclusion that the analysis of TG data from multiple curves would be preferred for the determination of the kinetics parameters and of degradation models.

Through multiple curve analysis (multivariate analysis) in which several measurements run at different heating rates and/or isothermal measurements run at different temperatures are combined in one analysis, the behaviour of the sample is examined in a more global way. With greater amount of information available as compared to a single curve, the desired improvement in distinguishability between reaction types can be achieved. Hence, this section of the chapter will provide some background about the analysis of multiple curves analysis as these methods will be used in the thesis.

II.2.1.a. ASTM E698 method

The analysis according to ASTM E698 [144] is based on the assumption that the maxima (for example maximum of the DSC or DTG curve) of a single step reaction is reached at the same conversion degrees whatever the heating rates [145].

Kissinger [146] introduced a procedure where the parameters of a first order reaction can be estimated by following the shift of the maximum temperatures of the first derivative of the TG signal (DTG) when studying multiple heating rates data. Others experiments such as DSC, Differential Temperature Analysis, Microscale Combustion Calorimeter *etc*. can also be used. The plot of **Eq. 44** shows a linear relation between ln(β) and 1/T leading to straight line as presented in **Figure 28** with a slope of $-\frac{E_r}{R}$ and $T_{max,j}$ being the maximum temperature for the heating rate ß$_j$.

$$\ln\left(\frac{\beta_j}{T_{max,j}}\right) = -\frac{E_r}{RT_{max,j}} \qquad \textbf{\textit{Eq. 44}}$$

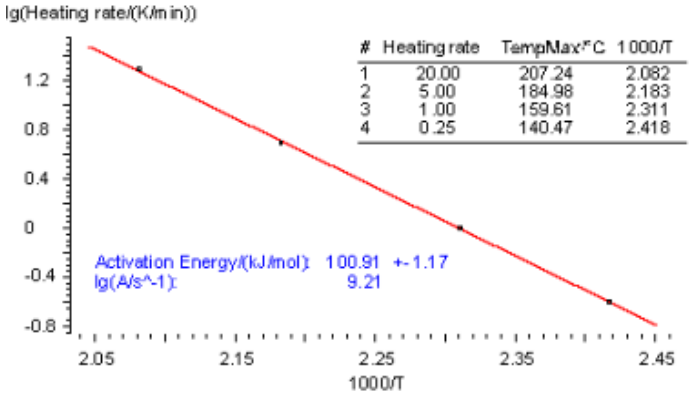

Figure 28: Example of ASTM E698 analysis on a single step reaction using four different heating rates

It is clear that this method is more precise that single curve analysis but is still limited. Indeed, even if it considers various heating rates, the method is assumed to be applicable only for single-step reactions.

II.2.1.b. Ozawa-Flynn-Wall method

Independently of each other, Ozawa [147] as well as Flynn and Wall [148] developed a method for the determination of the activation energy, which considers several curves measured at different, but constant heating rates into the analysis. The integration of **Eq. 40** (p.57) and considering that dT/dt= β leads to **Eq. 45**

$$G(\alpha) = \int_{T_0}^{T} \frac{d\alpha}{f(\alpha)} = \frac{A_r}{\beta} . \int_{T_0}^{T} \exp\left(-\frac{E_r}{RT}\right) . dT \qquad \textit{Eq. 45}$$

If T_0 lies below the temperature at which the reaction is noticeable, then one can set the lower limit of integration to $T_0 = 0$, so that **Eq. 46** is obtained after integration and taking logarithms. Note that $p(z) = \frac{\exp(-z)}{z} \int_{-\infty}^{z} \frac{\exp(-z)}{z} . dz$ with $z = \frac{E_r}{RT}$.

$$\ln\big(G(\alpha)\big) = \ln\left(\frac{A_r . E_r}{R}\right) - \ln(\beta) + \ln(p(z)) \qquad \textit{Eq. 46}$$

By using the approximation given by Doyle [149]: $\ln\big(p(z)\big) = -5.3305 + 1.052 \times z$ and by transposing it in **Eq. 46**, **Eq. 47** is obtained. This method is close to the one developed by Coats and Redfern [150] and only differs on the mathematical approximation used to simplify **Eq. 46.**

$$\ln(\beta) = \ln\left(\frac{A_r . E_r}{R}\right) - \ln\big(G(\alpha)\big) - 5.3305 + 1.052\frac{E_r}{RT} \qquad \textit{Eq. 47}$$

It can be seen from **Eq. 47**. that during a series of measurements with heating rates $[\beta_1, \dots, \beta_j]$ at a fixed degree of conversion $\alpha = \alpha_i$ the plot of $\ln(\beta_j) = f\left(\frac{1}{T_{j,k}}\right)$, shows straight lines with a slope of $1.052\frac{E_r}{R}$. The temperatures $T_{j,k}$ are those at which the conversion α_i is reached at a heating rate ß$_j$. The slope of the straight lines is thus directly proportional to the activation energy. An example of Ozawa-Flynn-Wall graph, with degree of conversion lying between 0.02 and 0.98, can be seen in **Figure 29**. This example is significant from a single step reaction as all the lines are parallel meaning that their slopes are close so only one value of activation energy is obtained in all the range of conversion.

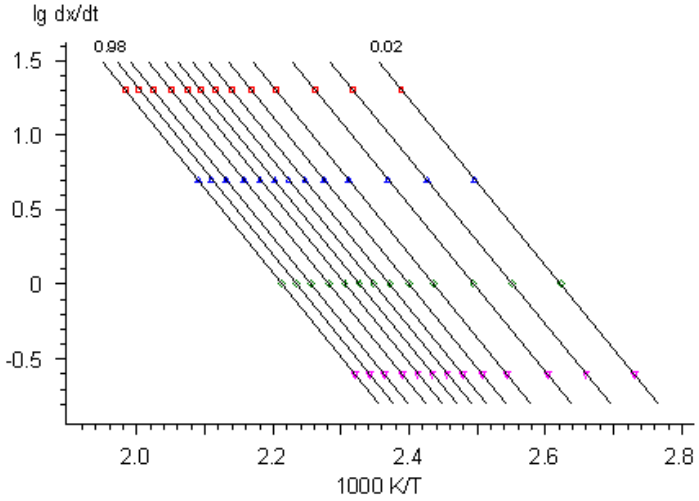

Figure 29: Ozawa-Flynn-Wall analysis for a simulated data set of a single step reaction obtained at four different heating rates and for conversion degree of 0.02 to 0.98

This analysis also permits to determine the pre-exponential factor but a reaction model have to be defined for this. Indeed, substituting the obtained activation energy (E_r) for all the computed degree of conversion α_i and for all heating rates β_j, allows to calculate the pre-exponential (A_r) using **Eq. 47** if and only if a reaction model (n^{th} order reaction *etc.*) is set (f(α) and thus G(α)). It can also be noted that this method (as well as the Coats and Redfern method) uses mathematical approximations. It can then be useful to use analytical methods that does not need any of these approximations. This is discussed in the following section.

II.2.1.c. Friedman method

Based on **Eq. 40** (p.57), Friedman [151] proposed to apply the logarithm to the conversion rate dα/dt (with α_i pre-set) and this leads to **Eq. 48**. With heating rates ranging in $[\beta_1, \dots, \beta_j]$ at a fixed degree of conversion $\alpha = \alpha_i$, $f(\alpha_i)$ is a constant and it is thus possible to plot $\ln\left(\frac{d\alpha}{dt}\right)_{\alpha_i}$ as a function of $1/T_{k,i}$, for all the heating rates β_k. The resulting line exhibits a slope of $-\frac{E_r}{R}$ and crosses the *x*-axis in $\ln[A_r.f(\alpha_i)]$.

$$\ln\left(\frac{d\alpha}{dt}\right)_{\alpha_i} = \ln(A_r) - \frac{E_r}{RT_{k,i}} + \ln(f(\alpha_i)) \qquad \textit{Eq. 48}$$

Examples of Friedman analysis plots are given in **Figure 30**. Similarly to Ozawa-Flynn-Wall method, the pre-exponential factor can be obtained only is a model f(α) is considered. This is only at this stage that the analysis becomes model-dependent. It is interesting to note that the approaches of Ozawa-Flynn-Wall and Friedman present some similarities but the main differences lay in the facts that no approximation have to be used in the Friedman analysis on the contrary to Ozawa-Flynn-Wall. This implies that Friedman method is more global and less susceptible to false analysis and mistreatments of the data.

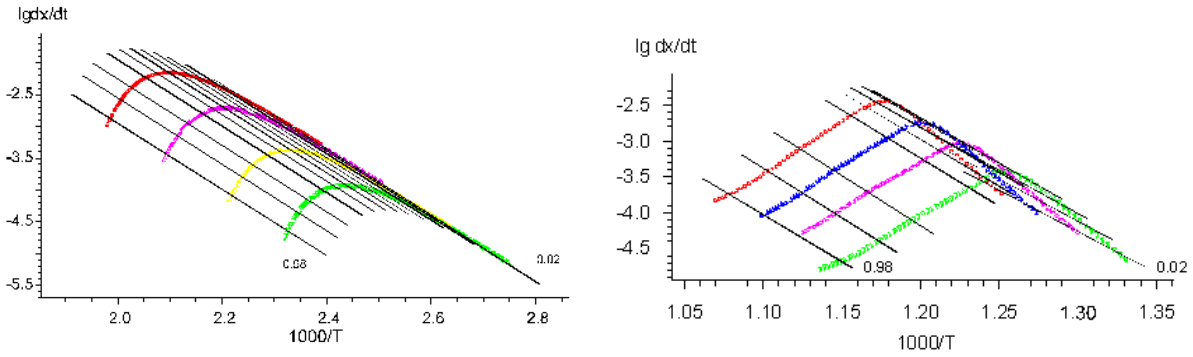

Figure 30: Friedman analysis for simulated data set of a single step decomposition reaction (left) and two steps decomposition reaction (right)

As explained at the beginning of this section, two parameters have to be defined to describe the heating decomposition: the Arrhenius parameters (E_r and A_r) and the reaction model (defining if the reaction is an n^{th} order reaction, an Avrami-Erofeev reaction *etc.*).The first part is represented by $k_r(T)$ in **Eq. 40** (p.57) and expressed as in **Eq. 41** (p.57). The second part is represented by the term f(α). This latter can be obtained through Friedman analysis without specifying any reaction model.

Indeed, Friedman analysis permits to access to $\ln(A_r.f(\alpha_i))$ for all the computed α_i, without any mathematical simplifications, on the contrary of Ozawa-Flynn-Wall or ASTM E698 methods. Instead of using several reactions and defining the kinetics parameters and reaction types for all of them as well as if they are successive or competitive reactions, it would be possible to implement the kinetics of decomposition in a more generalized way.

This approach was tested by Snegirev *et al.* [152] and an example of the results can be shown in **Figure 31** while analysing Microscale Combustion Calorimeter (MCC) results. For instance, three different peaks of decomposition can be observed for the decomposition of PVC. This would imply to define three reactions with specific activation energies (E_r), pre-exponential factors (A_r), reaction models ($f(\alpha)$) but also to define if these reactions are successive or competitive. Instead of this approach, activation energy, pre-exponential factor and reaction model were implemented as a function of total conversion degree. This was very effective for the simulation of material exhibiting multiple decomposition reactions.

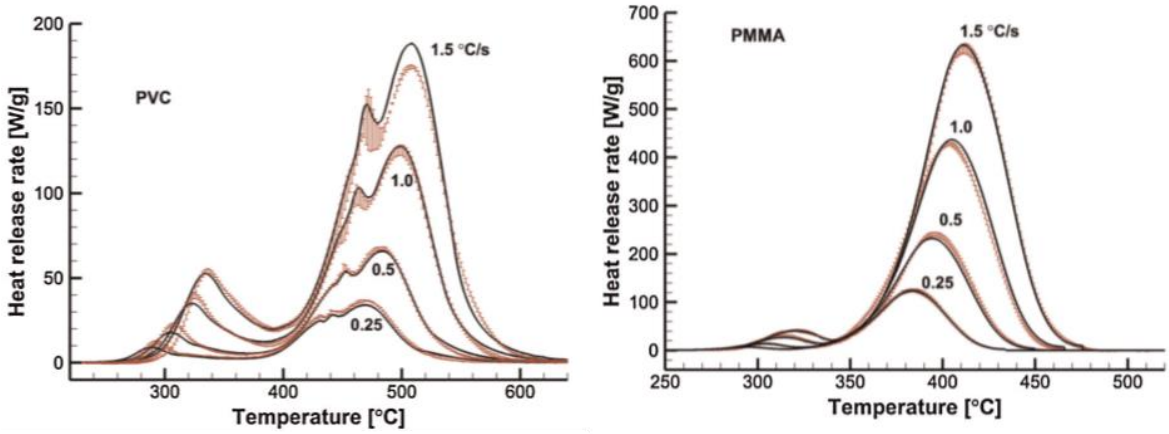

Figure 31: Experimental and predicted HRR from MCC for PVC (left) and PMMA (right) when implementing Friedman analysis without specifying the decomposition scheme [152]

II.2.2. THERMAL CONDUCTIVITY: TRANSIENT PLANE SOURCE METHOD

Transient Plane Source (TPS) method or Hot-Disc method is a widely used technique for the measurement of the thermal properties of materials. It was developed by Gustafsson in 1991 [153]. The basic principle of the method is as follows: a planar heat source (sensor) in the form of concentric circular line sources is placed inside an infinite medium (generally two moulded plate, large and thick enough so when heating, the heating front does not reach the boundaries of the samples). The sensor generates a constant, step-wised heating power by Joule heating which diffuses inside the material. The mean temperature of the sensor raises over time. Shape of this raise, called the temperature function, depends on several parameters such as heating power, radius of the sensor, number of concentric rings and thermal properties of the surrounding material. If the properties of the sensor are known and constant, the measurement of the temperature increase around the sensor can then lead to both the thermal conductivity and thermal diffusivity of the sample from one single measurement. This is an ideal scenario.

In the last twenty years numerous authors studied and improved the method. Gustavsson *et al.* [154] expanded the applicability of the method by introducing a formula for thin (slab) samples. Suleiman *et al.* [155] measured the temperature coefficient of resistance of the sensor over a wide range of temperatures. Boháč *et al.* [156] improved the accuracy of the method by computing an optimal time window for the measurement using both the difference analysis and the analysis of sensitivity coefficients. Gustavsson and Gustafsson [157] analysed the stability of the heating power generated by the sensor. They also introduced two additional model-fitted variables that improved the accuracy of the method, namely a thermal contact parameter and a time correction (t_c), responsible for non-instantaneous heating of the sensor. All these studies led to an international standard published in 2008 (ISO 22007 [158]). Theoretical model of the TPS method is based on the following assumptions:

- Planar sensor consists of concentric and equally spaced circular line sources.
- Thickness and heat capacity of the sensor are negligible.
- There is no thermal resistance between the sensor and the sample.
- The sample is infinite and isotropic in all directions.
- Input power of the sensor is step-wise.

Based on the heat transfer equation in the vicinity of the sensor and considering the particular design of the hot disc sensors (homogenously distributed concentric and planar circles), the main temperature at the surface of the sensor is given by **Eq. 49**, where *P* and *r* are the input power and radius of the sensor, respectively. *k* is the thermal conductivity of the material and $\tau = \sqrt{\frac{t}{\theta}}$ is the non-dimensional time. *t* is

the real time (in seconds), $\theta = \frac{r^2}{\alpha}$ the so-called characteristic time and α the thermal diffusivity of the material. The mathematical details and considerations can be found in [153,159–161].

$$T(\tau) = \frac{P}{\pi^{\frac{3}{2}}.r.k}.D(\tau) \qquad \textit{Eq. 49}$$

The shape function $D(\tau)$ is defined by **Eq. 50**, where *n* is the number of concentric circular sources, I_0 the modified Bessel function and *s* is the integration variable. It can be noted that the shape function $D(\tau)$ is dependent of the thermal diffusivity of the material through the variable τ and of the properties of the sensor (number of sources and diameter of the sensor). On the opposite, **Eq. 49** shows a dependency on experimental data (applied power) and of thermal conductivity of the material.

$$D(\tau) = \frac{1}{n^2(n+1)^2}.\int_0^{\tau}\frac{ds}{s^2}\sum_{i=1}^{n} l \sum_{j=1}^{n} j.\exp\left(\frac{-i+j}{4n^2s^2}\right).I_0\left(\frac{i.j}{2n^2s^2}\right) \qquad \textit{Eq. 50}$$

The sensor operates both as a heat source and simultaneously as a resistance thermometer. Joule heating is generated by the passage of an electrical current through the sensor. As the circular heat sources are made of nickel metal, the mean resistance of the sensor can be evaluated by **Eq. 51**, where T_0 is the initial temperature, R_0 is the initial resistance of the sensor at T_0 and α_s is the temperature coefficient of resistance of the nickel (also called TCR). Note that the TCR parameter is itself temperature-dependent. Nonetheless, except around 352 °C, at the Curie point of nickel, TCR values do not change significantly and it can be assumed that it is constant around the temperature of the experiment. The resistance of the sensor is measured using a Wheatstone bridge during the duration of the experiments.

$$R_s(T) = R_0.[1 + \alpha_s(T - T_0)] \qquad \textit{Eq. 51}$$

Based on the mathematical model described in **Eq. 49** and **Eq. 50** and on the actual measurement of the temperature field around the sensor defined by **Eq. 51**, it is possible to express the temperature as a function of the time as in **Eq. 52**, where a represents the total thermal resistance between the sensor and the sample, t_c is a time correction terms that takes into account the thermal inertia of the sensor and various delays of the electronics of the apparatus [157].

$$T(t) = a + \frac{P}{\pi^{\frac{3}{2}}.r.k}.D\left(\frac{\sqrt{\alpha.(t - t_c)}}{r}\right) \qquad \textit{Eq. 52}$$

An example of a temperature increase curve is presented in **Figure 32**. Different time windows where considered to get this analysis and the influence of this selection is showed in the plot of the residual prediction of the temperature increase. The analysis presented here corresponds to a material with a

measured thermal conductivity of 1.033, 1.075 or 1.073 W/m/K and a measured thermal diffusivity of 0.3649, 0.3984 and 0.3884 mm²/s for analysis in time windows of [0.2s-8.1s], [3.6s-11.7s] and [3.6s-18.8s] respectively. This shows the importance of the selection of the appropriate parameters for the acquisition (power and tests duration) and analysis of the results (number of points to analyse, *etc.*). In order to obtain reliable data, the first and last ten points of an experiment were never used and the analysis was performed on at least 80 points.

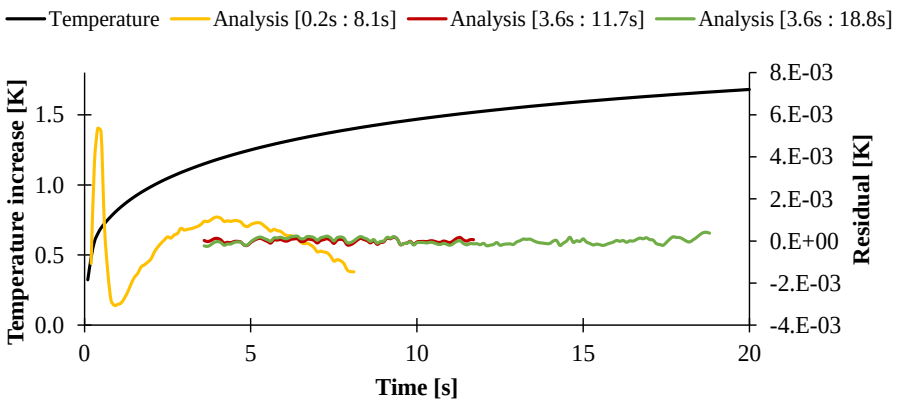

Figure 32: Temperature increase curve with temperature prediction residual assuming different time windows for the analysis

Eq. 52 contains two non-linear parameters, namely α and t_c. These parameters need to be iterated (in a proper time window) until the correlation coefficient between the measured values $[T_{t_i}, t_i]$ and modelled values $[D_{t_i}, t_i]$ reaches its maximum. Plot of $T(t_i)$ versus D_{t_i} should give a straight line. The thermal conductivity (k) can be calculated from the slope of this line and R_0 is the intersection. The thermal diffusivity (α) of the material is thus measured indirectly and the thermal conductivity (k) is then also measured. It can be noted that the volumetric heat capacity (in J/m^3/K) could thus be estimated as $Cp_{vol} = \rho . Cp = \frac{k}{\alpha}$.

II.2.3. DETERMINATION OF THE HEAT CAPACITY OF A POLYMERIC MATERIAL

II.2.3.a. Principle of heat capacity determination by DSC

As seen in the previous section, it is possible to evaluate heat capacity knowing the thermal diffusivity and the thermal conductivity. In that case, the heat capacity is more an estimation than a measurement as it is the thermal conductivity and the thermal diffusivity which are actually measured. The following section will be dedicated to the explanation and the calculation of the measurement of the heat capacity of materials using Differential Scanning Calorimetry (DSC).

For the determination of the heat capacity by DSC, three experiments are generally required. First, a baseline must be carried out, *i.e.* a measurement with empty crucibles. The recorded signal is directly proportional to the mass and the heat capacity of the crucibles (**Eq. 53**) and will be constant during the three experiments. In the second measurement, a standard material (generally sapphire) with known heat capacity is put in the sample crucible. The reference crucible remains empty. The recorded signal is thus the sum of the heat flow from the crucibles ($\dot{Q}_{crucible}$) and from the reference material ($\dot{Q}_{standard}$) as in **Eq. 54**. For the third measurement, the material is put in the sample crucible at the place of the reference material. Similarly to the reference standard, the signal contains a part coming from the crucible and a part which contains the heat capacity of the material (**Eq. 55**). Subtracting the contribution of the crucibles in **Eq. 54** and **Eq. 55** and by making the ratio between the obtained corrected signal leads to **Eq. 56**.

$$\dot{Q}_{crucible} = m_{crucible}.Cp_{crucible}(T).\frac{dT}{dt} \qquad \textit{Eq. 53}$$

$$\dot{Q}_{standard} = \left(m_{crucible}.Cp_{crucible}(T) + m_{standard}.Cp_{standard}(T)\right).\frac{dT}{dt} \qquad \textit{Eq. 54}$$

$$\dot{Q}_{sample} = \left(m_{crucible}.Cp_{crucible}(T) + m_{sample}.Cp_{sample}(T)\right).\frac{dT}{dt} \qquad \textit{Eq. 55}$$

$$Cp_{sample} = \frac{m_{standard}}{m_{sample}}.\frac{\dot{Q}_{sample} - \dot{Q}_{crucible}}{\dot{Q}_{standard} - \dot{Q}_{crucible}}.Cp_{sample} \qquad \textit{Eq. 56}$$

II.2.3.b. Linear dynamic heating ramps method

One of the first and most commonly used technique for the determination of the heat capacity of polymeric materials is based on standards ASTM E1269 [162], ISO 11357-4 [163] or DIN 51007 [164]. Other protocols which are similar to these standards such as the so-called "sapphire method" or "ratio method" can also be used. The main differences between all these protocols concern the baselines: their shift are considered or not. Indeed, before and after the heating ramp, isothermal steps can be recommended. During these isotherms, the apparatus is supposed to return to a thermal equilibrium. In reality, a shift between the first isotherm and the second isotherm can be observed. Some of the above mentioned methodologies consider this shift in the calculation of the heat capacity.

Moreover, recommendations about the optimum masses and heating rates are also given in the standards. As an example a heating rate of 20 K/min is recommended in the ASTM E1269 protocol [162]. Other heating rates are nonetheless also applicable. For instance, Li *et al.* [140] used a heating rate of 10 K/min while measuring the heat capacity of various thermoplastics. Note also that these protocols are assumed to be valid only if the mass loss during the duration of the experiment is lower than 0.3 wt% of the initial mass so they are supposed not to be applicable in case of decomposing materials.

II.2.3.c. Modulated techniques: quasi isothermal and dynamic heating ramps

The method described above, using linear and dynamic heating ramps is very useful for the determination of the heat capacity of materials. Nonetheless, it should be noted that the procedure are assumed to be valid only if there is no mass change which is complex to apply to polymers as they decompose at relatively low temperature (100-500 °C) when the apparatus can go up to 1500 °C. Moreover, polymers undergo phase changes such as melting or glass transition which can interfere with the measurement and can make some temperature ranges unanalysable. This led to the development of the modulated Differential Scanning Calorimetry (mDSC) which was developed by Reading *et al.* [165–169] in the early 90's. It was then standardised for the determination of the heat capacity of materials by ASTM E2716 [170]. Instead of using a linear heating rate, it employs a modulated or sinusoidal change in heating rate in order to automatically separate the heat capacity baseline from the total heat flow signal. This means that it is possible to identify, measure, and quantify kinetic processes such as crystallization and crystal perfection in a single experiment. Subsequently, the heat capacity can be determined independently of the other phenomena happening when heating the material.

In order to achieve this, the heating rate used is not constant but superimposed by a sinusoidal wave as shown in **Eq. 57**. In this equation, T_0 stands for the initial temperature, β is the underlying linear heating rate, Z is the amplitude of the sinusoidal wave and ω is its angular frequency. Depending on these parameters, different modes are then possible: "heat only" when Z.ω is higher than β; "heat-cool" when Z.ω is lower than β or "heat iso" when Z.ω is equal to β. Moreover, it is also possible to evaluate heat capacity of a material in quasi-isothermal conditions by imposing a heating rate β equal to 0. Then, the material is heated following the sinusoidal wave around a fixed temperature T_0. An example of each mode shown is in **Figure 33**.

$$T(t) = T_0 + \beta.t + Z.\sin(\omega.t) \qquad \textit{Eq. 57}$$

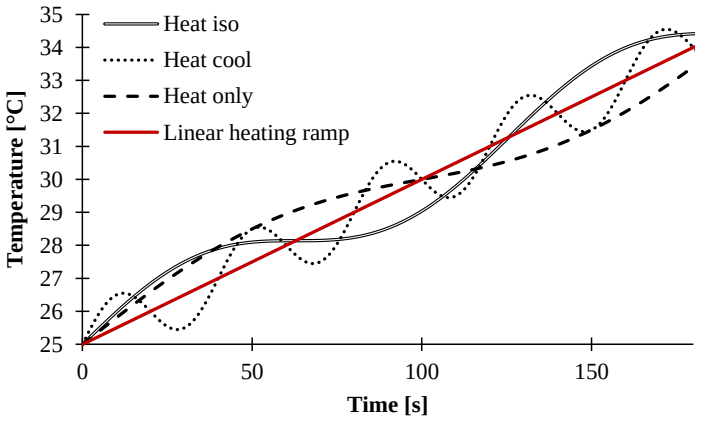

Figure 33: Temperature-time curves in "heat only", "heat iso" and "heat-cool" mode in the case of a 2 K/min underlying heating ramp and 1 K of amplitude

As explained above, the heat flow signal is composed of several parts. With mDSC, multiple signals are generated in a single experiment so that each of the components to the total heat flow signal can be shown and analysed independently as proposed in **Eq. 58**. $m.Cp.\frac{dT}{dt}$ is the reversing part of the total heat flow and $f(t,T)$ is the kinetic or non-reversing part of the total heat flow.

$$\dot{Q} = m.Cp.\frac{dT}{dt} + f(t,T) \qquad \textit{Eq. 58}$$

The reversing heat flow provides information about heat capacity and melting while the non-reversing signal shows the kinetic processes of enthalpic recovery at the glass transition temperature, cold

crystallization and crystal perfection. Note also that for the calculation of heat capacity through mDSC, additional consideration and corrections about the phase lag have to be carried out.

Indeed, in temperature ranges where no kinetic or time-dependent phenomena occur, the heat flow signal should be $\dot{Q} = m.Cp.\frac{dT}{dt}$. The sinusoidal modulated heat flow would then be perfectly in phase with the sinusoidal modulated heating rate. The material should respond instantaneously and should track the sinusoidal heating profile imposed by the furnace. In reality, this assumption is incorrect. Indeed, due to non-instantaneous heat transfer between the DSC cell and the sample, a lag between the measured modulated heat flow signal and the prescribed modulated heating rate occurs. In regions where no kinetic phenomena take place, this lag is entirely due to "instrumental" effect and when kinetics phenomena occur, this can also be attributed to sample effect.

As a result, the heat capacity measured by modulated DSC is actually a complex heat capacity which can be split into an in-phase and a real component Cp' (which is considered to be the thermodynamic heat capacity) and the out-of-phase and imaginary component Cp". To obtain a quantitative information about the thermodynamical heat capacity Cp', it is necessary to compensate the instrument lag in order to evaluate precisely Cp" and hence Cp'. This is made by calibrating the apparatus.

At the exception of this additional correction due to the modulated signal, the measurement of the heat capacity is done as presented in **Eq. 56** for non-modulated techniques. The only difference comes from the fact that instead of using the total heat flow signal, this is the reversing heat flow with or without phase correction that is taken into account for the calculation of the heat capacity.

II.2.4. OPTICAL PARAMETERS: IN-DEPTH ABSORPTION COEFFICIENT AND REFLECTIVITY

The radiative properties needed for the modelling of the fire behavior of materials are the scalar surface absorptivity (α) and the scalar in-depth absorption coefficient (A). It is noteworthy that those values have to be expressed independently of the incident wavelength λ.

To be able to calculate the scalar absorptivity for incident radiation for a given irradiation spectrum, information are required on the spectrally resolved absorptivity α_λ. The ratio between the total absorbed radiation and total incident radiation is given by the scalar absorptivity (α) as defined in **Eq. 59**. This is the weighted average of the spectrally resolved absorptivity which is actually measured, where the weight function is the excitance spectrum of the radiation source (M_λ) and can be defined as in **Eq. 60**.

$$\alpha = \frac{\int_0^\infty \alpha_\lambda M_\lambda d\lambda}{\int_0^\infty M_\lambda d\lambda} \qquad \textit{Eq. 59}$$

It was shown by Boulet *et al.* [171] that the excitance spectrum of the coil of a cone calorimeter can be described by a black body spectrum. In this study, the irradiation levels in the cone calorimeter were 35 and 50 kW/m², which correspond to coil's temperatures of 925 and 1025 K [172]. The excitance spectrum used for our experiments therefore corresponds to a black body spectrum given by the Planck law applied for these temperatures as defined in **Eq. 60**. In this equation, h_0 stands for the Planck constant (6.626 10^{-34} m².kg/s), c_0 for the speed of light in vacuum (2.997 10^8 m/s), k_B for the Boltzmann constant (1.381 10^{-23} m².kg/s²/K), *T* the temperature of the emitter and λ is the wavelength.

$$M_\lambda = \frac{2\pi . h_0 . c_0^2}{\lambda^5 . \left[\exp\left(\frac{h . c_0}{\lambda . k_B . T}\right) - 1\right]} \qquad \textit{Eq. 60}$$

From a single measurement of the absorbance α_λ of a material as a function of the wavelength, it is thus possible to calculate the scalar in-depth absorption coefficient for various incident heat flux. The results can change greatly as the excitance of the cone (or equivalent blackbody) varies as 1/exp(1/T). An example of excitance spectrum for different heat flux is shown in **Figure 34**. Note that the sun irradiance exhibits its maximum around 500 µm while that of a 50 kW/m² cone calorimeter is at 2820 µm.

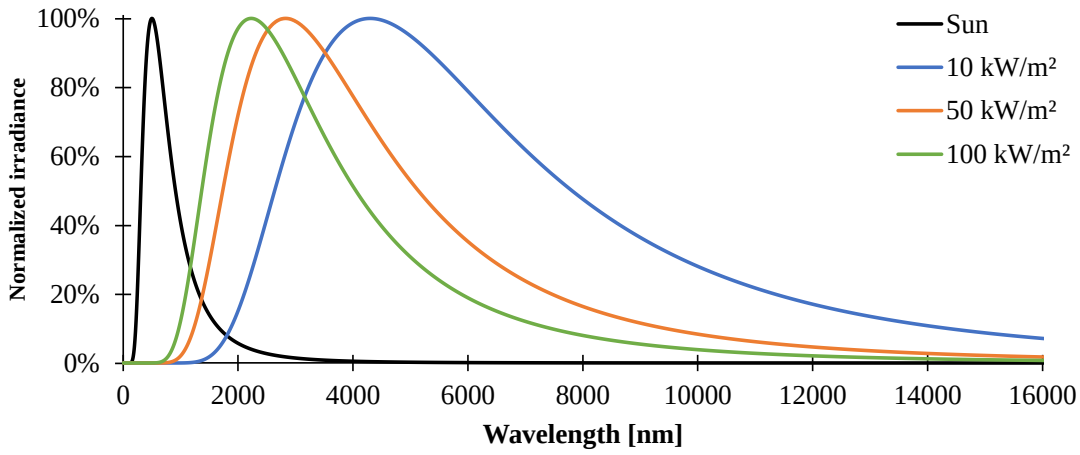

Figure 34: Normalized irradiance of blackbodies corresponding to sun and cone calorimeter coils at 10, 50 and 100 kW/m²

The calculation and experiments for measuring the scalar in-depth absorption coefficient A are more complex. The spectrally resolved irradiance at depth *x* into the sample is given by the Beer-Lambert law

as defined in **Eq. 61**. By integrating the contributions for all wavelengths, it is possible to evaluate the total irradiance at depth *x* as defined in **Eq. 62**.

$$I_\lambda(x) = I_\lambda(0)e^{-A_\lambda \cdot x} \qquad \textit{Eq. 61}$$

$$I(x) = \int I_\lambda(0)e^{-A_\lambda \cdot x}\, d\lambda \qquad \textit{Eq. 62}$$

Nonetheless, for modelling purposes, it is quite difficult and inconvenient to implement wavelength-dependent properties and, thus, only scalar optical properties can be handled. This is the parameter used in the standard expression for the Beer-Lambert law as defined in **Eq. 63**. I(0) is the integral of the spectral irradiance (*i.e.* the incident heat flux from the cone) of the overall wavelengths at the sample surface and can be expressed by **Eq. 64**. Note that **Eq. 61** and **Eq. 63** differ only on their wavelength dependency.

$$I(x) = I(0)e^{-A \cdot x} \qquad \textit{Eq. 63}$$

$$I(0) = \int I_\lambda(0)\, d\lambda \qquad \textit{Eq. 64}$$

Comparing **Eq. 62** and **Eq. 63,** and considering **Eq. 64**, it is possible to determine the scalar in-depth absorption coefficient as proposed in **Eq. 65**.

$$A = -\frac{1}{x} \cdot \ln\left(\frac{\int I_\lambda(0)e^{-A_\lambda \cdot x}\, d\lambda}{\int I_\lambda(0)\, d\lambda}\right) \qquad \textit{Eq. 65}$$

This scalar absorption coefficient is dependent on the depth *x*. The part of the radiation where the spectrally resolved absorption coefficient is high will rapidly be absorbed near the surface. As the radiation penetrates the sample, the radiation spectrum will be distorted such that relatively more energy is concentrated to the wavelengths where the spectral absorption coefficient is lower. It should be noticed that the absorption coefficient A given by **Eq. 65**, is *not* the local absorption coefficient at depth *x* but A is the parameter that gives the correct total irradiance at depth *x* according **Eq. 63**, with an irradiation spectrum $I_\lambda(0)$ at the sample surface.

The choice of depth *x* in **Eq. 65** is somewhat arbitrary and will affect A, but we propose to use the depth where the total irradiation has decreased to $e^{-2} \approx 0.135$. This depth is sometimes referred as the skin depth or the penetration depth of the electromagnetic field. This absorption coefficient can be obtained by an iterative procedure using **Eq. 63** and **Eq. 65**, where A is calculated for a given *x* in **Eq. 65**. Then, it is checked if $I(x) \approx 0.135\ I(0)$ in **Eq. 63**. Depending on the result, *x* is adjusted in **Eq. 65**, *etc.* until a self-consistent set of *x* and A is obtained.

Another approach would be to describe the absorption coefficient as a depth-dependent or local parameter. Indeed, by selecting smaller *x* values, it is possible to evaluate the part of heat which is

absorbed locally (instead of searching for the skin depth). Namely, the heat absorbed between the surface (x=0) and *x* is I(x)=I(0).exp(-$A_{[0;x]}$.x). Then, using I(*x*) as the incident heat flux in **Eq. 63**, and analysing the results for another depth *x*, it would be possible to calculate an absorption coefficient between *x* and *2x* and also the part of the heat absorbed in this depth (I(x).exp(-$A_{[x;2x]}$.x) but also the heat absorbed since the surface I(2x)=I(0).exp(-x.$A_{[0;x]}$ -x.$A_{[x;2x]}$). Then, by an iterative process, it would be possible to measure a depth-dependent absorption coefficient that would more realistically represent the absorption of heat inside a material.

The spectral transmittance through a thin sample is given by **Eq. 66** [173], where $T_{sample,\lambda}$ is the spectrally resolved transmittance through the entire specimen (that is actually measured), $T_{surface,\lambda}$ is the spectrally resolved transmittance through one surface of the specimen, $R_{surface,\lambda}$ is the spectrally resolved reflectance from one surface of the specimen and *d* is the thickness of the sample.

$$T_{sample,\lambda} = \frac{T_{surface,\lambda}^2 e^{-A_\lambda d}}{1 - R_{surface,\lambda}^2 e^{-2A_\lambda d}} \qquad \textit{Eq. 66}$$

The denominator is close to unity and is approximated here to not differ significantly for similar sample thicknesses. Furthermore, the surface transmittance is independent of sample thickness. Therefore, by dividing the sample transmittance for two different sample thicknesses, the **Eq. 67** is obtained. **Eq. 68** is thus used to calculate the scalar absorption coefficient A according to **Eq. 63** and **Eq. 65**.

$$\frac{T_{sample\ 1,\lambda}}{T_{sample\ 2,\lambda}} = e^{-A_\lambda (d_1 - d_2)} \qquad \textit{Eq. 67}$$

$$A_\lambda = \frac{\ln\left(\frac{T_{sample\ 1,\lambda}}{T_{sample\ 2,\lambda}}\right)}{d_2 - d_1} \qquad \textit{Eq. 68}$$

α_λ can be calculated from the reflectivity, R_λ, and the transmittance, T_λ, according to **Eq. 69**. The reflectance from a thin sample can be expressed as described in **Eq. 70** [173], where $R_{sample,\lambda}$ is the spectrally resolved reflectance from the entire specimen (that is actually measured), $R_{surface,\lambda}$ is the spectrally resolved reflectance from one surface of the specimen. The scalar absorption coefficient α can thus be calculated using **Eq. 59** and the measurement of the reflectance and transmittance.

$$\alpha_{sample,\lambda} = 1 - R_{sample,\lambda} - T_{sample,\lambda} \qquad \textit{Eq. 69}$$

$$R_{sample,\lambda} = R_{surface,\lambda}\left(1 + T_{sample,\lambda} e^{-A_\lambda d}\right) \qquad \textit{Eq. 70}$$

II.2.5. DETERMINATION OF THE HEAT CAPACITY OF GASES THROUGH FTIR QUANTIFICATION

Another important input parameter needed to model the pyrolysis of materials is the heat capacity of gases. Note that it is possible to predict the heat capacity of thermodynamics properties of gases using predictive tools and their chemical structure [174,175]. The determination of the heat capacity of gases does in fact depends on the composition of the decomposition gases released when the materials decomposes. The nature and quantities of the individual gases need thus to be characterized.

II.2.5.a. Principle of FTIR spectrometry

The analysis of fire effluent using FTIR gas analyzers is growing rapidly in research and regulatory testing. Since the first studies in the late 90's [176], it has become a standardized method under ISO 19702 [177]. FTIR spectroscopy is a well-known chemical analysis technique whose operating principle is based on the interaction of IR radiation with matter. It is commonly known that molecules can absorb infrared radiation, inducing vibrational transitions within the chemical bonds.

If the frequency of IR radiation matches the natural vibration frequency of molecular bonds, the radiation is absorbed causing changes in the amplitude of the molecule energy, which passes from its ground electronic state to an excited state. However, homo-nuclear diatomic molecules such as oxygen (O_2) and nitrogen (N_2) are transparent in IR because of their lack of polarized bonds. In the same way, noble gases like helium (He) and argon (Ar) cannot absorb infrared radiation and so have no infrared activity. In addition, since each molecule is an unique combination of atoms, two compounds will not have the same infrared activity. In consequence, IR spectroscopy will be used as an explicit approach to identify chemical species. However, as with all chemical techniques based on the interaction of matter with electromagnetic radiation, overlapping phenomena can occur between species having similar properties. This occurs when the species to be characterized have the same functional groups for example. This represents a limitation and should be taken into account during exploitation and interpretation of infrared spectra.

II.2.5.b. Principle of FTIR quantification

The IR light spectrum can be divided into three regions, near, mid and far-infrared. The region of interest in this study is mid-infrared, more precisely from 4500 to 650 cm^{-1}, this being because the absorption spectra of most organic and inorganic compounds lie within this region. Infrared quantitative analysis is based on Beer Lambert law (**Eq. 61** and **Eq. 71**) which states the relationship between the absorbance of an IR-absorbing substance and its concentration. This law links the absorbance α_λ of any specie at wavelength λ to its concentration C, the distance (l) where the IR irradiation and the specie interact (the length of the gas cell of the FTIR spectrometer) and are in contact and the molar absorption coefficient ε'_λ at wavelength λ.

$$\alpha_\lambda = -\log\left(\frac{I_\lambda}{I_{0\lambda}}\right) = \varepsilon'_\lambda . l . C \qquad \textit{Eq. 71}$$

Before its use, the FTIR analyzer have to be calibrated for each gas of interest and for the expected range of concentration using Classical Least Square (CLS) technique [178,179]. Sets of calibrations at different concentrations have to be built using pure reference gases cylinders and/or dilution system. Doing so, it is then possible to access to ε'_λ for any gases at any wavelengths.

Knowing ε'_λ, the next step for FTIR quantification is to set up the spectral regions in which each gas will be quantified. Baselines are interpolated linearly for each region used. In each region, the gases to be quantified are defined as well as the potential interferences with the other gases from the quantification method. Note that a polynomial correction can be applied to consider the non-linearity of the calibration over a large range of concentration. It is also possible to set up several region for a given specie in order to check unexpected interferences Guidance for the selection of the spectral regions were given by Hakkarainen *et al.* [176]:

- Absorbance should be as high as possible but limited to unity.
- If one have the knowledge about wavelengths in which interferences occur, avoid these wavenumber windows.
- If it is not possible to select wavelength regions where no interferences occur, the windows where the component is covered only by water should be considered.

The measured absorbance A_j in the j^{th} spectral region is given by **Eq. 72**. In this equation, the pathlength is not considered as it a constant and the same between the measurements on the unknown sample and the calibrations experiments. In this equation, the only unknown parameters are the concentrations C_i of each i^{th} specie. For all the spectral windows j used in the model, it is possible to define the error E_j

between the measured absorbance A_j^{exp} and a predicted absorbance $\sum_i \left(\varepsilon'_{i_j}.\, C_i\right)$ as defined in **Eq. 73**. The "least square" principle defines the fact that we want to minimize the sum squared errors $\sum_j {E_j}^2$ (**Eq. 74**) in the reproduction of values of A_j^{exp} and a calculated absorptivity $\sum_i \varepsilon'_{i_j}.\, C_i$ over all *j* wavelength windows. Using statistical tools for minimizing **Eq. 74**, it is then possible to calculate the concentration of each species.

$$A_j^{exp} = \sum_i \left(\varepsilon'_{j_i}.\, C_i\right) \qquad \textit{Eq. 72}$$

$$E_j = A_j^{exp} - \sum_i \left(\varepsilon'_{i_j}.\, C_i\right) \qquad \textit{Eq. 73}$$

$$\sum_j {E_j}^2 = \sum_j \left(A_j^{exp} - \sum_i \varepsilon'_{i_j}.\, C_i\right) \qquad \textit{Eq. 74}$$

II.3. EXPERIMENTAL TECHNIQUES

II.3.1. STUDY OF THE THERMAL STABILITY OF MATERIALS

II.3.1.a. Thermo-gravimetric analysis

Thermo-gravimetric analysis (TGA) were performed on a TA Instruments Discovery TGA, using 250 µL open alumina pans. Experiments were carried out under nitrogen to mimic pyrolytic decomposition. The balance purge flow was set to 15 mL/min nitrogen to avoid the oxidation of the balance. The balance was set at 40 °C in order to have controlled conditions and optimum sensitivity. All samples of 5.0 ± 0.5 mg underwent an isotherm at 50 °C for 30 min followed by a heating ramp from 50 to 800 °C at a chosen heating ramp (from 2 to 500 K/min). The experiments are performed two times to ensure the repeatability.

Calibration of the apparatus was conducted at least twice a year at a heating rate of 10 K/min. The temperature calibration was performed according to ASTM E1582-10 [180]. It relates the literature value of the Curie temperatures (T_{Curie}) of metallic samples to T_{Curie} of the same materials measured by the apparatus. The standard products used for the calibration were supplied by TA Instruments and are traceable from the National Institute of Standards and Technology (NIST). They are representative of the temperature range of interest in this study. Indeed, the lowest point is at 152.6 °C and the highest at 930.8 °C as shown in **Table 9**.

Table 9: Reference materials and associated Curie temperature used for TGA calibration

Substance	T_{Curie}
Alumel®	152.6 ± 1.0 °C
Nickel	358.2 ± 1.1 °C
$Ni_{83}Co_{17}$ alloy	554.4 ± 2.2 °C
$Ni_{63}Co_{37}$ alloy	746.4 ± 1.6 °C
$Ni_{37}Co_{63}$ alloy	930.8 ± 1.9 °C

In order to determine potential interactions between EVA and the flame retardant (FR) additives during the thermal degradation, a comparison between experimental and calculated TG curves was performed. The calculated curve is obtained by linear combination of the TG curves of each component (EVA, ATH and NC) weighted by their content in the formulation. Weight difference curves $\Delta W(T)$ were determined following **Eq. 75**. $W_{exp}(T)$ is the experimental TG curve of the formulations, $W_{theo}(T)$ is the theoretical TG curve obtained according to **Eq. 76** where ω_{EVA}, ω_{ATH} and ω_{NC} are the weight fraction in EVA, ATH and NC respectively.

$$\Delta W(T) = W_{exp}(T) - W_{theo}(T) \qquad \textit{Eq. 75}$$

$$W_{theo}(T) = \omega_{EVA}.W_{EVA} + \omega_{ATH}.W_{ATH} + \omega_{NC}.W_{NC} \qquad \textit{Eq. 76}$$

The main objective of this technique is to point out if the addition of the FR additives will stabilize or destabilize the system. When $\Delta W < 0$, the weight loss is higher than expected, showing that the reactivity of the polymer with the additives leads to a thermal destabilization of the material. On the opposite, when $\Delta W > 0$, the system is thermally stabilized.

II.3.1.b. Thermo-gravimetric analysis coupled with FTIR spectrometry

Thermogravimetric analysis coupled with Fourier Transformed Infrared spectrometry (TGA-FTIR) is performed using the same TGA (TA Instrument Discovery TGA) coupled with a Thermo Scientific Nicolet™ iS™10 spectrometer. Analyses were carried out in 250 µL open alumina crucibles. The balance flow was set to 15 mL/min whereas the purge flow was fixed to 50 mL/min. Samples were heated from 50 to 800 °C following a linear heating ramp of 10 K/min after an isothermal of 120 min at 50 °C. Gases evolved during the TGA experiment are detected continuously by the FTIR device.

The spectra were recorded using the OMNIC® software in a range from 450-4000 cm^{-1}. The number of scans is fixed at 8 and the resolution at 4 cm^{-1}. The temperature of the transfer line between the TGA and the FTIR instrument as well as the gas cell of the FTIR were set to 225 °C to avoid condensation of the evolved gases. The FTIR was equipped with a nickel-plated aluminium gas cell of 100 mm in length and 23 mL internal volume equipped with KBr windows.

II.3.1.c. Pyrolysis – Gas Chromatography – Mass Spectrometry

Pyrolysis-gas chromatography-mass spectrometry (py-GC/MS) analyses were performed on a Shimadzu GC/MS QP2010 SE and a Frontier Lab PY-2020iD micro-furnace pyrolyzer (**Figure 35**). Experiments were performed under inert conditions using helium. Sample size is about 500 µg for neat EVA and 600-800 µg for EVA/ATH materials.

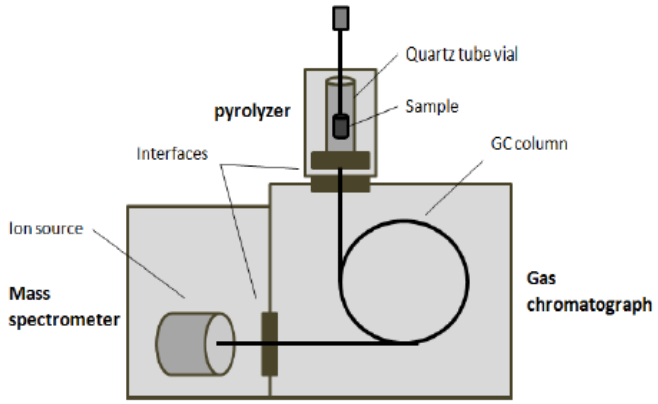

Figure 35: Schematic presentation of the py-GC/MS device

The experimental protocol is described in **Figure 36**. Samples (in a stainless steel cup) were first heated from 50 to 800 °C with a heating ramp of 20 K/min. After the decomposition process evolved gases were partially introduced into the GC/MS system. A part of the gases was split outside of the column to avoid the blockage or the saturation of the detector. Released decomposition gases were separated using a fused silica capillary column (30 m x 0.25 mm x 0.25 µm film thickness). The temperature of the column was set to 35 °C during the heating of the sample and only the volatile gases at ambient temperature were analyzed in this step. The column was then heated up to 300 °C with a heating rate of 5 K/min followed by an isotherm at 300 °C for 40 min. The linear velocity of the carrier gas was set to 40 cm/s.

The gases and fragments were analyzed using a quadrupole mass spectrometer with an Electron-Impact (IE) ionization source. The IE spectra were recorded at 70 eV with a mass scan of 2 scans/s. The interface between the pyrolyzer and the GC was heated up to 320 °C and the interface GC/MS to 280 °C. The temperature of the ion source was set at 230 °C. Data were analyzed using the GC/MS post-run analysis from Shimadzu and F-Search from Frontier lab, whereas products were identified using NIST database.

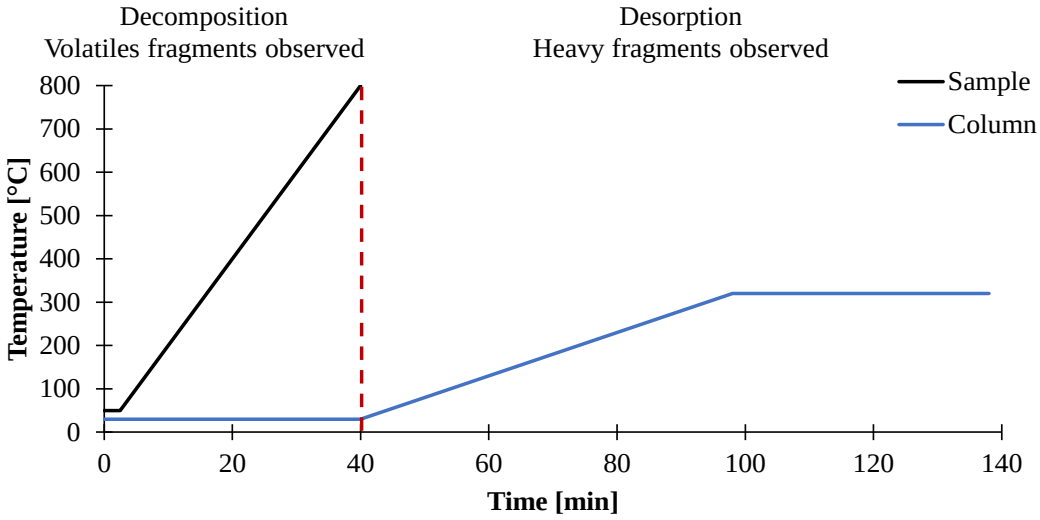

Figure 36: Scheme of the py-GC/MS procedure of use

II.3.2. DETERMINATION OF THE THERMO-PHYSICAL PROPERTIES

II.3.2.a. Simultaneous Thermal Analysis experiments

Differential Scanning Calorimetry (DSC) coupled with thermogravimetric experiments are conducted with a Netzsch 449 F1 Jupiter simultaneous thermal analyzer (STA). Samples were put in platinum/rhodium pans with lids. The lids had a small orifice (0.25 mm in diameter) for ventilation. This container configuration was used to maximize the thermal contact between a degrading sample and heat flow sensing thermocouples located underneath the pan. Before each experiments, a blank with empty crucibles was performed and subtracted to the experiments so both mass and heat flow signal were independent of the crucibles.

Temperature and sensitivity calibrations were conducted with the STA prior testing the samples at heating rate of 20 K/min according to the related ASTM standards [180–183]. The temperature calibration relates the literature value of the melting temperatures (T_{fusion}) of organic and inorganic samples to the melting temperature of the same materials measured by the apparatus. The sensitivity

calibration relates the literature value of the enthalpy of melting (ΔH_{fusion}) of organic and inorganic samples to the measured enthalpy of melting of the same samples.

The standards products used for the calibration were supplied by Netzsch company and are representative of the temperature range of interest in this study (50-800 °C). Indeed, the lowest point was at 69.2 °C and the highest at 808.0 °C as shown in **Table 10**.

Table 10: Reference materials and associated meting temperature and meting enthalpy used for STA calibration

Substance	**T_{fusion} [°C]**	**ΔH_{fusion} [J/g]**
1,1'-biphenyl	69.2	20.5
Benzoic acid	122.4	447.4
Cesium chloride	476.0	17.2
Barium carbonate	808.0	94.9

II.3.2.b. Thermal conductivity measurement

Thermal conductivity measurements were carried out from 20 °C to 700 °C, using a Hot Disk thermal constant analyser (TPS2500S) from Thermoconcept (Merignac, France), which is based on a Transient Plane Source method. The sensors (radius of 3.189 mm) were made of mica and are high temperature resistant. The sensor acts both as a heater and as a thermocouple and is hot pressed between two 25x25x7 mm^3 plates of the material to ensure a good contact between the sensor and the sample.

For each temperature, the measurements were performed as soon as the sample temperature was down to ± 0.5 °C of the desired temperature for 30 min by applying a power of 0.02 to 0.09 W for 10 to 80 s depending on the thermal properties of the sample. Between each measurements, the sample temperature was stabilized by waiting at least 15 times the acquisition time of the previous experiment. The furnace was directly connected to a nitrogen flow. Note that all experiments were carried out in an inert atmosphere to prevent oxidation of the sensor. The experiments were run as duplicates and were repeatable within 5 % margin of error.

II.3.2.c. Optical measurements

Transmittance and reflectance spectra in the UV, visible and near IR region, with wavelengths in the interval 0.3 to 2.5 µm, were recorded using a Perkin Elmer Lambda 900 double beam spectrophotometer equipped with an integrating sphere. In the infrared wavelength range (2.5 to 17 µm), a Bruker FTIR single beam spectrophotometer equipped with a gold coated integrating sphere was used. The principle of operation of an integrating sphere is shown in **Figure 37**. The figure shows a cross-section of an integrating sphere with the incident beam entering the sphere through the entry port to the left and hitting the sample (or reference) covering the sample port to the right. The total radiation reflected (R_{tot}) from the sample surface is reflected multiple times inside the sphere. This illumination intensity is seen by the detector, which records a signal proportional to all the reflected light, including both the specular (R_{spec}) and diffuse (R_{diff}) parts.

Measurements were performed at a stabilised temperature of 23 °C ± 2 °C. The samples were conditioned in the laboratory one hour prior to the test. The accuracy of the reflectivity measurements was ± 3 %. Transmittance measurements are performed in a similar manner to the reflectance measurements described above, but the sample was positioned across the beam entry port as shown in **Figure 37**.

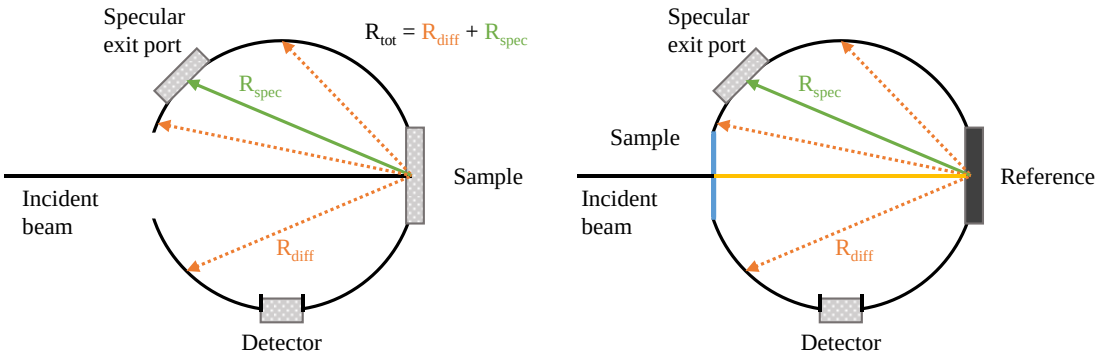

Figure 37: Principle of an integrating sphere: reflectance (left) and transmittance mode (right)

II.3.3. FIRE TESTS

II.3.3.a. Mass loss calorimeter

Mass loss calorimeter (MLC) is a bench-scale reaction to fire test which provides a forced-flaming combustion scenario that is typical of developing or developed fires. The measurements were carried out on a Fire Testing Technology (FTT) mass loss calorimeter device (ISO 13927 [184], ASTM E906 [185]). The schematic representation of the device is shown in **Figure 38**. The samples consist of plaques of 100x100 mm² of surface area and variable thickness (1.2 or 3 mm). Each plaque was covered by a 100x100 mm² grid to avoid contact between the material and the spark igniter due to the blowing or bending of the plaque before ignition (grid not mentioned in ISO 13927). The distance between the sample holder and the heat source was set to 35 mm. The heat flux is uniform on the 100x100 mm² plaques for such a distance [73].

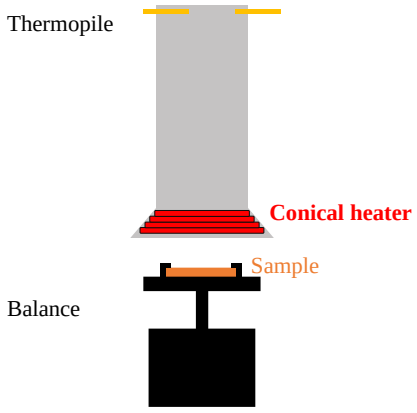

Figure 38: Schematic representation of the mass loss calorimeter

The samples were wrapped in an aluminium foil such that one face of the sample was exposed to the radiant heat flux. Each sample was placed on top of 50 mm insulating fire brick (IFP JM26 from Morgan Thermoceramics). The plaque was covered by a retainer frame that maintain the grid onto the sample and thus the surface area exposed to the heat source is limited to 88.4 mm².

An external heat flux (35 or 50 kW/m²) produced by a conical heater element was applied to the sample. The temperature of the gaseous combustion products was measured at the top of the chimney with a thermopile. The calibration of the heat release rate (HRR) is performed with methane. A methane flow

of 0.42 to 8.38 mL/min is burnt above the sample holder to obtain a calibration curve of the heat release as a function of the temperature.

The values measured by the mass loss calorimeter are: heat release rate (HRR), peak of HRR (pHRR), total heat released (THR), time to ignition (TTI) and to flameout (TTF), mass loss (ML) of the sample during the experiments as well as the mass loss rate (MLR). All measurements were performed in duplicate. The acceptable error of measurements is estimated at 10 % for all the values.

II.3.3.b. Gasification experiments

A special setup of the previously described MLC was designed by isolating the cone heater and the sample in order to control the surrounding atmosphere. This controlled atmosphere mass loss cone (CAMLC) apparatus was developed to study the influence of depleted oxygen environment (low ventilated fire) on thermal decomposition of materials. The main difference from the standard MLC unit is the addition of an enclosure under the cone heater. As shown in **Figure 39**, this chamber consists of a stainless steel enclosure with the standard cone heater at the top, a door with an observation window at the front and two gas inlet ports at the bottom.

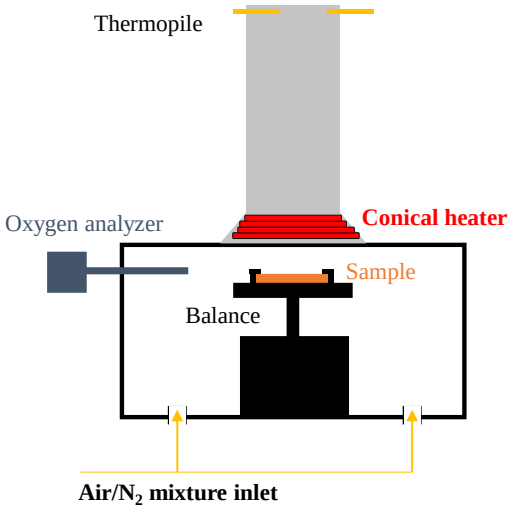

Figure 39: Schematic representation of CAMLC apparatus

The gas ports supply the chamber with a mixture of air and nitrogen to create the desired ambient atmosphere and to adjust the desired oxygen and nitrogen concentrations. The flow of the gas mixture

was maintained at 100 L/min through the enclosed chamber to facilitate the recirculation of combustion products over the specimen surface. The volume flow of air and nitrogen is controlled by two separate rotameters allowing the atmosphere in the chamber to be adjusted. Mixing is monitored by an additional oxygen analyzer (BA1000 from Bühler® Technologies), which is directly connected inside the enclosure. The oxygen concentration in the enclosure can be adjusted to any value between 0 vol%O_2 and 21 vol%O_2. The spark igniter was removed in this configuration. The effluents are collected in a hood and transported through an exhaust duct similar to that used in a classical mass loss cone.

The sample configurations (size, frame…) are similar to the previously described MLC apparatus. An external heat flux of 50 kW/m² was applied to the sample for the CAMLC experiments. The fire parameters measured in the CAMLC are limited to mass loss and mass loss rate.

II.3.3.c. Fire tests coupled with FTIR spectrometry

Gases evolved during MLC and CAMLC can be analyzed coupling an FTIR spectrometer (MLC-FTIR and CAMLC-FTIR respectively) to the chimney of the fire test. In that case, experiments were performed using the devices described above (**Figure 38** and **Figure 39**). The same conditions than non-coupled experiments were used.

Gas picking pistol and transfer lines (**Figure 40**) were provided by the M&C Tech Group. The transfer line between CAMLC and FTIR is 2 m long and was heated at 180 °C. To insure a constant temperature of the transfer line, two temperature controllers were installed. Before analyzing the gases by FTIR, soot particles were filtered off by two heated filters (2 and 0.1 µm) consisting of glass fibers and ceramic respectively.

The FTIR spectrometer (Antaris™ Industrial Gas System) was provided by ThermoFisher Scientific. It was equipped with a 2 m long and 200 mL internal volume gas cell, a nitrogen cooled MCT-A (Mercury Cadmium Telluride) detector and a KBr beam splitter. The chamber of the spectrometer is filled with dry air. Resolution was set at 0.5 cm^{-1} between 650 and 4000 cm^{-1}. The gas cell was made of nickel-coated aluminum. The mirrors were made of gold-coated aluminum and windows were made of barium fluoride (BaF_2). The gas cell was set at 180 °C and 650 Torr during the experiments.

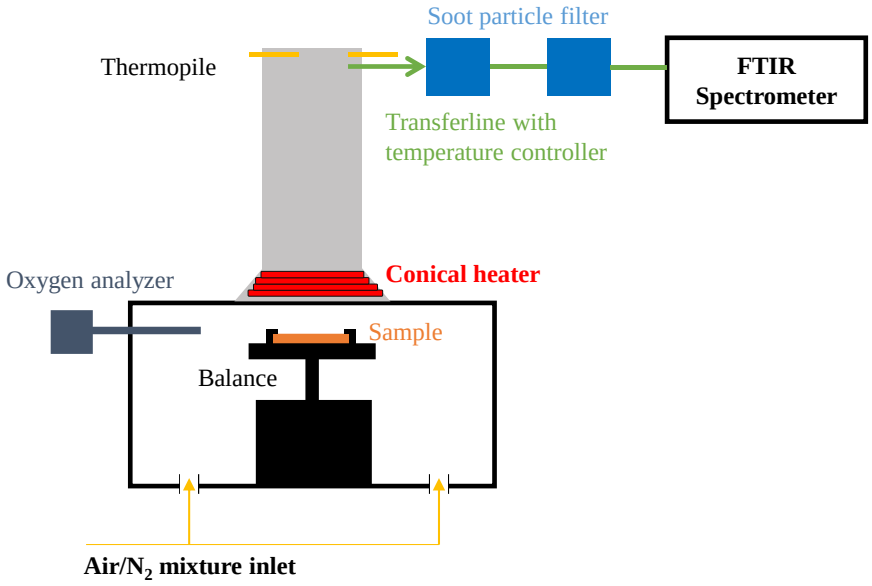

Figure 40: Schematic representation of CAMLC-FTIR apparatus

The calibration spectra used for the quantification method were supplied by ThermoFisher Scientific. The precision and accuracy of CLS computational model for the FTIR quantification is dependent on the appropriate selection of the wavelength windows selection and attribution of the main species and interfering species in each of these windows. The parameters of the method used in this study are detailed in **Table 11**. The method considers 14 different gases that are quantified using 35 wavelength regions and 203 spectra. The method was implemented using TQ™ Analyst software. The regions were selected based on the work of Guillaume *et al.* [186] and of the quantification methods supplied by ThermoFisher. Compared to the previous methods, acetic acid and acetone were added with respect of the interferences with the other gases.

Table 11: Calibrations regions, interfering species and ranges of calibration

Gas	Regions used for the quantification [cm^{-1}]	Interfering specie	Range of calibration [ppm]	Number of standards
CO_2	740.09-750.66 3683.61-3682.20	H_2O, C_2H_2, HCN	1960-84517	34
CO_2	2350.56-2347.91 2370.33-2353.21	NO	100-1000	11
CO	2049.96-2056.95 2071.95-2066.91 2092.15-2113.12 2130.47-2133.61 2153.37-2159.40	H_2O H_2O	1-99800	55
H_2O	3498.48-3512.46 3965.74-3945.29	NH_3, HCN NH_3, HCN	5000-150000	10
NO	1851.37-184.94 1873.89-1877.36 1911.18-1913.33 1925.09-1931.12	H_2O H_2O H_2O H_2O	1-10000	20
NO_2	1584.48-1588.33 1597.25-1600.15	H_2O, NH_3 H_2O	10-1000	10
NH_3	953.87-974.84 1104.77-1102.60	H_2O, Acetic acid C_2H_4	10-1000	10
HCN	3353.84-3352.69 3376.80-3369.61	H_2O, C_2H_4, C_2H_2 H_2O, NH_3, C_2H_2	45-2093	7
CH_4	3151.60-3143.64 3167.51-3165.10	H_2O, HCN, C_2H_4 H_2O, HCN, C_2H_4	9.9-10008	15
C_2H_4	903.49-899.87 952.42-944.95	H_2O, NH_3, Acetone H_2O, NH_3	10-510	10
C_2H_2	3250.91-3249.71	C_2H_4, CH_4, HCN	10-507	9
C_3H_8	2963.33-2960.20 2971.00-2964.00	H_2O, C_2H_4, CH_4, Acetone C_2H_4, CH_4, Acetone	10-490	10
CH_2O	2755.75-2750.89 2781.39-2777.20	H2O, CH_4, HCN H2O, CH_4, HCN	11-110	10
Acetic acid	1184.56-1125.02 1148.64-1142.62 1185.04-1181.67	H_2O, NH_3, C_2H_4, CH_4, Acetone H_2O, NH_3 H_2O, NH_3, C_2H_4, CH_4, Acetone	26.4-176.2	5
Acetone	1217.10-1213.73 1214.69-1224.34 1228.67-1227.23	CH_4, Acetic acid H_2O, NH_3, CH_4, Acetic Acid CH_4	25-500	7

II.4. CONCLUSION

In this chapter, the polymer and the additives, as well as the preparation of the materials used in this study were presented in a first part. Afterwards, methods to evaluate the decomposition in fire or gasification experiments were described. Background about the characterization of thermo-physical properties, kinetic of decomposition and optical properties were also given, as well as experimental techniques used to investigate the decomposition of the materials in the gas and condensed phase.

The following chapter will describe the development of methodologies for the characterization of thermo-physical properties of EVA/ATH materials using the techniques presented in this chapter.

CHAPTER III. THERMO-PHYSICAL PROPERTIES OF EVA/ATH MATERIALS

This chapter is dedicated to the investigation of the thermo-physical properties of EVA materials. As seen in **CHAPTER I** in order to model the fire performances of materials, the parameters describing how these materials decompose, transfer and absorb heat have to be measured. The first section of this chapter will thus emphasize the thermal decomposition of EVA/ATH composites and their kinetics. Then, the thermal properties of the materials will be investigated as a function of temperature but also of decomposition states. The optical properties such as emissivity and in-depth absorption coefficients will then be characterized. Finally, the heat capacity of the decomposition gases will be determined.

III.1. THERMAL DECOMPOSITION OF EVA/ATH COMPOSITES

Even if the thermal decomposition of EVA/ATH composites is already widely reported in the literature as stated in **I.3** (p.35), the first part of this chapter will be dedicated to the investigation of the thermal decomposition of the materials used in this study through TGA-FTIR and py-GC/MS. Then, the kinetics of decomposition of the additives will be examined. Finally, the kinetics of decomposition of the EVA/ATH formulations will be determined in regards of the previously defined decomposition pathway.

III.1.1. MECHANISM OF THERMAL DECOMPOSITION OF EVA/ATH COMPOSITES

III.1.1.a. Thermal stability

One of the goal of this work is to simulate the fire behavior of EVA/ATH composites. To do so, the knowledge of their thermal stability is of prime interest. EVA/ATH materials decompose in pyrolytic conditions with two apparent steps of decomposition as shown in **Figure 41**. According to the literature, the first step can be attributed to the dehydration of ATH and to the deacetylation of EVA. The second step can be attributed to the decomposition of the remaining polymer. Interestingly, a shift towards lower temperature (at around 460 °C) is observed for the last step of decomposition when NC are added into the material while for EVA/ATH, it is observed at the same temperature than for neat EVA (at around 480 °C).

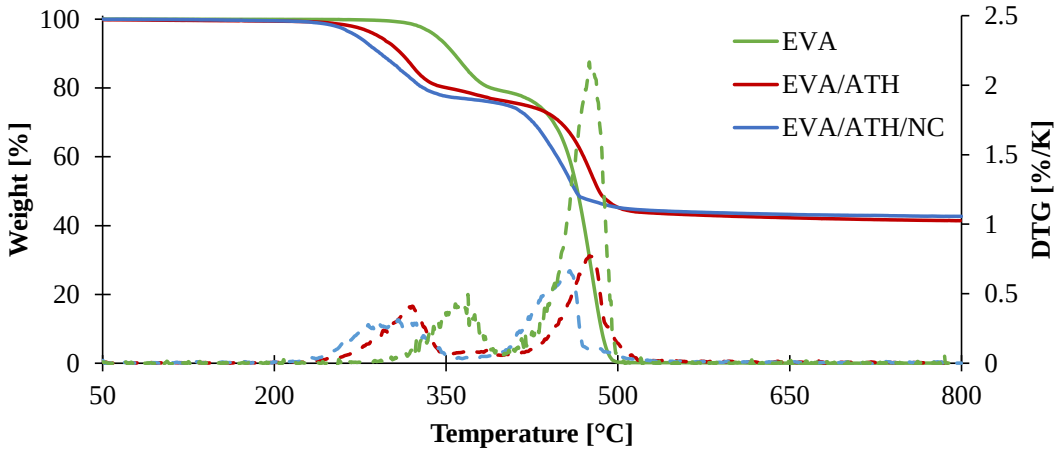

Figure 41: TG and DTG curves for EVA and EVA/ATH composites at 10 K/min under pyrolytic conditions

In order to compare the thermal stability of the EVA/ATH formulations to the ones of their individual components, weight difference (ΔW) curves are plotted in **Figure 42**. It is noteworthy that a stabilization ($\Delta W > 0$) is observed in both case. Either with or without NC, the maximum of stabilization occurs at 300 °C. Nonetheless, the stabilization is lower (around 6 %) in the case of EVA/ATH/NC than in the case of EVA/ATH (around 12 %). Then, between 350 and 450 °C, EVA/ATH is slightly stabilized (ΔW of around 5 %) while EVA/ATH/NC is less stabilized. It is interesting to note that this shift of deacetylation toward lower temperature was already observed by Costache *et al.* [98] for EVA and EVA/NC composites. According to this author, this can be attributed to a catalytic effect of the acidic sites of the clay [98] on the deacetylation reaction.

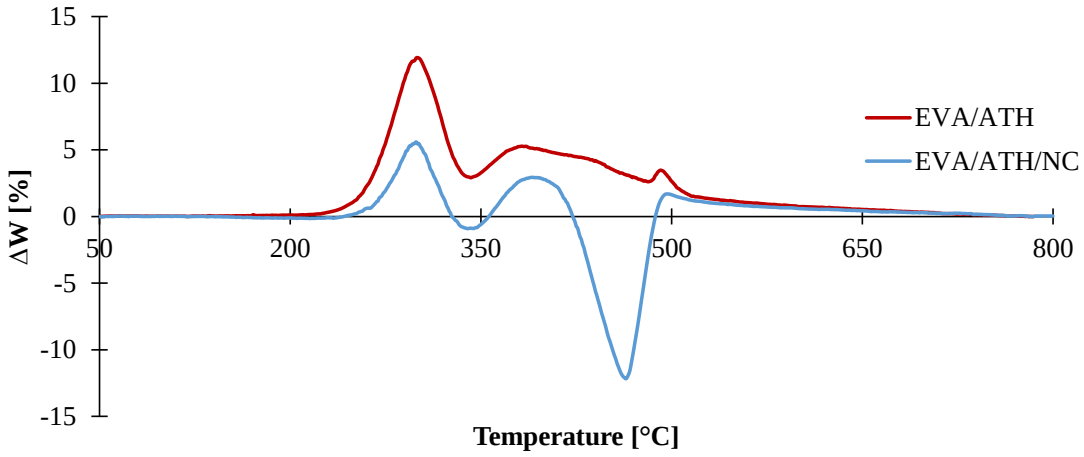

Figure 42: TG difference curves for EVA/ATH materials

The final step of decomposition (T > 450 °C) shows a low stabilization for EVA/ATH as ΔW lies between 0 and 5 % when a destabilization is noted in presence of NC. In order to better understand and to explain the various observed phenomena, the gases released while the materials decompose were analyzed.

III.1.1.b. Identification of decomposition gases

The identification of the decomposition gases was done using TGA-FTIR and py-GC/MS. The DTG curve of EVA/ATH is presented in **Figure 43**, together with the FTIR spectra taken at the peaks of the DTG curve. The temperatures of these peaks are 340 °C (a), 390 °C (b) and 490 °C (c). FTIR spectra are compared with spectra taken from the literature [187]. The corresponding attributions of the observed vibrations are presented in **Table 12**.

Table 12: Attribution of vibration observed by TGA-FTIR of EVA/ATH materials

Wavelength [cm^{-1}]	Corresponding chemical structure
2938	-CH_2 bending
2873	-CH_2 bending
1700-1400	-OH bending
3700-3400	-OH stretching
989	-CH_3 bending
1788	-C=O stretching for acetic acid
1182	-C-O stretching for acetic acid
1363	-CH_3 stretching for acetone
1215	-C-C stretching for acetone
1731	-C=O stretching for acetone

On the case of EVA/ATH, the typical vibrations assigned to water are observed between 3400 and 3700 cm^{-1} as well as between 1700 and 1400 cm^{-1} at the first peak of decomposition (**Figure 43.a**). This step can thus be attributed to ATH dehydration.

At the second peak of decomposition (**Figure 43.b**), the vibrations associated to acetone at 1731 and 1363 cm^{-1} are detected along with these of acetic acid at 1788 and 1182 cm^{-1}. These observations support the analyses of Witkowski *et al.* [110] and Ngohang *et al.*[116] that found a release of acetone with EVA/ATH. This is also supported by the studies of Pei *et al.* [113] and Pestman *et al.* [114,115] that showed a catalytic effect of mineral oxides in the ketonization of carboxylic acids.

The spectrum associated to the final peak of decomposition of EVA/ATH (**Figure 43.c**) shows a very simple shape. An intense peak between 2700 and 3100 cm^{-1} is observed. Namely, two intense peaks associated to the bending vibration of CH_2 in hydrocarbons chains at 2938 and 2873 cm^{-1} can be observed. Spectra associated to decane and eicosane are plotted in **Figure 43** for comparison. It can be

noted that at the exception of the shoulder around 2970 cm^{-1}, both spectra are identical. This shoulder is associated to CH_3 stretching and its relative intensity decreases with increasing the length of the carbon chain of a linear hydrocarbon. Indeed, there will be proportionally more CH_2 in the internal carbon backbone than CH_3 at the end of the chain. It is thus not possible to precisely elucidate the structure of gases evolved at that stage but we may conclude that it corresponds to long chains hydrocarbons.

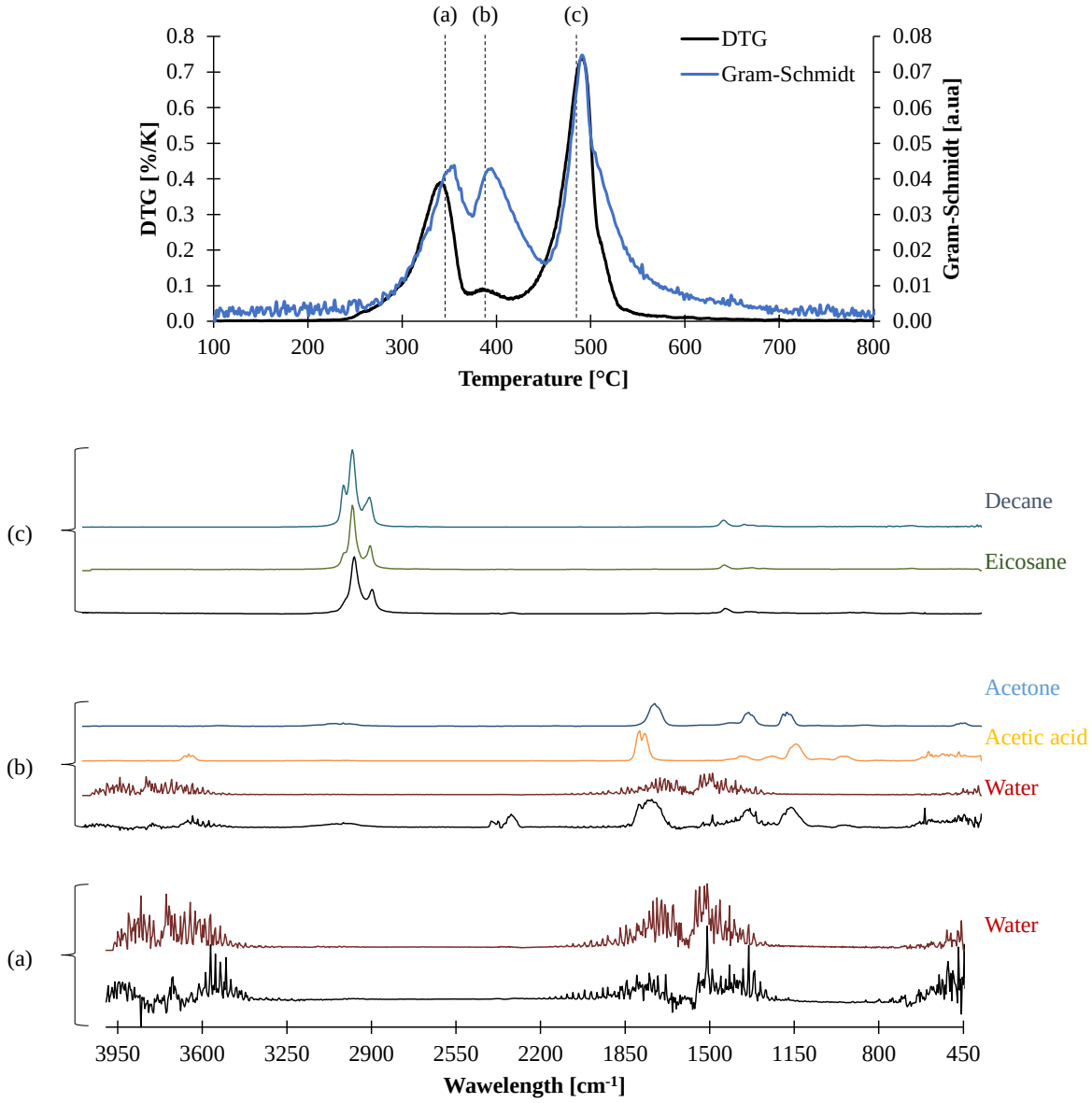

Figure 43: DTG curve and Gram Schmidt obtained under pyrolytic conditions at 10 K/min and associated FTIR spectra for EVA/ATH

Similar experiments were performed with EVA/ATH/NC and the DTG curve, Gram-Schmidt and its associated FTIR spectra are presented in **Figure 44**.

As stated in the previous section, the thermal decomposition of EVA/ATH/NC is significantly different than the one of EVA/ATH. Instead of having two consecutive peaks associated to ATH dehydration (250-360 °C) and then EVA deacetylation (360-430°C), EVA/ATH/NC shows only one DTG peak between 200 °C and 350 °C. However, this peak is broader than the one of EVA/ATH and it reaches a plateau between 290 and 330 °C. The final peak of decomposition is also splitted into two peaks. A comparison of the FTIR spectra associated with the beginning (a) and the end of this plateau (b) is presented in **Figure 44** as well as the spectra associated to the maximum of each peak for the decomposition of the polyene ((c) and (d)).

At 290 °C (**Figure 44.a**), the vibrations associated to water are observed between 3700 and 3400 cm^{-1}. This leads to the assumption that ATH dehydrates first as observed without NC. Note that even if the onset temperature of the decomposition of ATH of EVA/ATH and EVA/ATH/NC are similar, the maximum rate of decomposition appears earlier (290°C vs. 340 °C) in the presence of NC.

At 330 °C (**Figure 44.b**), the vibrations observed in the collected FTIR spectrum can be attributed to water in the region 3400-3700 cm^{-1}. Note that the relative intensities of these peaks are lower than for the spectrum collected at 290 °C. More intense peaks are nonetheless observed, in particular at 1182 cm^{-1} and 1788 cm^{-1}. These peaks can be attributed to acetic acid. Note that the peaks associated to acetone are not observed at this stage.

The final stage of decomposition can be attributed to peaks (c) and (d) on the DTG curve presented in **Figure 44**. As presented in **Figure 41**, the peak of highest intensity for EVA/ATH/NC is shifted towards lower temperature compared to the one of EVA/ATH (460 °C vs. 490 °C). Nonetheless, with the presence of NC, a shoulder appears at high temperature at the same temperature than the main peak of decomposition of EVA/ATH. This suggests that the presence of NC accelerates the decomposition of the main part of the remaining EVA. The spectra associated to these peaks are similar to the ones obtained for EVA/ATH: two main peaks are observed at 2938 and 2873 cm^{-1} and can be attributed to long chain hydrocarbons such as decane or eicosane.

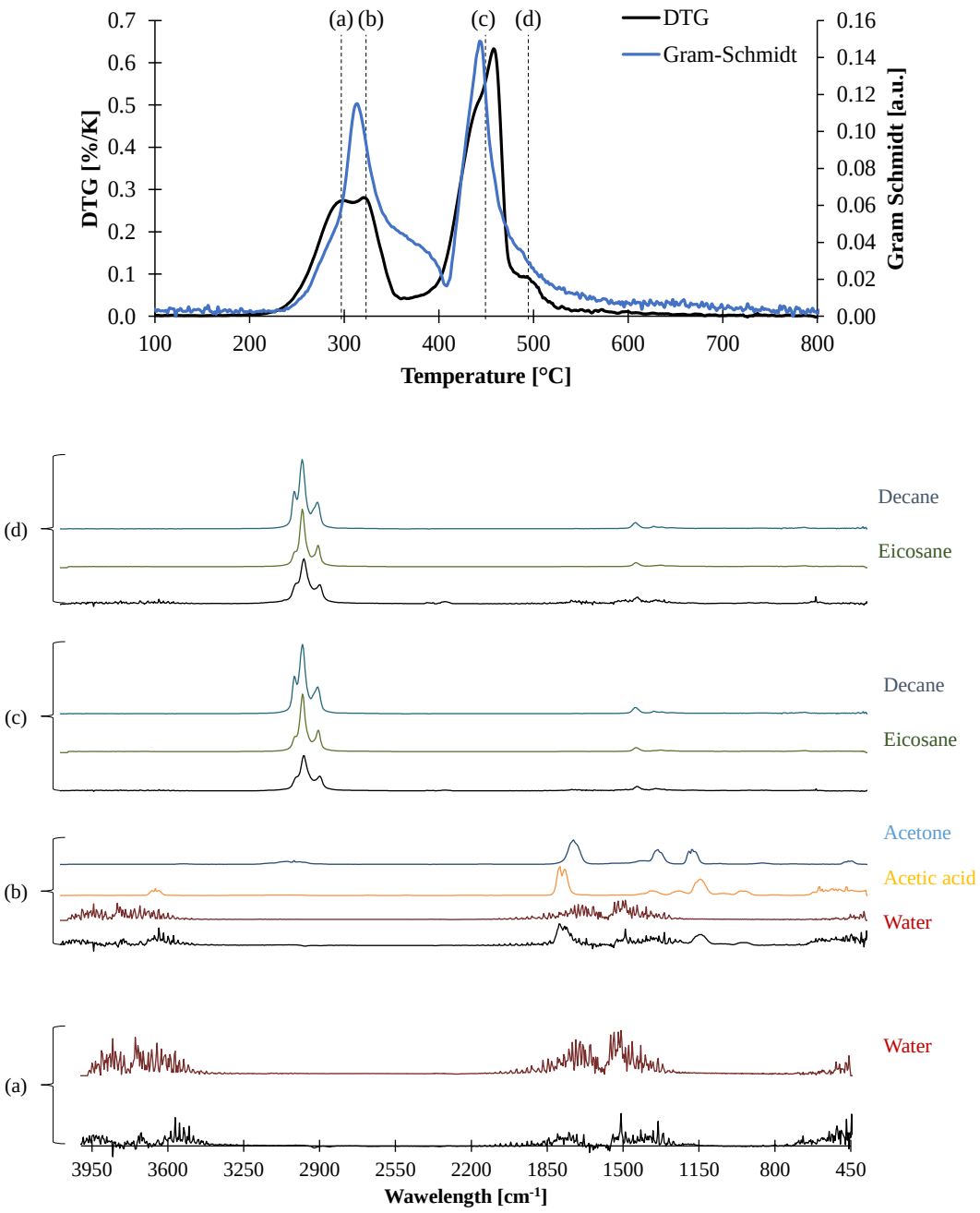

Figure 44: DTG curve and Gram-Schmidt obtained under pyrolytic conditions at 10 K/min and associated FTIR spectra for EVA/ATH/NC

More information can be obtained about the nature of the gases using py-GC/MS experiments. The chromatogram obtained from py-GC/MS experiments on EVA/ATH is presented in **Figure 45**. Note that DTG curve, Gram-Schmidt and py-GC/MS chromatogram are very similar in terms of shape. The only difference lies in the last step of decomposition which is the most intense peak in DTG while it is the

lowest in py-GC/MS. This is attributed to the fact that long-chains hydrocarbons are trapped in the GC column, lowering the intensity of this peak. On the opposite, the first peaks of decomposition are mainly composed of volatile products that are not trapped but eluted in the GC column.

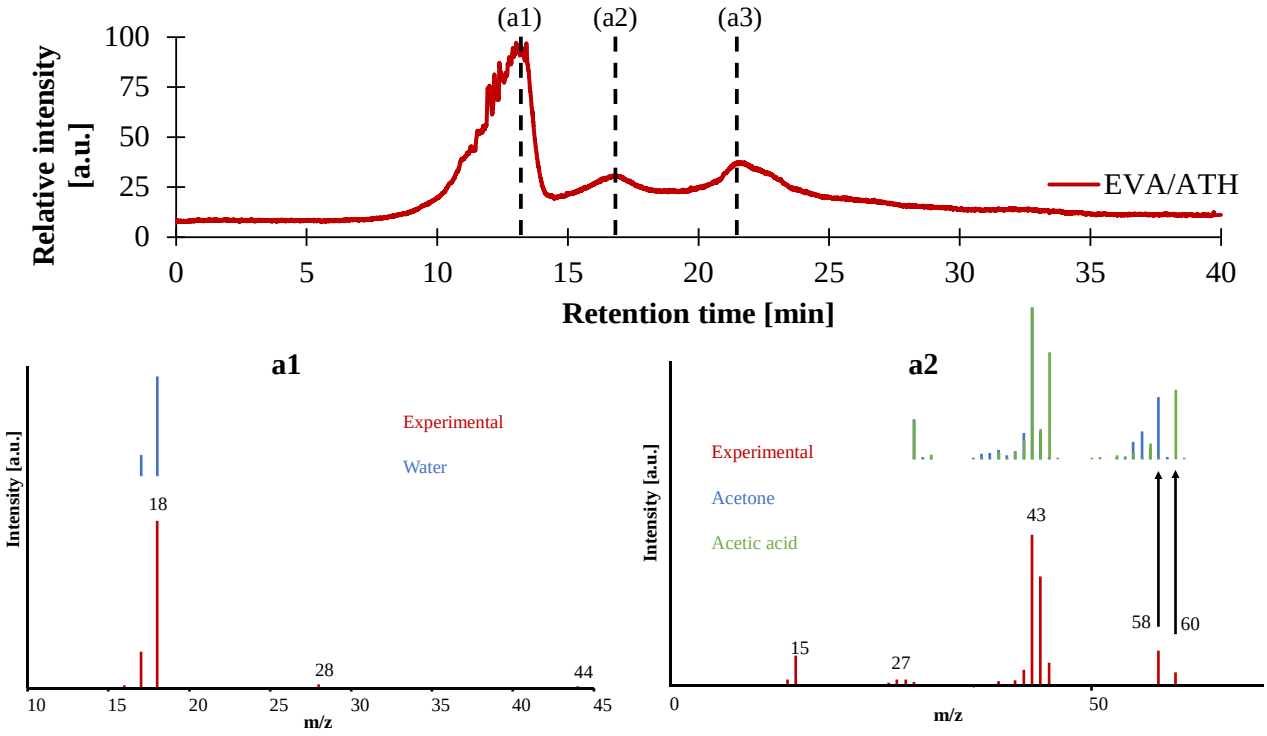

Figure 45: Chromatogram of EVA/ATH obtained by py-GC/MS at 20 K/min and associated mass spectra for (a1) and (a2)

As with TGA-FTIR technique, the first peak (a1) can be attributed to water as the characteristic peak of water at m/z=18 are observed (**Figure 45**). The MS spectrum taken at (a2) in the GC chromatogram showed the typical m/z traces of acetic acid and acetone (m/z of 60 and 58 respectively). Information about the hydrocarbons released in (a3) can be obtained from the py-GC/MS chromatogram (not shown). The gases identified at this peak of the chromatogram are associated to alkanes and/or 1-alkenes with a chain length between C_4 and C_7. Note that the latter describes the most volatiles gases. Hydrocarbons with longer chains can be observed between (a3) and the end of the pyrolysis experiment. In addition to this, hydrocarbons with a carbon chains longer than C_{10} are not observed at that stage as they are trapped in the GC column.

Similarly to EVA/ATH, the GC chromatogram of EVA/ATH/NC (**Figure 46**) is similar to its DTG and Gram-Schmidt curve. A first peak between 10 and 15 min retention time can be observed. The mass spectra associated to the beginning (b1) and end of the peak (b2) are also presented in **Figure 46**.

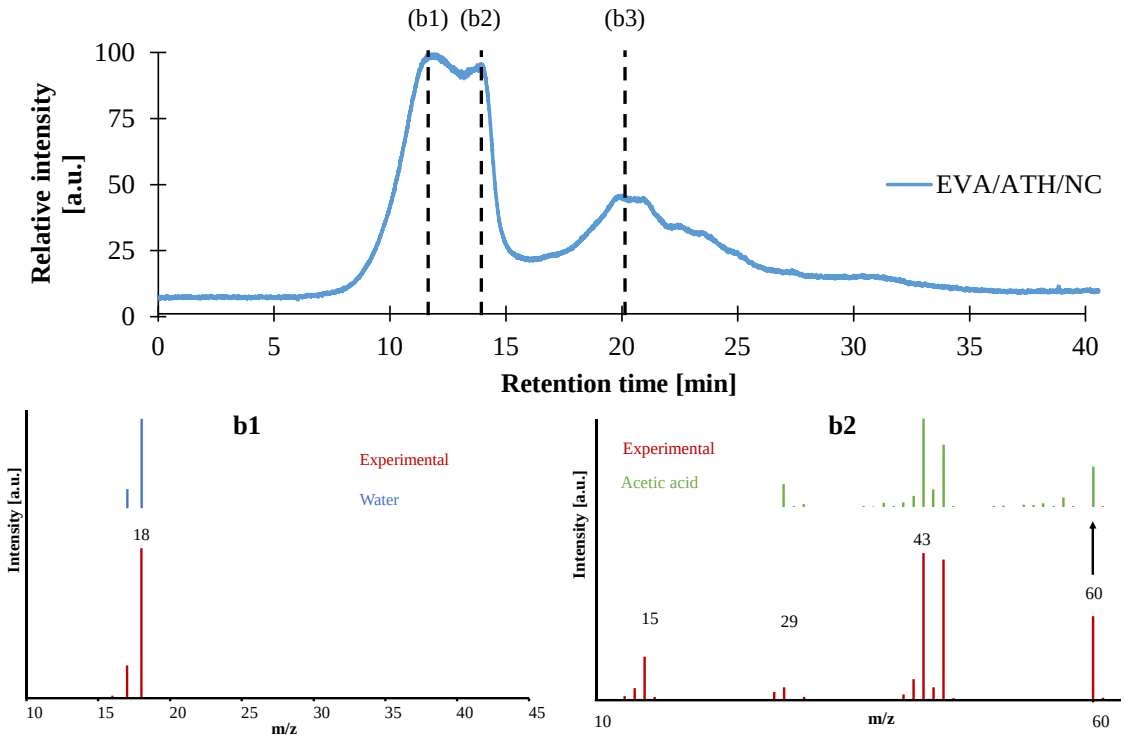

Figure 46: Chromatograms of EVA/ATH/NC obtained by py-GC/MS at 20 K/min and associated mass spectra for (b1) and (b2)

As for EVA/ATH, the first peak of the chromatogram (b1) can be attributed to the release of water as the characteristic peak at m/z of 18 is observed. At the end of the first peak of decomposition, only acetic acid is detected by FTIR (**Figure 46.b2)**. Indeed, the characteristic peaks of acetic acid (such as m/z of 60) are detected. More information can be found about the nature of the hydrocarbons in the py-GC/MS spectrum in (b3) (not shown). Similarly to the results obtained for EVA/ATH, alkanes or 1-alkenes with a chain length comprising between C_4 and C_7 are detected. Even if the released gases are similar, the relative intensity of the peak (b3) compared to the first peak in **Figure 41** indicates that hydrocarbons compounds with small chains are released in higher quantities than in the case of EVA/ATH. NC seems thus to promote the formation of smaller chains hydrocarbons.

At this stage of the study, it was shown that the gases released when EVA/ATH decomposes are different in presence of NC. The effect of NC in the release of acetone and long-chain hydrocarbons will then be further investigated

III.1.1.c. Impact of NC on the release of acetone

The averaged intensities of the characteristic peaks of acetic acid and acetone (as presented in **Table 12**) are plotted in **Figure 47**. It can be seen that the release of acetic acid for EVA/ATH/NC starts around 300 °C against 350°C for EVA/ATH. It was already reported that the early release of acetic acid is due to the catalytic effect of the acidic sites of the NC [98] that corresponds to the pending –OH groups at the edge of the clays. It can be noted that as soon as the deacetylation occurs, acetone is formed. Nonetheless, the concentration of acetone released by EVA/ATH/NC is lower than this of EVA/ATH validating the fact that it was not observed (or in fact hindered) in the previous section.

The signals presented in **Figure 47** were integrated and plotted as a function of temperature. The ratio between acetone and acetic acid were calculated for EVA/ATH and EVA/AT/NC. It was found that EVA/ATH exhibits a ratio acetone:acetic acid of 1.07 while it was only of 0.63 for EVA/ATH/NC. This further validates the fact that more acetic acid is released in the presence of NC and thus the transformation of acetic acid into acetone is hindered in presence of NC.

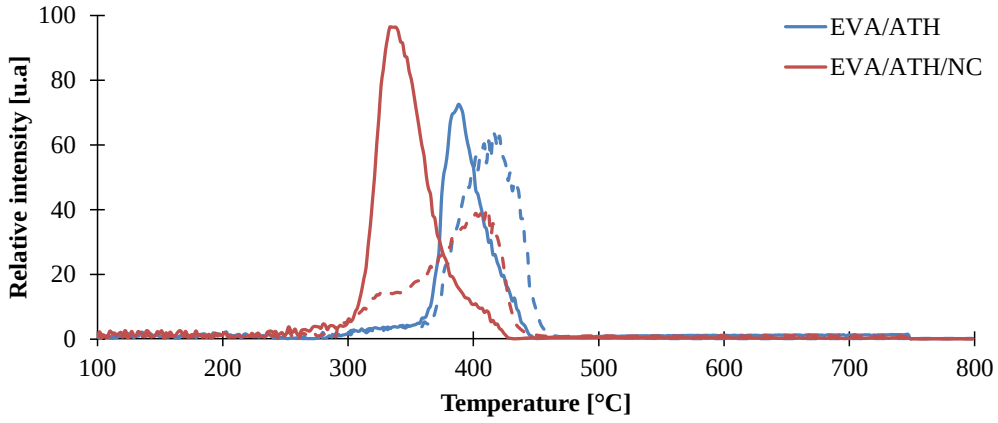

Figure 47: Acetone (dotted lines) and acetic acid (straight lines) release profiles for EVA/ATH materials

III.1.1.d. Impact of ATH and NC on the release of hydrocarbons

As stated in the previous sections, it is difficult to have information about the structure of the hydrocarbons released with FTIR technique. Similarly, py-GC/MS cannot be used for characterizing the structure of the most volatiles hydrocarbons, as they will be analyzed at similar retention times, an overlapping of the gases will thus occurs. It is nonetheless possible to analyze the long-chain hydrocarbons as they condense in the GC column. By heating the column to 300 °C at a constant heating rate, it is possible to desorb the compounds and to analyze them.

The chromatograms obtained during the desorption of the gases trapped in the GC column are presented in **Figure 48**. The chromatogram obtained for EVA/ATH exhibits the typical profile of a polyolefin. By looking at the MS spectra and the maximum mass obtained at a retention time of 15.5 and 15.9 min (m/z of 154 and 156 respectively), it is possible to attribute these peaks to 1-undecene and undecane (linear alkane of formula $C_{11}H_{24}$) respectively. Similar results can be obtained on the following peaks detected on the chromatogram with an increasing number of carbons in the aliphatic chain. Note that the mass spectra for EVA, EVA/ATH and EVA/ATH/NC are similar at each peaks on their chromatograms. Between 15 and 60 min of retention, 1-alkenes and *n*-alkanes ranging between C_{11} to C_{24} are thus analyzed.

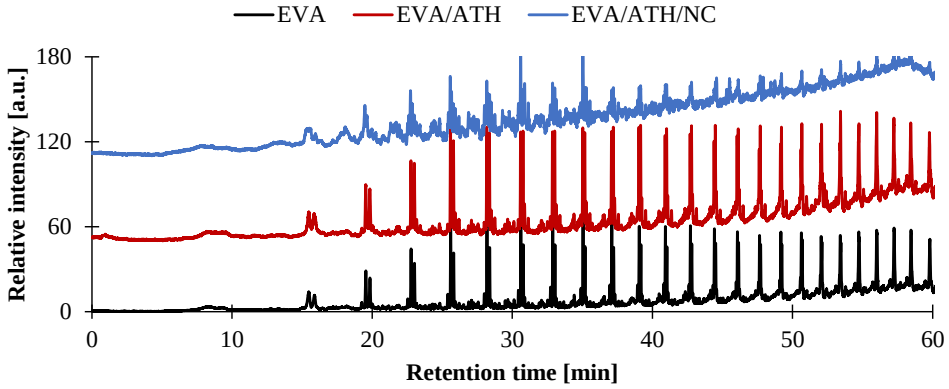

Figure 48: GC chromatograms of the desorption of the non-volatiles products of the decomposition of EVA and EVA/ATH composites

A close up of the C_{12}-C_{17} region for EVA/ATH materials is presented in **Figure 49**. Mass spectra of *n*-alkane and 1-alkene with a chain length of C_{13} are also presented. The GC chromatogram of EVA is also shown for comparison purpose.

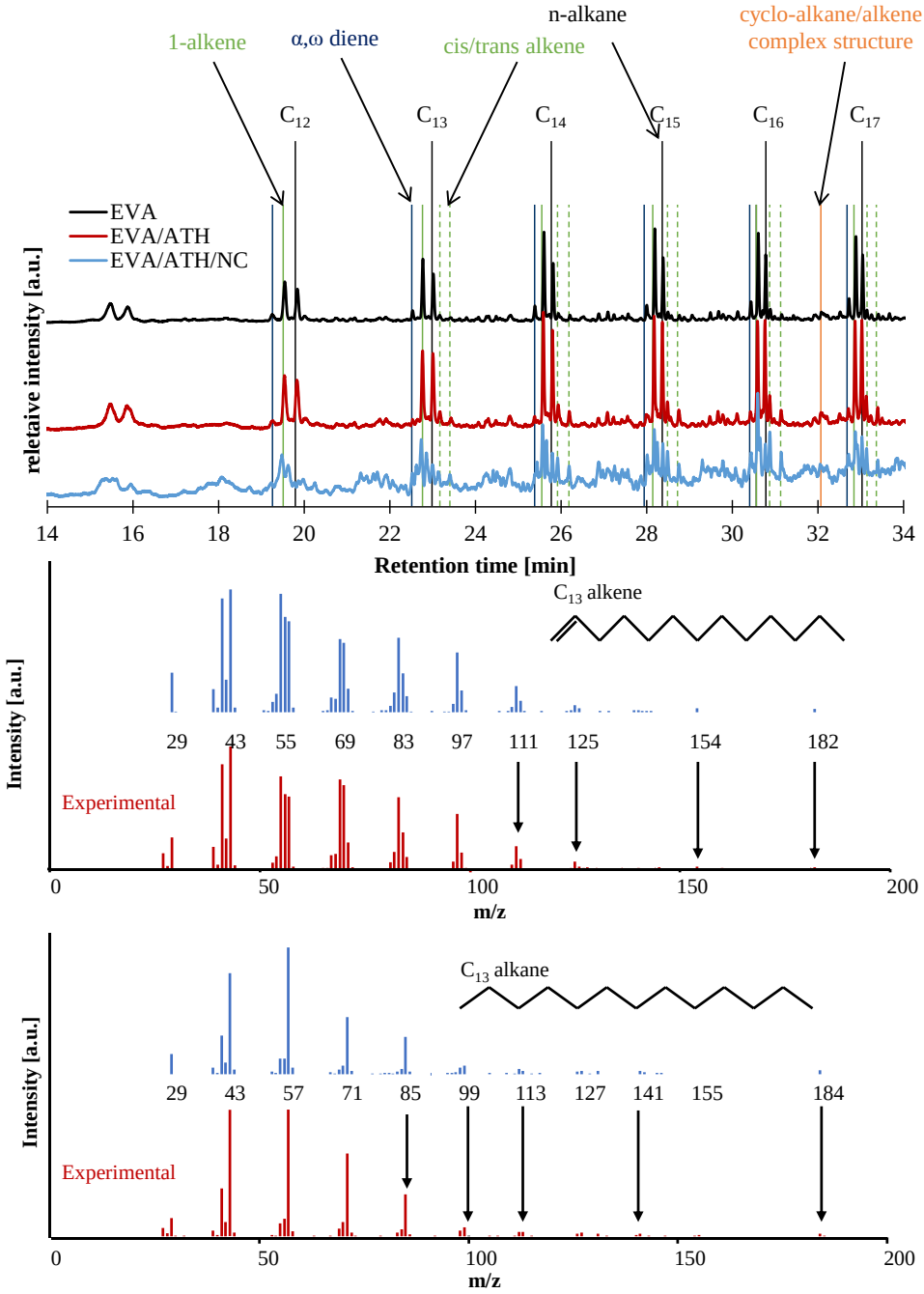

Figure 49: Chromatograms of EVA and EVA/ATH materials in the C_{12} – C_{17} region with their attributions and example of mass spectra for* n-*alkane and 1-alkene

On the chromatograms of EVA and EVA/ATH materials, each group of peaks can be associated to the following species (in the order of their appearance): α,ω-diene; 1-alkene, *n*-alkane, cis and trans alkenes. Note that the cis/trans alkenes are attributed to the formation of a polyene after the deacetylation of the EVA. Note also that EVA/ATH/NC exhibits additional and multiple peaks between the peaks of the

linear alkanes (around 21.5, 24.5, 29 or 32 min for instance in **Figure 49**). These peaks are associated to complex structures such as cyclo-alkane or alkene or cross-linked structure [98]. This effect was already studied by Costache *et al.* [98,99] and Jang *et al.* [130] for EVA/NC materials.

The formation of complex structures can be attributed to the ability of the NC to confine radicals when EVA decomposes and when the decomposition gases are diffusing in the NC network. This promotes the rearrangement of the released hydrocarbons. The effect of NC are even more highlighted for EVA/ATH/NC than for EVA/NC as the ratio between EVA and NC is of 7/1 in our study when it is of 97/3 in Costache's study [98].

Interestingly, it can also be noted that the height or area ratio between the characteristic peaks of the different alkenes and alkanes are similar for EVA and EVA/ATH. Indeed, in the C_{12}-C_{17} region, virgin EVA exhibits a ratio saturated:unsaturated compounds of 33:67 and 35:65 for EVA/ATH. This suggests that there would be no interactions of ATH with the hydrocarbons released as EVA decomposes. The ratio was not calculated for EVA/ATH/NC as the elucidation of structures and even their chemical nature (alkane or alkenes; linear, cyclic, cross-linked or aromatic structures) is too difficult to investigate. The integration and attribution of the peaks corresponding to linear compounds is thus not possible. However, the peaks associated to long chains hydrocarbons are of lower intensity in the presence of NC. Indeed, the peaks at retention times higher than 40 min are much lower than in the case of EVA/ATH. This further validates the observation made with the volatiles gases: hydrocarbons with lower carbon chains are formed in presence of NC.

As a conclusion, the differences in the chromatograms are a proof that NC reacts with the decomposition gases in the case of EVA/ATH/NC leading to different hydrocarbons.

III.1.1.e. Conclusion on thermal decomposition of EVA/ATH materials

We saw in this section that EVA/ATH composites decompose in a similar manner even if some differences were noted. First, ATH decomposes releasing water. Concurrently, the vinyl acetate part of EVA decomposes releasing acetic acid. A polyene network is assumed to remain in the condensed phase. Finally, this polyene decomposes at higher temperature. It was shown that the presence of ATH and NC slightly change the temperature at which these decomposition takes place. Moreover, as alumina is formed as ATH decomposes, a catalytic transformation of acetic acid into acetone occurs when EVA/ATH formulations decompose. Similarly, the presence of NC catalyzes the deacetylation step as well as the decomposition of the polyene network but limits the transformation of acetic acid into acetone.

The purpose of this work is to investigate and to develop several methods to evaluate the thermo-physical properties of EVA/ATH composites as a function of temperature. These parameters would then be used in a pyrolysis model in order to predict the fire performances of EVA/ATH materials. According to the results of this section, the decomposition of the materials can then be fully described as presented in **Figure 50** and explained as follows:

- "Formulation" refers to the initial and pristine EVA/ATH materials.
- "Intermediate" corresponds to the intermediate specie and refers to alumina, to the remaining part of the EVA obtained after the deacetylation step and to the remaining NC in the case of EVA/ATH/NC.
- "Gas1" refers to the water released during the decomposition of ATH into alumina and to acetic acid and acetone from the deacetylation of the EVA.
- "Residue" refers to alumina for EVA/ATH or the mixture of alumina with the decomposed NC for EVA/ATH/NC. EVA is assumed to be completely decomposed at high temperature
- "Gas2" is a mixture of hydrocarbons gases evolved during the decomposition of the polyene obtained after deacetylation of EVA.

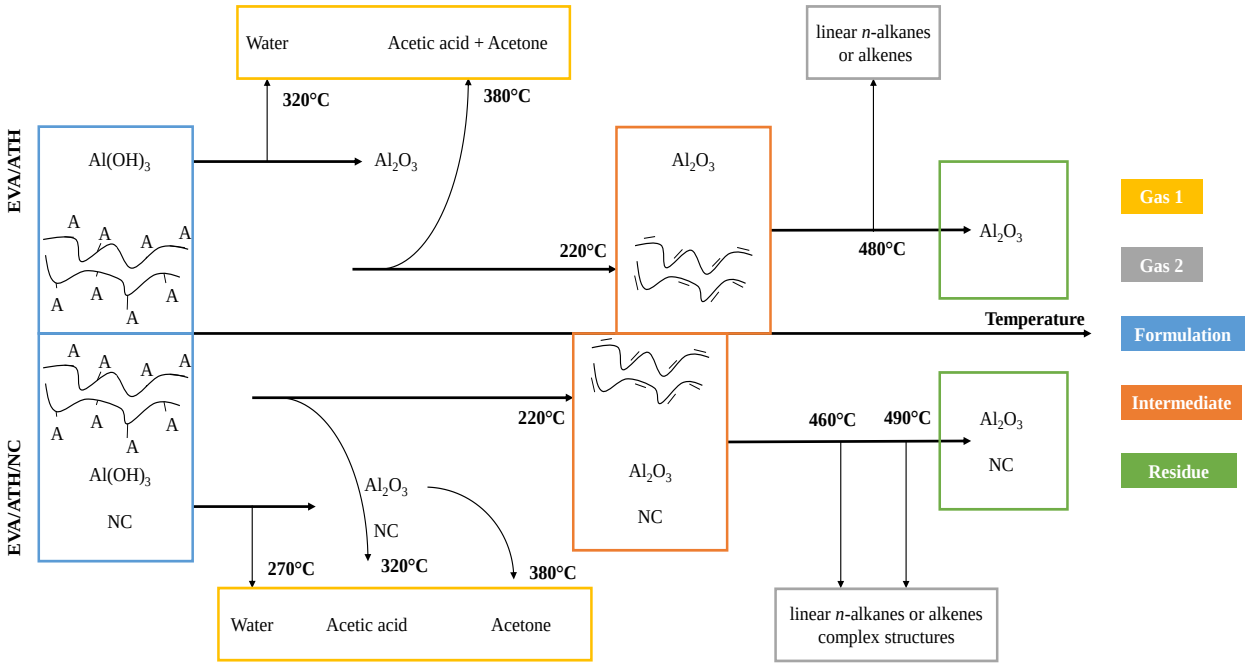

Figure 50: Decomposition pathway of EVA/ATH formulations

It is interesting to highlight that due to the interaction between the polymer and the FR additives as seen in **Figure 42**, it is not possible to evaluate the kinetics of decomposition of each component alone and to model the TG curve of the complete formulation as a linear combination of the individual kinetics. Indeed, such model would not take into account the synergism or antagonism effects between the additives and the polymer. Note also that these interactions are not necessarily modelled in pyrolysis models. As an example, heterogeneous reactions such as gas-solid reactions (the catalytic transformation of acetic acid into acetone over alumina for instance) are not included in the model. Note also that even if these reactions would be considered in pyrolysis models, it would be difficult to access to these kinetics and solve them accurately.

III.1.2. KINETICS OF THERMAL DECOMPOSITION OF EVA/ATH COMPOSITES

The modelling of the fire behavior is based on heat transfer and mass conservation equations. It is thus of high importance to know how EVA/ATH based materials decompose as a function of temperature and under various conditions (heating rates) *i.e.* it is needed to investigate the kinetics of decomposition and to determine heats of reactions occurring when the materials decompose. The following part of this chapter will thus describe how the kinetics of decomposition of EVA/ATH composites were determined. First, a model-free analysis of the TG data will be performed. Then, the TG data will be modelled by defining a reaction scheme but also using a global model.

III.1.2.a. Friedman analysis

The thermal decomposition of the material was studied at different heating rates from 2 K/min to 50 K/min. In these conditions, it is expected to capture the overall decomposition of the material in a wide range of conditions, from slow to high heating rates mimicking different fire scenarios.

Before starting any fitting procedure, it is first necessary to define a reaction model (combination of reactions) and to preset starting values for the kinetic parameters. A model-free analysis was then performed by using Friedman procedure (see **II.2.1.c** p.62) on thermogravimetric data of the EVA/ATH materials. As a result, the plot of the activation energy as a function of the degree of conversion is shown in **Figure 51**. For EVA/ATH, the curve exhibits two consecutive and distinct steps. The first one, at a degree of conversion lower than 0.35, exhibits an activation energy around 160 kJ/mol. At higher degree of conversion, the activation energy reaches a plateau at around 260 kJ/mol. Results for EVA/ATH/NC

are similar to the ones of EVA/ATH. Indeed, the plot of activation energy as a function of degree of conversion exhibits the same shape with two consecutive steps. The activation energies for EVA/ATH/NC are lower than these obtained for EVA/ATH on the whole range of conversion degree. At low degree of conversion (lower than 0.4), the first step shows an activation energy around 120 kJ/mol versus 160 kJ/mol without NC. Similarly, the activation energy determined for the second step at degree of conversion higher than 0.4 ranges between 190 and 230 kJ/mol. These data were then used as initial parameters and nonlinear regressions were carried out in order to find the best fit between experimental and simulated data for all the studied heating rates.

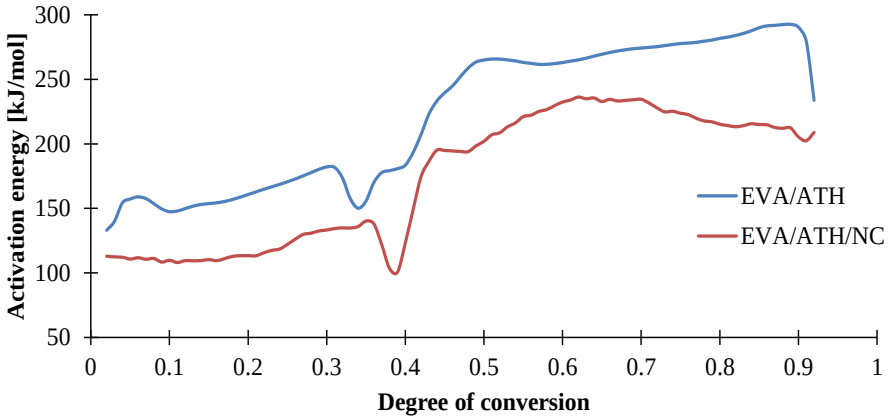

Figure 51: Activation energy as a function of conversion degree according to Friedman analysis for EVAT/ATH composites

III.1.2.b. Two steps kinetic model

According to the previous analysis, the decomposition of EVA/ATH materials was modelled using two successive steps with n^{th} order functions. This reaction model was selected as it represents a large array of chemical reactions easily encountered during the decomposition of polymers. The purpose of this model is not only to define elementary reactions but also to define the general reactions of decomposition of the materials. Even if the real reactions of the system are too complex to be characterized in any fundamental way, the reactions are described as pseudo (or lumped) species which are themselves complex materials or mixtures. N^{th} order reactions were used in these analyses as they are the easiest way to implement the kinetics of decomposition in the pyrolysis and because a good fit between simulated and experimental data was obtained

Considering this reaction model, optimum parameters were obtained and are shown in **Table 13**. The first reaction which can is related to the dehydration of the ATH but also to the deacetylation of the EVA is a third order reaction for EVA/ATH with an activation energy of 162 kJ/mol and a $\log A_r$ of 12.94. For EVA/ATH/NC, the same reaction is attributed to a second order reaction with a lower activation energy (115 kJ/mol) and a lower $\log A_r$ (8.32).

Table 13: Kinetics of decomposition assuming two consecutive steps mechanism

Formulation	Reaction	$\log A_r$	E_r [kJ/mol]	Reaction order	Stoichiometry
EVA/ATH	1	12.94	162	3	0.794
	2	17.09	268	1	0.547
EVA/ATH/NC	1	8.32	115	2	0.761
	2	12.72	207	1	0.578

The second reaction, which corresponds to the decomposition of the remaining organic part of the formulations, is modelled using a first order reaction for both EVA/ATH composites. It exhibits an activation energy of 268 kJ/mol and $\log A_r$ of 17.09 for EVA/ATH and of 207 kJ/mol and of 12.72 for EVA/ATH/NC. The comparison between the simulated and experimental data is shown in **Figure 52**. This kinetic model allows a good description of the decomposition of the materials and provides the best quality of fit between the computed and the experimental TG curves.

It is noteworthy that the values found for the activation energies are consistent with these already reported for EVA [35,100]. Indeed, for the first step of decomposition of EVA/ATH formulation corresponding to the deacetylation of the EVA, Rimez *et al.* [100] found a pre-exponential factor $\log A_r$ of 12.7 against 12.9 in this study and an activation energy of 164 kJ/mol for EVA (with a vinyl acetate contents lying between 9 and 33 wt %) against 162 kJ/mol in this study. On the other hand, Cérin *et al.* [35] found a value of 114 kJ/mol and a $\log A_r$ of 8.73 but a first order Avrami Erofeev reaction was used to model the decomposition of the ATH in an EVA/ATH formulation containing 60 wt% of vinyl acetate. As a consequence, the values obtained in this study are higher than those associated with ATH dehydration but similar to the ones reported for the deacetylation of EVA. Note that the kinetic parameters used for EVA/ATH composites are not associated with ATH dehydration or EVA deacetylation but more

generally describe the decomposition step from the pristine material to the alumina/polyene system as defined in **Figure 50**.

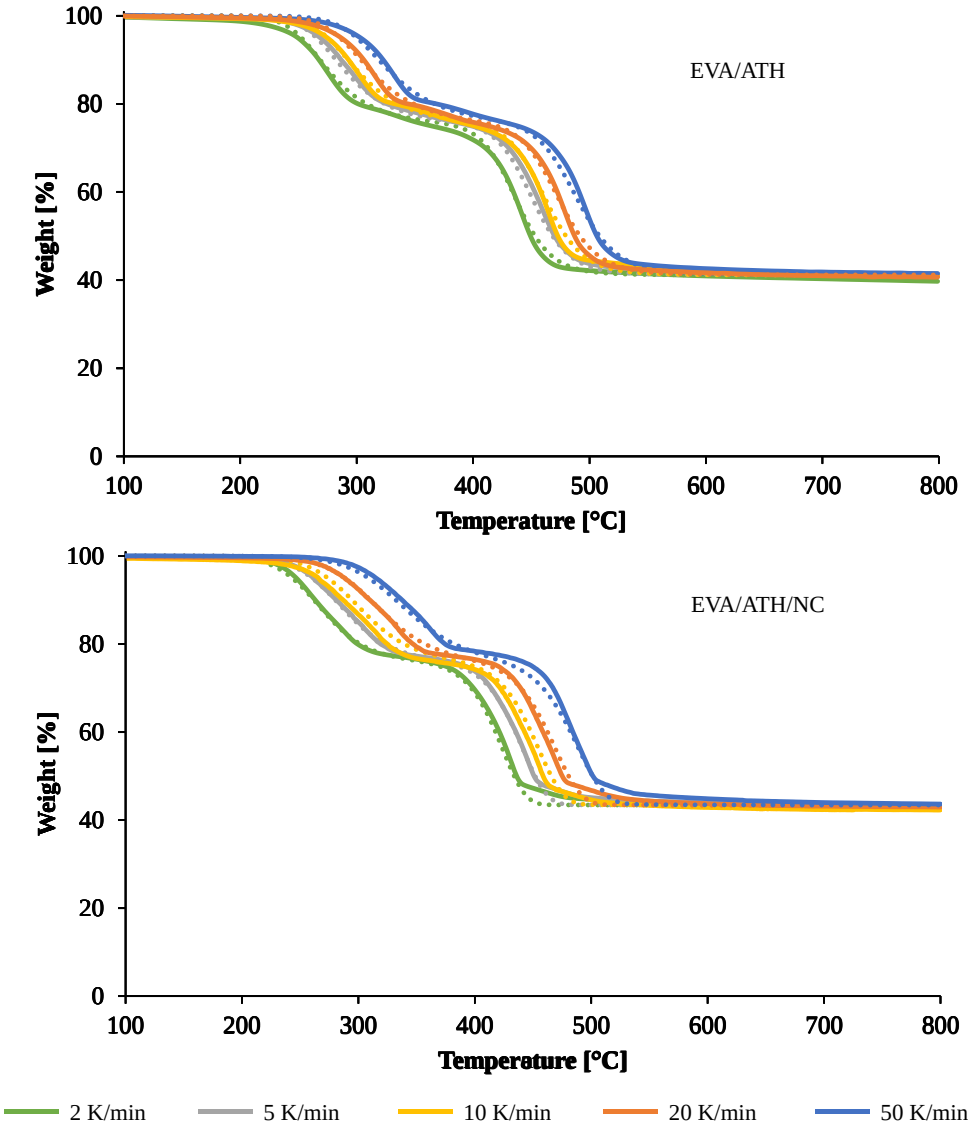

Figure 52: Simulated (dotted lines) and experimental (straight lines) weight loss curves under nitrogen at heating rates of 2, 5, 10, 20 and 50 K/min for EVA/ATH composites

Considering the second step of decomposition (reaction 2 in **Table 13**), Rimez *et al.* [100] studied the decomposition of the remaining polyene resulting from the deacetylation of the EVA. A pre-exponential factor $\log A_r$ of 16.3 and an activation energy of 261 kJ/mol in the case of the formation of aliphatic volatiles were found. These values are similar to the results obtained in this study since 17.1 was obtained for $\log A_r$ and 268 kJ/mol for the activation energy.

Interestingly, the kinetic parameters associated to the decomposition of EVA/ATH/NC are lower than the ones obtained for EVA/ATH without NC. The effect of the NC was expected according to the Friedman analysis reported in **Figure 51**. Several kinetic models were applied to EVA/ATH/NC and the best quality of fit between the computed and experimental data was obtained by using two successive n^{th} order reactions. Sánchez-Jiménez *et al.* [188] investigated the decomposition of EVA/ATH in the presence of nanoclays (organo-modified MMT). They showed that nanoclays promote the decomposition of polymers through nucleation. Indeed, clay-platelets showed to act as nucleation centers while the polymer decomposes, thus decreasing the activation energy required of the reactions. As most of the components of our EVA/ATH decompose through nucleation, it is expected that the kinetics parameters associated to EVA/ATH/NC are lower than these of EVA/ATH alone.

III.1.2.c. Global kinetics model

On the other side, the kinetics of decomposition can also be implemented using the results obtained from the Friedman analysis as shown in **Figure 51**. Indeed, the activation energy as well as the pre-exponential factor and the kinetic model can be extracted without specifying the reaction scheme (number of reactions, successive/competitive steps) and a reaction model (n^{th} order, Avrami-Erofeev, *etc.*). A comparison of such kinetic model with the experimental data and the two consecutive steps model is shown in **Figure 53**.

It can be seen that the prediction of the experimental data exhibits a better fit using the global kinetic model. Indeed, an averaged correlation coefficient (R^2) of 0.994 is obtained with EVA/ATH formulations with this model when it is only of 0.949 with the two-steps model previously described. It can be seen that EVA/ATH exhibit three peaks of DTG: around 270 °C, around 350 °C and the final one around 450 °C. The two steps-model does not allow to model the second peak, which is less intense. On the opposite, the three peaks are perfectly fitted using the global reaction model. Moreover, the first reaction was not perfectly predicted using the two steps-model since the predicted temperature of this peak is lower than the experimental one. The intensities of the peaks were not well predicted with the two-steps model whereas it is perfectly with the global approach.

Experimental TG curves of EVA/ATH/NC exhibits a two apparent decomposition steps with the last step showing a shoulder. The two steps model is able to simulate these two steps at the exception of the shoulder. At the opposite, the global model allows to describe it. The agreement between either the two steps model or the global model with the experimental data is excellent in the case of EVA/ATH/NC.

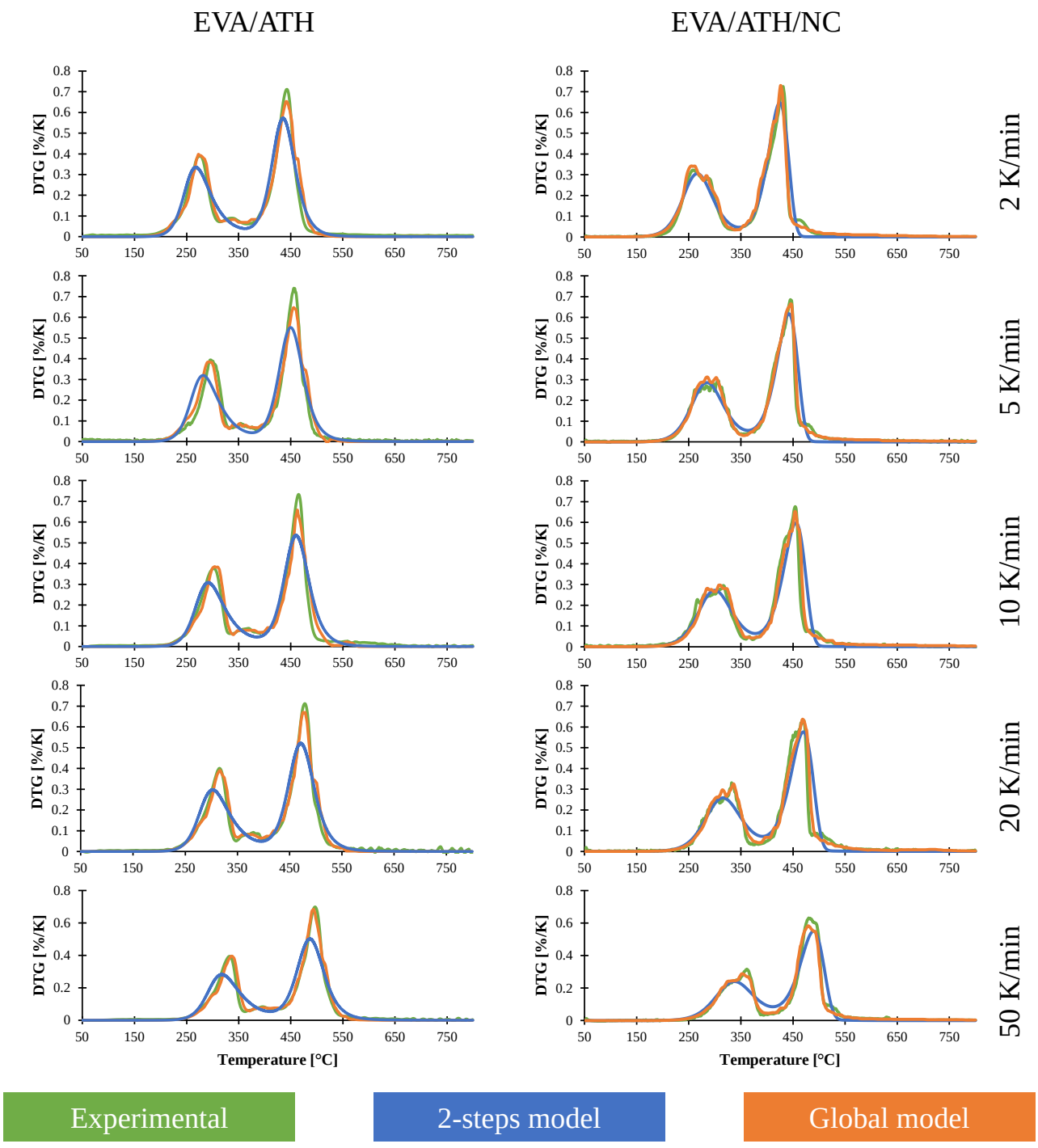

Figure 53: Comparison of experimental and predicted DTG curves under nitrogen at heating rates of 2, 5, 10, 20 and 50 K/min with a two consecutive steps model or a global kinetic model

We may thus conclude that the fit between the computed and the experimental TG curves are excellent for all the heating rates using the global kinetic model for both EVA/ATH materials, while for the two consecutive steps model, the higher the heating rates, the poorer the fit for EVA/ATH/NC.

It was shown in this section that it is possible to describe the decomposition of EVA/ATH materials using two consecutive n^{th} order reactions. Even if this kinetic model can be easily implemented in the pyrolysis model, its predictive capabilities are limited to the modelling of two peaks of decomposition. On the opposite, the global kinetic model was able to fit the multiple peaks processes of the decomposition of the EVA/ATH composites. However, in both case, the fit of the computed data with the experimental data is acceptable. The two-steps kinetic will be used in **CHAPTER IV** and compared to the global kinetic model in the case of gasification experiments. Another important parameter when studying the decomposition is the enthalpies of decomposition of the materials. This will be investigated in the following part.

III.1.3. ENTHALPIES OF REACTION

The enthalpies of decomposition were measured with a simultaneous thermal analyzer (STA) under nitrogen. They were obtained by integrating the area under the heat flow curve as a function of temperature. An example of such analysis for EVA/ATH/NC is shown in **Figure 54**. Baselines are taken as straight lines between the onset and endset on DSC and TG curves of each apparent step of decomposition.

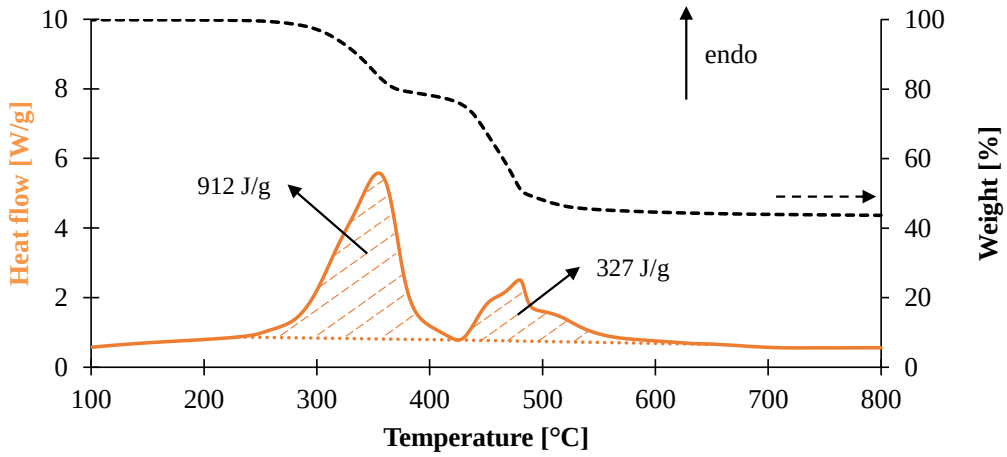

Figure 54: DSC (straight lines) and TG (dotted lines) signals of the decomposition of EVA/ATH/NC

The heat of reactions of each steps and for both EVA/ATH composites are presented in **Table 14**. ATH is known to undergo an endothermic reaction (dehydration) with an endothermic heat of reaction between

1190 [108] and 1300 J/g [31,109]. Indeed, $Al(OH)_3$ releases water, forming a ceramic residue made of alumina (Al_2O_3). It was found experimentally that the first step of decomposition exhibits an endothermic decomposition step with an enthalpy H_{r1} of 883 J/g for EVA/ATH and 912 J/g for EVA/ATH/NC. The second reaction of EVA/ATH materials associated with the pyrolytic decomposition of the polymer is still endothermic but the heats of reaction H_{r2} are only 236 J/g for EVA/ATH and 327 J/g in the presence of NC.

Considering the composition of the EVA/ATH composites, around 774-845 J/g can be attributed to ATH dehydration for EVA/ATH. The deacetylation shows an enthalpy of around 38-109 J/g in EVA/ATH whereas it would be of around 198-132 J/g in case of EVA/ATH/NC. The difference in the enthalpy of deacetylation could be explained either: (1) by the fact that the heat of reaction of montmorillonite is not considered; (2) by the exothermic heterogeneous reaction between acetic acid and alumina [189,190]. As it was shown in the previous section that more acetone is formed in the case of EVA/ATH than EVA/ATH/NC, more heat is thus evolved from this reaction, leading to lower the apparent heat of reaction of the first step of decomposition.

Table 14: Heats of reaction assuming a two-step decomposition mechanism

Formulation	**H_{r1}**	**H_{r2}**
EVA/ATH	883 J/g	236 J/g
EVA/ATH/NC	912 J/g	327 J/g

The heat flow signal corresponding to the heat of reactions presented in **Figure 54** can also be plotted as a function of the decomposition degree (**Figure 55**). Indeed, while the material is not decomposing, the heat flow corresponds to a change in heat capacity and not to chemical reactions. It can be seen, that the energies absorbed by the materials when they decompose are similar for both EVA/ATH composites. Before 40 % of conversion, around 73 % of the heat which is necessary for the materials to completely decompose is absorbed. This is attributed to the “heat sink” behavior of the ATH.

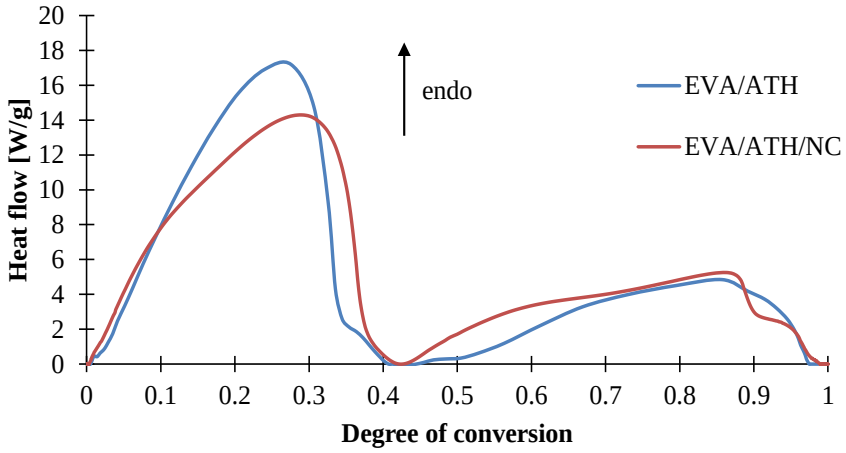

Figure 55: Heat flow signal associated to the decomposition of EVA/ATH materials as a function of degree of conversion

III.1.4. CONCLUSION ABOUT THE DECOMPOSITION OF EVA/ATH COMPOSITES

The investigation of the thermal decomposition of EVA/ATH composites showed that the deacetylation of EVA was promoted in presence of NC. Similarly, the decomposition of the remaining part of the EVA was catalyzed by NC. The release of hydrocarbons occurs at lower temperature. It was also shown that while alkanes and alkenes are released from the polyene formed for the deacetylation of EVA/ATH, more complex structures were evolved in the presence of NC. Moreover, the hydrocarbons released with the presence of NC showed shorter chains.

The decomposition of EVA/ATH materials was modelled by two consecutive n^{th} reactions and also using a global kinetic model. In all cases, a good fit between the computed and experimental data was obtained. The global model proved to have a better fit for multiple peaks data. However, the n^{th} order model will be used in priority, as it is the most common one in numerical studies. The impact of using a global or a two-steps model in the case of the gasification of EVA/ATH composites will be investigated in **CHAPTER IV**. On the other hand, it was also found that the kinetic parameters are lower in presence of NC but the enthalpies of reaction are higher for EVA/ATH/NC.

Among the important properties for pyrolysis modelling, the thermal properties such as thermal conductivity and heat capacity are also of particular interest. These properties affect the heat transfer in the solid that leads to the decomposition through the kinetics determined in this section. The next part of this chapter will thus be dedicated to the investigation of those thermal properties.

III.2. EVALUATION OF THE THERMAL PROPERTIES

This section of the chapter will detail the characterization of the thermal conductivity (the amount of heat that flows between two point distant of one unity of length and whose temperature differ of one degree) and heat capacity (the heat required to heat up one unity of mass by one degree). These properties will be measured as a function of temperature.

III.2.1. THERMAL CONDUCTIVITY OF EVA/ATH MATERIALS

For modelling purposes, it is necessary to determine the thermal conductivity of EVA/ATH materials. As these materials decompose in several steps, it can also be needed to characterize the thermal conductivities of each species formed during the decomposition of the EVA/ATH composites. In a first part, the thermal conductivity of the materials will be determined without considering the different decomposition state of the EVA/ATH. Then the procedures will be adapted so the thermal conductivities of the intermediate and of the final residue are obtained as a function of temperature.

III.2.1.a. Direct measurement of thermal conductivities of EVA/ATH formulations

The thermal conductivity of the material was first investigated using a Transient Plane Source method from ambient temperature up to 700 °C as shown in **Figure 56**. The thermal conductivity of EVA is also presented before it decomposes (T < 250 °C). Its thermal conductivity decreases as a function of the temperature. Indeed, it exhibits a thermal conductivity of 0.39 W/m/K at 50 °C but decreases to 0.33 W/m/K at 200 °C. This is in the range of the values found for polyolefins or EVA in the literature [103,104,106,107]. The addition of a high amount ATH leads to an increase in the thermal conductivity of the EVA/ATH composites to around 1.08 W/m/K at 50 °C for both EVA/ATH composites. Their thermal conductivities steadily decrease from ambient temperature to 250 °C for EVA/ATH and to 350 °C for EVA/ATH/NC.

Between 250 and 350 °C, the thermal conductivity of EVA/ATH exhibits an intermediate value around 0.28 W/m/K. This phenomenon can also be observed for EVA/ATH/NC between 350 and 400 °C presenting a thermal conductivity of 0.32 W/m/K. This decrease of thermal conductivity can be attributed to the complete decomposition of the remaining organic part of the formulations and thus to the modification of the insulative properties of the ceramic residue. At high temperature (T > 450 °C), the thermal conductivity of the EVA/ATH materials remains constant, equaling to 0.18 W/m/K for

EVA/ATH and to 0.24 W/m/K for EVA/ATH/NC. At high temperature, both materials mainly contain alumina (Al_2O_3) which can act as a thermal barrier.

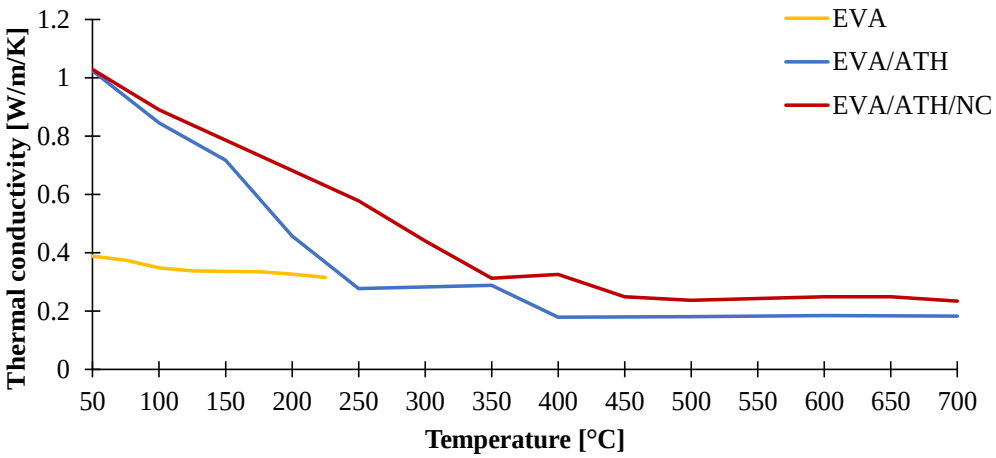

Figure 56: Comparison of thermal conductivities of EVA and EVA/ATH composites as a function of temperature

As far as we know, there are few indications in the literature about the expected range of thermal conductivity of flame-retardant materials at high temperatures especially for ATH-based formulations. Nonetheless, Hoffendahl *et al.* [38] studied the thermal conductivity of a 60 wt% vinyl acetate EVA material flame retarded with 65 wt% of ATH in combination with melamine derivatives. They found that the ambient thermal conductivity was in the range of 0.8–0.9 W/m/K and steadily decreased to around 0.3 W/m/K in the range 350–400 °C. At temperatures higher than 400 °C, the thermal conductivity of the residue formed by the decomposition of the EVA/ATH system with or without melamine, melamine borate, or melamine phosphate was in the range 0.2–0.3 W/m/K. These values are in agreement with those found in this study for EVA/ATH and EVA/ATH/NC.

III.2.1.b. Measurement of the thermal conductivities of decomposition species

As shown previously, EVA/ATH materials decompose with at least two apparent decomposition steps. For modelling purposes, it is important to evaluate the thermal properties of each species formed during the decomposition of EVA/ATH composites. In order to further investigate the thermal conductivity of the material, a second approach was followed. Indeed, even if we are able to describe the thermal conductivity of EVA/ATH material as a function of temperature, the parameters used in the

pyrolysis models are generally described both as a function of temperature and composition. Indeed, as previously explained, EVA/ATH formulations can be described using three independent species: the virgin material, an intermediate residue formed of alumina and polyene (defined as “Intermediate” in **Figure 50** p.101), and the final residue (defined as “Residue” in **Figure 50** p.101) consisting exclusively of alumina (and NC for EVA/ATH/NC).

The domain of stability and the presence of these three species depends on the heating conditions. Indeed, it is obvious that if the onset temperature of decomposition of EVA/ATH formulations at 2 and 50 K/min moves from 200 to 240 °C, it is not possible to define a temperature corresponding to the transition from one product to another. As thermal conductivity measurements were carried out using isothermal stepped experiments and because a steady state is required for the measurement and not dynamic heating ramps as in classical TGA experiments, we have no indications about the presence of the species at each step.

In order to obtain more information, in particular about the weight loss, the decomposition of materials was studied using specific stepped TGA experiments mimicking temperature stepping in thermal conductivity measurements as shown in **Figure 57**. The materials were exposed to isothermal steps of 150 min every 50 °C from 50 to 700 °C. The duration of the steps was chosen with respect to the measurement time required when evaluating thermal conductivity. The domains of stability can be expressed as follows (**Figure 57**):

- Between 20 and 200 °C, the EVA/ATH composites are not decomposing and the thermal conductivity determined in this range could thus be attributed to the virgin formulations.
- Between 300 and 350 °C, the intermediate species corresponding to a residual weight lying between 70 and 80 wt% is present
- At temperature higher than 450 °C for EVA/ATH and 500 °C for EVA/ATH/NC, the thermal conductivities are attributed to the final residues. They are defined when the organic materials are completely decomposed, corresponding to a residual weight of 40–45 wt %.

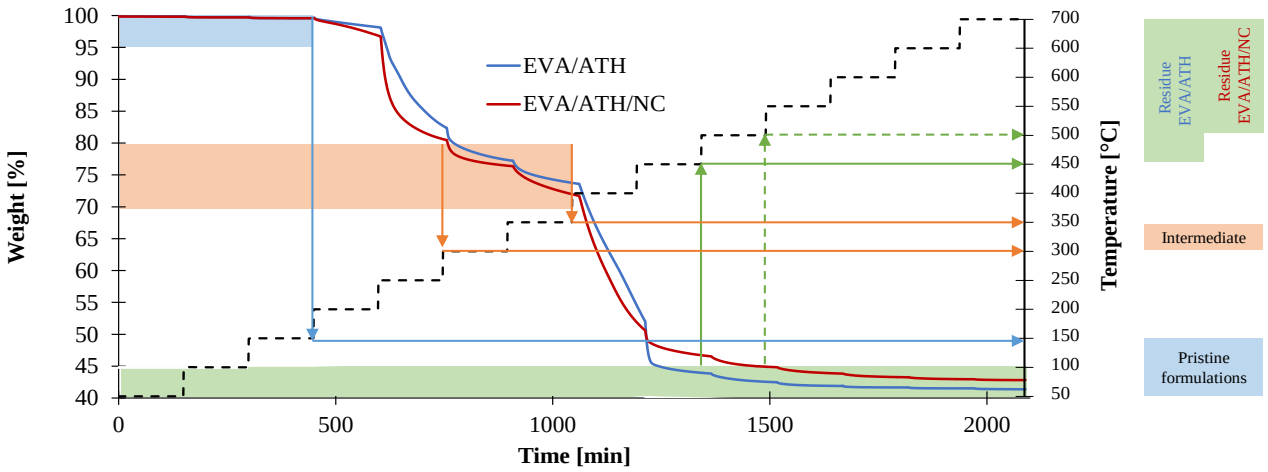

Figure 57: Isothermal TG experiments (straight lines) and temperature curve (dotted line) and associated domain of stability/presence of each decomposition specie

Based on these results, additional thermal conductivity experiments were performed in order to determine the thermal conductivity as a function of both temperature and composition. For the determination of the thermal conductivity of the pristine EVA/ATH, temperatures higher than 200 °C were not considered. For the determination of the thermal conductivity of the intermediate specie as a function of the temperature, the material was first exposed to an isothermal step of 150 min at 350 °C without carrying out any measurements. The objective was to form the intermediate specie. Then, the system was cooled down to 50 °C and the measurements were done from 100 to 400 °C by steps of 50 °C. Note that the point at 400 °C was not attributed to the intermediate specie as the materials start to decompose at this temperature. For the assessment of the thermal conductivity of the final residue as a function of temperature, a similar procedure was carried out: the system was exposed to an isothermal step of 150 min at 500 °C so all the polymer was decomposed. The system was then cooled down to 100 °C and the thermal conductivity was measured from 100 to 700 °C by steps of 100 °C.

Using these procedures, it was possible to evaluate the thermal conductivity both as a function of temperature and decomposition states. A comparison between direct measurements and decomposition- and temperature-dependent measurements is presented for EVA/ATH in **Figure 58**. It can also be noted that, in the range 250–350 °C, the direct measurement of the thermal conductivity of EVA/ATH as a function of temperature is consistent with that of the intermediate specie. Similar results are obtained at temperatures higher than 400 °C with the thermal conductivity of the final residue.

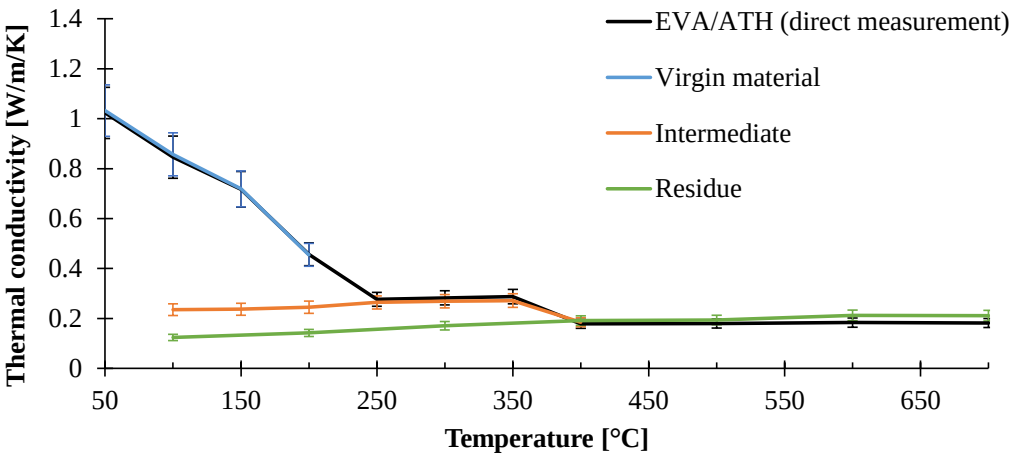

Figure 58: Comparison of the thermal conductivities of EVA/ATH and its decomposition species as a function of temperature

It was also possible to evaluate the thermal conductivity of EVA/ATH/NC both as a function of temperature and composition using the previously developed procedure. A comparison between direct measurement and composition and temperature-dependent measurements is presented in **Figure 59** for EVA/ATH/NC.

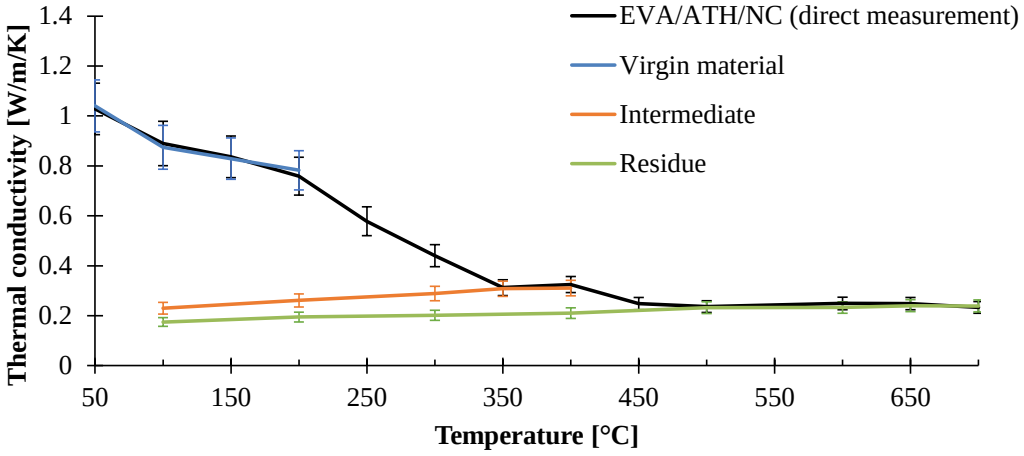

Figure 59: Comparison of thermal conductivities of EVA/ATH/NC and its decomposition species as a function of temperature

It is observed that both methods lead to similar values before 200 °C. At temperatures higher than 500 °C, similar results are also obtained for the thermal conductivity of the final residue. Note that between 200 and 350 °C, the thermal conductivity of EVA/ATH/NC measured using the temperature-dependent method is decreasing linearly as the material decomposes. This thermal conductivity then stabilizes around 0.32 W/m/K when the second decomposition step is finished. Even if the intermediate specie is obtained as early as 300 °C, its thermal conductivity still decreases until 350 °C and stabilizes only at 350 °C. On the opposite of EVA/ATH, the thermal conductivity of EVA/ATH/NC remains stable up to 400 °C even if the last step of decomposition had begun. This can be explained by the fact that the last step of decomposition of EVA/ATH/NC is split in two steps as observed in TGA. Some polymer is thus still present at the isothermal step at 400 °C.

Based on those results, the thermal conductivity can be implemented in two different ways in the pyrolysis model: either using the direct measurements, or as a linear combination of the thermal conductivities of the virgin material, of the intermediate specie and of the final residue. Indeed, the thermal conductivity of the whole material can be expressed numerically as a function of the thermal conductivities of the different species and of the kinetics of decomposition. The last approach is thus assumed to be more precise and more realistic, and is generally used in pyrolysis modelling studies. It can however lead to additional errors if the kinetics of decomposition cannot capture the entire heating ramp at which the material is exposed. On the contrary, using the direct measurement on the EVA/ATH materials cannot dynamically capture the process of decomposition. However, its characterization is easier (both in time and in procedure) than the approach consisting in the measurement of the thermal conductivities of each species, in particular if more than two species are observed (generally the initial polymer and the residue left by the decomposition).

III.2.2. MEASUREMENT OF THE HEAT CAPACITY OF EVA/ATH COMPOSITES

III.2.2.a. Evaluation of the heat capacity of EVA/ATH

The heat capacity of the EVA/ATH based formulations was investigated using modulated DSC coupled with a TGA. This was made possible by the resolution of the STA analyzer and by increasing the initial mass of the sample compared to the one usually used in DSC or TGA experiments (around 30 mg were used vs. 5 to 10 mg). As shown in **Figure 60**, the heat capacity of EVA/ATH increases steadily before decomposition (T < 220 °C) from 1.68 to 2.04 J/g/K at 200 °C and remains constant at around 2.07 J/g/K until 250 °C. Then, the heat capacity of the material decreases to 1.5 J/g/K when the mass stabilizes around 75 wt% residual weight. In the range 300–400 °C, corresponding to the stability domain of the intermediate specie of EVA/ATH, the heat capacity ranges between 1.58 and 1.68 J/g/K. The material undergoes its final decomposition step and the final residue exhibits a heat capacity, which ranges from 0.89 to 1.18 J/g/K between 500 and 800 °C.

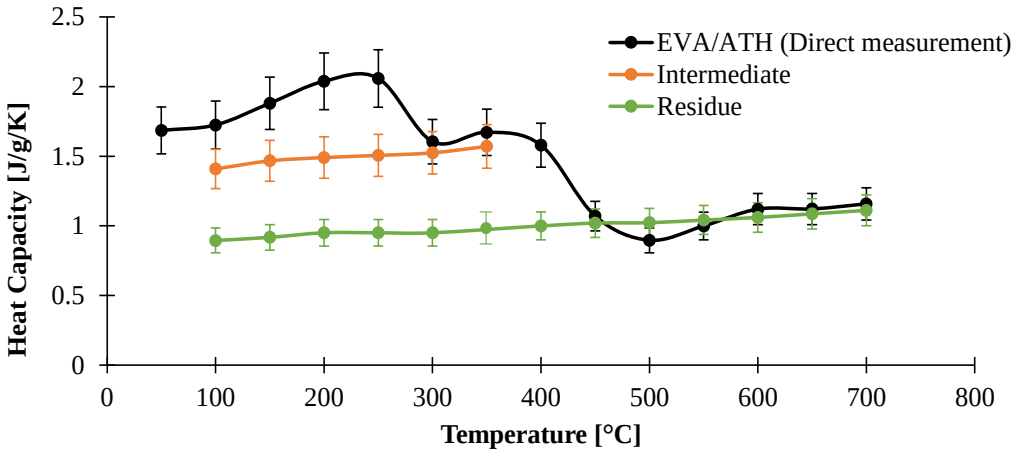

Figure 60: Heat capacity of EVA/ATH and its decomposition species as a function of temperature assessed through mDSC steps.

Those values are consistent with the heat capacity of charring and non-charring polymers found in the literature [78,81,191]. For instance, Stoliarov *et al.* [77] found values between 1.0 J/g/K at ambient temperature up to 2.4 J/g/K at the decomposition temperature for around 50 polymers. The values obtained in our study are also in the range of the heat capacity already reported for a polyethylene flame retarded with a high content of ATH [192]. On the other hand, EVA is a non-charring polymer and decomposes entirely at high temperature while EVA/ATH yields to an alumina ceramic. The values

obtained at high temperatures should thus be compared to the ones of alumina. The heat capacity commonly reported in the literature for alumina [193,194] ranges between 0.8 and 1.24 J/g/K in the range 25–727 °C, which is consistent with our results.

As it was done for thermal conductivities, the heat capacity was also determined by a stepped method. The same procedure as that defined for the thermal conductivity measurements was used. EVA/ATH composites were heated to 350 °C for 150 min in order to obtain the intermediate specie. After cooling to 100 °C, the heat capacity of the specimen was measured from 100 °C to 350 °C. The same procedure was used for the residue by heating the specimen up to 500 °C.

The results shown in **Figure 60** are consistent with the previous analysis. The intermediate specie exhibits a linearly increasing heat capacity from 1.4 J/g/K at 100 °C to 1.58 J/g/K at 300 °C. The heat capacity of the final residue also exhibits an increasing behavior as it starts from 0.89 J/g/K at 100 °C to 1.11 J/g/K at 700 °C. Between 300 and 400 °C for the intermediate species and at temperatures higher than 500 °C for the final residue, the measurements of the specie-dependent heat capacities are in agreement considering a 5 % standard deviation.

Another experimental approach, based on the ASTM E1269-11 [162] standard, was used to investigate the heat capacity of our material. Namely, the material underwent a 20 K/min heating rate ramp from 50 to 800 °C preceded and followed by 15 min isothermal steps. Those steps are necessary for heat flow signal equilibrium and the heating rate is recommended by the standard to ensure the best signal [162]. Before decomposition of the material, this method is in agreement with mDSC measurements (**Figure 61**). Indeed, EVA/ATH exhibit a heat capacity of 1.82 J/g/K at 100 °C and 2.20 J/g/K at 200 °C using this method against 1.78 J/g/K at 100 °C and 2.04 J/g/K for mDSC measurements.

It is noteworthy that this procedure does not allow us to have information about the heat capacity of the intermediate species, as the two decomposition steps are successive and the heat of the reactions overlap the DSC signal in the region where the intermediate species is stable. Even if it gives less information than mDSC measurements, this method is still useful as it is less time-consuming compared to isothermal mDSC measurements and also allows to determine the heat of reactions. Nonetheless, it should be noticed that ASTM E1269 is assumed to be valid only if the mass change is lower than 0.3 wt% and this technique is thus applicable only before the decomposition or on the final residue.

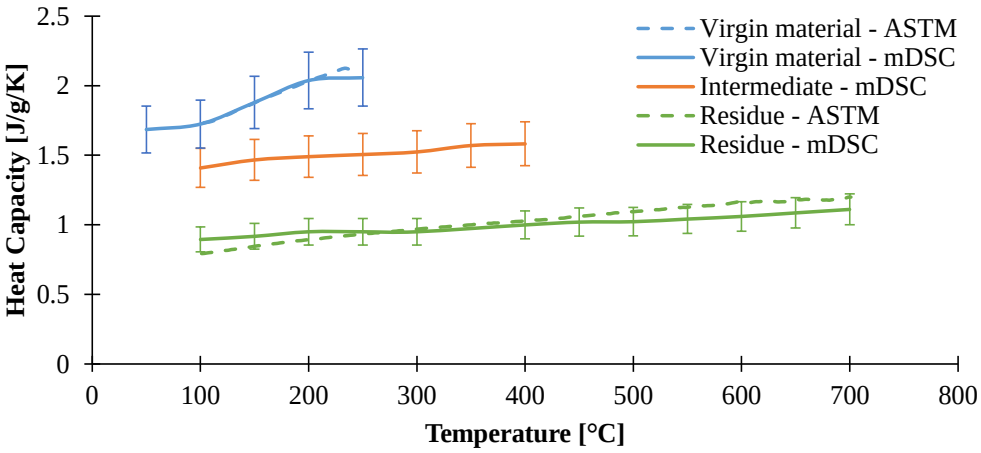

Figure 61: Heat capacity of EVA/ATH decomposition species as a function of temperature assessed through mDSC steps and dynamic heating ramps.

To determine the heat capacity of the final residue, a first experiment was carried out up to 700 °C and the residue was collected at the end and cooled to ambient temperature. Then it was exposed to a heating rate of 20 K/min from 100 to 700 °C and the heat capacity was measured according to ASTM E1269. As shown in **Figure 61**, the heat capacity of the final residue assessed by the ASTM method is consistent with mDSC measurements since the heat capacity varies from 0.73 J/g/K at 100 °C to 1.23 J/g/K. As a conclusion, the results for the final residue obtained with the ASTM method and the isothermal mDSC method are in agreement with each other, but also with the values of alumina found in the literature (between 0.8 and 1.24 J/g/K between 25 and 727 °C respectively [193,194]) considering 10% standard deviation

III.2.2.b. Evaluation of the heat capacity of EVA/ATH/NC

The same experimental protocols were applied to EVA/ATH/NC in order to investigate its heat capacity both as a function of temperature and decomposition state. The results are shown in **Figure 62**.

The heat capacity determined by direct measurement increases steadily before decomposition (before 220 °CC) from 1.69 J/g/K at 50 °C to 1.99 J/g/K at 200 °C. Then, the heat capacity decreases and remains constant around 1.55 J/g/K between 250 and 350 °C. At this stage, the material started to decompose and it corresponds to the temperatures where the mass stabilizes in the range 80-70 wt% residual weight. This corresponds to the range of stability of the intermediate specie as defined in **Figure 50** (p.101). Then, the material undergoes its final decomposition stage and the final residue exhibits a heat capacity, which

ranges between 1.08 and 1.14 J/g/K between 450 and 700 °C. As for EVA/ATH, the values obtained for EVA/ATH/NC are consistent with the ones reported in the literature for charring and non-charring polymers [78,81,191] as well as with the values of the heat capacity of EVA/ATH previously determined and with the heat capacity already reported for a polyethylene flame retarded with a high content of ATH [192].

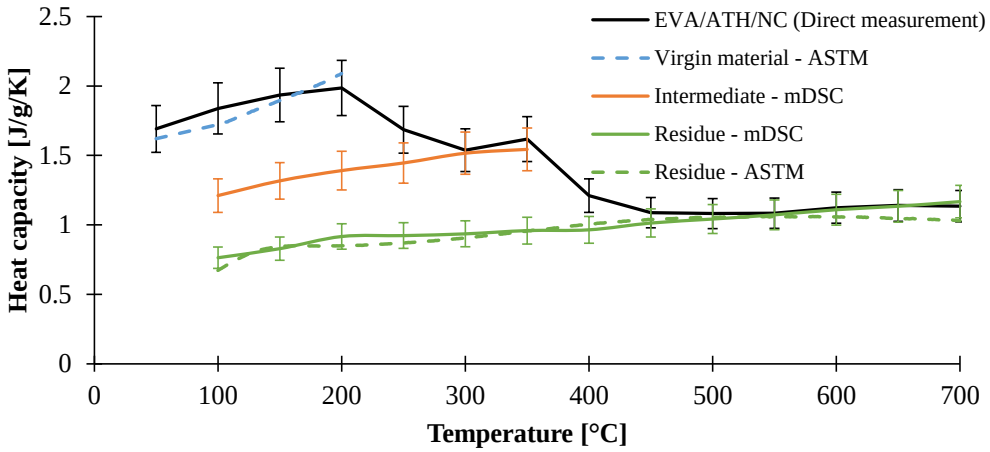

Figure 62: Heat capacity of EVA/ATH/NC and its decomposition species as a function of temperature assessed through mDSC steps and dynamic heating ramps

A comparison between the heat capacity of EVA/ATH composites determined by direct measurements is presented in **Figure 63**. The heat capacities of the EVA/ATH composites are similar with and without NC. Indeed, a heat capacity ranging between 1.68 to 2.04 J/g/K between 50 and 200 °C was obtained for EVA/ATH. It varies between 1.69 and 1.99 J/g/K in the same temperature range for EVA/ATH/NC. Interestingly, the heat capacities of the intermediate species are similar either. EVA/ATH exhibits a heat capacity of 1.60 and 1.67 J/g/K at 300 and 350 °C respectively while EVA/ATH/NC shows a heat capacity of 1.54 and 1.52 J/g/K at the same temperature. At the exception of the value at 500 °C, the heat capacity of the final residues obtained after the decomposition of the materials are similar and ranging between 1.00 and 1.18 J/g/K between 500 and 700 °C.

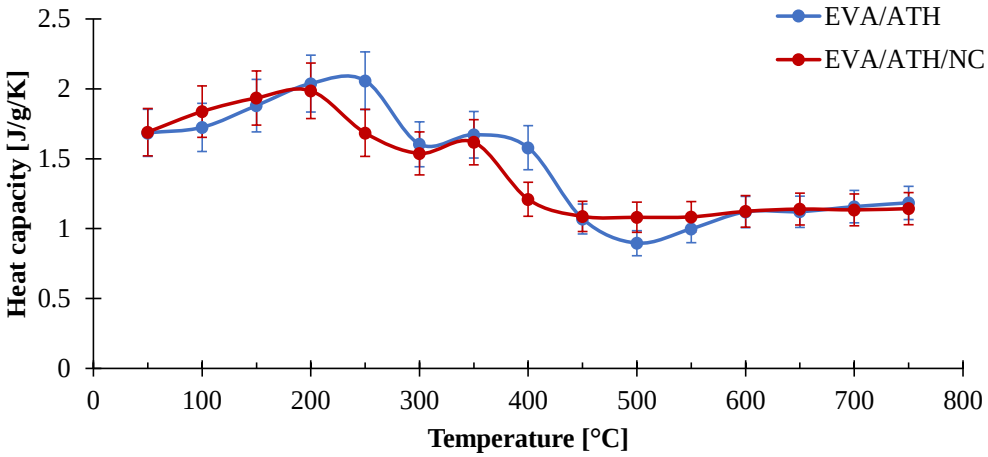

Figure 63: Comparison of the direct measurement of the heat capacity of EVA/ATH materials

The residue consists of alumina in the case of EVA/ATH while it is a mixture alumina/montmorillonite (with a ratio of 60:5) in the case of EVA/ATH/NC. It can be found in the literature that the heat capacities of montmorillonite are similar to the ones of alumina [194,195]. Indeed, alumina shows a heat capacity of 0.78 J/g/K at 20 °C [193,194] while the one of montmorillonite is reported between 0.78 and 0.81 [195]. Similarly, at 427 °C, the heat capacity of alumina is 1.15 J/g/K and the heat capacity of montmorillonite is between 1.16 and 1.20 J/g/K depending on the intercalated cations [195]. Due to the low fraction of montmorillonite compared to alumina and the comparable heat capacity values, it is normal that similar values were expected for the heat capacity of the final residues of EVA/ATH and EVA/TH/NC.

On the other hand, the values obtained before decomposition can be compared with calculated values obtained using a rule of mixture (**Table 15)**. The heat capacity of neat EVA was investigated using the ASTM E1269 [162] before its decomposition. **Table 15** presents the heat capacity of neat EVA measured at 50 °C and the values for montmorillonite [195] and alumina [194] obtained from the literature at 50 °C. Even if the values are taken for alumina instead of ATH and for montmorillonite instead of organo-modified montmorillonite (as Cloisite 30B^{TM}), a good agreement was found for both EVA/ATH and EVA/ATH/NC.

Table 15: Experimental and predicted heat capacity of EVA/ATH materials at 50 °C

		Heat capacity [J/g/K]
EVA		3.28
Alumina		0.82 [193,194]
Montmorillonite		0.82-0.85 [195]
Predicted	**EVA/ATH**	1.64
	EVA/ATH/NC	1.64-1.68
Experimental	**EVA/ATH**	1.68
	EVA/ATH/NC	1.69

III.2.3. CONCLUSION ABOUT THE THERMO-PHYSICAL PROPERTIES OF EVA/ATH MATERIALS

In this section, methodologies were adapted and used in order to measure the thermal conductivity and the heat capacity of both materials. It was shown that the heat capacities of EVA/ATH materials are similar as a function of their decomposition states and of temperature. It can be explained by the fact that heat capacity follows a linear law of mixture. As the decomposition of our materials differs only by the substitution of 5 wt% ATH by 5 wt% NC, it was expected that their heat capacities would be close. It was also shown that the heat capacity of the final residues exhibit a heat capacity close to the one of pure alumina which is in agreement with the decomposition pathway found in the previous section.

More differences were observed for the thermal conductivity of our material. Even if their thermal conductivities at ambient temperature were similar and relatively high compared to the one of neat EVA (1.08 W/m/K for EVA/ATH formulations against 0.39 W/m/K for neat EVA), their variation as a function of temperature appeared to be different. Indeed, it was shown that the thermal conductivity decreases as a function of temperature in both cases but EVA/ATH reaches a thermal conductivity of 0.71 W/m/K at 150 °C when the one of EVA/ATH/NC was equal to 0.83 W/m/K. The thermal conductivity of EVA/ATH decreases and reaches a plateau at around 0.24 W/m/K when both EVA and ATH decompose (250 °C) and remains stable until 350 °C before the final step of decomposition. On the opposite, the thermal conductivity of EVA/ATH/NC remains relatively high and does not stabilizes until all the polymer decomposes.

In the previous sections, the parameters used to describe the decomposition as a function of the temperature were investigated. The parameters governing heat transfer in the solid were also investigated as a function of the decomposition state and of the temperature of EVA/ATH materials. If a fire test such

as cone calorimeter has to be modelled, the optical parameters of our materials have also to be characterized. Indeed, they described how and how much energy from a fire or from a cone coil will be absorbed and heat up our materials. The next part of this chapter will thus be dedicated to their characterization.

III.3. MEASUREMENT OF THE OPTICAL PROPERTIES

III.3.1. IN-DEPTH ABSORPTION COEFFICIENT

III.3.1.a. Measurement of the in-depth scalar coefficient and skin depth

The radiative properties of interest for the modelling of the fire behavior of materials are the emissivity (ε), which quantify the amount of incident heat flux that will really impact the material (net heat flux) and the in-depth absorption behavior (A). This latter quantifies how the net irradiance penetrates in the materials. In order to investigate this penetration, the transmission of IR radiation inside a material has to be studied. A comparison of the transmittance spectra of EVA/ATH composites with the one of neat EVA is presented in **Figure 64**.

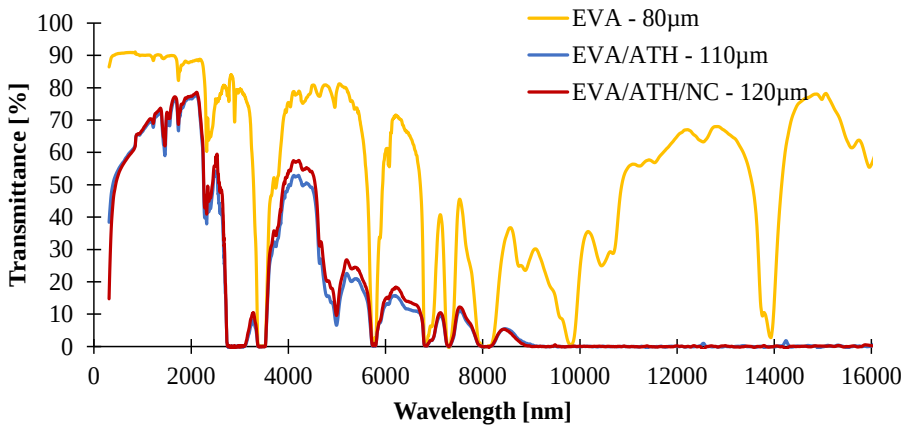

Figure 64: Comparison of the transmittance of pure EVA and EVA/ATH materials

Note the transmittance spectra are dependent on the thickness of the studied materials. It can be seen that EVA/ATH/NC behaves similarly as EVA/ATH. For both materials, some wavelength windows show no transmission and all wavelengths higher than 10000 nm do not transmit the irradiance for EVA/ATH composites while it is the case for neat EVA. Wavelength windows such as 3400-3500 nm, 5700-

5800 nm, around 6800 nm, around 7300 nm and between 7900 and 8200 nm do not transmit irradiance for both EVA/ATH composites and for neat EVA. An additional wavelength range between 2700 and 3100 nm does not transmit energy for both EVA/ATH composites but as EVA does, it can be attributed to the presence of ATH. This latter window is of importance as it is close to the area of maximum irradiance of cone calorimeter as shown in **Figure 34** (p.71).

Using the transmittance spectra obtained on films of two different thicknesses for each materials, and using the equations developed in **II.2.4** (p.70), it is possible to evaluate a wavelength dependent in-depth absorption coefficient. In this work, the simple and very approximate approach from Witkowski *et al.* [192] is to set $A_\lambda = 50000\ m^{-1}$ for the spectral ranges when the signal-to-noise ratio is too low. The scalar in-depth absorption coefficients are presented in **Table 16**. As a wide range of wavelengths is measured at 0 % transmittance for EVA/ATH formulations, a higher absorption coefficient than for neat EVA was expected. The skin depth of EVA is three to four time higher than these of EVA/ATH composites. Note also that the substitution of 5 % of ATH by NC leads to a small decrease of the in-depth absorption coefficient. Note that the skin depth of EVA/ATH composites are close to 250 µm under 50 kW/m² irradiance and decreases to around 210 µm under 35 kW/m² irradiance.

Table 16: In-depth absorption coefficient for 35 and 50 kW/m² irradiance for neat EVA and EVA/ATH formulations and corresponding skin depth (in parentheses)

Formulation	35 kW/m² irradiance	50 kW/m² irradiance
Neat EVA	2880 m^{-1} (694 µm)	2419 m^{-1} (826 µm)
EVA/ATH	9875 m^{-1} (202 µm)	7955 m^{-1} (251 µm)
EVA/ATH/NC	8900 m^{-1} (225 µm)	7611 m^{-1} (263 µm)

III.3.1.b. Measurement of depth-dependent absorption coefficients

As soon as the heat penetrates inside the material, a part of it will be reflected and a part of it will be absorbed. This implies that the neat irradiance at a depth *x* is not the initial irradiance. As the radiation penetrates the sample, the radiation spectrum will be distorted so that relatively more energy will be concentrated to the wavelengths where the spectral absorption coefficient is low. As demonstrated in **II.2.4** (p.70), it is possible to consider the absorption of heat by three ways:

- Assuming that the heat absorbs only on the surface.
- Assuming that the heat absorbs inside the materials with a global in-depth absorption coefficient.
- Assuming that the heat absorbs inside the materials with a local in-depth absorption coefficient.

It has to be remained that the absorption coefficient (A) measured in the previous section, is not the local absorption coefficient at depth *x*. Instead, A is the parameter that gives the right total irradiance at depth *x*, given an irradiation spectrum I_λ at the sample surface.

The local absorption coefficient at depth *x*, A(x) can be obtained after an iterative process described in **II.2.4** (p.70). Note that calculation of the local in-depth absorption coefficient is dependent of the increment used in the iterative process as shown in **Figure 65** for EVA/ATH. Indeed, the local absorption coefficient decreases sharply until reaching a plateau around 1700 m^{-1} after 500 µm. Note also that the lower the increment, the higher the local absorption coefficient. Indeed, if the increment in which the local absorption coefficient is calculated is low, then less heat will be absorbed so the in-depth absorption coefficient will be higher. In this study, it was decided to work with a 10 µm increment as it has a similar size than the mesh used for the numerical modelling. Moreover, it shows that the values of absorption coefficient are similar for 10 to 30 µm.

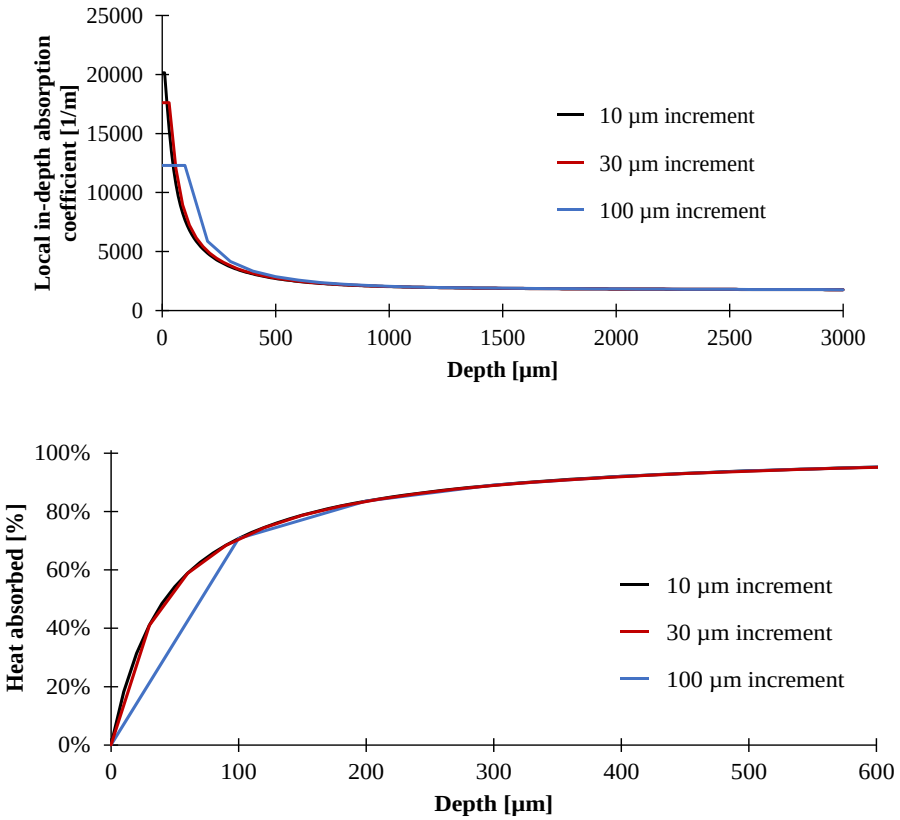

Figure 65: Local absorption coefficient calculated with 10, 30 and 100 µm increment (top) and related heat absorbed (bottom) by EVA/ATH under 50 kW/m² irradiance

A comparison of the global in-depth absorption model and of the local absorption model is presented in **Figure 66**. It can be seen that using the local coefficient, the absorption of heat is higher at low depth. Then, the heat absorbed assuming a local absorption becomes lower than with the global model. The heat absorbed assuming the global or the local absorption coefficient is the same at the skin depth. (*i.e.* 250 µm). The relative higher intensity at low penetration depth is due to the fact that in the global absorption model, the absorption is averaged over the skin depth and the absorption coefficient is thus lower than the local one at lower penetration depth. This implies that less heat/irradiation is absorbed as shown in **Figure 66** after 50 µm of penetration.

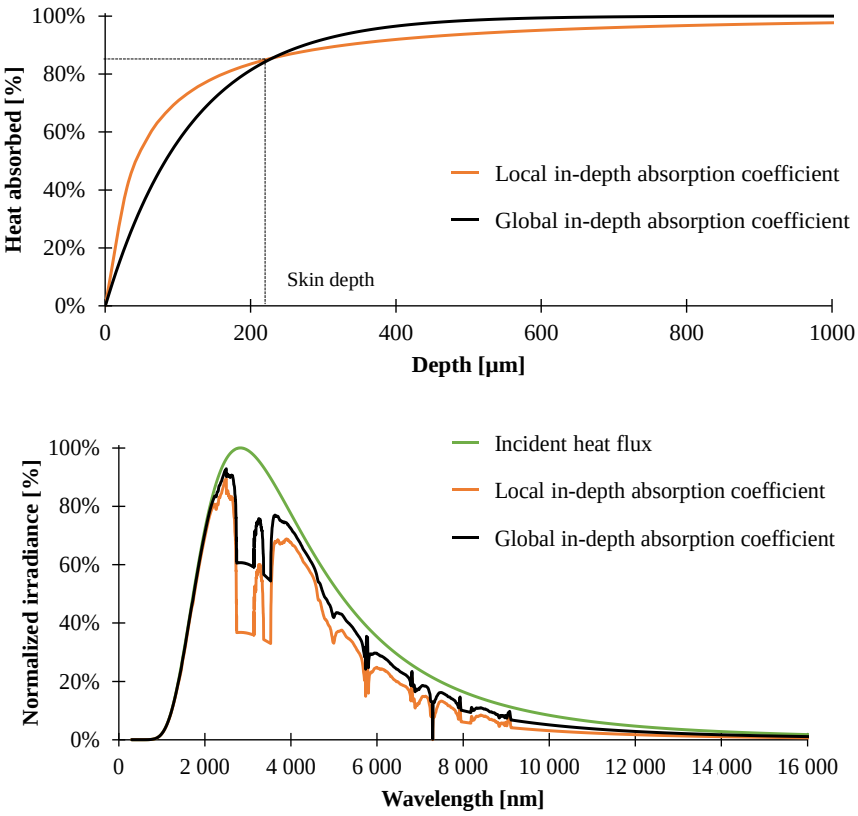

Figure 66: Heat absorbed by EVA/ATH under 50 kW/m² irradiance using the local or global in-depth absorption coefficient (top) and irradiance strum at 50 µm (bottom)

The depth-dependent absorption coefficients of neat EVA as well as the ones of EVA/ATH materials are presented in **Figure 67**. At the exception of EVA, these coefficients do not significantly change with the irradiance. For both EVA/ATH materials, the depth-dependent coefficients are measured in the first 10 µm of the material around 21000 m^{-1} under 35 kW/m² and around 20000 m^{-1} under 50 kW/m². Then, they decrease sharply until reaching 7600-7000 m^{-1} at 50 kW/m² and 8500-7900 m^{-1} at 35 kW/m². These values are obtained after 90 µm of penetration inside the materials. Then, the coefficients reach their steady state around 1770 m^{-1} for EVA/ATH and 2190 m^{-1} for EVA/ATH/NC for both irradiance. The steady state is reached after around 1 mm of penetration.

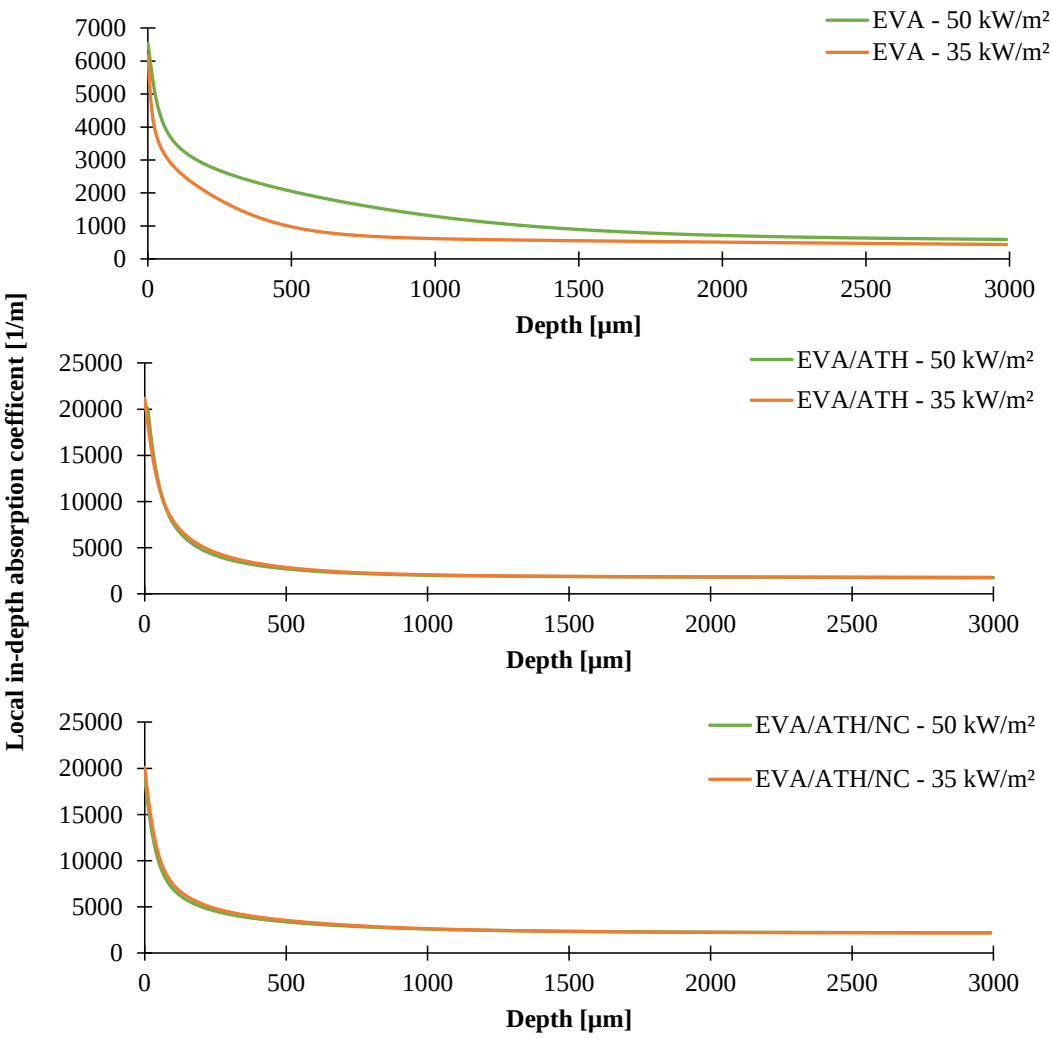

Figure 67: Depth-dependent in-depth absorption coefficient for neat EVA and EVA/ATH composites under 35 and 50 kW/m²

III.3.2. EMISSIVITY/REFLECTIVITY OF EVA/ATH MATERIALS

Due to Kirchhoff law of thermal radiation, the emissivity of EVA/ATH materials is their absorptivity. As shown in **II.3.2.c** (p.81), the scalar absorptivity can be measured from reflectance spectra.

A comparison of the reflectance spectra of EVA/ATH composites as well as this of neat EVA is presented in **Figure 68**. It can be seen that EVA/ATH/NC behaves similarly as EVA/ATH. Their maximum of reflectance appear before 2300 µm and are below 10 % between 2300 and 16000 nm. Interestingly, EVA does not reflect the irradiance more than 10 % over the all range of studied wavelength.

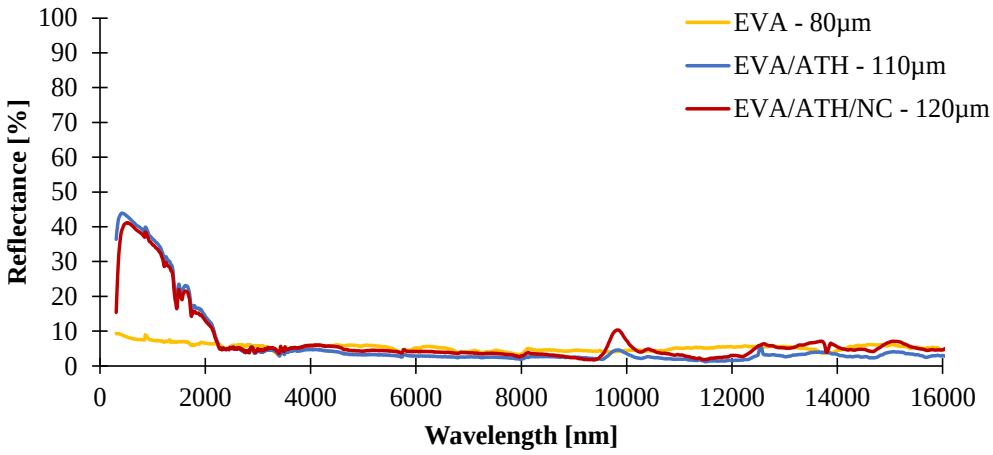

Figure 68: Comparison of the reflectance of pure EVA and EVA/ATH formulations

Using the reflectance spectra as well as the transmittance spectra for two different thicknesses of films for each materials and their in-depth absorption coefficient measured in **III.3.1**, the scalar absorptivity can be estimated (**Table 17)**. As the reflectivity of EVA and EVA/ATH materials is nearly constant and low over the whole range of wavelength, the absorptivity does not significantly change depending on the irradiance. For both EVA/ATH and EVA/ATH/NC, the absorptivity decreases with the irradiance level. Nonetheless, it can be noted that their absorptivity are similar and also close to this of neat EVA and thus an averaged scalar absorptivity of 94.9 ± 0.6 % is obtained for both EVA/ATH materials at 35 and 50 kW/m² irradiance. This value will be used for further numerical simulation of the EVA/ATH compounds.

Table 17: Scalar absorptivity depending of the irradiance level for neat EVA and EVA/ATH materials

Formulations	35 kW/m² irradiance	50 kW/m² irradiance
Neat EVA	94.7	94.6
EVA/ATH	95.3	94.6
EVA/ATH/NC	94.5	93.9

III.3.3. CONCLUSION ABOUT THE OPTICAL PROPERTIES

In this section, the optical properties representing how and how much heat is absorbed inside EVA/ATH materials were determined. It was found that EVA/ATH materials exhibit a skin depth (representing the depth at which 86.4 % of the incident heat flux is absorbed in the material) of around 250 µm at 50 kW/m² irradiance and around 210 µm at 35 kW/m². EVA/ATH/NC exhibits a higher skin-depth meaning that the substitution of ATH by NC decreases the absorption of heat inside the materials. The in-depth absorption coefficients as a function of depth or independent from the depth were measured and will be used in the next chapter as inputs for implementing the heat flux a cone heater. Finally, it was found that both materials exhibits a scalar absorptivity *i.e.* emissivity of 94.9 ± 0.6 %. This value was obtained at both 35 and 50 kW/m².

In the previous sections, thermo-physical parameters for both EVA/ATH composites were defined and characterized. They represent the decomposition of the materials (kinetics of decomposition and heats of reactions), how EVA/ATH composites transfer heat (thermal conductivity and heat capacity) and how they absorb or reflect incident radiation (emissivity and absorption coefficient). The last part of this chapter will be dedicated to the investigation of the heat capacity of the decomposition gases. Indeed, as mentioned in the heat balance equations (**Eq. 25** p.30 for instance), the diffusion of the decomposition gases inside the material contributes to the cooling or the heating of the materials. If the fire behavior of EVA/ATH composites has to be modeled, this ability needs to be characterized.

III.4. HEAT CAPACITY OF THE DECOMPOSITION GASES

For modelling purposes, it is of interest to measure the heat capacities of the decomposition gases as they can transport energy when they diffuse inside the decomposing material. The amount of energy that gases can transport is directly proportional to the mass flow inside the material but also to the heat capacity of these gases C_p^g. As the quantity and nature of those gases can influence the temperature distribution inside the material, it is important to have more qualitative and quantitative data about them.

III.4.1. GASIFICATION EXPERIMENTS COUPLED WITH FTIR SPECTROMETRY

The identification of gaseous decomposition products can be obtained through TGA experiments coupled with FTIR analysis. This was shown to be very effective when investigating the thermal decomposition of EVA filled with various metal oxides [38,116]. In this study, it was decided to use a

controlled-atmosphere mass loss calorimeter coupled with a calibrated FTIR spectrometer (CAMLC-FTIR) to detect and to quantify the products of the gasification of EVA/ATH formulations in similar conditions to cone calorimeter experiments. This approach proved to be effective for the quantification of the decomposition products and was already used in the case of the investigation of flaming and non-flaming cone calorimetry experiments [38,116,196–199]. CAMLC-FTIR experiments were performed with an oxygen level as low as 2 vol% in the gasification enclosure.

The results for EVA/ATH are presented in **Figure 69**. In the first part of the experiment, the material simultaneously releases acetic acid and water, coming from the deacetylation of the vinyl acetate part of the polymer and from the dehydration of the ATH. It is noteworthy that the peaks of water and acetic acid emission appear concurrently with the peak of mass loss rate (pMLR) at around 120-150 s. The behaviors of these two gases are similar. They start to evolve when the material degrades at 30 s and increase until reaching a peak at around 150 s, then decrease until the end of the test. Acetone is also detected and exhibits the same behavior but its maximum of concentration is delayed to 180 s.

As already reported by Witkowski *et al.* [110], acetone comes from the catalytic reaction of acetic acid on alumina. When exposed to the incident heat flux, the material starts to degrade, releasing water and acetic acid and forming alumina and polyene. As an alumina layer is formed on the top of the decomposing material during the test, the acetic acid evolves from the underlying material can then reacts at the surface and form acetone. The delay between the peak of acetone and acetic acid release can be due to the time required for the alumina layer to be formed in a sufficient quantity to promote the formation of acetone or the time required for this layer to reach the temperature to activate the catalytic process. A small amount of methane (lower than 60 volppm) is also observed at that stage.

A second stage of decomposition appears after 120 s. During this step hydrocarbon compounds are released in larger quantities, while acetic acid, acetone, and water release decrease as the decomposition front reaches the bottom of the sample and so ATH is completely turned into alumina. More precisely, propane and ethene are detected together with methane already identified in a lower amount in the first stage of decomposition. These three gases start to evolve at around 120 s and their concentrations steadily increase until a maximum at around 160 volppm is reached between 600 and 1000 s. It can be noted that propane concentration increases more rapidly than methane and ethene as it reaches its maximum after 350 s. From 600 s until the end of the experiment, a volumetric ratio of 1/1/1 between methane, ethane, and propane is detected.

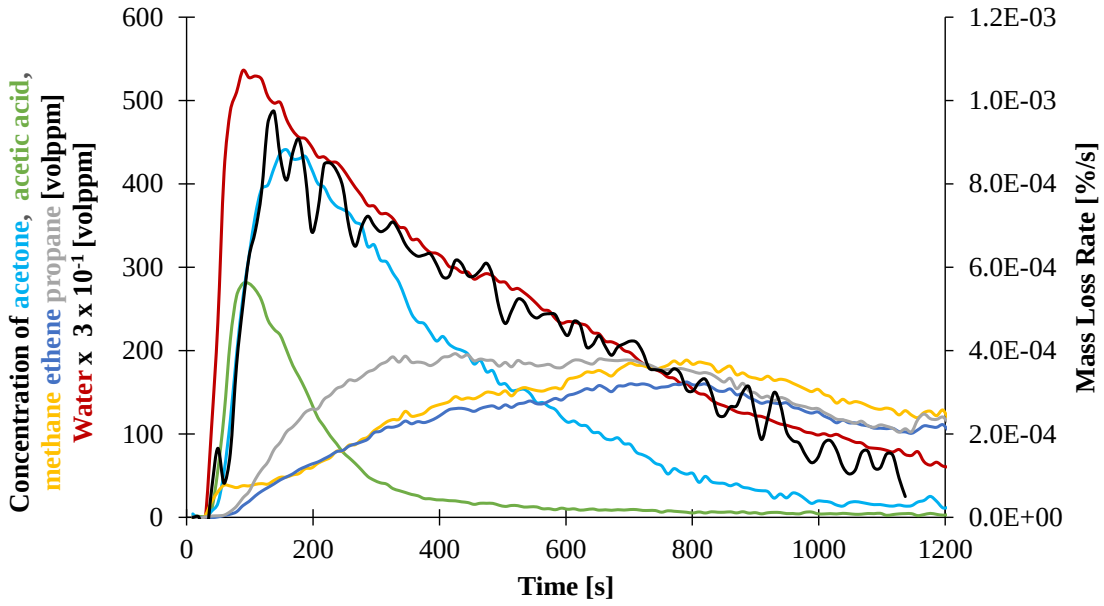

Figure 69: Mass loss rate and gas concentrations during CAMLC-FTIR experiments for EVA/ATH exposed to 50 kW/m²

Similar experiments were performed for EVA/ATH/NC and the results are presented in **Figure 70**. Even if the mass loss (MLR) curve is similar to this of EVA/ATH, the release of the gases is slightly different. As for EVA/ATH, the main detected gases are water, acetic acid, acetone, methane, ethene and propane. The peaks of water and acetic acid occur congruently at around 90-120 s while the acetone peak is delayed to 210 s. These three gases behave similarly: the gases start to evolve when the material decomposes around 30-60 s and increase sharply before reaching their maximum. Then, water and acetone release decreases steadily until the end of the experiment.

Note that the release of acetone and acetic acid is significantly different than in the case of EVA/ATH. Indeed, for this latter, acetic acid reaches its peaks at around 280 volppm while in the case of EVA/AT/NC, it reaches 500 volppm. The release of acetone follows the opposed trend: while it is released with a maximum intensity of around 500 volppm for EVA/ATH, it is only of around 400 volppm in the presence of NC. The early release of acetic acid is similar with the observation previously done with TGA/FTIR: the presence of NC catalyzes the deacetylation. Thus, more acetic acid is released before alumina either reaches a temperature high enough for the reaction of transformation of acetic acid into acetone to be effective or is formed in a sufficient amount that allows the reaction to occur.

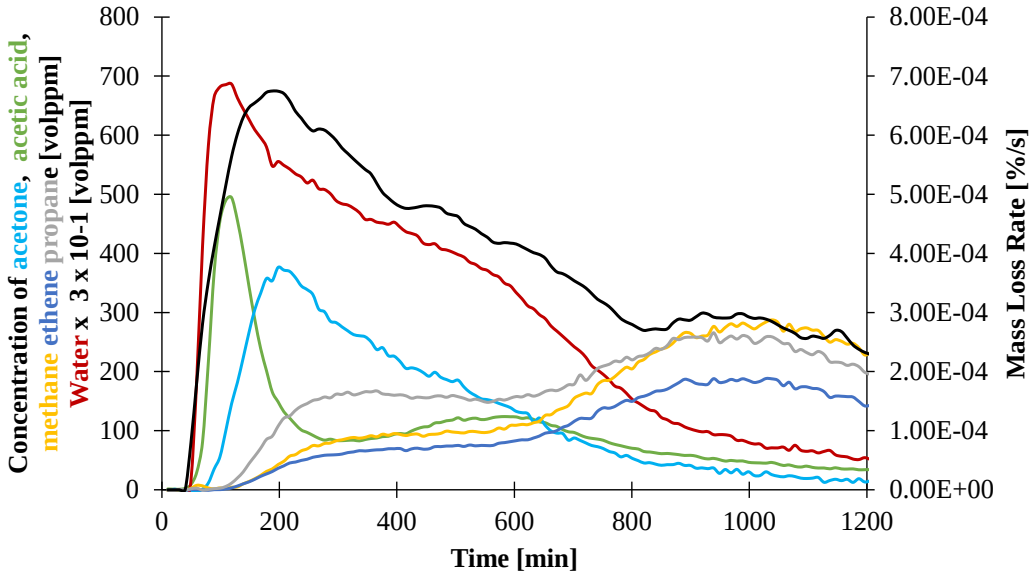

Figure 70: Mass loss rate and gas concentrations during CAMLC-FTIR experiments on EVA/ATH/NC exposed to 50 kW/m²

As for EVA/ATH, hydrocarbons compounds are released in a second step of decomposition after 120 s of experiments. During this step, acetic acid, acetone, and water release decrease as the decomposition front reaches the bottom of the cone plaque. Propane and ethene are detected as well as methane. These gases start to evolve around at 120 s and their concentrations reach a plateau at around 400 s. Nonetheless, their concentrations increase in a more important way from around 700 s to reach a maximum between 700 s and 1200 s at around 300 volppm for methane and ethene and 200 volppm for ethene. This increase could be attributed to the cracking of the ceramic residue layer formed when the material decomposes. This layer seems thus to be more dense than in the case of EVA/ATH and could release additional gases while cracking. On the other hand, it can be noted since it started to be produced, propane concentration increases more rapidly than methane and ethene as it reaches 160 volppm after 300 s of experiment.

III.4.2. HEAT CAPACITY OF THE DECOMPOSITION GASES

In order to obtain to the heat capacity of the decomposition gases, the total amount of evolved gases for each product was evaluated. The results are presented in **Table 18**. The quantification of the gases in gasification experiments was done in terms of volumetric concentrations, but the pyrolysis model is solved versus mass. The volumetric ratio of the different individual gases have thus to be translated to

mass ratio. Assuming that the ideal gas law is valid for all the quantified gases, it is possible to define the weight ratio between two gases as the ratio between the yields of the volumetric quantification obtained via FTIR and the molar masses of the studied gases. Mass ratio between acetone, acid acetic, and water for the first decomposition gas and propane, ethene, and methane for the second decomposition gas are then calculated and the composition of the decomposition gases is presented in **Table 18**.

It can be noticed that during the first decomposition step, mainly water is released. This is consistent with the composition of the material composed of 65 wt% of ATH, which releases water when dehydrating. Due to the difference in molar masses, Gas2 is composed of more than 50 wt% of propane for both EVA/ATH materials. In the first step of decomposition (Gas1 as defined in **Figure 50**, p.101), acetic acid represents around 1.7 wt% for EVA/ATH and around 4.1 wt% for EVA/ATH/NC. Nonetheless, the concentration of Gas1 in water is predominant for both materials (more than 90 wt%). Similarly, in the second stage of the decomposition (Gas2 as defined in **Figure 50,** p101), the presence of NC promotes the formation of propane compared to that of ethene.

Table 18: Total volumetric concentrations of gases and mass composition in Gas1 and Gas2 for EVA/ATH formulations

			Total Gas Evolved [volppm]	**Mass ratio of evolved gases**	**Composition in individual gas [wt%]**
EVA/ATH	**Gas1**	Acetic acid	237	0.02	1.7
		Acetone	2936	0.06	5.8
		Water	151337	1.00	92.5
	Gas2	Ethene	2588	1.50	28.1
		Propane	3110	2.80	53.1
		Methane	3017	1.00	18.8
EVA/ATH/NC	**Gas1**	Acetic acid	2457	0.04	4.1
		Acetone	2924	0.05	4.7
		Water	182012	1.00	91.2
	Gas2	Ethene	2588	1.10	21.4
		Propane	4585	3.10	59.6
		Methane	4036	1.00	19.0

Based on these compositions, and using heat capacities values of each individual gases from the literature [200], it was possible to evaluate the heat capacity of the decomposition gases (Gas1 and Gas2). The results are presented from 100 to 900 °C in **Figure 71**. The heat capacity of Gas1 varies following a gradual increase from 2.0 J/g/K at 127 °C up to 2.5 J/g/K at 927 °C. Interestingly, the heat capacity of Gas1 is close to that of water. On the contrary, the heat capacity of Gas2 constantly increases and greatly varies in the considered range of temperature. It starts at 2.15 J/g/K at 127 °C and rises up to 4.26 J/g/K at 927 °C. The relatively high value for the heat capacity of Gas2 compared to Gas1, or even of the condensed phase species previously measured (between 0.8 and 2 J/g/K), is due to the composition in hydrocarbon volatiles and their relative high heat capacity compared to water [200].

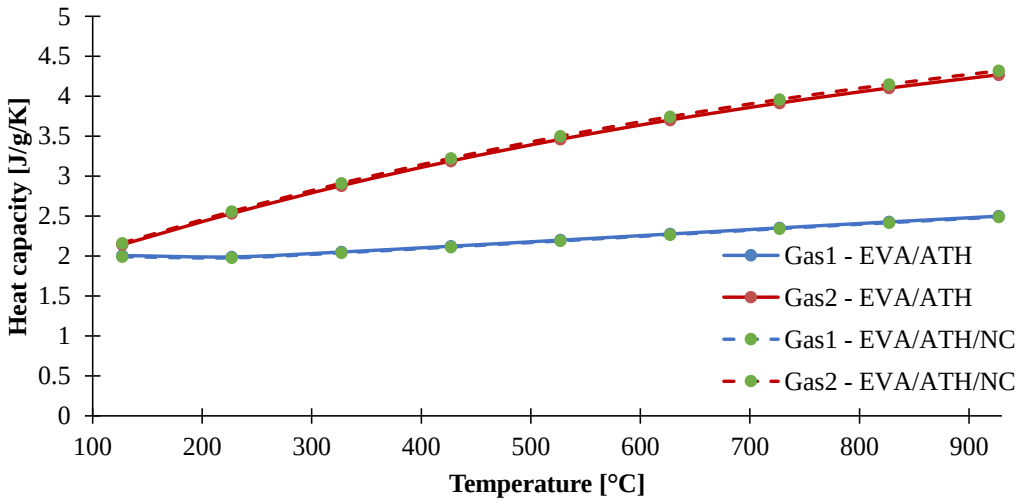

Figure 71: Heat capacities of Gas1 and Gas2 as a function of temperature for EVA/ATH materials

It can be noted that the obtained values are different to other heat capacities of gases reported in other studies dealing with pyrolysis modelling. For example, Li *et al.* [78] used the temperature-averaged heat capacity of gaseous hydrogen chloride (0.84 J/g/K) when modelling pyrolysis of PVC. Hydrogen chloride was chosen assuming that PVC releases more than 80 wt% of this gas. To model the pyrolysis of other polymer such as polycarbonate, high impact polystyrene, or polyoxymethylene, Li *et al.* [82] used the average heat capacity of linear C_1-C_8 hydrocarbon gases between 400 and 500 K and a value of 1.8 J/g/K was obtained and used for further modelling. Even if the heat capacities of C_1–C_8 linear hydrocarbons are very similar as they are in the range 2–2.4 J/g/K at 100 °C and exhibit an increasing behavior up to 2.7–3.4 J/g/K at 900 °C [200], other compounds such as alkenes and aromatic volatiles

can be released and should also be considered. However, limited values for those gases are found in the literature. Moreover, the temperature increase in gasification experiments can go up to 600 K [82] and it can be questionable to use 400–500 K averaged values and not temperature-dependent values. All those assumptions can be acceptable if the transport of the gaseous component out of the materials is fast, but it leads to higher uncertainties if the diffusion of the decomposition gases inside the material is slower. Indeed, gases can transport and evacuate energy from the decomposition front out of the material.

III.4.3. CONCLUSIONS ABOUT THE HEAT CAPACITY OF DECOMPOSITION GASES

In this section, the heat capacity of the product of decomposition of EVA/ATH and EVA/ATH/NC was investigated. Using a controlled-atmosphere cone calorimeter coupled with a calibrated FTIR spectrometer, it was possible to identify and to quantify the gases released when EVA/ATH materials decomposes. As for the identification with TGA-FTIR presented in the first section of this chapter, it was found that the addition, of NC induces a higher release of acetic acid compare to acetone. Similarly, it was shown that EVA/ATH releases more propane and less ethene than EVA/ATH/NC.

Finally, after having quantified the amount of each gases released when the materials decompose, the heat capacity of the decomposition gases were calculated using heat capacity values of several gases reported in the literature. Even if the decomposition products of EVA/ATH and EVA/ATH/NC are different, this does not lead to significant differences between the heat capacity of the decomposition gases of EVA/ATH composites. The first gas released from the decomposition of our materials (Gas1 as defined in **Figure 50**) is composed of water, acetic acid and acetone and exhibits an increase of heat capacity as a function of temperature. Indeed, it varies from 2.0 J/g/K at 127 °C to 2.5 J/g/K at 927 °C. The second gas of decomposition (Gas2 as defined in **Figure 50**) follows the same trends but its values are much higher. Namely, it varies from 2.15 to 4.26 J/g/K between 127 and 927 °C.

III.5. CONCLUSION

This chapter was dedicated to the investigation of the thermo-physical properties of EVA/ATH composites. Thermal analyses of these materials were performed showing that their pyrolytic decomposition is a multi-step process. It was shown that the addition of ATH promotes the catalytic transformation of acetic acid into acetone. Similarly, the presence of NC catalyzes the deacetylation of EVA and also changes the decomposition mechanism of EVA into different hydrocarbons in the second decomposition step. Based on a model-free analysis, the kinetics of decomposition of EVA/ATH based materials were investigated. The heats of decomposition reactions were also investigated and no significant differences were obtained.

Additionally, standardized characterization techniques (Hot Disc, modulated DSC) were used in order to evaluate to the thermal conductivity and heat capacity of our materials. The application of these protocols was extended to estimate the properties of the species formed during the decomposition of the materials. Tailored TG experiments mimicking the protocols used for the characterization of the thermal conductivity were performed. It was then possible to adapt these protocols and to measure the thermal properties of the final residues as well as of the intermediate species as a function of temperature. It was shown that the thermal conductivity of EVA/ATH formulations was higher in the presence of NC. On the contrary, the heat capacities of both EVA/ATH materials were similar. The measured heat capacities of the final residues were consistent with the ones of alumina. Moreover, it can be noticed that the heat capacity of both EVA/ATH materials before their decomposition follow a linear rule of mixture. This was attributed to the few differences on the composition of both materials and to the great similarities of the heat capacity of the additives (ATH and NC). If more information about the heat capacity of the FR additives and polymers were available in the literature, it would then be possible to estimate the heat capacity of materials, thus researchers have to put efforts on these characterization in the future.

Other parameters of importance for pyrolysis modelling were determined in this chapter. Namely, the optical properties, which drive how the heat from a fire or from a heat source will be absorbed, were determined. It was found that EVA/ATH based materials exhibit an emissivity of 94.9 ± 0.6 %. Moreover, the in-depth absorption of the incident heat was also investigated using a global or a local in-depth absorption coefficient. In both cases, it was shown that around 86 % of the net irradiance was absorbed in the first 200-250 µm of the materials.

Finally, the heat capacity of the decomposition gases, which relates to the amount of energy that the gases can “remove” from a material was quantified with a CAMLC apparatus coupled with a calibrated

FTIR spectrometer. It was shown that the heat capacities of the first decomposition gases (Gas1) were in the range 2-2.5 J/g/K between 127 and 927 °C. On the contrary, the second products of decomposition (Gas2) show high values of heat capacities (between 2 and 4 J/g/K). These relatively high values were explained by their composition in hydrocarbons. Note that these values are limited to the literature values found for the individual gases (methane, ethene *etc.*) but also mainly to the possibility to quantify them. Most authors do not characterize and quantify the gases released when a material decomposes but generally assumed that they are composed of one main gas. Great discrepancies can thus be obtained between the values obtained in this study and other studies reported in the literature. Even if our characterizations are limited to the gases that can be quantified and thus by the quantification methods, our values are based on experimental data on the opposite of most authors and we are thus confident with these values.

As a conclusion of this chapter, all the parameters required for the numerical simulation of the fire behavior of both EVA/ATH materials were determined experimentally. Standardized procedures were adapted and extended beyond their scope in order to access to the measurement of the inputs data (kinetics of decomposition, thermo-physical properties and optical properties of EVA/ATH materials and/or of their decomposition gases) as a function of temperature and decomposition states. The next chapter will thus focus on the numerical modelling of the fire behavior of EVA/ATH and EVA/ATH/NC using these data as inputs.

CHAPTER IV. MODELLING THE FIRE BEHAVIOR OF EVA/ATH COMPOSITES

This chapter is dedicated to the modelling of the fire behavior of the EVA/ATH composites. Using the properties determined in the previous chapter, the temperature, the mass loss and the heat release rate will be modelled in gasification and flaming conditions. The first section will describe the model used in this chapter. Then, the second section will comment the prediction of the gasification of EVA/ATH composites and how the implementation of the kinetics, of the thermo-physical and of the optical properties impact the prediction of the mass loss rate and temperature profiles. Then, the parameters describing the flaming conditions will be defined and the temperature, the mass loss rate and the heat release rate profiles in flaming conditions will be modelled and compared to experimental data.

IV.1. DESCRIPTION OF THE MODEL

The pyrolysis model used in this study is close to the one developed in the frame of the ThermaKin software (**I.2.3** p.24). It was selected as it shows a good balance between the accuracy of the phenomena involved in the pyrolysis of polymers (in-depth absorption, gas diffusion, *etc.*) without needing the characterization of parameters such as permeabilities as a function of temperature and decomposition states or pressure conditions in case of flaming conditions. This model was already used to simulate the pyrolysis of PE/ATH and gave similar results than both ThermaKin and FDS v.06 [192]. More precisely, the model is implemented in the commercial solver Comsol® Multiphysics and couples mass and heat conservation equations.

The variation of mass inside the system can be described as in **Eq. 77**. It can be described either in a global way or by defining several reactions.

$$\dot{r}(m) = \sum_{r}^{N_r} \dot{r}_r = \sum_{r} -\frac{1}{\nu_r^i}\frac{\partial m_{i,r}}{\partial t} = \sum_{r} A_r . \exp\left(\frac{-E_r}{RT}\right) . m^n{}_{reactant,r}$$

$$\dot{r}(\alpha) = \frac{\partial \alpha}{\partial t} = A(\alpha) . f(\alpha) . \exp\left[\frac{-E(\alpha)}{RT}\right]. \qquad \textit{Eq. 77}$$

Based on this equation, it is then possible to express the variation of gaseous component using **Eq. 78** and **Eq. 79**. In these equations, the mass flux of each i^{th} gas can be described using the rate of decomposition $\dot{r}$, and a mass transfer coefficient D_{gas} associated to each gases. The mass diffusion is driven according to the Fick law. This was selected as it requires less parameters to be characterized. Indeed, using the Darcy law would require the characterization of pressure boundaries in flaming conditions, of the permeabilities of the different species (intermediate species and final residues) and of the viscosities of the gases as a function of the temperature. The latter parameters are not easy to evaluate and the Fick law is therefore more appropriate.

$$\dot{m}''_{gas,i} = -D_{gas,i}\frac{\partial m_{gas,i}}{\partial x} \qquad \textit{Eq. 78}$$

$$\frac{dm_{gas,i}}{dt} = \nu_r^i . \dot{r} - \frac{\partial \dot{m}''_{gas,i}}{\partial x} \qquad \textit{Eq. 79}$$

The mass conservation equations need the resolution of the temperature field inside the material as the kinetics of decomposition are temperature-dependent. The general form of this equation is given in **Eq. 80**. In this equation, the enthalpy of decomposition ΔH_r can be described in two ways as proposed in **Eq. 81**. If several reactions were set in the mass balance equation, an enthalpy of reaction can be associated

to each of these reactions and thus, ΔH_r is the sum of $\dot{r}_r(m).H_r$. If a global kinetic model is used, the heat of reaction can be implemented as in **Figure 55** (p.110).

$$\rho Cp\frac{\partial T}{\partial t} = \frac{\partial\left(k\frac{\partial T}{\partial x}\right)}{\partial x} + \Delta H_r - \sum_i^{N_g}\left(\dot{m}''_{gas,i}.\frac{\partial\left(\int_0^T Cp_{gas,i}dT\right)}{\partial x}\right) - \left\{\varepsilon\frac{\partial \dot{q}''_{rad}}{\partial x}\right\}_{Scenario\ I} \quad \textbf{Eq. 80}$$

$$\Delta H_r = \sum_r \dot{r}_r(m)\,H_r \quad \textbf{Eq. 81}$$

$$\Delta H_r = H_r(\alpha)$$

$$\dot{q}''_{rad}(x) = \exp(-A.x).\left[\dot{q}''_e. + \dot{q}''_{flame}\ \text{if}\ (J_{gas} > CMF)\right] \quad \textbf{Eq. 82}$$

$$\dot{q}''_{rad}(x) = \exp(-A(x).x).\left[\dot{q}''_e. + \dot{q}''_{flame}\ \text{if}\ (J_{gas} > CMF)\right]$$

The incident heat flux can be implemented in two ways in the equations:

- In scenario I: the heat is considered to be absorbed inside the material. The part $\left\{\varepsilon\frac{\partial \dot{q}''_{rad}}{\partial x}\right\}$ in **Eq. 80** have to be considered and can be defined by a Beer Lambert law as presented in **Eq. 82**. $\{-\varepsilon\dot{q}''_e\}$ is not used in **Eq. 83** and **Eq. 84**.
- In Scenario II: the heat is supposed to be absorbed only at the surface, $\{-\varepsilon\dot{q}''_e\}$ is then used in **Eq. 83** and **Eq. 84** and there is no need to define $\left\{\varepsilon\frac{\partial \dot{q}''_{rad}}{\partial x}\right\}$ in **Eq. 80**.

Additional parameters are required to describe the ignition and the flaming conditions. Considering either surface or in-depth absorption of the incident heat flux, the boundary condition for flaming conditions are presented in **Eq. 84**:

- An additional heat flux from the flame $\dot{q}''_{flame}$ is added when the total mass flux of gases $J_{gas} = \sum_{gases}\dot{m}''_{gas}$ is higher than a critical mass flux for ignition (hereafter called CMF). Similarly, the flame is turned off when J_{gas} becomes lower than CMF.
- There is no general agreement on how to describe the convection when a flame is present at the surface of the sample. The convective term $\{h_{conv}(T_{surface} - T_\infty)\}$ can thus be considered or not in **Eq. 84**.

Boundary condition before ignition/gasification experiments

$$-\frac{\partial\left(k\frac{\partial T}{\partial x}\right)}{\partial x}_{x=\delta} = -\varepsilon\left\{\dot{q}''_e\right\}_{Scenario\ II} + h_{conv}(T_{surface} - T_\infty) + \varepsilon\sigma\left(T^4_{surface} - T^4_\infty\right) \quad \textbf{Eq. 83}$$

Boundary condition after ignition (when $J_{gas} > CMF$)

$$-\frac{\partial\left(k\frac{\partial T}{\partial x}\right)}{\partial x}_{x=\delta} = -\varepsilon\left\{\dot{q}''_e + \dot{q}''_{flame}\right\}_{Scenario\ II} + \left\{h_{conv}(T_{surface} - T_\infty)\right\}_{Scenario\ III} + \varepsilon\sigma\left(T^4_{surface} - T^4_\infty\right) \quad \textit{Eq. 84}$$

The boundary conditions for the mass conservation equation need to be fixed. The face of the cone plaque which is not exposed to the cone heater is impermeable to the gases (**Eq. 85**). On the exposed face, the mass of each i^{th} gas is set to 0 as proposed by Statler *et al*. [201]. It represents the fact that the gases are instantaneously removed from the surface due to the convective environment or that their concentrations are negligible or that they are fully consumed by the flame.

$$\dot{m}''_{gas,i} = 0 \quad \textit{Eq. 85}$$

$$m_{gas,i} = 0 \quad \textit{Eq. 86}$$

The computational domain was divided in element size of 1.0 10^{-5} m and a 0.1 s time step was used for the simulations. These parameters are similar to the ones used by Stoliarov *et al.* [4]. Using these parameters allowed a convergence of the simulations. Increasing or decreasing each of these parameters by a factor two did not impact the simulation results.

As the sample material was heated, convective cooling to the atmosphere occurred with a convection coefficient of 10 W/m²/K, as determined in other studies [81,103,202]. The boundary conditions at the rear face of the exposed specimen are represented by a 50 mm thick domain, representing the insulation, without thermal contact resistance with the studied material. The thermal properties associated with this insulation (IFP JM26® from Morgan Thermoceramics) are given by the producer and are assumed to be constant with the temperature. The insulation has a density of 890 kg/m^3, a heat capacity of 1100 J/g/K, and a thermal conductivity of 0.26 W/m/K. The initial temperature is taken at 300 K and the initial amount of material corresponds to the mass of a plaque. The gaseous component, final residue, and intermediate species masses are set to 0 at the initial stage as the material consists exclusively of initial material.

The pyrolysis model will be used to predict the mass loss, the heat release and the temperature profiles of 1 and 3 mm thick plaques at 35 or 50 kW/m² incident heat flux both in CAMLC and in MLC apparatus. The model, previously described is based on equations that are generally accepted to depict the pyrolysis of various materials. It is not the purpose of this study to develop a new model or to improve existing models by considering additional phenomenon. On the contrary, the implementation of well-known

phenomena will be discussed. For instance, there are different ways to consider the thermo-physical properties of the materials. Namely, they can be considered either as:

- A function of temperature as presented in **Figure 56** (p.112) for k(T) and **Figure 63** (p.121) for Cp(T)
- A function of conversion degree and the temperature-dependent properties of the decomposition species $k(T) = \sum_i \omega_i(T).\, k_i(T)$ and $Cp(T) = \sum_i \omega_i(T).\, Cp_i(T)$
- A function of conversion degree but temperature constant properties of the decomposition species $k(T) = \sum_i \omega_i(T).\, k_i(T_{cst})$ and $Cp(T) = \sum_i \omega_i(T).\, Cp_i(T_{cst})$.

Moreover, it was also shown in **III.1.2** (p.102) that it is possible to define the kinetics of decomposition either by setting two consecutive reactions or by using a global kinetic model. The impact of one type of kinetics or of the other will be discussed in the following sections of this chapter.

Finally, as presented in the previous chapter, the use of global or local in-depth absorption coefficient as well as the fact to consider surface absorption of the incident heat flux can be used to describe the incident heat flux and the heating of a material. The impact of using one of this conditions or another will be discussed as well.

IV.2. VALIDATION OF THE INPUT DATA: GASIFICATION EXEPRIMENTS

In this part, the numerical model is used to generate mass loss and temperature curves obtained for gasification (CAMLC) experiments performed at 50 kW/m² on 3 mm thick plaques. In a first part, the inputs will be validated comparing the experimental temperature and mass loss profiles in CAMLC experiments with the data obtained from the model. For that section, temperature- and composition-dependent heat capacity and thermal conductivity were used as they are the most common way to implement the inputs data in a pyrolysis model. Then, the way to implement the inputs will be discussed with a specific emphasis on the thermo-physical properties, the kinetics of decomposition and the optical properties.

IV.2.1. MODELLING OF GASIFICATION EXPERIMENTS

IV.2.1.a. Prediction of mass loss rate of EVA/ATH formulations

In the previous chapter, methodologies were developed to characterize the inputs data needed for a pyrolysis model. At the exception of the mass transfer coefficients (D_{gas} in **Eq. 78** p.140), all the data were experimentally characterized. It is generally found in the literature that the decomposition gases are released rapidly or instantaneously from the materials [78,80,203]. This is mathematically described by a mass transfer coefficient arbitrarily fixed at 2.10^{-5} m²/s [78,81]. Using this assumption, it was not possible to successfully predict the mass loss curves for EVA/ATH composites in CAMLC experiments as presented in **Figure 72**. Indeed, it is obvious that assuming fast diffusion of the gases in the model over-predicts the mass loss since the simulated mass loss is always below the experimental curve. Moreover, the final mass loss after 1200 s is assumed to be 41 wt%, when it was found experimentally to be 50 wt% for EVA/ATH. Similarly, the residual weight after 1200 s of experiment for EVA/ATH/NC is 53 wt% when it is predicted at 43 wt% assuming the rapid release of gases. Slower diffusion must therefore be considered and lower D_{gas} values should be relevant and have to be considered. Slow diffusion would imply that the materials could be fully decomposed while decomposition gases are still released.

Indeed, Hoffendahl *et al.* [38] investigated the thermal decomposition of EVA/ATH together with melamine borate as a synergist in a mass loss cone calorimeter under 35 kW/m² irradiance. The bottom and front of a 3 mm thick plaque were analyzed using ^{13}C and ^{27}Al solid-state NMR. As soon as the material ignites at around (starting pyrolytic decomposition of the material), it was found that it took around 500 s for the ATH to be turned into alumina at the bottom of the plaque. Similarly, it was found

that around 600-1000 s were necessary for the polymer part of the material to decompose at the backside of the plaque. Even if the materials studied here are different (lower VA content and no synergistic melamine derivative), it can be assumed that both EVA/ATH formulations will decompose in a similar manner or even faster. as the incident heat flux is higher. This would mean that in the first 1000 s of the CAMLC experiments, the material would completely decomposes, and thus no mass loss would be observed afterwards. Moreover, it was found in the literature that acetic acid adsorbs onto alumina oxide when reacting to form acetone [111,113,204]. This would also promote the assumption of slower release of the decomposition gases.

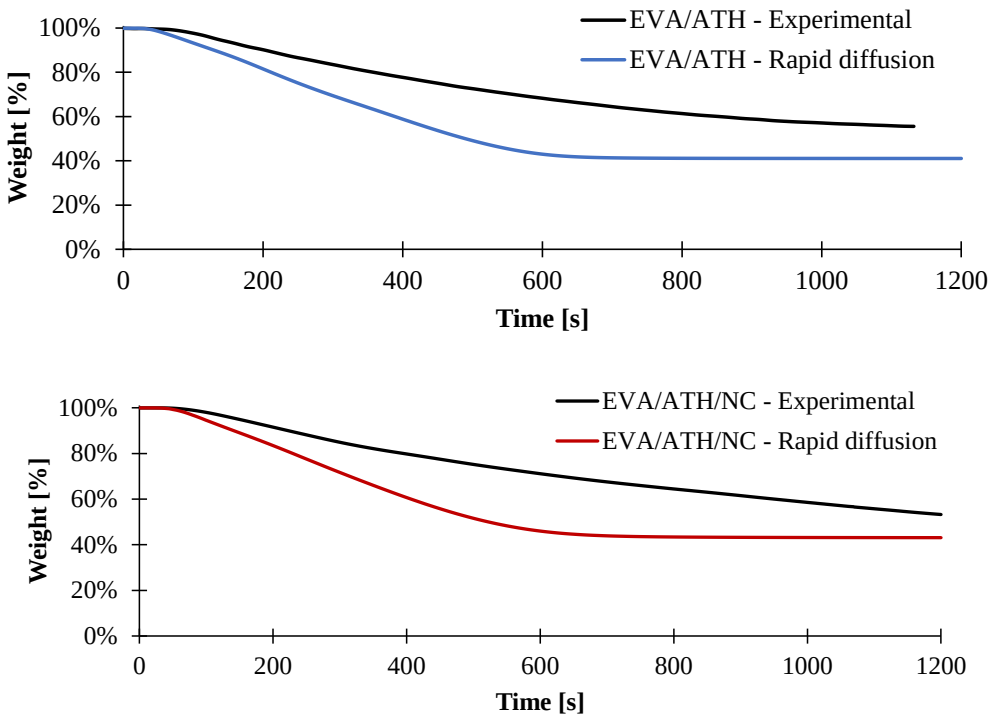

Figure 72: Experimental and predicted mass loss curves assuming rapid release of the gases for EVA/ATH composites in CAMLC experiments

It was thus decided to tune the mass transfer coefficients of each released gases in order to fit the experimental mass loss and mass loss rate curves for EVA/ATH formulations obtained in gasification experiments (CAMLC). This fitting procedure is a way to estimate those mass transfer coefficients, as they are the only unmeasured parameters in the model.

A mass transfer coefficient for Gas1 as defined in **Figure 50** (p.101) ranging between 21.10^{-9} and 18.10^{-9} m²/s and a second mass transfer for Gas2 as defined in **Figure 50** (p.101) between 5.10^{-9} and 7.10^{-9} m²/s were thus estimated to give an acceptable fit of the experimental data (**Figure 73**).

A special attention was given to the prediction of the final mass loss but also to the fit of the last part of the mass loss rate curve as it is the part driven by the diffusion of the gases. Note that these parameters are in the same range of magnitude of the mass transfer coefficient used by Witkowski *et al.* [192] (8.10^{-9} m²/s), validating the approach and the values found in this study. This approach was also used by Statler *et al.* [201] for the modelling of an intumescent PC, but a value of $1.8.10^{-6}$ m²/s was however used.

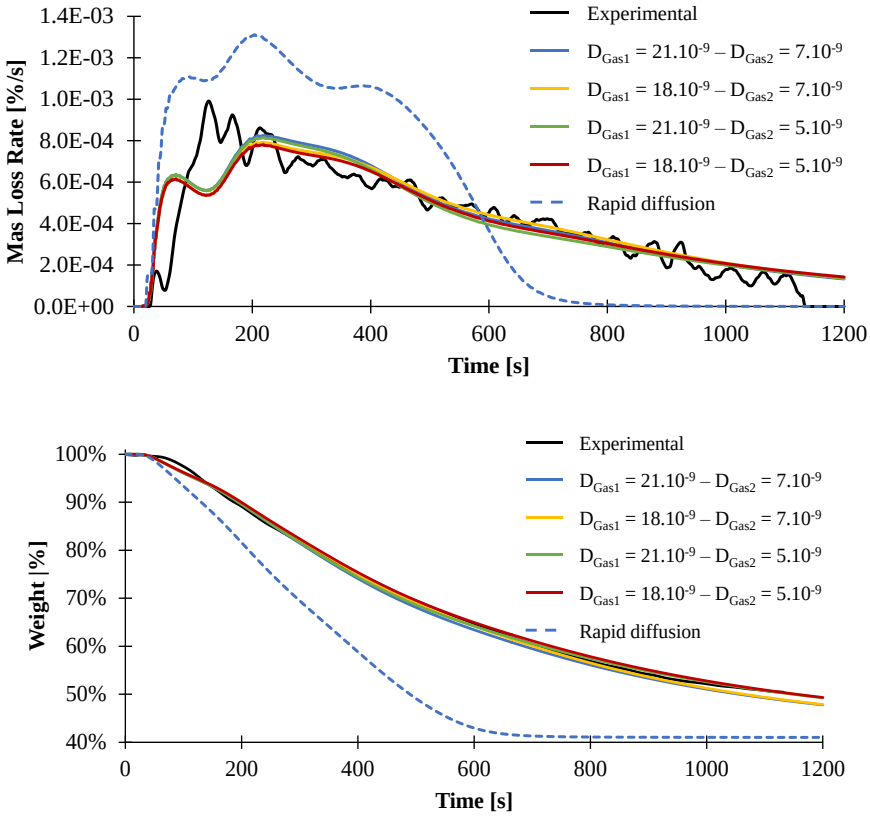

Figure 73: Experimental and predicted mass loss and mass loss rate curves for EVA/ATH assuming slow or rapid release of decomposition gases

A similar procedure was used for EVA/ATH/NC in order to fit the mass loss and MLR. It was found that using a mass transfer coefficient for Gas1 in the range $6\text{-}10.10^{-9}$ m²/s and a mass transfer coefficient for

Gas2 of 6.10^{-9} or 7.10^{-9} m²/s allow to obtain a good fit of the experimental data (**Figure 74**). According to the simulations, EVA/ATH/NC exhibits a higher barrier effect to the diffusion of gases as the mass transfer coefficient for Gas1 is lower. This is in agreement with the mode of action of NC which are known to act as gas barrier [63,205]. Interestingly, the mass transfer coefficient associated to the diffusion of Gas2 for both EVA/ATH formulations are similar.

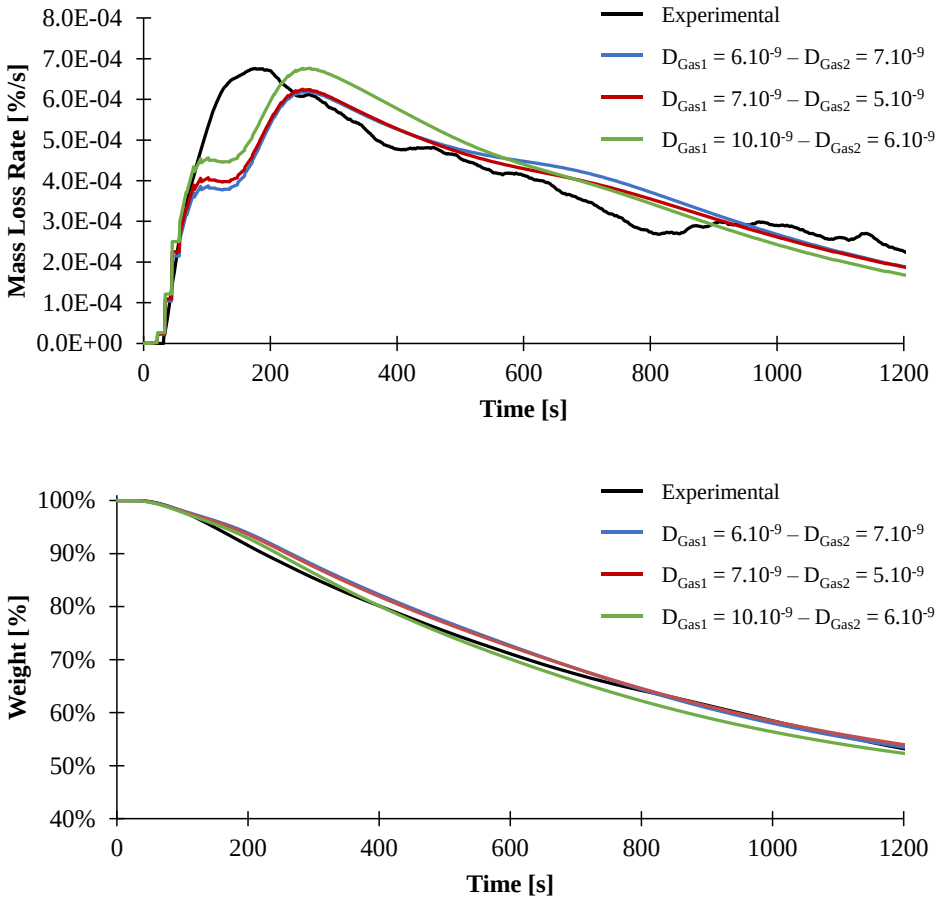

Figure 74: Experimental and predicted mass loss and mass loss rate curves for EVA/ATH/NC assuming slow or rapid release of decomposition gases

IV.2.1.b. Validation of the inputs data: temperature increase and FTIR quantification

As previously stated, all the input data were measured in **CHAPTER III**, at the exception of the mass transfer coefficients. In order to further validate these data, including D_{gas} values, the temperature profiles at the backside of the CAMLC plaques were predicted and compared with experimental data. Furthermore, it is possible to collect temporally resolved gas concentration profiles during CAMLC-

FTIR experiments. Two main gases are evolved: Gas1, which corresponds to approximately 90-95% of water, and Gas2, which corresponds to hydrocarbon compounds. The mass flux of both Gas1 and Gas2 were also simulated assuming either rapid diffusion using a mass transfer coefficient of 2.10^{-5} m²/s or assuming slow diffusion. For this latter, the mass transfer coefficients for Gas1 were fixed and will be considered equal to 21.10^{-9} m²/s and 10.10^{-9} m²/s for EVA/ATH and EVA/ATH/NC respectively and the mass transfer coefficients for Gas2 will be taken at 7.10^{-9} m²/s for the two formulations.

It can be seen in **Figure 75** that the temperature increase at the backside of EVA/ATH plaque is well predicted. Indeed, a reasonable agreement between the predicted and experimental data was obtained assuming both slow and rapid release of gases. Only the first six minutes of the experimental data are presented for EVA/ATH since after that time the thermocouple was not embedded in the polymer anymore.

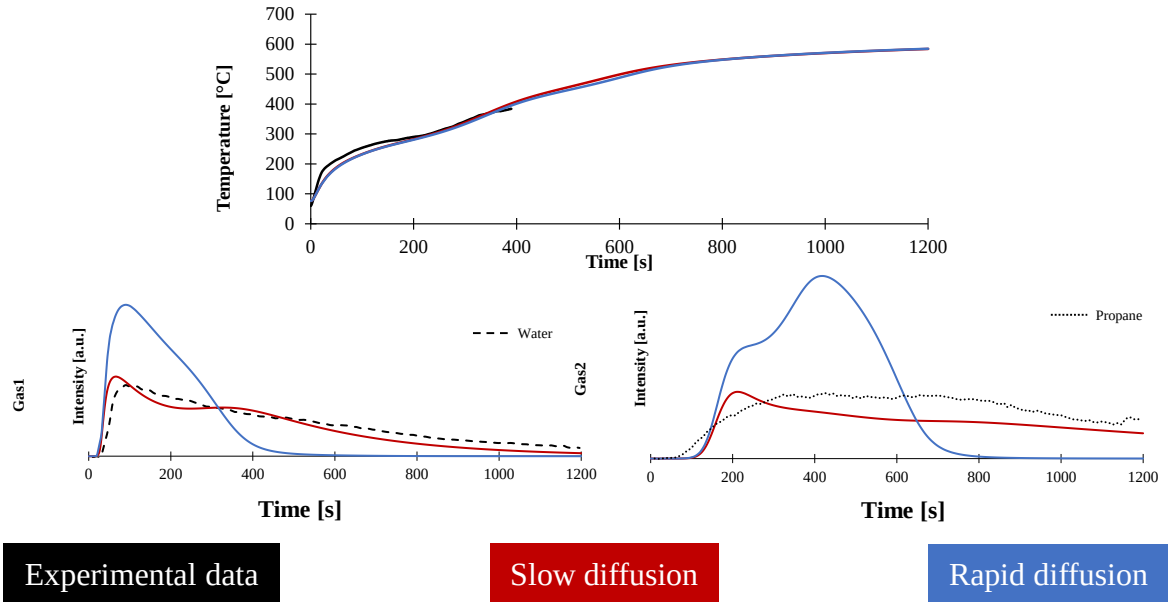

Figure 75: Experimental and predicted temperature increase at the backside of the cone plaque, release of water and propane assuming slow or rapid release of the gases for EVA/ATH

The predicted mass flux of Gas1 was compared to the release of water. Note that the predicted time to reach the peak of Gas1 release (66 s and 90 s considering rapid or slow release of gases respectively) is consistent with the experimental data (79 s). The difference between the experimental and predicted time to peak can be attributed to the acquisition time of the FTIR spectrum (one spectra consists of twenty

scans). Nonetheless, the prediction of the mass flux of Gas1 compared to the experimental data is poor assuming the rapid release of the gases. The prediction of the mass flux of Gas1 is good before 400 s experiments but also at longer exposure time. Similarly, the fit between the predicted mass flux of Gas2 and the hydrocarbon release is significantly increased considering the slow diffusion of the gases.

Similar simulations were performed with EVA/ATH/NC and compared to the experimental data. The results are presented in **Figure 76**. Note that only the first 600 s of the experimental data are presented for EVA/ATH/NC since similarly to the case of EVA/ATH, the thermocouples molded at the backside were not retained anymore after that time. The predicted temperature curve reasonably fits with the experimental curve in the time window where reliable temperature measurements were obtained.

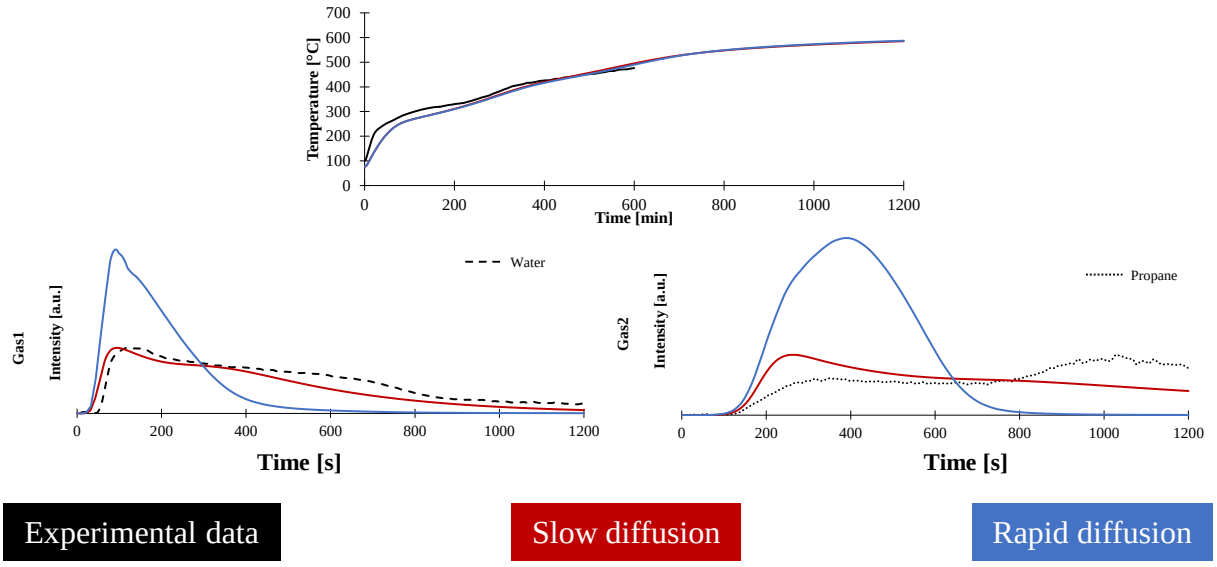

Figure 76: Experimental and predicted release of propane and water and temperature increase at the backside of the cone plaque assuming slow or rapid release of the gases for EVA/ATH/NC

A good prediction of release of water during all the duration of the experiments is moreover obtained. On the other hand, tuning the mass transfer coefficient for Gas2 to 7.10^{-9} m²/s permits to have a better fit with the experimental data. Nonetheless, EVA/ATH/NC exhibits an increase in its hydrocarbon release between 800 and 1200 s. This increase is not captured by the pyrolysis model. Indeed, this increase was previously attributed to the formation of cracks in the ceramic residue leading to an increase of the diffusion of the gases.

IV.2.2. IMPACT OF THE DEPENDENCE ON THE COMPOSITION OF THE INPUTS DATA

In the previous section, the inputs data determined in **CHAPTER III** were validated considering the temperature- and composition-dependent data. However, in **CHAPTER III**, we also investigated several ways to determine the main thermo-physical properties parameters of EVA/ATH composites and of their decomposition products. The objectives of this part are to determine how this will affect the model. Thus, the model was used considering:

(1) Direct measurements: k(T) and Cp(T)

(2) Composition- and temperature-dependent heat capacity and thermal conductivity ($\mathrm{Cp(T)} = \sum_i \omega_i(\mathrm{T}).\mathrm{Cp_i(T)}$ for example)

(3) Composition- dependent but with values determined at a fixed temperature ($\mathrm{Cp(T)} = \sum_i \omega_i(\mathrm{T}).\mathrm{Cp_i}(\mathrm{T_{constant}})$ for example)

The predicted mass loss rate assuming slow diffusion and thermal parameters as a function of composition and temperature or just as a function of temperature leads to similar results and are in good agreement with the experimental data as shown in **Figure 77**. However, the MLR curve considering temperature constant values is slightly different than the two curves considering temperature- dependent values. Indeed, the second peak of MLR exhibits a higher intensity when considering temperature constant inputs. This can be attributed to the fact that the simulated temperature considering this approach is higher until 580 s so a faster decomposition is predicted. Note also that the temperature after 600 s of experiments is lower in the case of temperature constant values. This can be attributed to the fact that value for thermal conductivity is taken at 0.12 W/m/K whereas the thermal conductivities of the residues are increasing with the temperature. Higher values are considered when a temperature-dependent approach is followed.

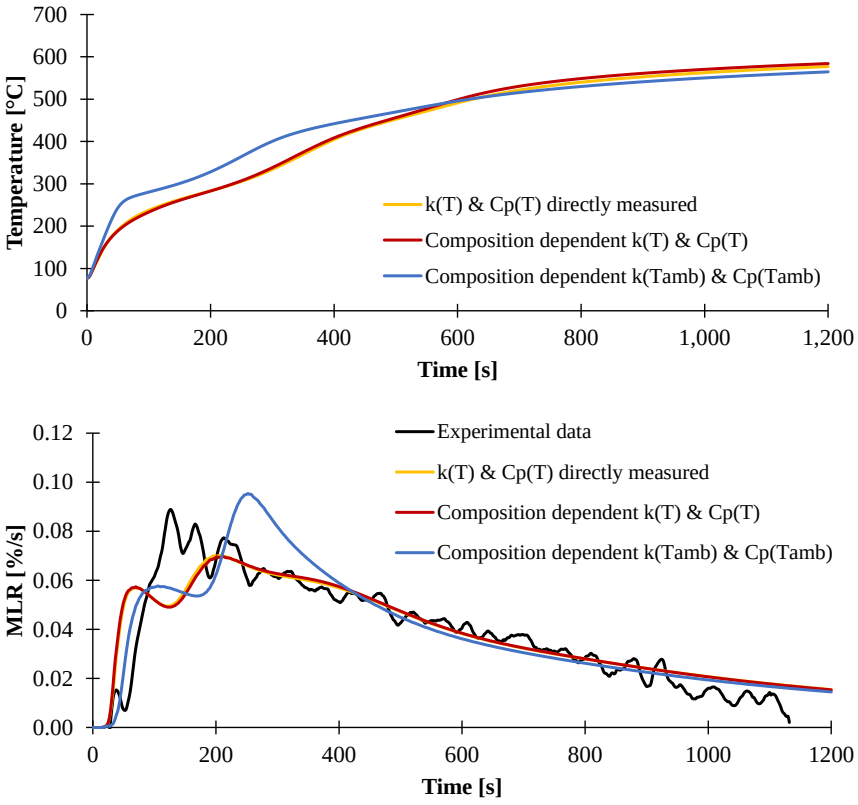

Figure 77: Predicted temperature and weight assuming slow diffusion and different implementation of the thermo-physical properties

This is confirmed by the averaged thermal conductivities and thermal diffusivities of the plaque for both temperature-dependent and temperature constant approaches as presented in **Figure 78.** It can be seen that for the two temperature-dependent inputs, both thermal conductivity and thermal diffusivity are in good agreement on the contrary of composition-dependent but temperature constant parameters. Taking into account the composition-dependent but temperature-constant thermal parameters leads to some differences in the thermal conductivity and thermal diffusivity profiles. The temperature at the backside of the plaque is higher due to a higher conductivity and higher diffusivity inside the plaque during the first 500 s compared to temperature-dependent thermal parameters.

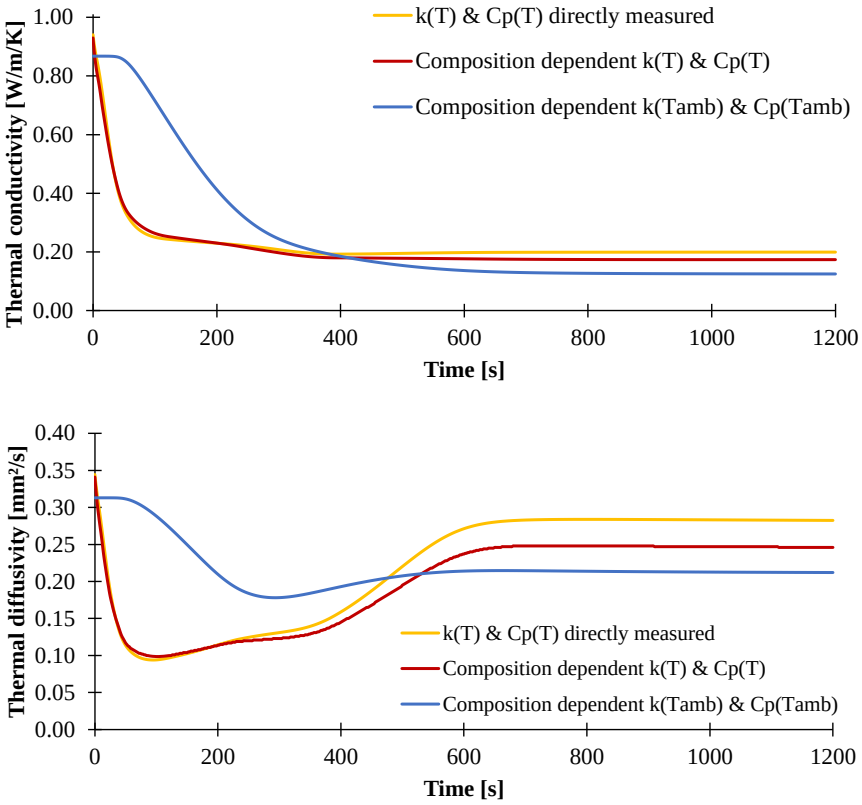

Figure 78: Averaged thermal conductivity and thermal diffusivity assuming slow diffusion and different implementation of the thermo-physical properties

These results demonstrate that the methods used to determine the thermo-physical properties of materials are of prime interest. As previously stated, the determination of the properties of a material at ambient temperature is the easiest approach, but it is not sufficient to predict well the decomposition of materials. On the contrary, these results also show that direct measurement seems to be as efficient as “stepped” methods, which are time-consuming.

IV.2.3. IMPACT OF THE KINETIC MODEL

As previously discussed, the inputs data can be implemented either with temperature-dependent or temperature constant value. The objective of this part is to investigate the effect of the use of a global kinetics model as inputs data instead of defining a reaction scheme.

In the case of composition-dependent inputs, the change from one specie to another is driven by the kinetics of decomposition. Composition-dependent inputs are considered as a linear combination of each species weighted by their content. As shown in the previous chapters, it is possible to describe the decomposition of the EVA/ATH formulations either with a two steps mechanism or using a global kinetic model. It was shown in **III.1.2.c** (p.106), that the latter allows a better prediction of the mass loss in TG experiments.

In the case of the global kinetics model, we have to define a conversion window where the properties of the intermediate species would be applied. Indeed, if the conversion degree is at zero, the properties would be the ones of the virgin materials. If the conversion degree is close to unity, the properties will be assigned to the residue. In the two steps model, the first reaction is assumed to be responsible to 0.424 of the total mass loss for EVA/ATH. The conversion range selected to associate the thermo-physical properties the intermediate specie is thus taken at ± 0.05 of this value (**Figure 79**). In the case of EVA/ATH, it was then determined that if the conversion degree is in the range 0.374-0.474, the properties would be the ones of the intermediate specie.

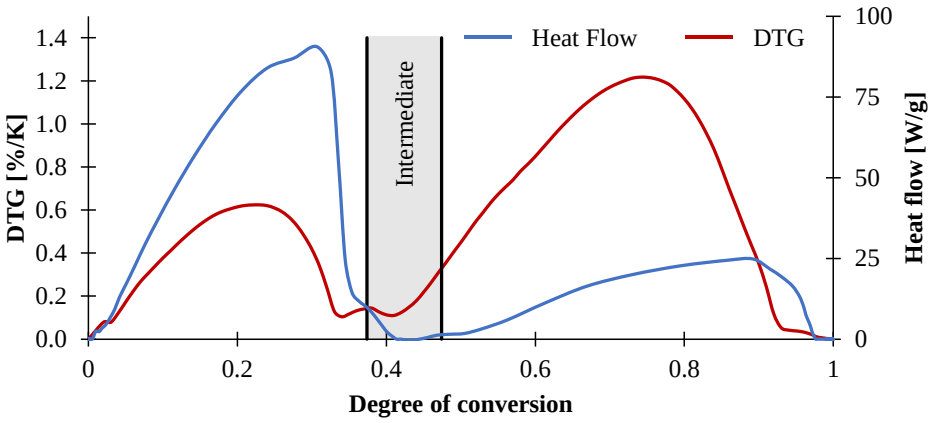

Figure 79: First derivative of the degree of conversion and heat flow signals as a function of conversion degree for EVA/ATH

A comparison of the predicted MLR using both global and two-steps model is shown in **Figure 80**. The predicted MLR curves assuming a slow diffusion of the released gases are very similar and are in reasonable agreement with the experimental data. It can be observed that the beginning of the decomposition is not impacted by the change of the implementation as the times for the MLR to begin are similar in both case.

However, in case of rapid diffusion of the gases the MLR profiles show some differences. Before 200 s of experiments, the predictions are similar but then the MLR predicted using the global model exhibits two distinct peaks (around 200 and 400 s).The predicted MLR using the two-steps model shows a single peak at 200 s and then the MLR decreases until 1200 s. However, these data do not fit the experimental data.

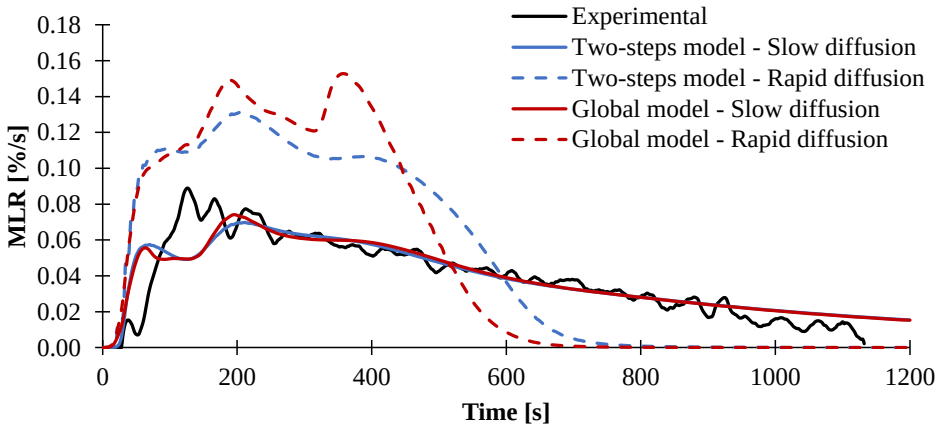

Figure 80: Prediction of the MLR using the two-steps model and the global model assuming either rapid and slow diffusion of the released gases.

The evolution of the temperature and heating rates at the backside of the plaque assuming either slow or rapid diffusion are presented in **Figure 81** for both two-step and global kinetic models. Except between 300 and 400 s, both temperature and heating ramps are similar for the two kinetic model.

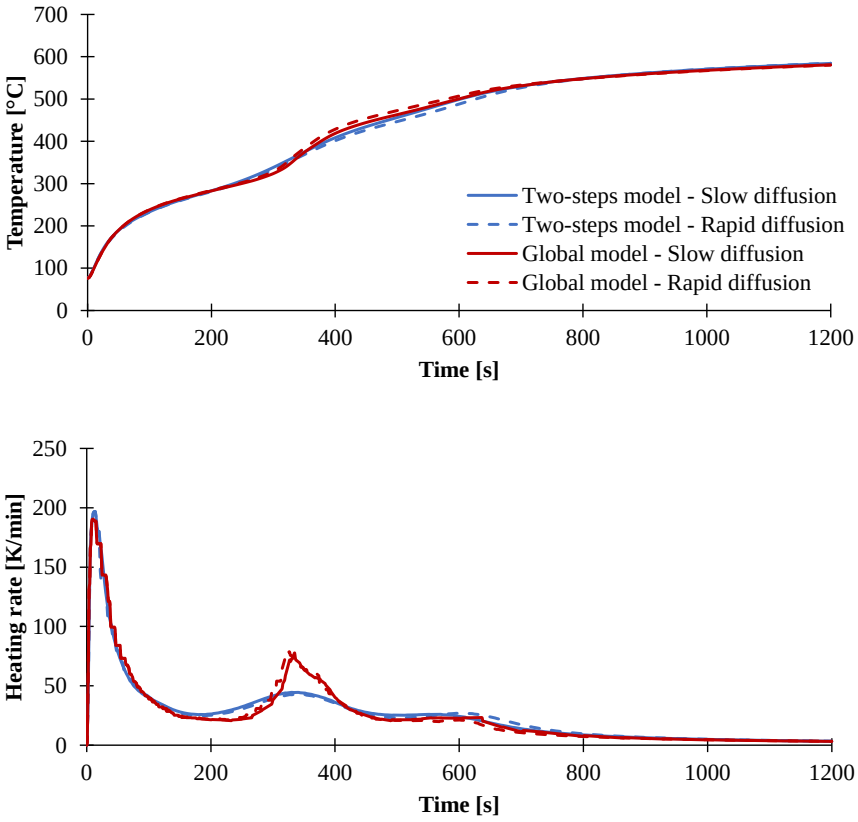

Figure 81: Predicted temperature increase (top) and heating profiles (bottom) at the backside of a cone plaque with a two-step model and a global kinetic model.

It was shown in this section that using a global kinetic model does not really improve the accuracy of the pyrolysis model. Indeed, the MLR and temperature profiles are similar using the global model or the two-step kinetic model. Even if the modelling of the MLR in TG experiments were improved by the global model as it allow to better fit the multiple peaks curves, its impact on the modelling of cone calorimetry experiments is low. This also validates the use of kinetic models (like the two-steps model) that describe the decomposition of materials in a general way, without solving true and elementary reactions such as deacetylation or dehydration of the ATH. The two steps kinetic model will then be used in the next sections of this chapter as it allows a good description of the decomposition of our material.

IV.2.4. IMPACT OF THE OPTICAL PROPERTIES

The approach used to determine the thermo-physical parameters as well as the implementation of the kinetics of decomposition were investigated in the last sections. On the other hand, considering the modelling of the gasification experiments, it is also possible to implement the incident heat flux (from a fire, a flame or from a cone heater) in at least three different ways:

- by setting the heat flux as a boundary heat flux.
- by considering the in-depth absorption of the heat flux with a Beer-Lambert law using a local/depth-dependent in-depth absorption coefficient.
- by considering the in-depth absorption of the heat flux with a Beer-Lambert law using a global in-depth absorption coefficient.

This part will investigate the effect of the different approaches used in the model. Indeed, setting the heat flux as a boundary condition does not consider the in-depth absorption of the heat and can influence the temperature distribution inside the material and thus the MLR and HRR profiles but it requires less parameters (the in-depth absorption coefficients) to be characterized.

The results obtained in the prediction of the MLR profiles following the three previously described approaches are presented in **Figure 82**. It can be seen that assuming both rapid and slow diffusion of the gases, considering local or global in-depth absorption coefficient does not impact the MLR profile. On the opposite, setting the incident heat flux in the boundary conditions slows down the releases of the gases. Indeed, considering either slow or rapid diffusion of the gases, the peak of MLR exhibits a lower intensity compared to in-depth absorption conditions. In case of rapid diffusion of the gases, the time for the steady state (no more mass lost) to be achieved is around 100 s higher with the boundary conditions implementation.

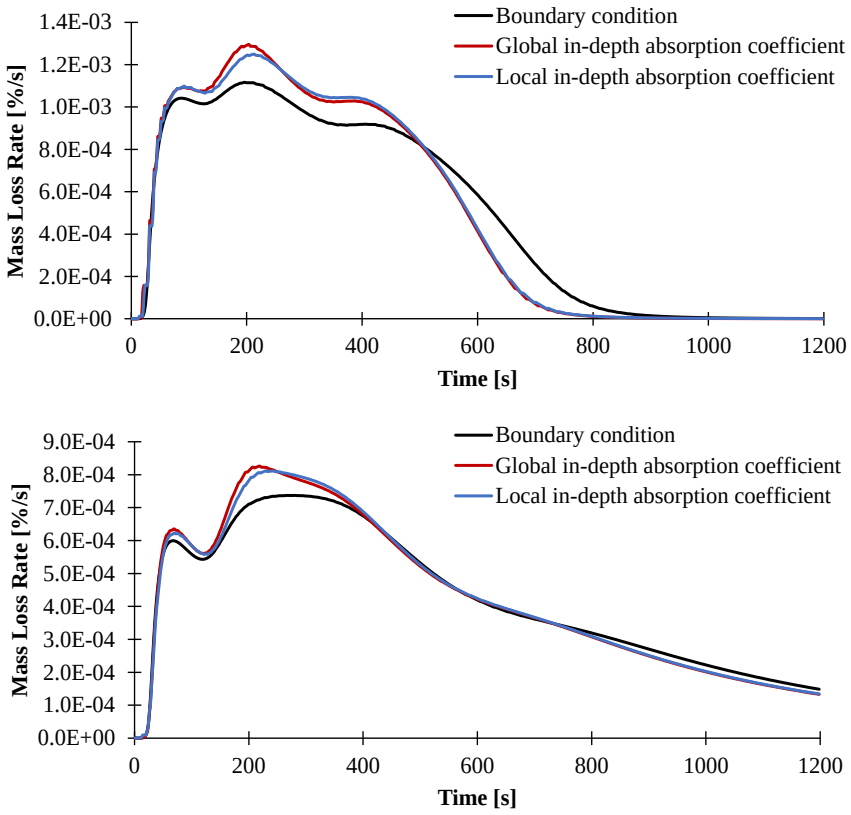

Figure 82: Comparison of the MLR profiles in case of rapid (top) or slow (bottom) diffusion of the gases with different implement of the incident heat flux

The higher rate of decomposition in case of in-depth absorption of the incident heat can be attributed to the fact that more heat is absorbed in the material considering the in-depth absorption. The prediction of the temperature using both local or global in-depth absorption coefficient are almost identical (less than 2 °C difference) at both the front and the bottom of the cone plaque as presented in **Figure 83**. On the opposite, it can be seen that some differences can be observed in the temperature profiles predicted using the boundary condition. Indeed, after 300 s, the predicted temperature when the incident heat flux is implemented as a boundary condition is lower of around 30 °C until the end of the experiment.

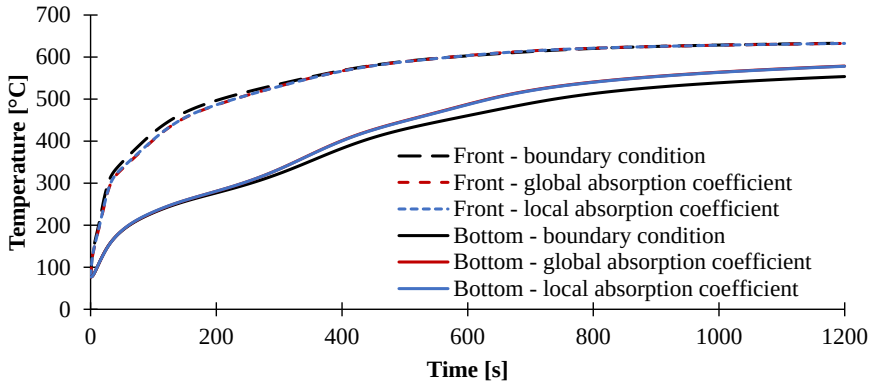

5

Figure 83: Predicted temperature at the front (dotted lines) and the rear face (straight lines) of a cone plaque

As the predicted temperatures using in-depth absorption are very similar, it was decided to plot the difference between predicted temperature when the incident heat flux is implemented as a boundary condition and considering either local or global in-depth absorption. The results are presented in **Figure 84** for the front, the bottom and at 0.5 mm of the front of the cone plaque. It can be seen that before 400 s, the predicted temperature using the boundary condition is up to 20 °C higher than in case of in-depth absorption. After this time, the predicted temperatures at the front of the cone plaque are similar. On the opposite, at both 0.5 mm from the front and at the rear face of the plaque, the temperature difference steadily decreases until reaching around 30 °C difference after 400 s until the end of the experiments.

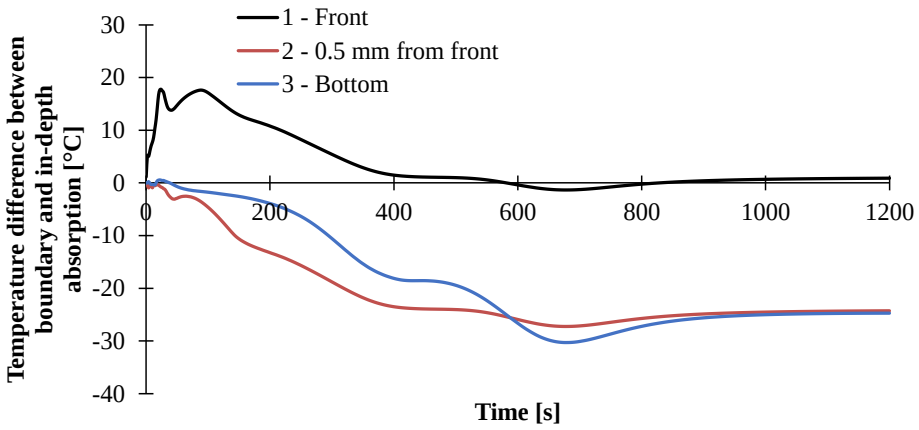

Figure 84: Temperature difference at the front, the bottom and 0.5 mm inside the plaque in between boundary and in-depth absorption implementation

Using in-depth absorption of the incident heat flux promotes the absorption of heat inside the material as more heat will be absorbed in the first 200 µm of the material (the skin depth of the material) compared to boundary implementation. At the beginning of the experiment, the thermal conductivity of the EVA materials is high. The combination of these two effect leads to a decrease of the surface temperature as the heat is not accumulated at the surface of the plaque but is absorbed or conducted inside the material. Similarly, as more heat is absorbed, the temperature at 0.5 mm of the plaque surface or at the rear face of the plaque is higher considering in-depth absorption of the incident heat. After 400 s, most of the ATH has decomposed and the thermal conductivity of the material as decreased (see **Figure 78** p.152) leading to an insulative layer. Even if the heat is absorbed inside the material, the surface temperatures in both absorption or surface mode are similar. This can be attributed to the fact the temperatures are almost similar in the first millimeter of the plaque after 400 s of experiments as presented in **Figure 85**. Note that the temperature is higher at 0.5 mm of the surface than at the surface if the heat is supposed to be absorbed inside the material.

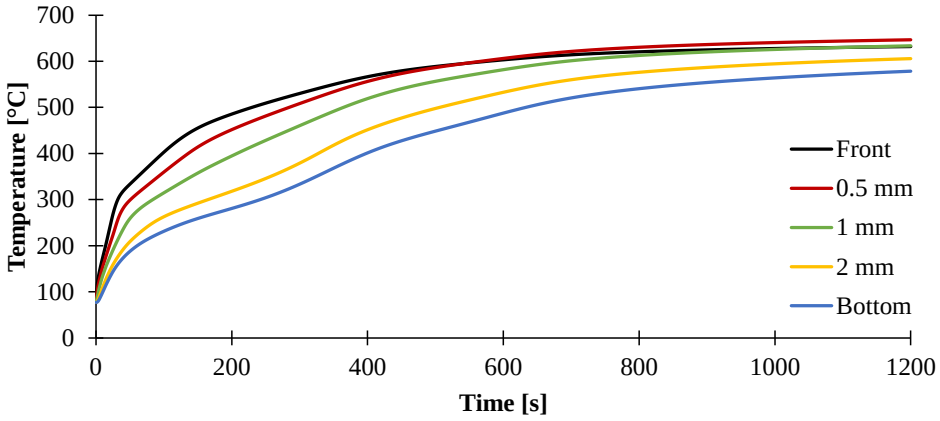

Figure 85: Predicted temperature using global in-depth absorption coefficient at the front and bottom of the plaque and at 0.5, 1 and 2 mm of the surface

It was shown in this section that considering the in-depth absorption of the heat inside the material compared to the implementation of the incident heat flux as a boundary condition exhibit some differences in the MLR and temperature profiles. Indeed, assuming that the heat absorbs inside the material, leads to a higher temperature inside the material and at the backside of the plaque and thus to a higher MLR. This effect is less observed in the case of the slow diffusion of the gases, as it is the diffusion and not the decomposition of the materials that governs the MLR at long exposure time. Note also that

considering a global or a local in-depth absorption coefficient does not have a real impact on both MLR and temperature profiles. In the following sections of this chapter, the incident heat flux will thus be implemented using a global in-depth absorption coefficient. Indeed, its characterization is easier than the local in-depth absorption coefficient but still represents the absorption of the incident heat flux inside the material. The absorption of heat inside the materials will thus be considered in the pyrolysis model, as it is more realistic than to implement the incident heat flux as a boundary condition.

IV.2.5. CONCLUSION ABOUT THE MODELLING OF THE GASIFICATION

In this section of the chapter, the inputs data determined in **CHAPTER III** were used to model the gasification of EVA/ATH materials. It was found that the rapid diffusion of the decomposition gases inside the materials does not allow to predict the MLR. Moreover, it was not representative of the mode of action of ATH and NC, as for example the latter is known to exhibit a barrier effect to the diffusion of gases. Ranges of mass transfer coefficient that describe well both MLR, temperature and gas release profiles were found. More precisely, for Gas1 (as defined in **Figure 50** p.101) D_{gas} values can range between 18.10^{-9} and 21.10^{-9} m²/s for EVA/ATH and between 6 and 10 m²/s for EVA/ATH/NC. For Gas2 representing the hydrocarbons compounds, both EVA/ATH materials exhibit a mass transfer coefficient between 6.10^{-9} and 7.10^{-9} m²/s. Using these parameters, it was possible to model the MLR in a gasification experiments and to validate the inputs data as the temperature at the rear face of the plaque and MLR profiles were well predicted.

Furthermore, different methods to determine the thermo-physical properties, the kinetics of decomposition of the material and the optical properties were studied and the effect of the methods used in the model was discussed. It was shown that the use of temperature-dependent parameters gives similar MLR and temperature profiles than using composition and temperature-dependent properties. On the opposite, the use of only composition-dependent (determined at a fixed temperature) changes the temperature distribution but also the MLR profiles. It was also demonstrated that even if the prediction of TGA results were improved by using a global kinetic model (without defining a reaction scheme), the prediction of the MLR and temperature profiles in gasification experiments were not significantly improved. Finally, it was concluded that it is important to consider the in-depth absorption of the incident heat flux even if using local (or depth-dependent) coefficients, which are more representative of physics of the phenomena, gives the same results than using a single global in-depth absorption coefficient. On the opposite, considering that the heat only absorbs at the surface slows the temperature increase and thus the MLR.

IV.3. APPLICATION TO MASS LOSS CONE CALORIMETER

To model gasification experiments is of prime interest to validate the inputs parameters. However, the modelling of the behavior of materials in flaming conditions is required. In the next part of this chapter, the pyrolysis model will be used to model the MLR and HRR behavior of EVA/ATH materials in standard flaming mass loss cone. In the following section, the model will consider temperature- and composition-dependent thermo-physical properties, the two-steps kinetic model and a global in-depth absorption coefficient. Two additional parameters have to be estimated in order to describe the flaming conditions in cone calorimeter: an additional heat flux from the flame and a critical mass flow for ignition.

IV.3.1. IMPLEMENTATION OF THE FLAMING IN THE MODEL

There are several ways to implement the flaming of a material in the cone calorimeter. Some authors changed the conditions of radiative or convective cooling, adding an additional heat flux from the flame or used a flame temperature. Other authors investigated the flame temperature or the radiative fraction of a flame [206–211] as the convective and radiative transfer from the flame could be modelled. Information about the part of radiation and convection and how the flame heat backs the materials surface are necessary but difficult to be characterized. In this study, it was decided to use the critical mass flux for ignition (CMF) and additional heat flux from the flame criteria ($\dot{q}''_{flame}$ as in **Eq. 82** and **Eq. 84**) in order to describe the flaming conditions in the mass loss calorimeter. Some values can be found in the literature for these parameters.

In this section, CMF values of 1 and 2 g/m²/s will be investigated as there are close to the values determined by Staggs for PE/ATH [79]. Note that for all kind of materials, CMF values usually range between 0.5 and 6 g/m²/s [79,212–217]. $\dot{q}''_{flame}$ values will be taken at 10 or 20 kW/m² as they are representative of the values generally found un pyrolysis studies [3,4]. Moreover, in some case (ThermaKin for example [4]), the convective cooling is turned off when the MLR is higher than the CMF value so when the material ignites.

IV.3.1.a. Impact of CMF and $\dot{q}''_{flame}$ on n the prediction of MLR

It can be seen that the MLR is well predicted using the assumption of slow diffusion of the gases as for the modelling of the gasification of the gases (**Figure 86**). Nonetheless, turning off the convective cooling when the flame appears (*i.e.* when the MLR gets higher than the CMF value) leads to an increase in the peaks of MLR (pMLR) value and to a decrease of the time to reach the pMLR (t_{pMLR}). A similar effect is observed by increasing the additional heat flux from 10 kW/m² to 20 kW/m².

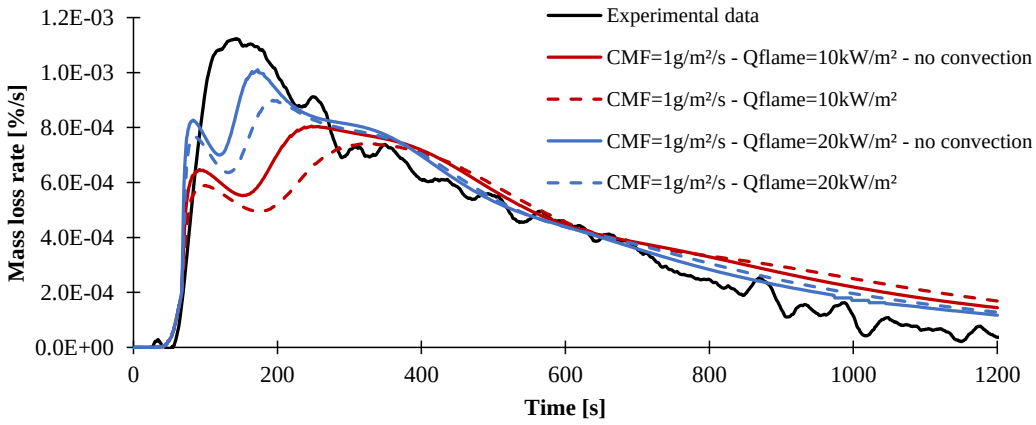

Figure 86: Experimental and predicted MLR assuming a CMF of 1 g/m²/s and a $\dot{q}''_{flame}$ of 10 or 20 kW/m² with and without turning off the convection during burning

A comparison of the predicted MLR curves assuming different CMF values is presented in **Figure 87** for an additional heat flux from the flame of 20 kW/m². This latter value was selected as it shows a better fit (in terms of t_{pMLR} and pMLR values) than when using a value of 10 kW/m². The impact of the CMF values on the MLR profiles is lower than the one of $\dot{q}''_{flame}$. Either with or without turning off the convection, changing the CMF value shifts the t_{pMLR} towards higher time. This shift is around 13 to 18 s depending on the conditions.

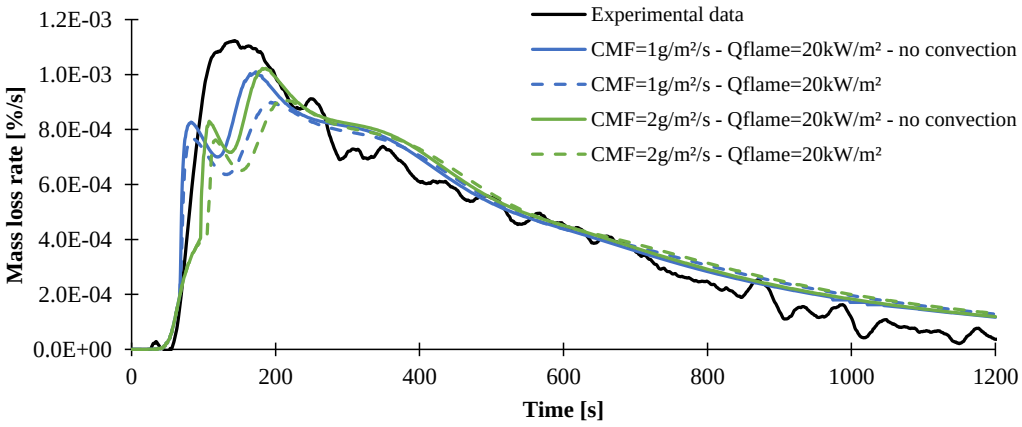

Figure 87: Experimental and predicted MLR ² assuming a CMF of 1 or 2 g/m²/s with a $\dot{q}''_{flame}$ of 20 kW/m² with and without turning off the convection during burning

IV.3.1.b. Impact of CMF and $\dot{q}''_{flame}$ on the prediction of temperature

Changing CMF and $\dot{q}''_{flame}$ values will impact the temperature distribution in the material. The experimental and predicted temperatures at the backside of a 3 mm cone plaque for EVA/ATH under 35 kW/m² irradiance are presented in **Figure 88**.

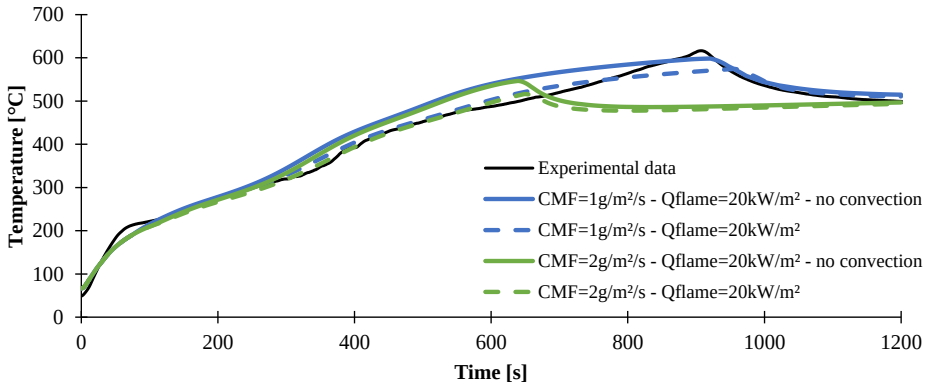

Figure 88: Experimental and predicted temperature increase at the backside of the plaque assuming a CMF of 1 or 2 g/m²/s with a $\dot{q}''_{flame}$ of 20 kW/m² with and without turning off the convection during burning

It can be seen in the experimental data that the temperatures increase sharply in the first 100 s to reach a temperature of around 200 °C. Then, the temperature increases smoothly from 100 s until flameout

(around 930 s) when it reaches its maximum at 616 °C. Then after flameout, the temperature decreases and stabilizes until the end of the experiment at around 500 °C at 1200 s. Either using a CMF of 1 and 2 g/m²/s, this decrease is well modelled when the flame extinguishes as well as the final temperature.

IV.3.1.c. Impact of CMF and $\dot{q}''_{flame}$ on the prediction of ignition and flameout

The predicted and experimental time to ignition (TTI), time to flameout (TTF) and t_{pMLR} are presented in **Table 19** for the two defined value if CMF and of $\dot{q}''_{flame}$. Using a critical mass flux for ignition of 1 g/m²/s leads to predict a time to ignition of 68 s whatever the conditions (tuning of the convection or $\dot{q}''_{flame}$). Using a CMF of 2 g/m²/s and a $\dot{q}''_{flame}$ of 10 kW/m² leads to a predicted TTI of around 98 s when it is predicted at around 106 s if $\dot{q}''_{flame}$ is taken at 20 kW/m². The prediction of the TTI seems to be improved by the use of high CMF values. Nonetheless, using a high critical mass flux for ignition leads to a bad prediction of the TTF. Indeed, using this assumption, the TTF ranges between 648 and 655 s when the experimental TTF is 831 s.

Table 19: Experimental and predicted time to ignition, time to pMLR and time to flameout assuming various flaming conditions for 3 mm thick EVA/ATH under 35 kW/m² irradiance

CMF [g/m²/s]	$\dot{q}''_{flame}$ [kW/m²]	Convection	TTI [s]	t_{pMLR} [s]	TTF [s]
Experimental data			90	143	831
1	**10**	**Turned off**	68	248	1029
1	**10**	**No changes**	68	320	1100
1	**20**	**Turned off**	68	173	936
1	**20**	**No changes**	68	194	976
2	**10**	**Turned off**	98	261	653
2	**10**	**No changes**	104	335	652
2	**20**	**Turned off**	97	187	648
2	**20**	**No changes**	106	212	655

IV.3.2. DETERMINATION OF THE OPTIMUM CRITICAL MASS FLUX FOR IGNITION

It was shown in the previous section part that the different parameters describing the ignition impact the mass loss and temperature profiles. Based on EVA/ATH results, it was decided to use an additional heat flux from the flame $\dot{q}''_{flame}$ of 20 kW/m² and to keep the convection term in **Eq. 84**.

In order to model the fire behavior of the EVA/ATH formulations in a standard flaming mass loss calorimeter, parametric studies were performed to fit the experimental data. The critical mass flux for ignition was then tuned so the times to flameout (TTF) are well predicted. The results obtained for EVA/ATH with a thickness of 1 and 3 mm at 35 and 50 kW/m² heat flux are shown in **Figure 89**. The data are taken with 5 % standard deviation that corresponds to the experimental uncertainties obtained with the EVA/ATH formulations. It can be seen that the CMF plays an important role in the prediction of the TTF. Indeed, a 3 mm thick plaque under 35 kW/m² can show a TTF of 684 up to 934 s with CMF values of 1.9 and 0.7 g/m²/s respectively. It can be noted that using a single heat flux or a single thickness cannot help for the determination of a parameter describing several conditions. Indeed, CMF values between 1.9 and 0.9 g/m²/s can be acceptable considering 1 mm thick under 35 kW/m². With a 3 mm thick plaque and the same irradiance, acceptable CMF values would be 0.9-1.6 g/m²/s.

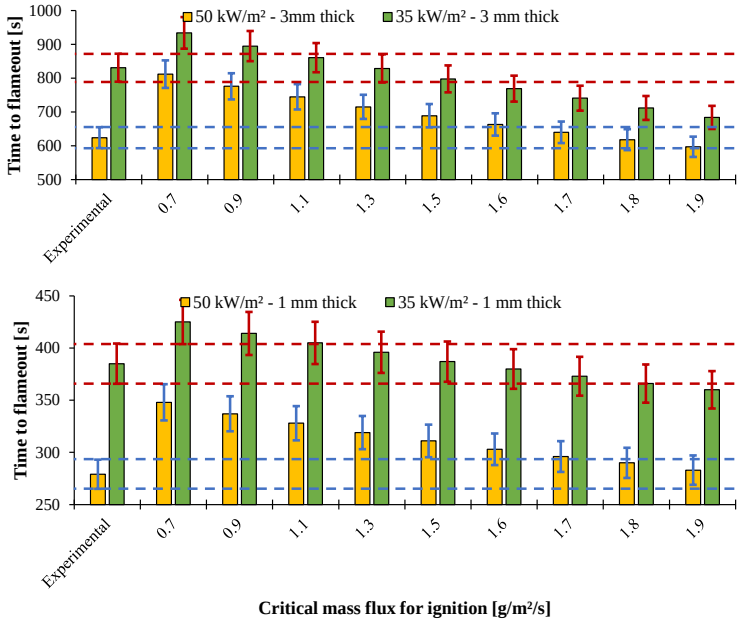

Figure 89: Experimental and predicted time to flameout with CMF between 0.7 and 1.9 g/m²/s for 1 and 3 mm thick EVA/ATH under 35 (top) and 50 kW/m² (bottom) irradiance

The range of CMF values that would predict the time to flameout of EVA/ATH under various conditions are presented in **Figure 90**. Under 35 kW/m², the acceptable critical mass flux for ignition range starts at 0.7 g/m²/s while it is 1.5-1.6 g/m²/s under 50 kW/m² irradiance. As a consequence, it can be concluded that with a CMF value of 1.6 g/m²/s, the flameout of 1 and 3 mm plaque of EVA/ATH under 35 and 50 kW/m² irradiance are predicted within 5 % of standard deviation.

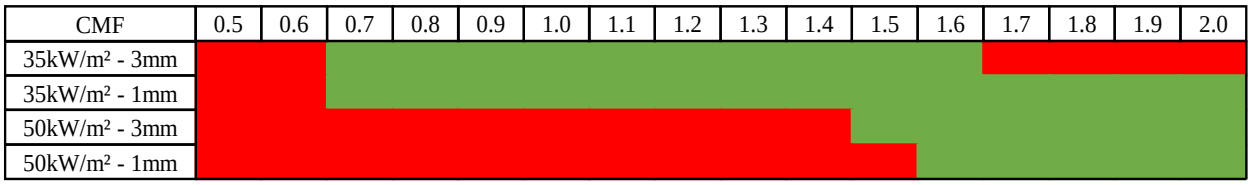

Figure 90: Acceptable CMF (green) ranges for 1 and 3 mm thick EVA/ATH under 35 and 50 kW/m² in terms of TTF prediction

The optimum CMF value for EVA/ATH/NC was obtained using the same approach. The predicted and experimental TTF are presented in **Figure 91**.

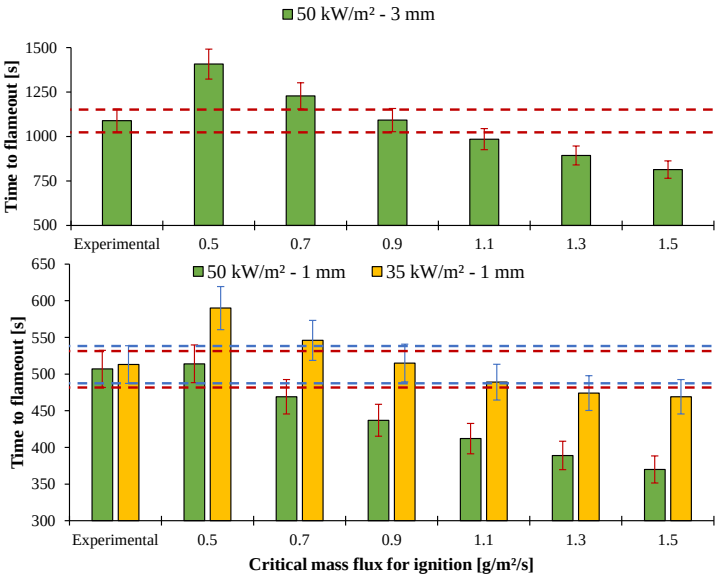

Figure 91: Experimental and predicted time to flameout with CMF between 0.5 and 1.5 g/m²/s for 1 (bottom) and 3 mm (top) thick EVA/ATH/NC under 35 and 50 kW/m²

Note that the data are not presented for 3 mm thick plaque under 35 kW/m². Indeed, the predicted TTF is always higher than 1000 s when the experimental TTF is 396 s. The other results are presented with 5 % standard deviation. The TTF of 1 mm thick EVA/ATH/NC under 35 and 50 kW/m² can be predicted using CMF values between 0.5 and 0.7 g/m²/s.

Finally, **Figure 92** presents the CMF range that can predict the TTF of 1 and 3 mm thick EVA/ATH/NC under 35 and 50 kW/m². It can be seen that only a critical mass flux for ignition of 0.7 g/m²/s can predict the flameout in all conditions at the exception of the 3 mm plaque under 35 kW/m² irradiance with 5 % standard deviation.

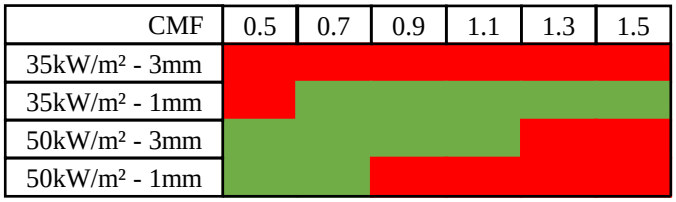

Figure 92: Acceptable CMF ranges (green) for 1 and 3 mm thick EVA/ATH/NC under 35 and 50 kW/m² in terms of TTF prediction

IV.3.3. VALIDATION OF THE CRITICAL MASS FLUX FOR IGNITION

In the previous section, the critical mass fluxes required for sustained ignition were estimated using parametric studies. It was found that the flameout of EVA/ATH could be predicted using a CMF value of 1.6 g/m²/s while it was found at 0.7 g/m²/s for EVA/ATH/NC. In order to validate these values, the experimental HRR and MLR were plotted for EVA/ATH in **Figure 93**. Indications about the time to ignition (TTI) and time to flameout (TTF) are also shown as well as indications about the experimental MLR at these characteristic times. It can be seen that the experimental mass flux when flameout occurs is between 1 and 2 g/m²/s. At the opposite, the mass flux when ignition occurs is between 4 and 8 g/m²/s. The difference is due to the fact that ATH decomposes and that water is released before ignition. This was already reported by Hoffendahl *et al.* [38,218] et Ngohang *et al.* [116] when studying the decomposition for EVA/ATH by MLC coupled FTIR.

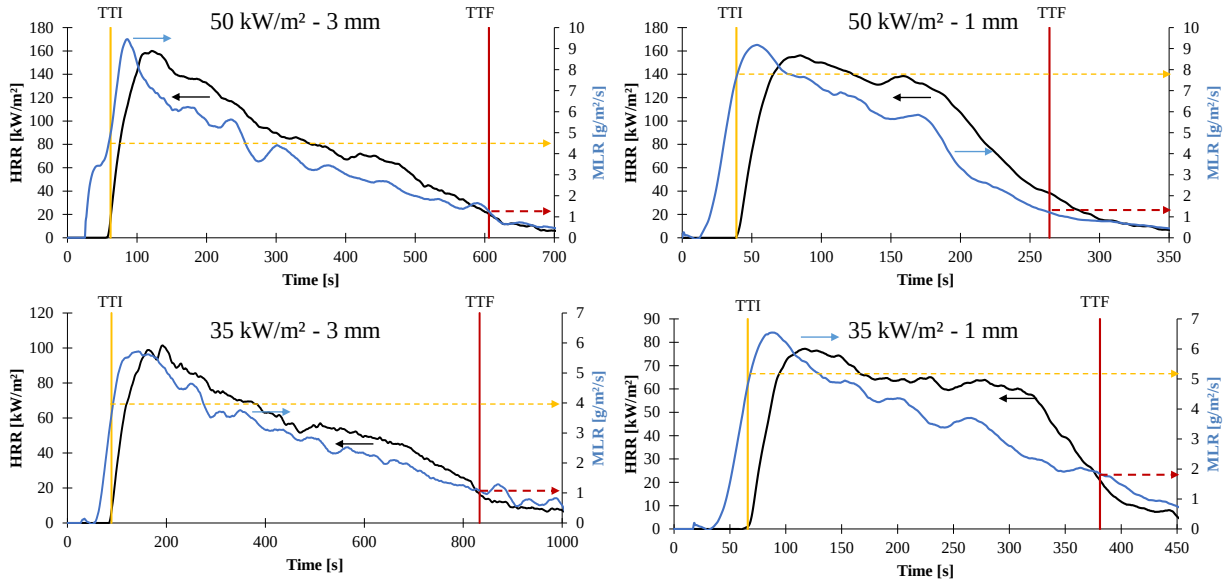

Figure 93: Experimental HRR and MLR of 1 and 3 mm thick EVA/ATH under 35 and 50 kW/m²

The plot of experimental HRR and MLR for EVA/ATH/NC is presented in **Figure 94**. The ignition occurs when the MLR is higher than 4 to 6 g/m²/s. Note that the mas loss before ignition is higher in case EVA/ATH/NC compared to EVA/ATH. The flameout of EVA/ATH/NC occurs when the MLR is lower than 0.1-3 g/m²/s depending on the experimental conditions. For 3 mm thick samples of EVA/ATH/NC under 35 kW/m², the flameout occurs after 396 s and when the MLR is lower than 2.3 g/m²/s. On the

opposite, at 1 mm and 50 kW/m² irradiance, the flameout occurs when almost no gases are evolving from the material, as the observed MLR at flameout is 0.1 g/m²/s.

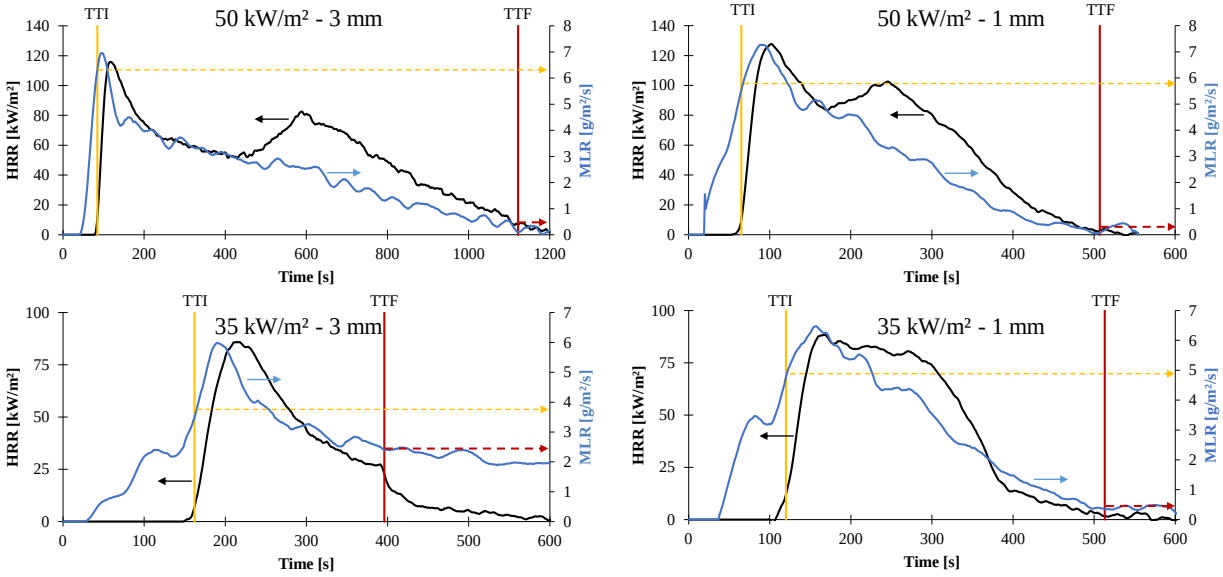

Figure 94: Experimental HRR and MLR of 1 and 3 mm thick EVA/ATH/NC under 35 and 50 kW/m²

A comparison of the experimentally and numerically determined CMF values is presented in **Table 20**. The results were averaged with all the considered thickness and irradiance for EVA/ATH (the data at 3 mm and 35 kW/m² were not considered for EVA/ATH/NC). Note the good agreement between the experimental data and the value determined by fitting the flameout of the materials.

Table 20: Experimental and numerically predicted CMF values for EVA/ATH formulations

Formulation	Experimental CMF	CMF from parametric analysis
EVA/ATH	1.4 ± 0.3 g/m²/s	1.6 g/m²/s
EVA/ATH/NC	0.6 ± 0.2 g/m²/s	0.7 gm²/s

IV.3.4. MODELLING THE MASS LOSS RATE IN FLAMING CONDITIONS

Using the inputs determined in **CHAPTER III** and the conditions describing the flaming, mass loss calorimeter experiments were modelled. **Figure 95** presents the experimental and predicted mass loss and mass loss rate results for 1 and 3 mm thick plaque of EVA/ATH under 35 kW/m². The temperature at the backside of the 3 mm plaque is also presented. It can be noted that the intensity of the peak of MLR for the 1 mm plaque is well predicted as well as the final mass loss. Nonetheless, the fit of the mass loss during the first 200 s is poor as well as the predicted time to pMLR, which is shifted of around 100 s towards longer time. The mass loss of the 3 mm thick plaque is also well predicted. Indeed, the beginning of the MLR curve fits the experimental MLR curve. At the exception of the intensity of the pMLR, the MLR is well predicted. Note the excellent agreement on the measured and predicted temperature at the backside of the plaque. The relative higher temperature after 800 s obtained on the simulations is due to the fact that the presented experimental data corresponds to an experiment where the flameout was higher than the predicted one.

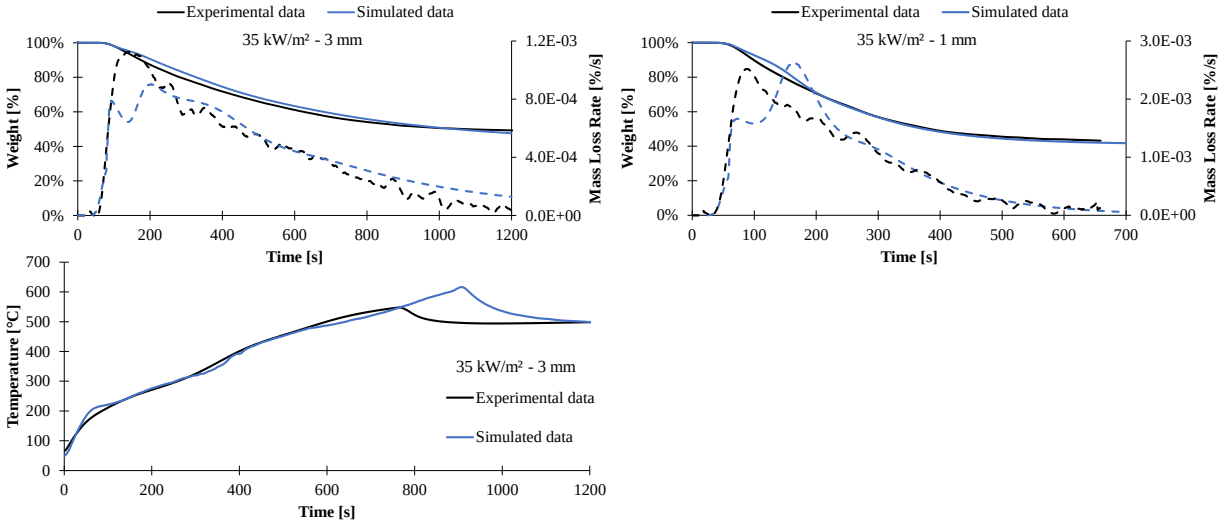

Figure 95: Experimental and predicted mass loss and mass loss rate and backside temperature of 1 (right) and 3 mm (left) EVA/ATH under 35 kW/m² irradiance

The results for EVA/ATH under 50 kW/m² irradiance are presented in **Figure 96**. Note that the temperature measurements were not reliable for these conditions as the thermocouples unglued from the plaque and the results will thus not be presented. As for 35 kW/m², the pMLR for 1 mm thick sample is shifted towards longer times. For both 1 and 3 mm thick plaques, the final mass losses are well predicted

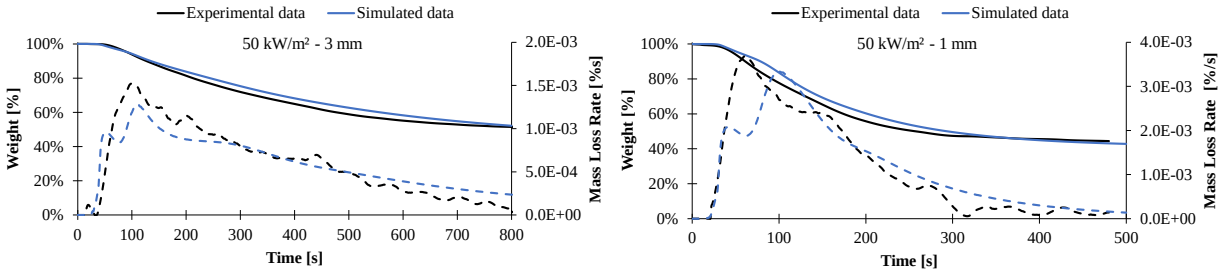

Figure 96: Experimental and predicted mass loss and mass loss rate and backside temperature of 1 (right) and 3 mm (left) EVA/ATH under 50 kW/m² irradiance

The results obtained with EVA/ATH/NC under 35 kW/m² irradiance are presented in **Figure 97**. Note that the temperature was measured at the backside of the 3 mm thick plaque for around 500 s. After this time, the K-type thermocouple molded at the backside of the plaque unglued and the measurements were not reliable. The prediction for the 1 mm thick plaque is excellent. At the exception of the intensity of the pMLR, the final mass loss, MLR between 300 and 1000 s and temperature between 0 and 500 s were well predicted. The prediction in the case of the 3 mm thick plaque is poorer but still acceptable.

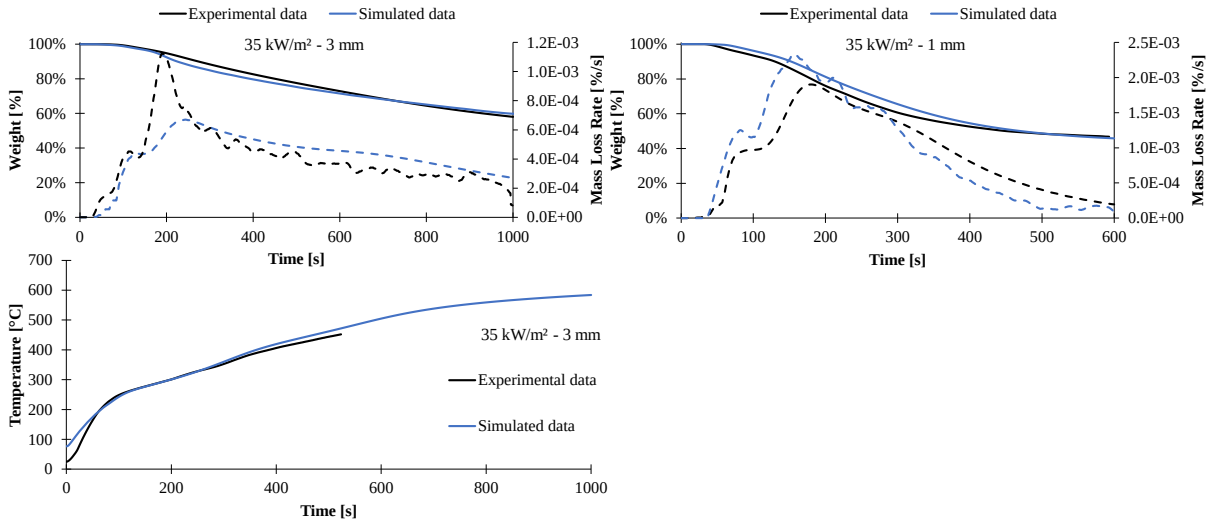

Figure 97: Experimental and predicted mass loss and mass loss rate and backside temperature of 1 (right) and 3 mm (left) EVA/ATH/NC under 35 kW/m² irradiance

The results obtained for EVA/ATH/NC under 50 kW/m² are presented in **Figure 98**. The prediction for the 3 mm thick plaque is excellent. The prediction of the MLR fits the experimental data at the exception of the intensity of pMLR. As the pMLR value is under-predicted, a difference of 4 % between the prediction of the 1 mm thick plaque is poorer but acceptable. Indeed, the shape of the MLR is well predicted but shifted of around 40 s toward longer times.

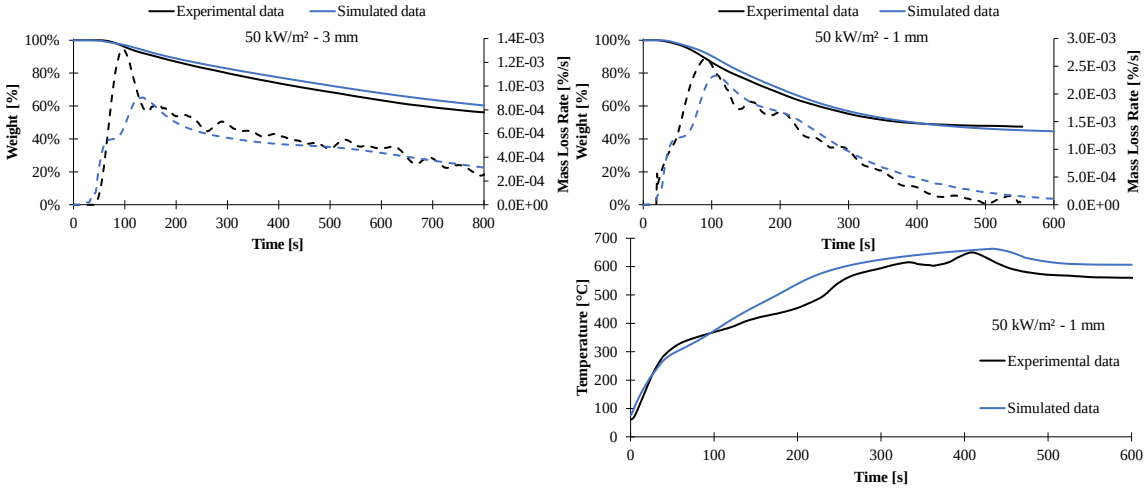

Figure 98: Experimental and predicted mass loss and mass loss rate and backside temperature of 1 (right) and 3 mm (left) EVA/ATH/NC under 50 kW/m² irradiance

It was shown in this section that it was possible to predict the mass loss and temperature profiles of EVA/ATH formulations in various conditions with a reasonable agreement. Indeed, a good agreement was found between the experimental and the simulated data for the two formulations and for 1 or 3 mm thick samples under 35 or 50 kW/m². This validates all the parameters determined or estimated in the previous chapters. The purpose of the next part of this chapter is to investigate the modelling of the heat release rate.

IV.3.5. MODELLING THE HEAT RELEASE RATE

IV.3.5.a. Characterization of the effective heats of combustion

It is possible to express the heat released by a material as the yield of the mass loss rate to its effective heat of combustion (EHC) determined in calorimetry experiments (**Eq. 87**). Another approach to determine the HRR in pyrolysis model could be to use the effective heat of combustion determined in MCC [219] and the mass flux J_g of each gases (***Eq. 88***). Both features are used on pyrolysis models [3,5,81,83,84].

$$\mathrm{HRR_{MLC}} = \mathrm{EHC_{MLC}} \times \mathrm{MLR_{MLC}} \qquad \textit{Eq. 87}$$

$$\mathrm{HRR_{MCC}} = \sum_{g} \mathrm{EHC_{g_{MCC}}}.\mathrm{J_g} \qquad \textit{Eq. 88}$$

The effective heats of combustion of EVA/ATH materials were determined using both MCC and mass loss calorimeter. The value of the effective heat of combustion in cone calorimeter is taken as an averaged value when a steady state burning rate is reached. The plots of the EHC as a function of normalized experimental burning time (equal to 0 at ignition and 1 at flameout so all experiments in different conditions and different burning duration can be comparable) are plotted in **Figure 99**. For EVA/ATH, the plot of EHC as a function of normalized burning time shows that the EHC is constant over the all duration of the tests. An averaged value of 22.3 ± 2.3 MJ/kg is taken. The plot of EHC as a function of time for EVA/ATH/NC is different. Indeed, it exhibits a two-steps shape. The first step between 0 and 40 % of burning duration shows an averaged EHC of 19.1 ± 1.3 MJ/kg. Then the EHC increases and reaches a second plateau at higher burning duration at 33.2 ± 4.2 MJ/kg.

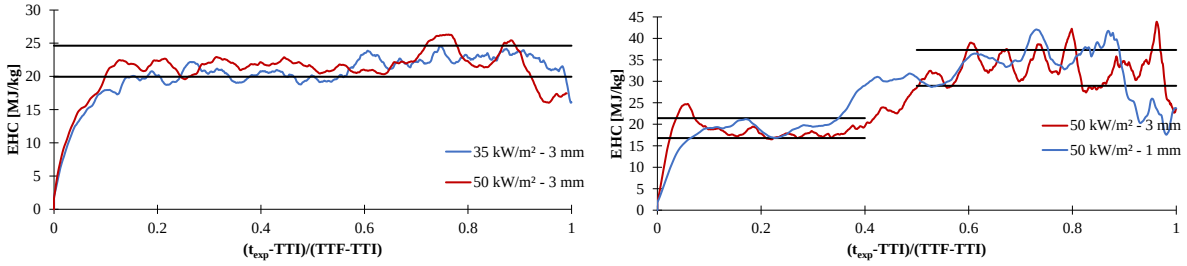

Figure 99: Plot of EHC from MLC as a function of normalized burning time for EVA/ATH (left) and EVA/ATH/NC (right)

The heat of combustion can also be determined according to the ASTM D7309 [219] using the MCC and can be described in **Eq. 89**. Information about the initial mass of tested sample $m(T_{ini})$, mass at a given temperature or final temperature $m(T_{end})$ of decomposition and the integral of the HRR signal between these two temperatures $\int_{T_{ini}}^{T_{end}} HRR(T)$ has to be determined. No information in the standard is given if two reactions or more are observed and whether it is possible to calculate two or more effective heat of combustion.

$$EHC_{g_{MCC}} = \frac{m(T_{ini})}{m(T_{ini}) - m(T_{end})} . \int_{T_{ini}}^{T_{end}} HRR(T) \qquad \textbf{Eq. 89}$$

The MCC results for EVA/ATH/NC are presented in **Figure 100** along with the MLR in TG experiments performed under nitrogen at 60 K/min. It was decided to calculate the effective heat of combustion for Gas1 and Gas2 as defined in **Figure 50** (p.101) by considering the mass loss in TGA and the integral of the HRR signal obtained in MCC between 220 and 350 °C for Gas1and between 350-550 °C for Gas2. Similar temperature ranges were used to determine the effective heats of combustion of EVA/ATH. Namely, EHC_{Gas1} was determined between 200 and 340 °C when EHC_{Gas2} of EVA/ATH was determined between 340 and 500 °C. Finally, the effective heat of combustion was also calculated considering the whole temperature range (200-550 °C and 220-550 °C for EVA/ATH and EVA/ATH/NC respectively as no heat is released before or after these ranges) and referred as EHC_{MCC}. Note also that the HRR curve ion MCC are very similar as presented in **Figure 101**.

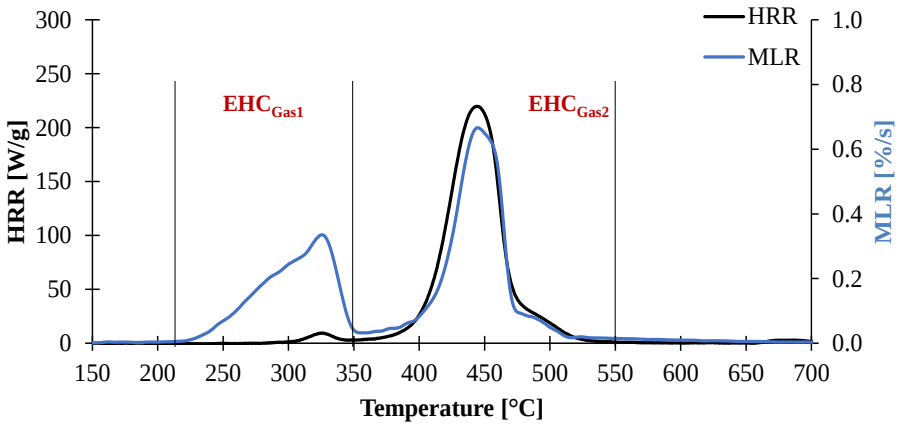

Figure 100: Plot of HRR from MCC experiments and MLR from TGA at 60 K/min under inert atmosphere for EVA/ATH/NC

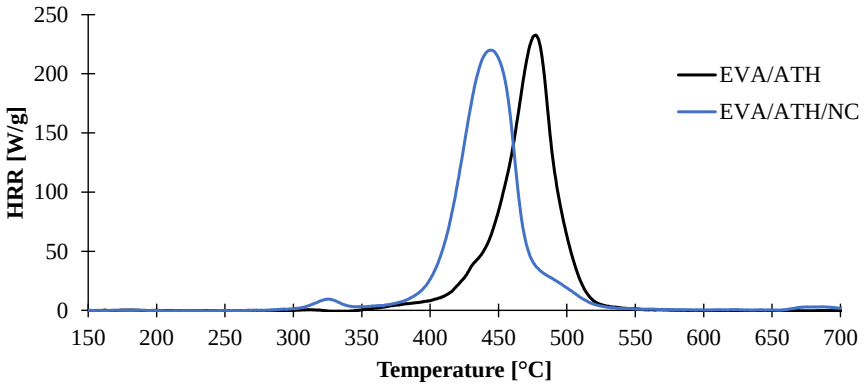

Figure 101: Comparison of MCC results for EVA/ATH and EVA/ATH/NC

The effective heats of combustion of either EVA/ATH formulations or their different gases (Gas1 and Gas2 as defined in **Figure 50**) determined by the analysis of MLC or MCC results are compared in **Table 21**. It can be seen that the EHC determined by the MLC and by the MCC are close for EVA/ATH (22.3 and 21.0 MJ/kg respectively). In the case of EVA/ATH/NC showing a two-steps plot of EHC in the MLC. The first value obtained in MLC is close to the one obtained with the MCC (19.1 vs. 21.34 MJ/kg respectively) and the second value from the MLC is close to the one of Gas2 for EVA/ATH/NC (33.2 and 34.0 MJ/kg respectively).

Table 21: Effective heat of reactions assessed though mass loss cone or MCC experiments

EHC [MJ/kg$_{gas}$]	EVA/ATH	EVA/ATH/NC
EHC$_{Cone}$	22.3	19.1 / 33.2
EHC$_{MCC}$	21.0	21.3
EHC$_{Gas1}$	1.2	1.4
EHC$_{Gas2}$	29.6	34.0

Note also that the values of EHC$_{Gas1}$ for both EVA/ATH formulations are close to each other (1.18 and 1.36 MJ/kg respectively). They are also much smaller than the EHC determined by MLC as Gas1 is mainly composed of water, which is a non-combustible gas. On the opposite, EHC$_{Gas2}$ for both EVA/ATH formulations are higher than the EHC determined by MLC. These values are in agreement with the heat of combustion of hydrocarbons and pristine polymers.

IV.3.5.b. Prediction of the heat release rate of EVA/ATH formulations

Using the prediction of MLR in flaming conditions, the mass fluxes of Gas1 and Gas2 for each EVA/ATH formulations and the EHC values previously determined in the previous section, it was possible to model the heat release rate behavior of the EVA/ATH formulations.

The predicted and experimental HRR curves of EVA/ATH in various conditions are presented in **Figure 102**.

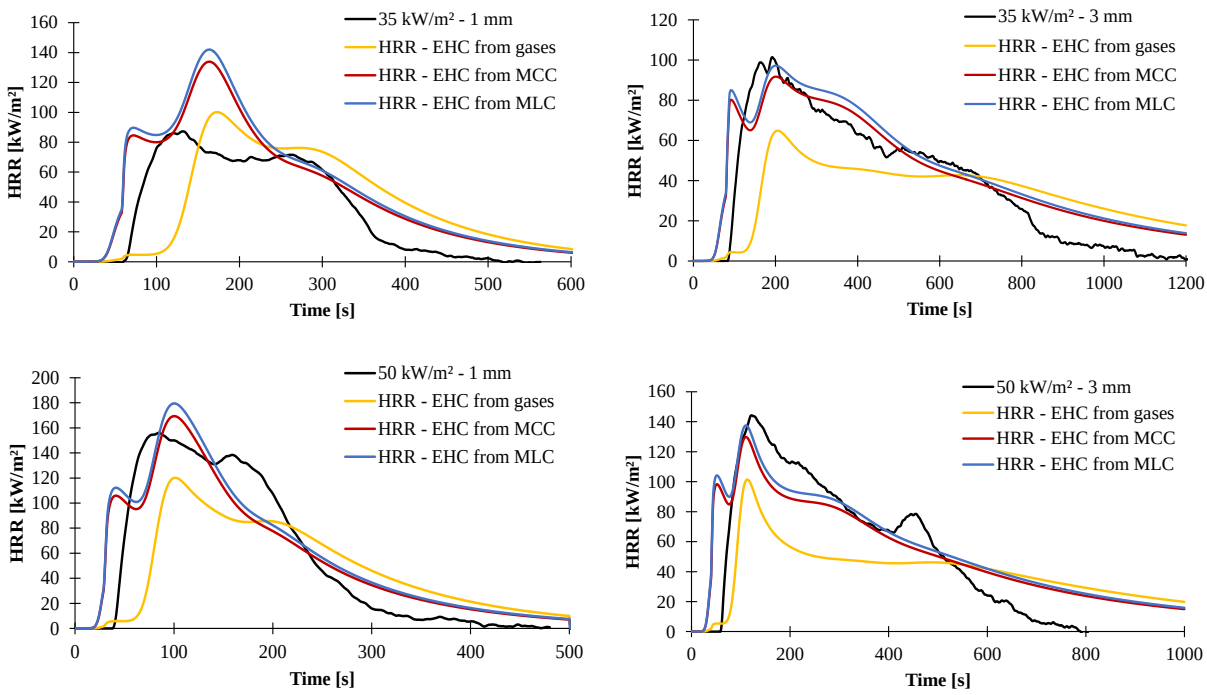

Figure 102: Experimental and predicted HRR curves assuming different EHC values for 1 and 3 mm thick EVA/ATH under 35 and 50 kW/m² irradiance

Using the EHC of each individual gas leads to an under-prediction of the pHRR values for all the irradiances and thicknesses. Note also that for both 35 and 50 kW/m² irradiance and 1 mm thickness, the pHRR as well as the t_{pHRR} are over-estimated using EHC from MCC. It is noteworthy that the prediction of the HRR of 3 mm thick EVA/ATH is closer to the experimental curves than for 1 mm thick EVA/ATH.

The predicted and experimental HRR curves for EVA/ATH/NC in various conditions are presented in **Figure 103**. On the opposite of EVA/ATH, the prediction of the HRR using EHC values of individual gases leads to similar results than using EHC values from the MCC or from the MLC. Note that the second apparent peak of HRR is not predicted using the model. Indeed, as previously discussed, this peak

was associated with the apparition of cracks on the residue and the model used in this study cannot describe this phenomenon.

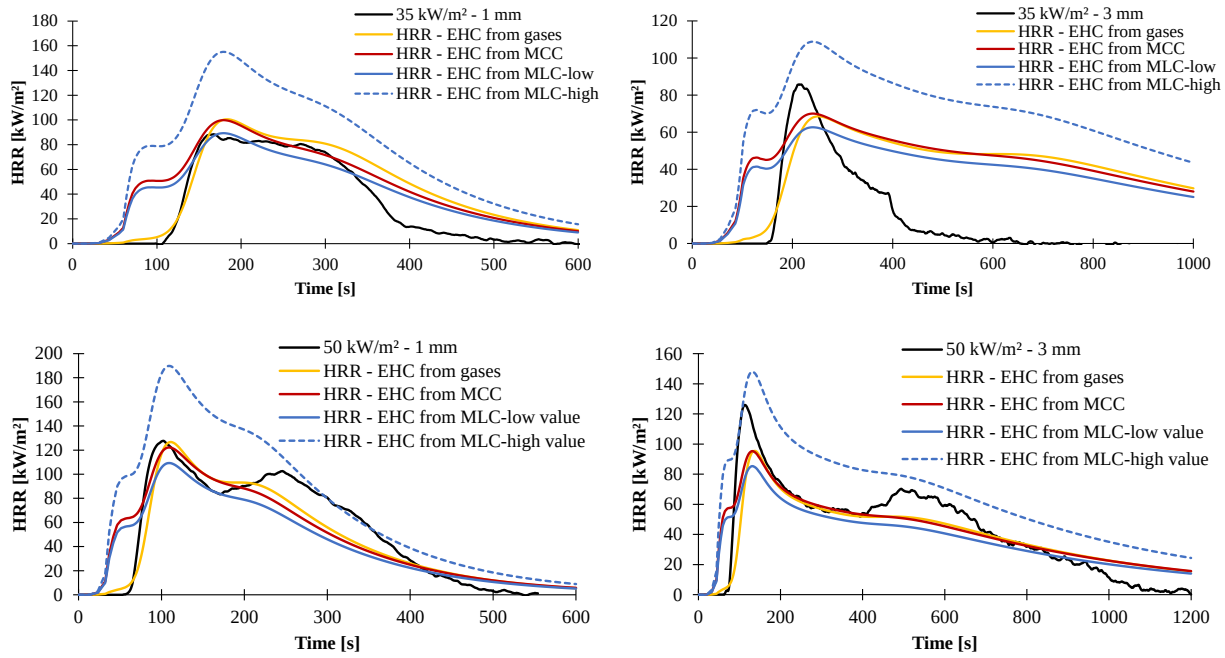

Figure 103: Experimental and predicted HRR curves assuming different EHC values for 1 and 3 mm thick EVA/ATH/NC under 35 and 50 kW/m² irradiance

It was shown in this section that the prediction of the heat release rate is not an easy task. Indeed, even if the mass loss rates were well predicted, their conversion into heat release rates are more difficult. Several effective of combustion were determined but no general agreement was obtained on the prediction of the HRR profiles of the materials. This highlights the facts that more efforts should be put in the characterization of the gas phase on a modelling aspect. Indeed, using EHC from the cone calorimeter or from the MCC is generally sufficient in the case of pristine polymers [78,81] but not in the case of formulated materials. The effect of flame retardant additives and especially ATH that dilutes the combustibles gases by releasing water is more difficult to predict.

IV.4. CONCLUSION

This chapter was dedicated to the modelling of the mass loss and heat release of EVA/ATH formulations in inert and flaming conditions. From the gasification experiments, it was found that the temperature profile was well modelled for 5 to 8 min for EVA/ATH and EVA/ATH/NC respectively. During these times, the mass loss was well predicted by using the assumption that the gases diffuses inside the materials and were not released instantaneously. Through parametric studies, it was possible to tune mass transfer coefficients of each individual gases. Thanks to this, the experimental mass loss and mass loss rate curves were well fitted by the model. The fact that ATH and NC can produce a layer limiting the diffusion of oxygen inside the materials [31] and subsequently, limiting the diffusion of the decomposition gases out of the materials was then estimated. The good prediction of the temperature and mass loss rate thus validates the inputs characterized in the previous chapter.

The implementation of the kinetic of decomposition, of the dependence on the composition and of the optical properties was also investigated for the gasification experiments. It was found that implementing the incident heat flux as a boundary condition limits the temperature increase at the backside of the specimen. Considering local or global in-depth absorption of the heat promotes the absorption of the heat inside the material. The decomposition of the materials thus happens at shorter times.

It was also shown that a global kinetic model does not significantly improve the MLR and temperature profiles in the case of slow and rapid diffusion of the gases even if a global kinetics shows a better fit than using a two-successive reaction when modelling the decomposition in TGA. Moreover, it was found that using temperature-dependent thermo-physical parameters was more appropriate than using composition-dependent parameters. Indeed, using only temperature-dependent or temperature- and composition-dependent properties lead to similar results whereas it is not the case considering only composition-dependent data. This also showed the importance of the methodologies developed in **CHAPTER III** for the characterization of the thermo-physical properties experimentally determined as a function of temperature.

Finally, mass loss calorimetry results were modelled and compared to experimental results. Additional parameters such as critical mass flux for ignition and heat flux from the flame had to be determined. A flame feedback of 20 kW/m² was selected through parametric studies as it allowed the best prediction of the temperature increase in the material. Critical mass flux for ignition of 1.6 and 0.7 g/m²/s for EVA/ATH and EVA/ATH/NC were estimated by fitting the times to flameout of the materials. These values were also experimentally verified and a good agreement was observed between experimental and

numerical parameters. The mass loss rate of EVA/ATH formulations was then modelled and a good agreement with the experimental data for both 1 and 3 mm thick specimen under 35 and 50 kW/m² irradiance was obtained.

The heat release by the materials was then modelled. Using effective heats of combustion determined in MCC and MLC, it was possible to convert MLR in HRR data. While the agreement between experimental and predicted MLR curves was excellent, the modelling of the HRR curves showed less agreement with the experimental HRR curves. Indeed, the presence of ATH leads to the dilution of the decomposition gases. The release of combustible products is thus different to the release of all the gases. Moreover, the materials decompose before the heat release starts as some ATH dehydrates (and cools down the material) thus delaying the ignition. Additional effort have thus to be made in particular on how to translate MLR into HRR in that case. One way to improve the model would be to separate the release of water to the release of other flammable products (acetic acid and acetone) so the real composition in flammable gases and the ignition could be predicted.

Up to now, efforts were made to characterize the chemical, optical and thermo-physical properties of cables materials such as EVA/ATH and EVA/ATH/NC. The methodologies developed allowed to determine to inputs data for a pyrolysis model. This model showed to be reliable for the modelling of temperature and mass loss rate in both flaming and gasification conditions. However, the modelling of the HRR is more challenging and less agreement can be observed between the experimental and numerical results.

Furthermore, since the objectives of this study is to be able to predict the large scale behavior of cables in order to support materials development, another approach than modelling consists in the development of a small scale test that would be easier to perform but also to model. The next chapter will thus be dedicated to the development of a small-scale test for electrical cable with a clear link to large-scale test fire scenario. Thanks to this approach, it will be possible to find correlations between this small-scale test and a large-scale certification test.

CHAPTER V. NOVEL BENCH-SCALE TEST FOR EVALUATION OF CABLES

This chapter is dedicated to the development of a novel bench-scale test for the evaluation of the fire behavior of electrical cables. Background on cable regulations as well as a description of the large-scale test apparatus of interest will be given in the first section. The strategies for the conception of novel bench-scale apparatus as well as the tested specimen will be detailed in a second part. The ability of the novel bench-scale test to differentiate benchmark cables with different Euroclass classification will be investigated. Finally, the bench-scale test will be used for the development of a new cable.

V.1. CONCEPTION OF THE TEST

V.1.1. DESCRIPTION OF EN 50399 APPARATUS

V.1.1.a. Background about electrical cable regulation

In the past years, every country had their own standards regarding cables and thus manufacturers needed to comply with each of them leading to a high cost of development of the cables. However, in order to develop more eco-friendly, less toxic and less hazardous cables, a harmonization of the European fire safety test requirements for different building products, including cables have taken place in the frame of the European Construction Products Regulation (CPR) [220,221] since the last decades and cables will need to be CE-marked in the future. The purpose is to ensure the free movement of all construction products within the European Union by harmonizing national laws with respect to the essential requirements applicable to these products in terms of health and safety. Cables are then classified in the so-called "Euroclass". The EN 13501 [18] standard summarizes the criteria and the tests to be performed for the Euroclass of a cable. The Euroclasses are defined according to the results of either ISO 1716 [19], EN 50399 [21] and EN 60332-1-2 [20] tests as defined in **Table 22**.

The EN/IEC 60332-1 is a small scale test method where a 1 kW burner tilted at 45 ° is applied for 60 s on 500 mm long cable (in the case of our cables as their outer diameter is lower than 2.5 cm). Then, the final damaged length is noted after flameout of the cable. The EN 50399 is a large-scale test method where several cables are mounted on a ladder and impacted by a 20.5 kW (or 30 kW if classification $B1_{ca}$ is recommended) methane burner for 20 min. Then the heat release rate (HRR) is monitored along with the smoke production rate as well as the final damaged length. Additional classification for smoke production, acidity of the gases and flaming droplet are also considered.

Table 22: Classes of reaction to fire performances according of the EN 13501 [18,221]

Class	Test method(s)	Classification criteria	Additional classification
A_{ca}	EN ISO 1716	PCS ≤ 2.0 MJ/kg	
$B1_{ca}$	EN 50399 (30 kW flame source) *and*	FS ≤ 1.75 m *and* THR ≤ 10 MJ *and* Peak HRR ≤ 20 kW *and* FIGRA ≤ 120 W/s	Smoke production flaming droplets/particles acidity
	EN 60332-1-2	H ≤ 425 mm	
$B2_{ca}$	EN 50399 (20.5 kW flame source) *and*	FS ≤ 1.5 m *and* THR ≤ 15 MJ *and* Peak HRR ≤ 30 kW *and* FIGRA ≤ 150 Ws^{-1}	Smoke production flaming droplets/particles acidity
	EN 60332-1-2	H ≤ 425 mm	
C_{ca}	EN 50399 (20.5 kW flame source) *and*	FS ≤ 2.0 m *and* THR ≤ 30 MJ *and* Peak HRR ≤ 60 kW *and* FIGRA ≤ 300 Ws^{-1}	Smoke production flaming droplets/particles acidity
	EN 60332-1-2	H ≤ 425 mm	
D_{ca}	EN 50399 (20.5 kW flame source) *and*	THR ≤ 70 MJ *and* Peak HRR ≤ 400 kW *and* FIGRA ≤ 1300 Ws^{-1}	Smoke production flaming droplets/particles acidity
	EN 60332-1-2	H ≤ 425 mm	
E_{ca}	EN 60332-1-2	H ≤ 425 mm	
F_{ca}	No performances determined		

V.1.1.b. EN 50399 apparatus

The EN 50399 [21] standard was initiated in a major study of the reaction to fire properties of cables *e.g.* the EU-funded FIPEC-project (Fire Performance of Electric Cables) [222]. The main purpose of the project was to develop a test method, based on the IEC 60332-3-10 standard [223] test apparatus as shown in **Figure 104**, complemented with modern fire measurement technology.

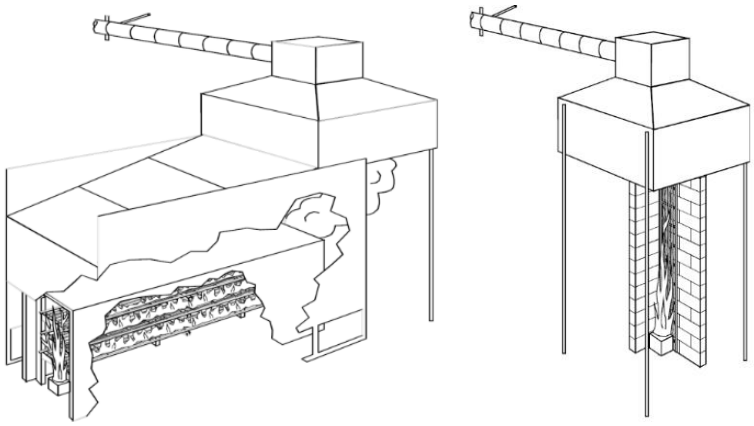

Figure 104. Horizontal (left) and vertical (right) reference scenario in the FIPEC project [222]

A schematic of the EN 50399 is presented in **Figure 105**. The inner dimensions of the apparatus are 1x2x4 m^3 (width × depth × height). The cables are mounted on a vertical ladder. For cables with diameters between 5 mm and 20 mm the cables are distributed over an approximately 300 mm wide layer with a spacing between the cables equal to one cable diameter. The cables are exposed to a 20.5 kW propane burner at the lower part of the ladder for 20 min, see **Figure 105**. During the test, heat and smoke release from the fire are measured, as are the falling droplets. The former are automatically measured whereas the droplets are noticed manually by the operator. After the test, the extend of flame spread is measured manually by the operator.

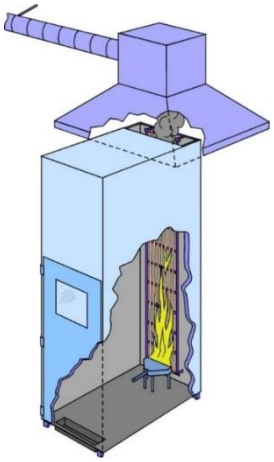

Figure 105: Schematic representation of the EN 50399 test apparatus

In order to develop the EN 50399 standard an extensive test campaign (test data from almost 2000 experiments) was performed with real scale tests and different protocols. A hood system for measuring heat release and smoke production was attached to the apparatus. Parameters that were studied for the protocols were *e.g.* type of burner (premixed or diffusion), burner power, test duration, and mounting procedures for cables on the ladder. The report concludes that a test duration of 20 min with a 20.5 kW premixed burner are appropriate parameters for most cables.

Regarding the mounting procedures, it was found that for cables with a diameter larger or equal to 20 mm, a 20 mm spacing between the cables on the ladder is required. For cable diameters between 5 mm and 20 mm the spacing should correspond to one cable diameter. For cable diameters lower than 5 mm, the cables should be bundled into bundles of 10 mm diameter with 10 mm spacing between each of them. The proposal from the FIPEC project laid the basis for the latest revision of the EN 50399 standard.

Within the framework of the CEMAC-project (CE-MArking of cables) [224,225], further developments of the EN 50399 test standard were implemented. For example, a grid was prescribed for the air inlet to achieve a more uniform flow of the air in the apparatus. Two round robins were also performed on behalf of Europacable and CENELEC and included many test sites. The results were good and comparable to the results of the SBI test used for linings (Single Burning Item, used for lining materials) [226]. EN 50399 is now under its first revision and voting is expected to take place in 2016. One suggested amendment is to include the possibility to test non-circular cables. The suggestion is to mount the non-circular cables in the same manner as circular cables with the diameter equal to the major axis diameter of the non-circular cables.

V.1.1.c. Limitations of the EN 50399 apparatus

One of the limitation when developing new materials for cables is the relevance of the tests performed for evaluating the fire performances of materials. Indeed, small-scale tests on cables are generally not discriminant and large-scale tests are time and materials consuming. The development of new materials for cables implies then to test the materials themselves rather than the cables. These tests on the materials have then to be representative of the fire scenario involved when cables burn.

In that frame, cone calorimetry is widely used even if it does not permit to examine flame spread. Some studies tried to investigate the lateral [227] or vertical [228] flame spread with a modified and/or inclined cone calorimeter with more or less success. Indeed, these studies considered forced and radiative burning conditions when the specimen are ignited with a flame in in the EN 50399 apparatus or IEC 60332-1 apparatus. Moreover, the size of the ignition source (the heating cone) used in these study is similar to that of the sample size (the size of the cone plaque). On the contrary, in the previously mentioned tests, the height of specimen is much larger than the one of the ignition source and thus allows to study flame spread.

The development of a small-scale test is thus clearly needed in which flame spread has to be considered. The next section of this chapter will first be dedicated to the development of the relevant specimen that could be used for such bench-scale test.

V.1.2. TESTED SPECIMEN

V.1.2.a. Description of the tested materials

In this study, cables with known fire performances at EN 50399 were used. These benchmark cables were provided by Leoni Stüder A.G (Däniken, Switzerland). They are based on the cable design described in **Figure 106**. They consist on three 1.5 mm² conductors (4), one is insulated by a non-flame retarded thermoplastic (3) while the two remaining conductors are insulated with a halogen-free flame retarded (HFFR) thermoplastic (2). The thicknesses of the insulations are around 1 mm for the three conductors. Then, these insulators are stranded and this assembly is embedded in an outer sheathing (1) without the presence of any bedding. The outer sheathing is made of polyolefin flame retarded mainly with a high amount (higher than 50 wt%) of aluminum tri-hydroxide (ATH). The cables have an outer diameter of 12 mm. The five benchmark cables only differ in the nature of the external sheathing

material: the cable design as well as the inner components (number of conductors, nature and thicknesses of the insulators) were the same for the five studied cables. The cables will be referenced as follows:

- "Ca_" to indicate that a cable is tested

- "Classification at EN 50399"

- "Be" to indicate that it is a benchmark. If several benchmark cables with the same Euroclass are selected, they will be numbered Be1, Be2, *etc.*

For example, Ca_$B2_{ca}$_Be1 refers to a benchmark cable presenting a $B2_{ca}$ classification. Ca_C_{ca}_Be2 will represents the second cable presenting a Euroclass C_{ca}.

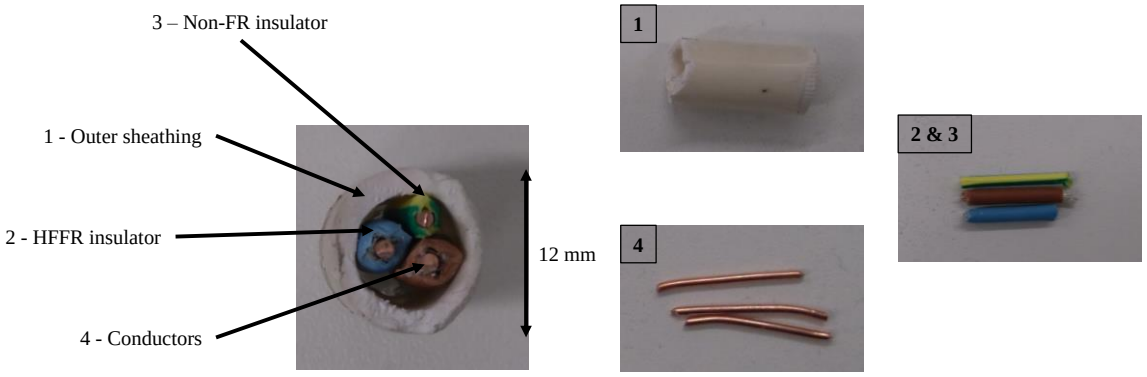

Figure 106: Design of the cable used in this study

The EN 60332-1 test was used on the benchmark cables and the results for Ca_D_{ca}_Be1, Ca_C_{ca}_Be1 and Ca_$B2_{ca}$_Be1 are shown in **Figure 107**. It is clear that the benchmark cables behave similarly. According to the EN 13501 standard, a damaged length lower than 425 mm is required for getting a classification from $B1_{ca}$ to E_{ca} depending on the results obtained in EN 50399. In our case, the flame spread is much lower than this criterion since the final damaged length is around 150 mm for all cables.

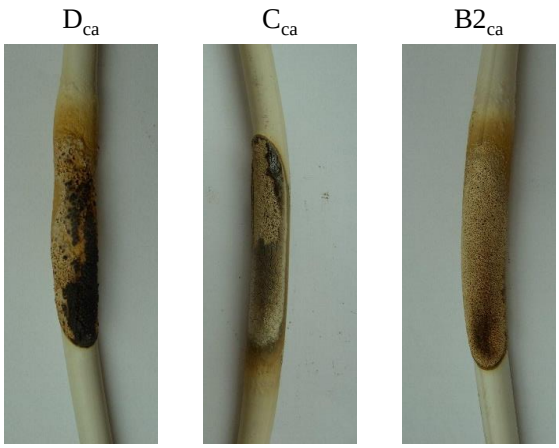

Figure 107: Results of the IEC/EN 60332-1 test Euroclass $B2_{ca}$, C_{ca} and D_{ca}

It is obvious that no differences between the Euroclasses can be found using IEC-60332-1-2. EN 50399 tests were thus performed and the results are presented in **Table 23**. The damaged lengths at the end of the test vary from 0.6 m for Ca_$B2_{ca}$_Be1 to 2.3 m for Ca_D_{ca}_Be1. The flame spread is different for each benchmark cables, thus the heat release behavior is impacted. For instance, the Total Heat Released (THR) varies from 7.2 MJ for Ca_$B2_{ca}$_Be1 to 41.8 MJ for Ca_D_{ca}_Be1. Peak of Heat Release Rate (pHRR) for Ca_C_{ca}_Be1 is 32.7 kW so higher than the required value to be classified Euroclass $B2_{ca}$ (*i.e.* 30 kW). Even if the other criteria are acceptable for being $B2_{ca}$, pHRR implies that Ca_C_{ca}_Be1 is Euroclass C_{ca}.

Table 23: Fire performances of the selected benchmark materials according to EN 50399 standard

	Damaged length [m]	pHRR [kW]	THR [MJ]	FIGRA [W/s]	Euroclass
Ca_D_{ca}_Be1	2.3	58.5	41.8	113.0	D_{ca}
Ca_C_{ca}_Be1	1.2	32.7	16.5	63.9	C_{ca}
Ca_C_{ca}_Be2	1.4	36.8	23.9	62.8	C_{ca}
Ca_$B2_{ca}$_Be1	0.6	22.6	7.2	55.3	$B2_{ca}$
Ca_$B2_{ca}$_Be2	0.7	24.8	7.1	62.9	$B2_{ca}$

Ca_$B2_{ca}$_Be2 performances are close to that of Ca_$B2_{ca}$_Be1 as the damaged length and pHRR are slightly higher with 0.72 m and 24.8 kW (against 0.6 m and 22.6 kW for Ca_$B2_{ca}$_Be1 respectively) and

a similar THR at 7.1 MJ is obtained. Similarly to Ca_B2$_{ca}$_Be2, Ca_C$_{ca}$_Be2 was selected as it exhibits slightly worst behavior than Ca_C$_{ca}$_Be1. Namely, a damaged length of 1.44 m (against 1.2 m for Ca_C$_{ca}$_Be1), a pHRR of 36.8 kW and a THR of 23.9 MJ.

It is noteworthy that the Fire Growth Rate values (FIGRA) of the five benchmark cables are under the criterion for being Euroclass B1$_{ca}$ (120 W/s). This means that this parameter is not discriminant for the determination of the Euroclass in the case of our selected cables.

V.1.2.b. Design of the specimen for the bench-scale test

The first step of our study consists in the determination of the most appropriate design for the specimen (nature, size…). Details of the architecture of the cables including their weight composition are presented in **Figure 108**. In a first approach, benchmark cables Ca_B2$_{ca}$_Be1, Ca_C$_{ca}$_Be1 and Ca_D$_{ca}$_Be1 will be studied. Indeed, they belong to the three different Euroclass classification and the aim of our test is to be able to differentiate materials according to their classification.

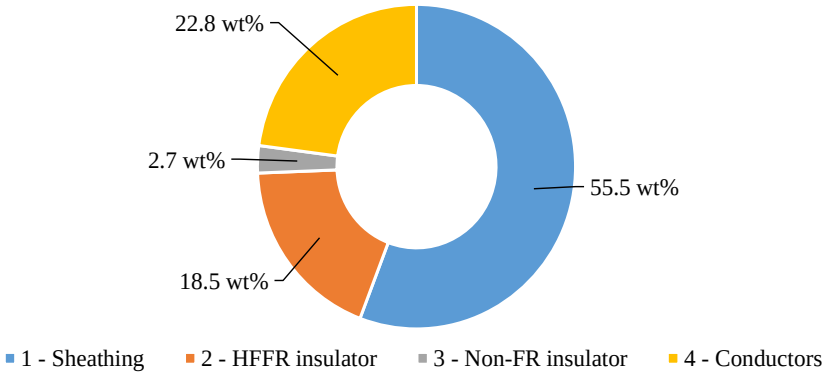

Figure 108: Weight composition of the cables (averaged values of Ca_B2$_{ca}$_Be1, Ca_C$_{ca}$_Be1 and Ca_D$_{ca}$_Be1)

Each part of the cables was weighted for 10 cm of cable and their weight compositions were determined. Note that the most important part of the cable is the outer sheathing as it represents more than 55 wt % of the composition of the cable. Then, the conductors and the insulators contribute equally to the composition of the cable (around 18-23 wt%).

In order to understand the contribution to fire of each part of the cables, the different materials used to design the benchmark cables Ca_$B2_{ca}$_Be1, Ca_C_{ca}_Be1 and Ca_D_{ca}_Be1 (except their conductors which are non-combustible) were tested as triplicates in a cone calorimeter at an external heat flux of 35 kW/m² and 50 kW/m². The tests were performed according to the ISO 13927 standard [229] on 6 mm plaques of each cables' part materials. These plaques were prepared by extrusion and compression molding. The effective heats of combustion of each material are presented in **Table 24**. The outer sheathing of cable Ca_D_{ca}_Be1 exhibits the highest heat of combustion (24.5 MJ/kg) while the two other sheathing materials exhibit lower heats of combustion (around 20 MJ/kg). The material used for the HFFR insulator which embeds the two conductors shows a heat of combustion close to that of the sheathing of Ca_D_{ca}_Be1 (25.3 MJ/kg). Finally, the material used for the non-flame retarded insulator release around twice more heat than the other formulations (38.2 MJ/kg). Its contribution to fire is nonetheless compensate by its low weight content in the cables.

Table 24: Effective heat of combustion [MJ/kg] of the different components of the benchmark materials determined at 35 and 50 KW/m² (averaged values)

	Ca_D_{ca}_Be1	**Ca_C_{ca}_Be1**	**Ca_$B2_{ca}$_Be1**
1 – Sheathing	24.5 ± 4.5 %	20.0 ± 8.4 %	20.6 ± 7.0 %
2 – HFFR insulator	25.3 ± 2.9 %	25.3 ± 2.9 %	25.3 ± 2.9 %
3 – Non-FR insulator	38.2 ± 6.3 %	38.2 ± 6.3 %	38.2 ± 6.3 %

Based on these results, the contributions to fire of each components of the cables were calculated and the results are presented in **Table 25**. It can be noted that for the three benchmark cables, the sheathing represents between 65 and 71 % of the heat released when they burn. The HFFR insulator is responsible for around 25 % of the heat produced and the remaining is due to the non-flame retarded insulator. It is noteworthy that even if Ca_$B2_{ca}$_Be1 is expected to release slightly more heat (3.18 MJ/m_{cable}) than Ca_C_{ca}_Be1 (3.02 MJ/m_{cable}), its classification according to the EN 50399 test is better ($B2_{ca}$ versus $C_{ca.}$).

The key role of the outer sheathing in the fire behavior could thus be suspected and enhancing its fire performances is then mandatory to improve the fire retardant properties of the whole cable. Indeed, it was shown that the sheathing will release most of the heat in case of fire but it will also protect the underlying material forming a protective and/or an insulative ceramic layer. Decreasing the flammability of the sheathing and enhancing the efficiency of the protective residue will affect the heat released by

the cable and will contribute to delay the combustion of the insulators and therefore, decrease the flammability of the whole cable. On the other hand, those results also showed that it does not make sense to measure only the heat release rate by cone calorimetry in order to predict the behavior of cable in large-scale test such as EN 50399. Indeed, the tested sheathing material's plaques will not allow to investigate and to understand how it will react when impacted by a flame as soon as the cone calorimeter is a purely radiative and horizontal test. This will also lead to a different ranking considering Ca_B2$_{ca}$_Be1 and Ca_C$_{ca}$_Be1, which present the best performances.

Table 25: Total Heat Released by one meter of cable for the three benchmark materials and contribution of the outer and inner sheathings to the heat released

	Ca_D$_{ca}$_Be1	**Ca_C$_{ca}$_Be1**	**Ca_B2$_{ca}$_Be1**
1 – Sheathing	71 %	66 %	68 %
2 – HFFR insulator	24 %	28 %	26 %
3 – Non-FR insulator	5 %	6 %	6 %
Total Heat Released [MJ/m$_{cable}$]	3.47	3.02	3.18

The key role of the outer sheathing is also observed considering the behavior of the three benchmark cables in the standard tests (EN 60332-1 and EN 50399). Indeed, whereas testing cables at the small scale using a gas burner does not allow to differentiate the different cable, if their behaviors at the large scale are significantly different. Considering the fact that the same cable design and the same inner components were used for the three tested cables, the only differences between the benchmark cables was the outer sheathing. It thus confirmed that this component plays the most important role in the reaction to fire of the cable. Note that this assumption cannot be generalized to other cables' design and it may not be valid for other design, especially when a bedding is present.

Based on these results, it was decided to investigate the possibility to estimate the flame spread capabilities of the whole cable only by studying the flame spread of a thin sample of sheathing material. Indeed, as the sheathing releases most of the heat of the cable and could also contribute to the protection the underlying components, it is assumed it is the key part of the cable governing the fire behavior of the whole cable. The specimen will thus consist of 500 mm long, 23 mm wide and 1 mm thick strips. The width of the specimen was chosen as the perimeter of the cable and the thickness is in accordance with

this of the sheathing in the cable. The specimens consist of the outer sheathing of Ca_$B2_{ca}$_Be1, Ca_$B2_{ca}$_Be2, Ca_C_{ca}_Be1, Ca_C_{ca}_Be2 and Ca_D_{ca}_Be1 respectively.

The denomination of the specimen to be tested in the bench-scale test will be obtained by substituting the "Ca_" part of the previously defined name by "Sh_" (for sheathing). The specimen to be tested will be thus named Sh_$B2_{ca}$_Be1, Sh_$B2_{ca}$_Be2, Sh_C_{ca}_Be1, Sh_C_{ca}_Be2 and Sh_D_{ca}_Be1. The $B2_{ca}$, C_{ca}, D_{ca} part of the reference will be linked to the Euroclass of the related cables.

V.1.2.c. Conclusion about the design of the specimen

The results presented in this section showed that it does not make sense to measure only the heat release rate by cone calorimetry results in order to predict the behavior of cable in large-scale test such as EN 50399. Indeed, testing sheathing material in cone calorimeter does not allow to investigate and to understand how it will react while impacted by a flame as soon as the cone calorimeter is a purely radiative and horizontal test. Novel or adapted test methods have thus to be developed to mimic EN 50399 tests at the reduced scale and, it is the purpose of the following part.

V.1.3. NOVEL BENCH-SCALE DESIGN

V.1.3.a. Design of the test enclosure

In order to mimic the fire scenario involved in the EN 50399 apparatus and to have similar burning behavior, it was proposed to use a methane burner applied on the previously defined specimen during all the duration of the test. As previously described, the relevant specimen to be tested is a long strip of external sheathing on which both flame spread and heat release rate behavior when burning will be studied. It is then questionable if a standard test enclosure can be used for this purpose. Nonetheless, UL-94 or EN 60332-1-2 enclosures are not designed for HRR measurements, cone calorimeter is not suitable to study flame spread and also for applying a burner. It was thus decided to create a scaled-down enclosure of the EN 50399.

For that, a 550 W burner was applied at 45 ° of the specimen. The methane is supplied by Air Liquid (N35, purity of 99.95%). The burner impacts the specimen at 10 cm from its bottom. It was chosen not to impact the specimen on its edge to eliminate undesirable side effect and to match the EN 50399, in which the cables are impacted by the burner 500 mm over the bottom of the cables ladder.

The test enclosure consists of a scaled-down "telephone box" composed of 10 cm wide, 20 cm deep and 60 cm high insulated enclosure as shown in **Figure 109**. The enclosure is insulated by 5 cm thick insulation backboard (Vermibloc 11 from Distrisol with a density ranging between 550 and 650 kg/m^3 and a thermal conductivity of 0.17, 0.20 and 0.23 W/m/K at 200, 400 and 600 °C respectively). The front face of the apparatus (a door) is made of a stainless steel structure in which a 5 cm wide and 50 cm high temperature resistant and translucent glass is embedded. The size of the enclosure was chosen after preliminary test to optimize the enclosure size in order to improve the accuracy of the oxygen consumption measurement. The door let a space of 4 cm high and 10 cm wide at its bottom so the air can enter into the enclosure. This was designed in order to mimic the air supply of the EN 50399 apparatus. The flame spread was assessed by visual observation every 30 s and the HRR was measured by oxygen depletion with a zirconia-based oxygen analyzer (BA1000 from Bühler Technologies) which was placed in the exhaust chimney equipped with an anemometer and a 0.5 mm thin K-type thermocouple. The oxygen analyzer is protected by a pre-filter made of sintered steel with a retention rate of 2-5 µm placed at the extremity of the probe.

The specimen is fixed on a grid and placed in the enclosure. The distance between the specimen holder and the rear face of the enclosure is fixed at 4 cm. The specimens are fixed with a copper wire (with a diameter of 0.4 mm) at 10 mm of the bottom of the specimen and with a clamp at the upper side of the specimen.

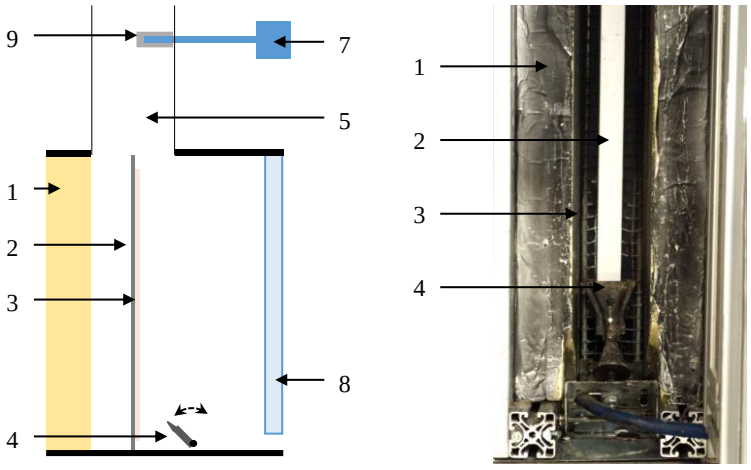

Figure 109: Picture of the interior of the test apparatus (left) and side view of the test (right)

1: insulation backboard; 2: tested specimen; 3: specimen holder (grid); 4: 45° tilted methane burner; 5: exhaust chimney; 6: stainless steel structure; 7: oxygen analyzer; 8; front door; 9; pre-filter for probe protection

The measurement of heat release rate based on oxygen consumption is the core principle of the cone calorimeter and of a number of fire tests from small (Microscale Combustion Calorimeter for example) to large-scale tests (the EN 50399 test for example). The principle was explained in details by Hugett [230] and others [231–233] (**Eq. 90**). It links the measurement of the heat release rate $\dot{q}(t)$ to the he initial mass flow of oxygen ($\dot{m}_{O_2}^0$) and to the instantaneous mass flow of oxygen at time *t* ($\dot{m}_{O_2}^t$) using the constant *E* (13.1 MJ/kg O_2).

$$\dot{q}(t) = E\left(\dot{m}_{O_2}^0 - \dot{m}_{O_2}^t\right) \qquad \textbf{Eq. 90}$$

It can be noted that in most of the apparatus aiming at measuring heat release rate, corrections terms are applied for water or relative humidity, carbon monoxide or dioxide production or for incomplete combustion. For simplification purposes, and in order to simplify the acquisition of the data as well as limiting the instrumentation around the test, these corrections were not applied in this study. Moreover, while it is not feasible to measure oxygen mass-flow, volume-fraction is readily determinable. By measuring the speed of the evolving air in the exhaust chimney, it is possible to have an estimation of the volumetric flow $(\dot{V})$, by taking into account the diameter of the chimney. Then, the mass flow of air in the chimney is calculated knowing the density of the air. Note that the mass flow was normalized at 298 K as in the EN 50399 standard [21]. The density of air at 298 K is taken at 1.184 kg/m^3. The measurement of the heat release rate in our study is then based on **Eq. 91**. In this equation, *E* is a constant taken at 13.1 MJ/kg [230], $\dot{V}$ is the volume flow and is measured with the anemometer placed in the chimney, T(t) is the instantaneous temperature measured by a 0.5 mm thin K-type thermocouple placed nearby the oxygen analyzer, $X_{O_2}^0$ and $X_{O_2}^t$ are respectively the initial and instantaneous volume fraction measured by the oxygen analyzer at time *t*.

$$\dot{q}(t) = E.\dot{m}_{air}^{norm}.\left(X_{O_2}^0 - X_{O_2}^t\right) = E.\dot{V}.\rho_{air}^{298}.\frac{298}{298 + T(t)}.\left(X_{O_2}^0 - X_{O_2}^t\right) \qquad \textbf{Eq. 91}$$

V.1.3.b. Experimental protocols

The specimen and the test designs were established in the previous section. This part details the protocol (**Figure 110**) used to evaluate the fire behavior of our specimen in the newly defined small-scale test. The first step (1) of a test consists to establish the baseline of the oxygen content in the enclosure without a flame. This ensures that the oxygen analyzer is working properly as it measures the oxygen content of the ambient air and set the measured value of $X_{O_2}^0$. The door of the test apparatus is then opened and the burner is ignited (I). The burner is oriented in a position to not impact the specimen.

Then the oxygen level is monitored until it stabilizes (2). A value $X_{O_2}^{burner}$ is then measured for 60 s after the steady state is reached. Thanks to (1) and (2), it is possible to evaluate the burner power and to be sure that it is repeatable for each experiment. Next, the burner is applied on the specimen (II) without opening the door. The heat release rate is measured and the flame spread is recorded every 30 s until the end of the experiments (3). The latter is done by visual observation of the decomposition front versus time. To facilitate this measurement, marks are placed every 2 cm on the tested specimen. The third step of the test (3) lasts at maximum 600 s or end up 180 s after the flameout. At the end of the test, the burner is removed from the specimen (III). The oxygen content is measured for at least 60 s. This enables to evaluate a potential drift of the burner power and to consider it.

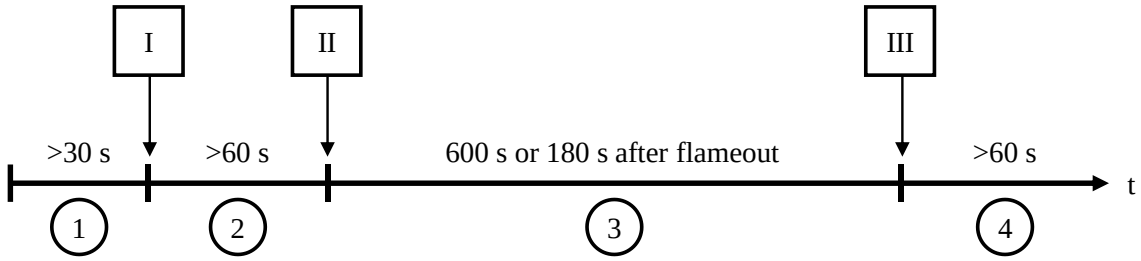

Figure 110: Experimental protocol used for the test; I: ignition of the burner; II: application of the burner; III: Removal of the burner; 1: baseline of oxygen in ambient conditions; 2: baseline of oxygen for burner power calibration; 3: heat release rate and flame spread measurement; 4: oxygen baseline for burner power check

Note that the flame spread or damaged length is presented as normalized value and is calculated from **Eq. 92**. L_t is the damaged length (in cm) expressed at time *t*. $(L_c - L_0)$ is the difference between the minimum damaged length (L_0) and the length to reach the clamp (L_c). The impact of the burner to the specimen corresponds to 0 % flame spread. If the flame reaches the upper clamp, then the flame spread is 100 %.

$$\text{Flame spread}(t) = \frac{L_t - L_0}{L_c - L_0} \qquad \textit{Eq. 92}$$

V.1.4. CONCLUSION

In this section, the large scale test EN 50399 apparatus as well as the standards required for electrical cables in building were described. Benchmark materials, representative of a wide range of fire performances in these standards test were selected. Then, a careful analysis of the contributions of each components of the cables showed that the outer sheathing contributes the most to the heat release when cables burn. It was thus decided to test a specimen of 500 mm long, 1 mm thick and 2.3 mm wide of only this material. These dimensions were chosen so they are representative of the thickness and perimeter of the outer sheathing in the studied cables. A EN 50399 reduced scale enclosure was then developed. A protocol was then set up in order to be able to determine several parameters (flame spread, HRR, THR and FIGRA) when the sheathing specimen is exposed to a gas burner.

The next section of this chapter will be dedicated to the investigation of the fire behavior of the cables using this newly developed small-scale test. The repeatability of the test measurement will be first evaluated. Then, the ability of the test to differentiate the fire behavior of the previously defined benchmark cables' materials will be determined. Finally, correlations between the small-scale test and the EN 50399 results will be established.

V.2. PROOF OF CONCEPT

V.2.1. REPEATABILITY STUDY

Bench-scale tests were performed several times on Sh_$B2_{ca}$_Be1, Sh_C_{ca}_Be1 and Sh_D_{ca}_Be1 in order to ensure the repeatability of the measurement and the reliability of the methodology developed in this study. Measurements obtained after four experiments are presented in **Figure 111** for Sh_D_{ca}_Be1. Both HRR and damaged length curves show a good repeatability. This material ignites at 19 ± 4 s and the HRR increases sharply around 0.8 kW at around 50 s. Then, the HRR increases steadily until reaching its maximum at 1.19 ± 0.08 kW after 309 ± 13s. When the HRR increases steadily, the damaged length increases linearly until the flameout corresponding to the time at which the flame reaches the clamp. It is noteworthy that while burning, the specimen exhibits dripping. By integrating the HRR signal over the duration of the test, the total heat released is measured at 260 ± 17 kJ.

It is possible to estimate the heat released by the sample considering the effective heat of combustion assessed through cone calorimeter (**Table 24** p.189) and the actual mass of specimen burned during the test. Considering the length of burned specimen as well as the width and thickness of the specimen and

the density of Sh_D_{ca}_Be1 outer sheathing, 281 kJ should be released. This value is in the same range of the experimental THR obtained in our test (260 ± 17 kJ). This permits to validate the HRR measurement in the small-scale test

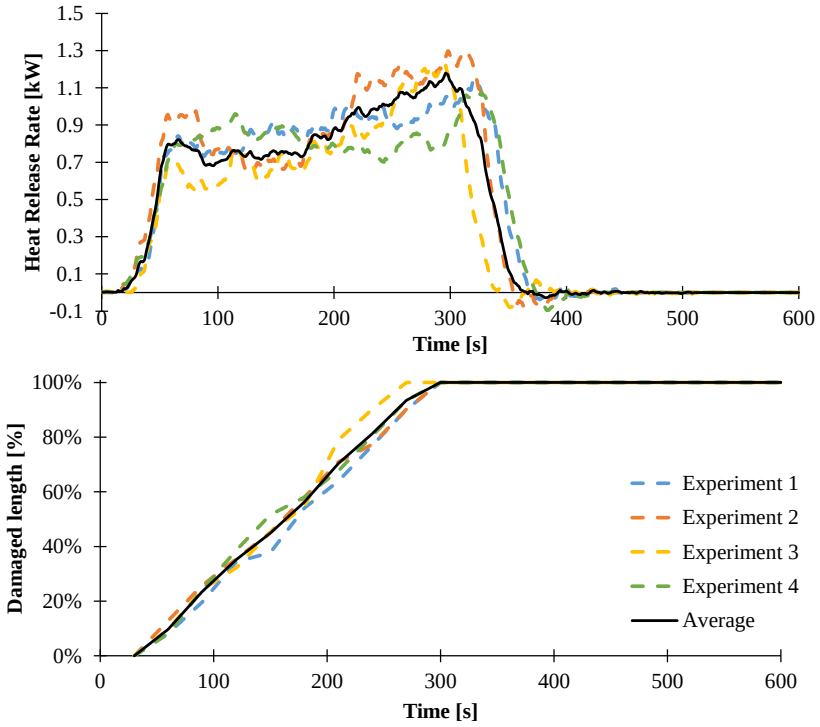

Figure 111: HRR and damaged length measurements with Sh_D_{ca}_Be1

Similar experiments were performed with Sh_$B2_{ca}$_Be1 and Sh_C_{ca}_Be1 and the results are shown in **Figure 112** and **Figure 113** respectively. Sh_$B2_{ca}$_Be1 ignites after 16 ± 2 s when Sh_C_{ca}_Be1 ignites after 20 ± 5 s. These results are not significantly different from the ones obtained for Sh_D_{ca}_Be1 meaning that based on a burner test, the three materials ignite simultaneously while it is not the case in cone calorimeter tests (time to ignition of 83 s for Sh_D_{ca}_Be1, 147 s for Sh_$B2_{ca}$_Be1 and 113 s for Sh_C_{ca}_Be1 at 50 kW/m² irradiance and for 6 mm thick plates). This can be due to the fact that the lower the thickness, the shorter the ignition time [73,91] so by studying 1 mm thick material, it is expected that less differences between the materials are observed.

On the contrary, the flame spread and HRR are significantly different for the three materials. Indeed, Sh_$B2_{ca}$_Be1 specimen starts releasing heat quickly and reaches a peak of HRR of 0.30 ± 0.02 kW after 80 s. Similarly, its damaged length is relatively low as only 20 ± 4% of the specimen length is damaged.

Sh_C_{ca}_Be1 shows a pHRR of 0.62 ± 0.03 kW after 100 s. During this time, the flame spreads over 35.2 ± 3.6 % of the specimen length. It has to be noted that Sh_C_{ca}_Be1 shows some undesired and uncontrolled effects such as melting and bending during the experiment. This explains the relative higher standard deviation obtained for this material compared to the one obtained for Sh_D_{ca}_Be1 and Sh_$B2_{ca}$_Be1 even if the results are still acceptable. These effects are less important with Sh_D_{ca}_Be1 as it burns more intensively and mainly exhibits melting/dripping in a repetitive manner whereas Sh_$B2_{ca}$_Be1 leaves a strong ceramic residue that does not crack, break or fall off during the test.

As a conclusion, the margin of error of the test methods for all the parameters is lower than 10 % validating the design of the apparatus as well as the protocol

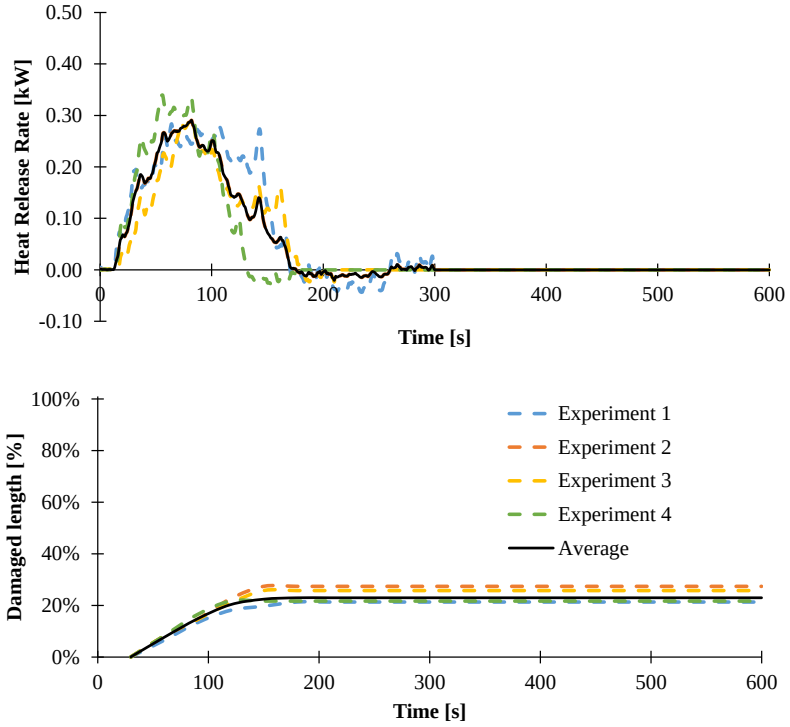

Figure 112: HRR and damaged length measurements with Sh_$B2_{ca}$_Be1

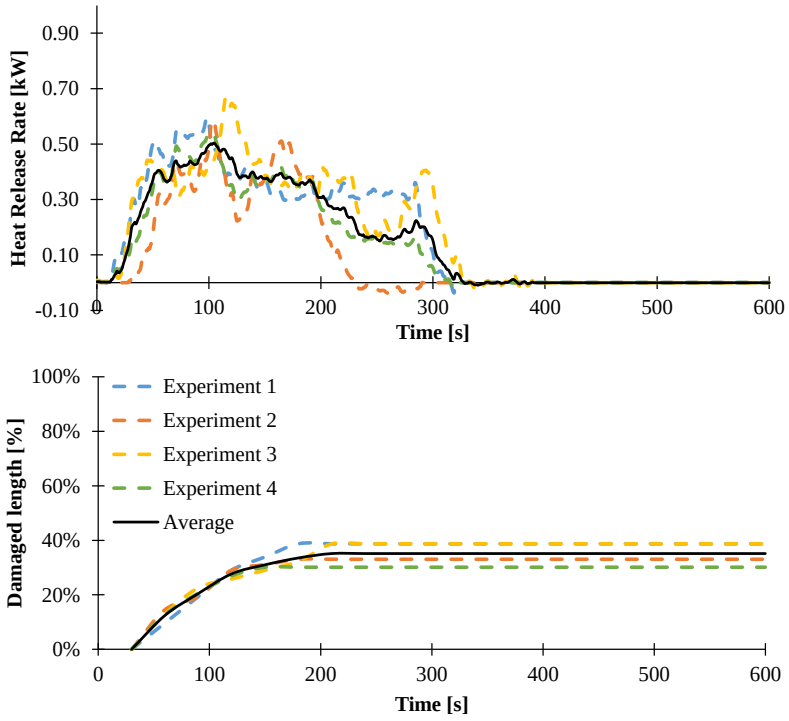

Figure 113: HRR and damaged length measurements with Sh_C_{ca}_Be1

V.2.2. CLASSIFICATION OF BENCHMARKS

In order to further validate our approach, the fire behavior of benchmark cables' materials were evaluated and compared with the data obtained in the EN 50399 apparatus. The five benchmarks materials were evaluated using the new small-scale test.

Considering the flame spread (**Figure 114)**, three different behaviors are observed. Sh_C_{ca}_Be1 and Sh_C_{ca}_Be2, as well as Sh_$B2_{ca}$_Be1 and Sh_$B2_{ca}$_Be2 behave similarly whereas Sh_D_{ca}_Be1 presents a singular behavior. It is noteworthy that the final damaged length of $B2_{ca}$ cables materials is of 24 ± 5 % while C_{ca} materials exhibit a damaged length of 36 ± 4 %. The addition of two benchmark materials helps us to ensure the fact that the small-scale test allows to differentiate the damaged length at the small scale.

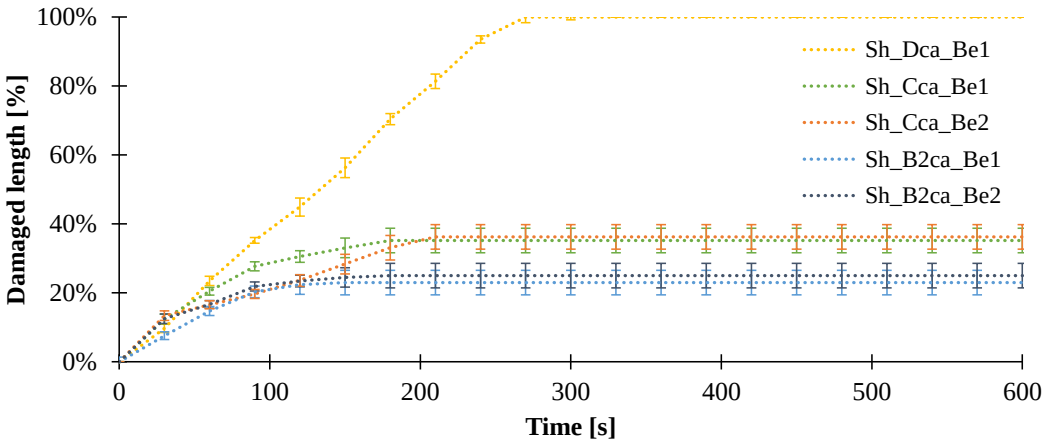

Figure 114: Damaged length using the small-scale test for different benchmark materials

Similarly to flame spread, the HRR behavior of the two additional materials were studied using our small-scale test in order to validate the possibility to differentiate the behavior of materials with the bench-scale test **Figure 115)**. Sh_B2$_{ca}$_Be2 exhibits a pHRR of 0.25 kW, which is slightly lower than that of Sh_B2$_{ca}$_Be1. The opposite observation can be made with the THR as Sh_B2$_{ca}$_Be2 releases 32 MJ while burning when Sh_B2$_{ca}$_Be1 releases 27 MJ with similar damaged length. Sh_C$_{ca}$_Be2 shows a pHRR of 0.72 kW and a THR of 85 MJ. It is interesting to note that the behaviors of Sh_C$_{ca}$_Be2 and Sh_C$_{ca}$_Be1 are different in this case. Sh_C$_{ca}$_Be1 exhibits a lower pHRR value but a higher THR value than Sh_C$_{ca}$_Be2. Sh_C$_{ca}$_Be1 releases more heat for the first 150 s of the experiment, which is consistent with the flame spread behavior shown in **Figure 114**. Between 0 and 120 s, the damaged length of Sh_C$_{ca}$_Be2 shows a 10 % difference with that of Sh_C$_{ca}$_Be1.

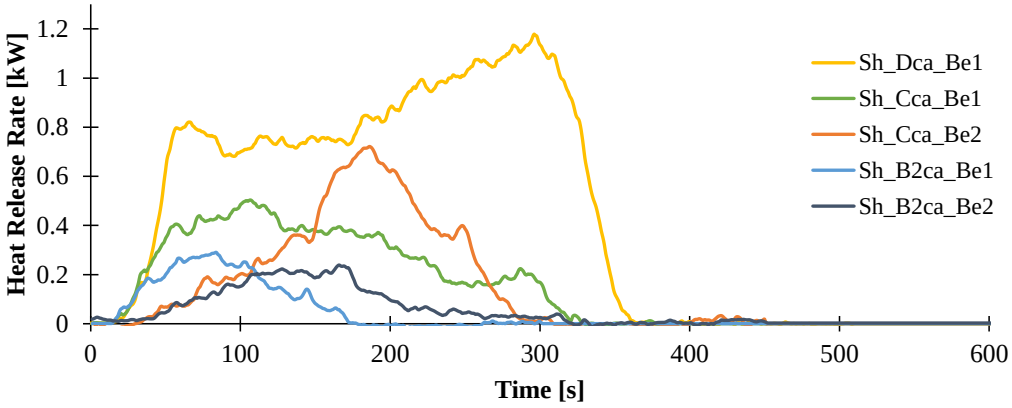

6

Figure 115 HRR curves using the small-scale test for five benchmark materials

Interestingly, these results show that the differences observed at the small scale followed the same trends as the one observed in the large-scale cable test EN 50399. These results were achieved only by testing a specimen of sheathing material instead of a whole cable. It is now questionable how to investigate the possibility of using the small-scale test for materials screening and for the prediction of the Euroclass ranking. Indeed, testing materials at the small scale would avoid the cable production phase, which can be costly and time consuming (especially if it has to be done in an industrial production unit). Therefore, it is important to determine criteria for the small-scale test that could be used to determine to the Euroclass classification.

V.2.3. DEVELOPMENT OF CORRELATIONS

In order to investigate correlations between the small-scale test and the EN 50399 test, the evolution of the previously determined parameter (pHRR, THR and damaged length) were plotted versus those measured at the large-scale tests. FIGRA was not considered since even the worst cable, Ca_D_{ca}_Be1, reached the certification level of $B2_{ca}$.

The plot of pHRR obtained at the large scale as a function of the pHRR obtained using the small-scale test shows a linear correlation (**Figure 116**). Cables with a pHRR higher than 30 kW cannot be classified $B2_{ca}$. Similarly, cables with a pHRR higher than 60 kW cannot be Euroclass C_{ca}. Using the equation of the linear correlation, it is thus possible to transpose these criteria to the small-scale test. It suggests that 0.45 and 1.25 kW are the limits for being $B2_{ca}$ and C_{ca} respectively in regards of the pHRR at the small scale.

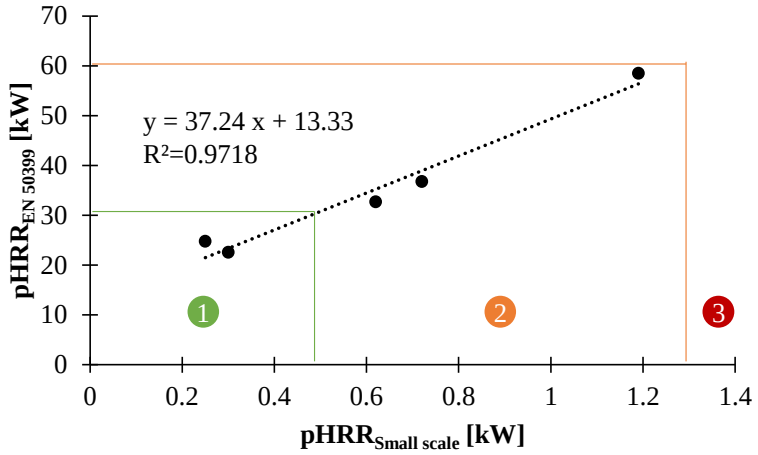

Figure 116: Correlation plot for pHRR. 1 represents the zone of Euroclass $B2_{ca}$; 2 represents the C_{ca} domain and 3 the D_{ca} domain

The approach used for the damaged length and THR is different from that used for pHRR. Indeed, Sh_D_{ca}_Be1 was not considered for the determination of the linear regression. Indeed, as the flame spread is limited to the length of the specimen, when the material burns up to the clamp, we had no indication to confirm or not if it would be the case with longer specimen. The fact that the flame spreads over the entire specimen at the small scale does not systematically indicates that a cable would burn completely at the large scale. In other words, 100 % of flame spread at the small scale does not represent 3 m of damaged length at the EN 50399. It can be argued that tests should then be carried out with longer specimen but for practical reasons (processability of the specimen in particular), a specimen size of 50 cm was selected.

Considering benchmark materials of cables classified $B2_{ca}$ and C_{ca}, it can thus be noted that a good correlation between the EN 50399 and the small-scale test is found (R^2 > 98%) as shown in **Figure 117**. According to the EN 50399 standard, with respect to the other parameters, cables exhibiting a damaged length higher than 2 m are classified D_{ca}, whereas cables exhibiting a damaged length lower than 1.5 m are classified $B2_{ca}$ and cables that in between are classified C_{ca}. Using the equation of the linear correlation, it is possible to define the same levels for the small-scale test. Namely, materials with a damaged length higher than 56.5 % are assumed to be D_{ca}. Materials with a damaged length lower than 44.2 % are $B2_{ca}$ and the materials presenting a damaged length in between are expected to be classified C_{ca}.

A limitation of the approach of the small-scale test and damaged length in particular, is due to the narrow range of damaged length for C_{ca} materials. Nonetheless, for the selected benchmark materials, flame spread is critical only for the D_{ca} cable. For this cable, the parameter driving its classification is the damaged length (pHRR and THR values are sufficiently low for getting C_{ca} classification) and this material behaves clearly differently than the others. For C_{ca} and $B2_{ca}$ classified benchmark, the damaged length values at the EN 50399 test are good enough for being classified $B2_{ca}$ (even if Ca_C_{ca}_Be1 and Ca_C_{ca}_Be2 are classified C_{ca}) and the correlation found using the selected benchmark material keeps the classifications.

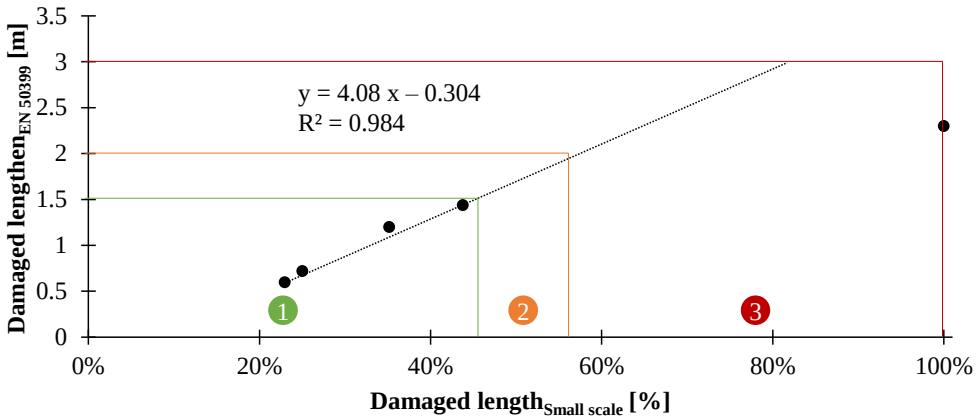

Figure 117: Correlation plot for Damaged length. 1 represents the zone of Euroclass B2ca; 2 represents the Cca domain and 3 the Dca domain

The correlation for THR is presented in **Figure 118**. A linear correlation is also found for the experimental data. Using the equation of the slope, it was found that materials exhibiting a THR higher than 63 kJ at the small scale should have a THR higher than 15 MJ at the EN 50399 and thus cannot be classified $B2_{ca}$. Similarly, materials with THR values higher than 133 kJ are assumed to be classified D_{ca} at the EN 50399 test. Note that there is a gap between the values obtained at the small scale: the highest value for C_{ca} materials is 89 kJ while the value for the material classified D_{ca} is at 263 kJ.

It can be noted that both pHRR and THR exhibit a good correlation between the small scale and the large-scale test even if the tested specimen at the small scale were dramatically simplified. The assumption considering that the sheathing governs the fire performance in the EN 50399 is thus verified

as the heat produced by the sheathing in the fire propagation test developed in this study correlates well with the heat released by the whole cable when tests are carried out at large scale.

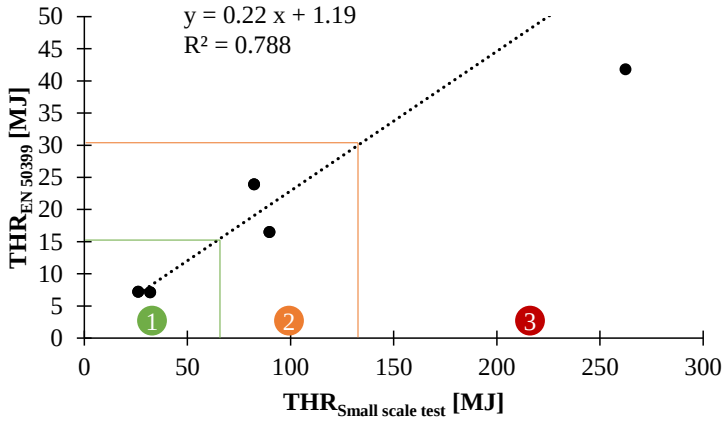

Figure 118: Correlation plot for THR. 1 represents the zone of Euroclass $B2_{ca}$; 2 represents the C_{ca} domain and 3 the D_{ca} domain

A summary of the level needed for reaching a given Euroclass according to the EN 50399 standard for pHRR, THR and damaged length is given in **Table 26** along with their translation found with the linear correlations presented from **Figure 116** to **Figure 118**. This shows that the developed small-scale test allows to differentiate both $B2_{ca}$, C_{ca} and D_{ca} materials.

Table 26: Euroclass criteria according to EN 50399 and the novel small scale test found using the correlations for pHRR, THR and damaged length

Euroclass	EN 50399	Small scale test
$\mathbf{B2_{ca}}$	Damaged length < 1.5 m	Damaged length < 44.2 %
	THR < 15 MJ	THR < 63 kJ
	pHRR < 30 kW	pHRR < 0.45 kW
$\mathbf{C_{ca}}$	Damaged length < 2.0 m	Damaged length < 56.5 %
	THR < 30 MJ	THR < 133 kJ
	pHRR < 60 kW	pHRR < 1.25 kW
$\mathbf{D_{ca}}$	-	Damaged length > 56.5 %
	THR < 70 MJ	THR > 133 kJ
	pHRR < 400 kW	pHRR >1.25 kW

V.2.4. CONCLUSION

In this section, five different benchmark cables' materials were tested in the previously developed bench-scale test in order to validate the approach. It was possible to evaluate the ability of the bench-scale test to differentiate the fire behavior of the cables. Indeed, the fire performances of the sheathing specimen in the bench-scale test followed the same trends that the EN 50399 results carried out on the whole cables. Correlations were thus developed between the bench-scale test and the EN 50399 results. It was shown that it is possible to correlate the values of pHRR, THR and damaged length from the large scale to the results in the newly developed small-scale test. This allowed to define criteria for predicting Euroclass classification based on small-scale test results.

In the next section of this chapter, the test as well as the developed correlations will be used for the development of a new cable.

V.3. NEW MATERIALS SCREENING

V.3.1. DESCRIPTION OF THE DESIGN OF EXPERIMENT

For demonstrating the ability of the novel small-scale test to allow rapid materials development, formulations were produced in the frame of a design of experiments (DoE). The materials were produced in order to investigate the effect of two additives in the fire behavior of polyolefin based cable flame retarded with ATH. These additives are proprietary and will not be detailed. Namely, the DoE was a central composite design (**Figure 119**) used in order to produce surface response and found the area where a $B2_{ca}$ classification can be obtained. The adjustable parameters are the amount of the two additives (Additive 1 and Additive 2). The concentrations of the additives were normalized. A third and main additive (ATH) is also used and the total loading of additives was set at 65 wt%. The polymer is the same material than the one used to prepare the benchmark cables $Ca\_C_{ca}\_Be1$ and $Ca\_B2_{ca}\_Be1$. Note that five levels of concentration for Additive 1 and Additive 2 were tested (-0.21, 0, 0.5, 1, 1.21).

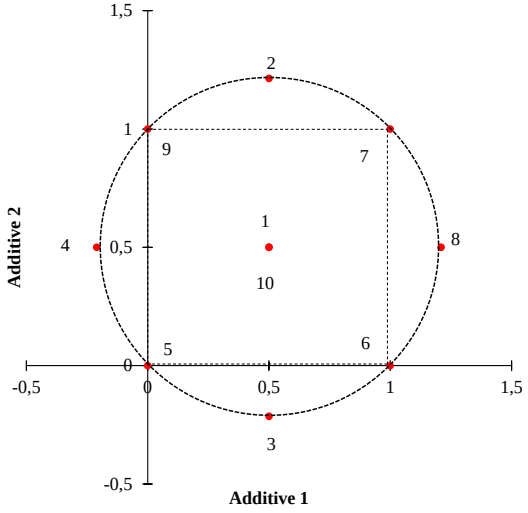

Figure 119: DoE and formulations number used in the study

The responses of this DoE are pHRR, THR and damaged length from the small-scale test but also pHRR and THR determined from standard cone calorimeter. The latter experiments were performed in order to investigate the fire performances of the designed materials and to evaluate if standard fire tests would give the same information about the most promising formulation. For both small-scale test and cone calorimeter, the experiments were run in triplicate to ensure the repeatability of the measurement.

V.3.2. EXPERIMENTAL RESULTS AND VALIDATION AT THE LARGE SCALE

V.3.2.a. Comparison of the bench-scale test results and cone calorimeter results

The behavior of the materials defined in the DoE was studied using our bench-scale test and cone calorimeter. The results are presented in **Figure 120**. According to the results obtained in the cone calorimeter, Sh_DoE7 and Sh_DoE2 exhibit the highest pHRR values (around 124 kW/m²) while on the opposite Sh_DoE3 and Sh_DoE5 exhibit the lowest values (around 96 kW/m²). However, considering a 10% of standard deviation [234,235], it could be concluded that most of the DoE formulations behave similarly. This would mean that there are no differences in terms of pHRR values for the ten formulations according to cone testing. At the opposite of the results obtained in the cone calorimeter, the formulations from the DoE showed significantly different behavior in the small-scale test.

Assuming a 10 % standard deviation, Sh_DoE1, Sh_DoE4, Sh_DoE9 and Sh_DoE10, exhibit a pHRR of 0.44 ± 0.05 kW. This would mean that these formulations would meet the criterion to reach a $B2_{ca}$ classification even if this value is close to the limit. Sh_DoE2, which shows one of the highest pHRR value according to cone testing, shows lowest pHRR value (0.31 kW) in the small-scale test demonstrating a totally different behavior depending on the test. Sh_DoE3 and Sh_DoE5 to Sh_DoE7 show the highest pHRR values in the small-scale test but do not reach the D_{ca} classification as there were below 1.25 kW.

As a conclusion, according to the pHRR values obtained in the bench-scale test Sh_DoE3, Sh_DoE5, Sh_DoE6 and Sh_DoE7 are at least classified C_{ca} while the other formulations can be classified $B2_{ca}$ depending on damaged length and THR results.

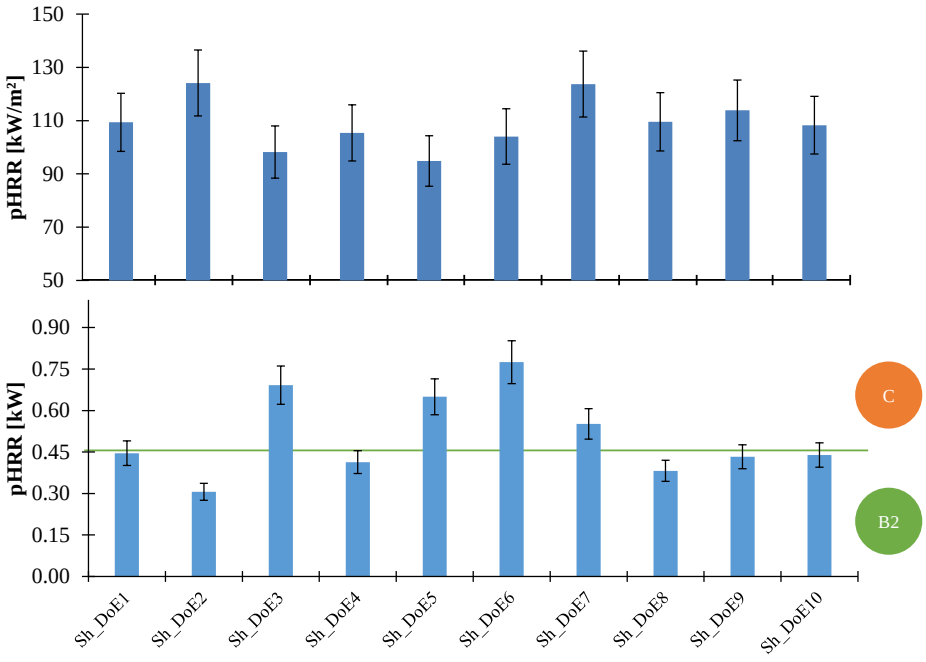

Figure 120: pHRR obtained for the DoE formulation in cone calorimeter (top) and small-scale test (bottom)

The results of the damaged length using the small-scale test on the DoE materials are presented in **Figure 121**. Sh_DoE2 and Sh_DoE9 exhibit the lowest damaged length as the flame spread over less than 20 % of the specimen length. Then, Sh_DoE1, Sh_DoE7, Sh_DoE8 and Sh_DoE10 show similar behavior with a damaged length between 25 and 30 % of the specimen. The damaged length of Sh_DoE4 and Sh_DoE5 is still under the criterion to reach a $B2_{ca}$ classification but these formulations are less performant since the flame spread to 35 and 44 % of the specimen. Note also that Sh_DoE5, which was among the worst formulation considering pHRR values, does not spread more than 45% and is thus classified C_{ca} (the damaged length is good enough for a $B2_{ca}$ classification but the pHRR is not). Finally, Sh_DoE3 and Sh_DoE6 are damaged at 71 and 98 % respectively. Sh_DoE6 and Sh_DoE3 behave then similarly than benchmark material Sh_D_{ca}_Be1.

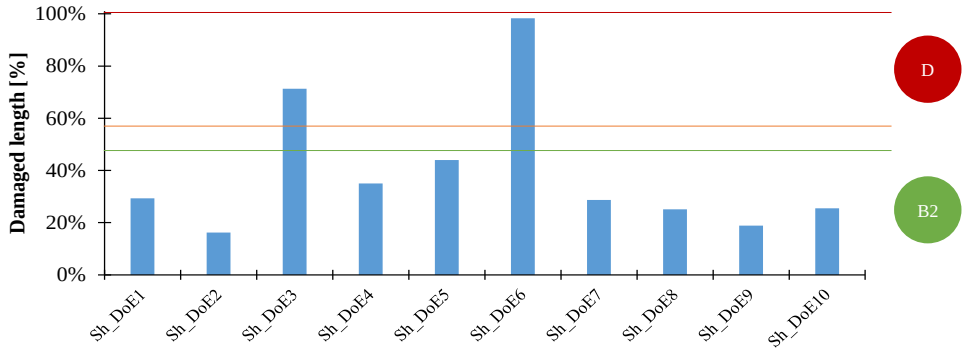

Figure 121: Damaged length obtained for the DoE formulation the small-scale test

As it was observed for the pHRR values, THR values obtained with the cone calorimeter exhibit few significant differences (**Figure 122**). THR values for Sh_DoE1, Sh_DoE3 to Sh_DoE6 and Sh_DoE8 to Sh_DoE10 are similar with respect to the margin of error of cone calorimeter. Those formulations exhibit an average value of 41.5 MJ/m². Sh_DoE2 and Sh_DoE7 exhibit higher THR values with an average value of 47.2 MJ/m². It is interesting to note that even if these formulations release a high amount of heat when measured in the cone calorimeter conditions, their performances in the small-scale test are rather good since Sh_DoE2 exhibits the lowest THR.

It can thus be seen in **Figure 122** that they are clear differences between THR values measured with the small-scale test compared to those measured in the cone calorimeter. This can be attributed to the fact that THR is linked to the damaged length whereas in the cone calorimeter, a constant surface and thus a constant amount of materials burns. In the small scale test, as the flame spread, more and more material burns and the THR increases up to the flame out. As a consequence, the highest THR values are obtained for the materials exhibiting the highest damaged length. Sh_DoE3 and Sh_DoE6 show the worst behavior (THR of 101 and 179 kJ respectively). It can be noted that Sh_DoE6 is the only formulation, which exceed the level for being classified D_{ca} considering THR (133 kJ).

Note that formulation Sh_DoE5 (62.5 kJ) is at the limit of the criterion for being classified C_{ca} (63 kJ). Nonetheless as it exhibits a high pHRR value (0.65 kW) it is classified C_{ca}. Interestingly, Sh_DoE1, Sh_DoE4 and Sh_DoE9 to Sh_DoE10 showed pHRR values close to the limit for being classified C_{ca} but for THR, their values (25-35 kJ) are below the limit (63 kJ). This shows that they release a high amount of heat after ignition but they present good enough fire-retardant properties for limiting the flame

spread and thus the specimens flame out rapidly. Indeed, the time to flameout for Sh_DoE1, Sh_DoE4 and Sh_DoE9 to Sh_DoE10 is lower than 180 s when the flame out appears after 230 s for Sh_DoE3, Sh_DoE5 and Sh_DoE6 which exhibit the highest THR.

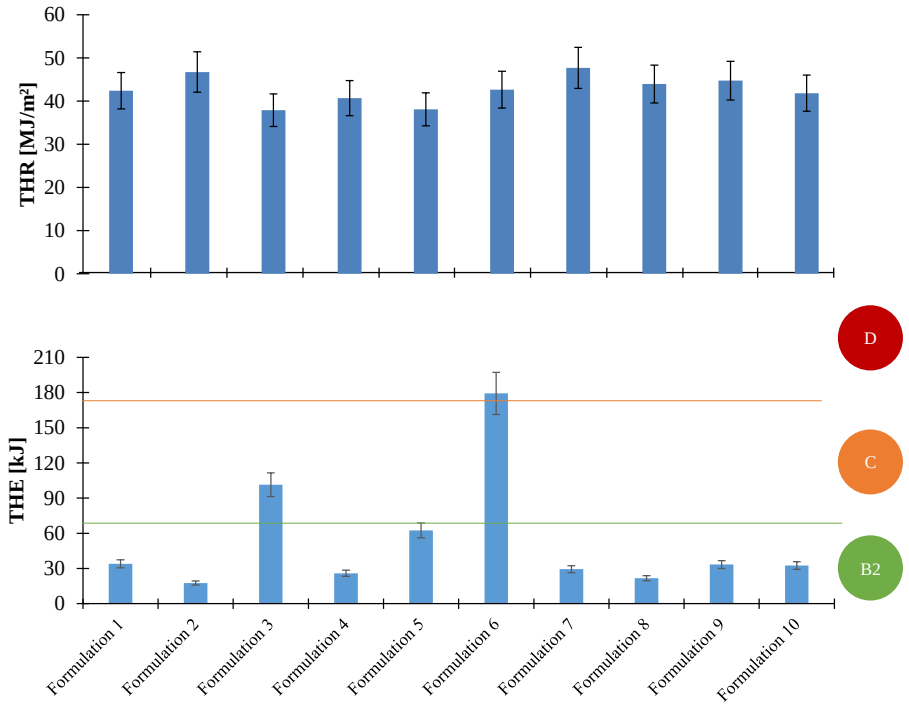

Figure 122: THR obtained for the DoE formulation in cone calorimeter (top) and small-scale test (bottom)

V.3.2.b. Predicted Euroclass of the DoE materials

Based on these experiments and using the levels defined for THR, pHRR and damaged length defined in **Table 26**, it is possible to predict the Euroclass of the formulations from the DoE. The expected classification is presented in **Table 27**. Note that in the DoE, Sh_DoE6 and Sh_DoE3 are expected to achieve a D_{ca} classification. These formulations correspond to the formulation containing a low amount of Additive 2 and medium to high amount of Additive 1. Two formulations are expected to be Euroclass C_{ca}: Sh_DoE5 and Sh_DoE7. These materials correspond to formulation with low amount of each additive or high amount of each additives respectively. The other formulations (Sh_DoE1, Sh_DoE2, Sh_DoE4, Sh_DoE8, Sh_DoE9 and Sh_DoE10) are expected to reach a $B2_{ca}$ classification. They correspond to formulation with a high or medium amount of Additive 2 and low to medium amount of

Additive 1. Among them, Sh_DoE1, Sh_DoE9 and Sh_DoE10 are close to be classified C_{ca} because of their high pHRR values.

Table 27: Expected Euroclass for DoE materials according to the small-scale test.

Formulation	Predicted Euroclass
Sh_DoE1	$B2_{ca}$ (limit C_{ca} - pHRR)
Sh_DoE2	$B2_{ca}$
Sh_DoE3	D_{ca}
Sh_DoE4	$B2_{ca}$
Sh_DoE5	C_{ca}
Sh_DoE6	D_{ca}
Sh_DoE7	C_{ca}
Sh_DoE8	$B2_{ca}$
Sh_DoE9	$B2_{ca}$ (limit C_{ca} - pHRR)
Sh_DoE10	$B2_{ca}$ (limit C_{ca} - pHRR)

V.3.2.c. Choice of the most promising formulation

Based on the DoE, it was thus possible to produce a surface response combining the three criteria for the Euroclass as defined in **Table 26**. The results are presented in **Figure 123** and it is clearly shown that a large array of formulation is possible for getting a Euroclass $B2_{ca}$ using Additive 1 and Additive 2 in combination with ATH. It is clear that there is an antagonism effect using Additive 1 at high loading with the other flame-retardants as it is the only area of the surface response giving Euroclass D_{ca}.

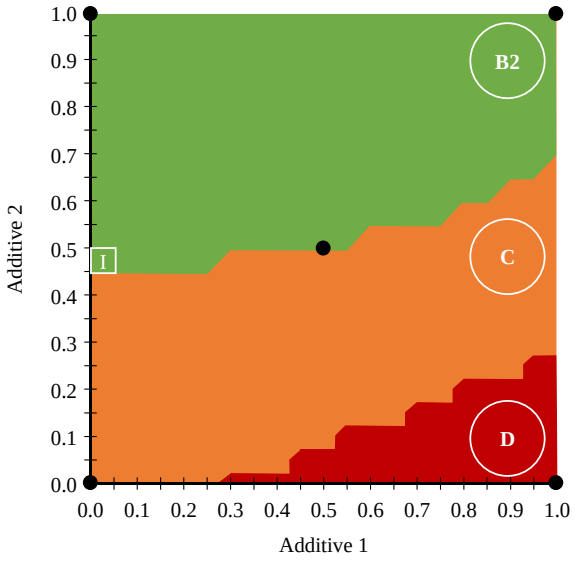

Figure 123: Surface response obtained through the DoE and experimental tested formulations (points)

The analysis of this DoE went further with a cost analysis and the analysis of the mechanical properties (tensile strength, elongation at break and melt flow index) of the formulations. Using these surface responses analysis, an optimized formulation was selected and tested in the large-scale test according to the EN 50399 standard (formulation I in **Figure 123**). We may thus calculate that the prototype should exhibit a damaged length of 34 ± 6 % along with a pHRR value of 0.40 ± 0.02 kW and a THR of 25 ± 8 kJ. The expected EN 50399 results obtained according to the correlations from the bench-scale test results are presented in **Table 28**. The experimental results obtained on the final cable prototype are also presented.

Table 28: Predicted small scale test according to the DoE analysis, predicted EN 50399 and experimental EN 50399 results

	Small scale test	**EN 50399 predicted**	**EN 50399 experiment**
Damaged length	34.2 ± 6.1 %	0.84-1.34 m	0.66 m
pHRR	0.43 ± 0.02 kW	28-30 kW	15 kW
THR	25 ± 8 kJ	4.9-8.4 MJ	6 MJ
Classification		$B2_{ca}$	$B2_{ca}$

The predicted values for the EN 50399 obtained from the fire retardant parameters determined in the small-scale test overestimate the experimental results. Indeed, the damaged length is measured at 0.66 m while it is predicted between 0.84 and 1.34 m. Similarly, a value of 15 kW was obtained for the pHRR while a value between 28 and 30 kW was predicted. The agreement for those two parameters is nonetheless acceptable considering the uncertainties of either EN 50399 [21,236,237], of the bench scale test and of the surface response analysis. The THR is very well predicted. A value of 6 MJ is obtained within the EN 50399 test while it was expected between 4.9 and 8.4 MJ. The most important result lies in the fact that the Euroclass is well predicted using the approach proposed in this part since the prototype shows a $B2_{ca}$ rating.

V.4. CONCLUSION

The development of new cables truly lacks for efficient and accessible fire tests that can be used for fast and reliable materials screening. By analyzing the cable design and studying the fire behavior of each component of a cable, it was shown that the outer sheathing is the key component of the cable delivering more than 60 % of the heat released during the tests. It was suggested to focus our attention on this component for the specimen design leading to a dramatic simplification of the production of the tested specimen that is of high interest for fast screening and hence, for fast development of new cables.

Then, a bench-scale enclosure fire test of around $1/8^{th}$ of the size of the large-scale certification test EN 50399 was developed and allowed to evaluate the flame spread as well as the heat released rate of cable sheathing materials when exposed to a flame. Preliminary tests with benchmark materials showed that the measurements of flame spread and HRR was reliable and repeatable. It was also demonstrated that the novel bench-scale test carried out on the sheathing materials was able to discriminate the behavior of cables presenting various classification according to the Euroclass. It was highlighted that testing outer sheathing specimen using this bench-scale test correlates well with a large-scale test carried out on bunched cables. Linear correlations between the small-scale test and the large scale EN 50399 results were obtained for the benchmark materials considering pHRR, THR and damaged length. This further validates our approach consisting of a downscaling of the EN 50399 to predict Euroclass classification of cables.

The ability of the bench-scale for fast material screening was then used for designing a new cable. More precisely, new materials based on ATH and two flame-retardants additives were then produced in the frame of a Design of Experiments. The evaluation of their fire performances was conducted using both

a standard cone calorimeter and the novel bench-scale test. Clear differences were observed between the formulations using the novel bench-scale test while no significant differences were observed with the cone calorimeter. Moreover, at the opposite of cone testing, it was also possible to evaluate the flame spread behavior of the materials in a fire scenario close to the one of the certification test. Finally, considering fire retardant, cost and mechanical properties, an expected optimum formulation was selected and tested in the EN 50399 in order to validate the approach developed in this study. A reasonable agreement between the predicted results based on a cable sheathing specimen at the bench-scale and the fire performance of the whole cable was obtained. Indeed, the right Euroclass was predicted and a $B2_{ca}$ cable was thus developed.

Based on these results, it was demonstrated that it is possible to evaluate and to predict the fire performance of complex products based on small scale testing of a relevant component of the product. The novel bench-scale test offers a reliable, fast and promising method for the prediction of the fire behavior of cable.

GENERAL CONCLUSION

This study was dedicated to the development of tools, such as numerical models and small-scale tests, to support the development of new materials for cables. As more and more cables are based on polyolefins flame retarded with a combination of metal hydroxide (ATH for instance) and synergists such as nanoclays, a literature review showed that their thermo-physical properties were seldom studied. Moreover, up to now, the developed pyrolysis models differ in their complexity but almost none of them were used to predict the fire behavior of formulated materials. This was attributed to the lack of methodologies developed to characterize flame-retarded materials or to missing data that described these materials such as EVA/ATH materials.

The first purpose of this PhD was to develop methodologies for the characterization of the parameters describing the materials so they can be used as inputs for a pyrolysis model. Using model free analysis of TG data, the kinetics of decomposition of EVA/ATH formulations were determined in a reliable manner. Hence, the kinetic parameters describing the decomposition of the formulations in various conditions (from slow to high heating rates) were determined. Similarly, by carefully investigating the decomposition of the materials, it was possible to separate the different decomposition species that are formed when the materials decompose. It was then possible to characterize the heat capacity and the thermal conductivity of each species as a function of temperature using novel protocols. The optical properties of the materials were also investigated as well as the heat capacity of the decomposition gases.

Using all the experimentally determined inputs data characterizing the materials, it was then possible to model their pyrolysis in CAMLC experiments where no flaming could occurs. By comparing the experimental and simulated mass loss and temperature profiles, it was shown that using the previously determined inputs, the behavior of the materials could be predicted with a reasonable agreement validating the methodologies developed in this study. It was also shown that the decomposition gases diffuse slowly inside the materials as they decompose. Parametric studies were then performed in order to estimate the impact of the implementation of the thermo-physical properties, of the kinetics of decomposition and of the optical properties. It was found that it is essential to use temperature-dependent thermo-physical parameters. It was also shown that it is important to consider the absorption of heat inside the materials with a Beer-Lambert law and not just to set the incident heat flux as a boundary conditions. Finally, parametric studies were also performed in order to find suitable parameters to describe the flaming conditions. The prediction of the mass loss of EVA/ATH composites can be modelled using an additional heat flux from the flame of 20 kW/m² and critical mass flux for ignition of 1.6 and 0.7 g/m²/s for EVA/ATH and EVA/ATH/NC respectively, the conversion of MLR data into HRR is more challenging. This can be attributed to the presence of ATH as this flame retardant releases water.

The HRR is thus not directly proportional to the MLR, as generally met in other studies, as the combustibles gases are diluted by water.

On the other hand, cables are multi-components products with complex geometries. While it is uneasy to predict the behavior of flame retarded materials, the modelling of the interaction of several materials in a complex geometry is even more difficult. A second approach was then used in order to propose new tools for the development of new materials for cable application and a small-scale test was thus created. By carefully analyzing the contribution to fire of each cable component, it was found that the external sheathing was the component governing the fire performance of the whole cable. A scaled down enclosure mimicking the fire scenario of the large-scale certification test was then created. By testing strip of jacket's materials from benchmark cables, it was shown that the downscaling approach allows to predict the Euroclass classification of the corresponding cables. Moreover, it was found that the bench-scale test results carried out on the jacket specimen correlate with the large-scale test on a ladder of cables. The small-scale test was then used as a screening tool for the development of new flame-retarded materials. It was shown that the bench-scale test was able to predict the fire performance at the large scale of a new material. A prototype of the most promising formulations was produced and tested in a large-scale certification test which results were well predicted by the bench-scale test experiments.

OUTLOOK

It was shown in this study that is possible to estimate the fire behavior of cables by testing a thin strip of jacket specimen. It was also shown that the characterization of the inputs data required for pyrolysis modelling was achievable even for flame-retarded materials. This permits to accurately model the mass loss in flaming conditions. Even if the prediction of the heat release rate was not excellent, it was reasonably modelled. It is then questionable if the behavior of cables based on polyolefin flame retarded with ATH in a large-scale test could be modelled. For that purpose, an industrial formulation of sheathing material based on PE/ATH was characterized using the methodologies presented in this PhD. This corresponds to the jacket of the cable Ca_Dca_Be1 and its properties are reported elsewhere [192]. A FDS model was created in the frame of the FP7 project DEROCA by Michael Försth and Petra Andersson from SP Technical research Institute of Sweden. This model was not published yet but more explanation about it can be found in **Appendix 1**.

One of the limitations of large-scale models is that it is impossible to implement the cables design. In a first approach, the cables will be described as cylindrical Lagragian particle made only of jacket material with a radius of 6 mm. The HRR is described using either a pyrolysis model from FDS or by using a HRR curve from the cone calorimeter. For this matter, an ignition temperature of 302 °C was determined with the approach of Janssen as presented in **I.2.1.a** (p.17) by testing 6 mm plaque of materials under 5, 15, 20, 25, 35 and 50 kW/m² irradiance. It can be seen in **Figure 124** that the prediction of the HRR in the EN 50399 apparatus is poor using FDS. Indeed, with the two approaches, the HRR is delayed of around 100 or 200 s compared to the experimental data.

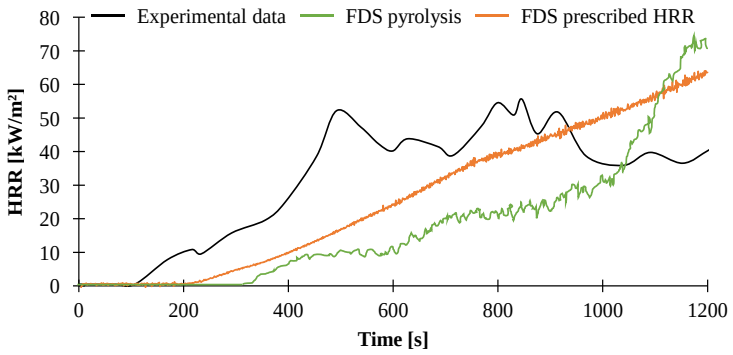

Figure 124: Experimental and simulated HRR in the EN 50399 test using FDS pyrolysis model and using FDS implemented with a cone calorimeter curve

It is then questionable if this effect is due to the model itself or to the implementation of the cable design. In order to further investigate this effect, the cables were described as a tube and no more as a cylinder. This approach considered the prescribed HRR model as it is faster to use and gives similar results than the pyrolysis model. The size of the inner hole was also studied as shown in **Figure 125**. It can be seen that the higher the hole radius, the faster the heat released and the higher the HRR values. Nonetheless, there is no purpose to use this kind of cables description, as it does not increase the predictive capabilities of the FDS model.

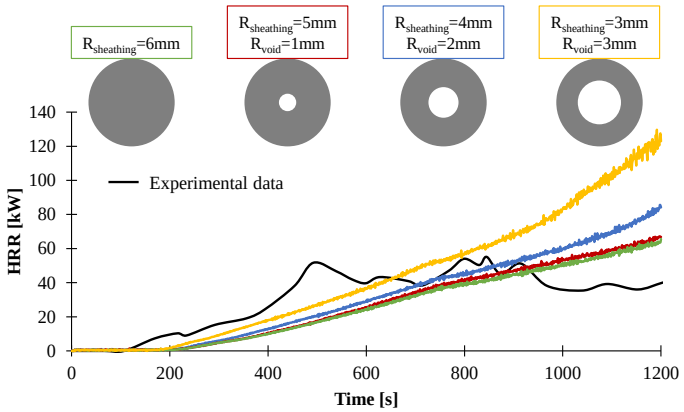

Figure 125: Experimental and simulated HRR in the EN 50399 test using FDS prescribed HRR model for different hole radius

Finally, using the prescribed HRR model, it was decided to plot the temperature profiles of the particles in one location. In each location, several oriented particles are placed so they can take into account the anisotropy of the thermal exposure in the test apparatus. It can be seen in **Figure 126** that the model is able to take into account the anisotropy of the EN 50399 apparatus. Indeed, the particles oriented through the rear face of the apparatus (particles 4 to 6) can be up to 200 °C hotter than the particles oriented through the front face of the cable ladder (particles 8, 1 and 2). Experimentally, a temperature difference up to 400 °C was observed [238]. Note also that the predicted maximum temperature 43 cm higher than the burner should be around 700 °C when it is predicted at 615 °C only. The use of multiple Lagragian particle shows to be very effective to consider the anisotropy of the thermal exposure of the cables.

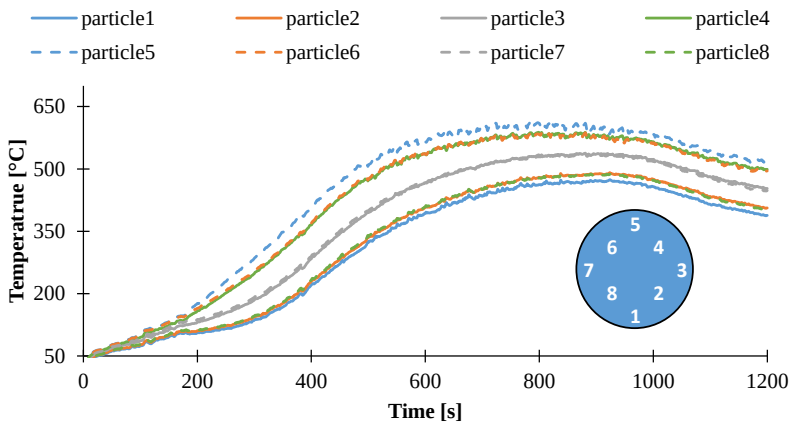

Figure 126: Simulated temperature using FDS model 30 cm above the burner depending on the orientation of the particle

The modelling of complex products, based on formulated materials at the large scale is uneasy. It was shown in this PhD that it is possible to characterize and model the MLR and HRR behavior of formulated materials and to develop a small scale test that allows the prediction of the behavior of cables at large scale test. It can be assumed that the modelling of such test should be more easily achievable. The use of numerical model and the correlations between the bench-scale test and the EN 50399 should permit to predict the Euroclass using intrinsic materials properties. Such numerical model should thus be investigated.

Moreover, it was shown here that it was possible to describe in a reliable manner the thermal exposure and the anisotropy of complex test such as the EN 50399. However, the prediction of large-scale tests results is not achievable yet. Some efforts have to be put on the coupling of a CFD model such as FDS with another pyrolysis model that could solve the heat transfer inside a real cables' design instead of using cylindrical made of one materials.

LIST OF TABLES, FIGURES AND REFERENCES

List of figures

List of tables

List of tables

References

1. van Hees, P.; Andersson, P.; Hjohlman, M.; Wenne, N.; Hassan, M. A. Use of the Cone Calorimeter and ConeTools software for development of innovative intumescing graphite systems. *Fire Mater.* **2010**, *34*, 367–384.

2. McGrattan, K.; Hostikka, S.; McDermott, R.; Floyd, J.; Weinschenk, C.; Overholt, K. Fire Dynamics Simulator (version 6) User's guide. National Institute of Standards and Technology Special Publication, 1019. **2013**.

3. Lautenberger, C.; Fernandez-Pello, C. Generalized pyrolysis model for combustible solids. *Fire Saf. J.* **2009**, *44*, 819–839.

4. Stoliarov, S. I.; Lyon, R. E. Thermo-kinetic model of burning for pyrolyzing materials. **2008**, Federal Aviation Administration, DOT/FAA/AR–TN08/1.

5. Snegirev, A. Y.; Talalov, V. A.; Stepanov, V. V.; Harris, J. N. A new model to predict pyrolysis, ignition and burning of flammable materials in fire tests. *Fire Saf. J.* **2013**, *59*, 132–150.

6. Williams, E. G.; Paton, J. G.; Fawcett, E. W.; Perrin, M. W. Improvements in or relating to the interpolymerisation of ethylene with other organic compounds 1938.

7. Perrin, M. W.; Fawcett, E. W.; Paton, J. G.; Williams, E. G. Interpolymerization of ethylene 1940.

8. Roedel, M. Ethylene/vinyl acetate polymerization process 1955.

9. Schellenberg, W.-D.; Bartl, H. Process for the continuous preparation of ethylene/vinyl acetate copolymers using serially arranged reaction zones 1967.

10. Bartl, H. Process for the production of copolymers of ethylene 1960.

11. Junsuke, T.; Kenji, M. Proces for continuous production of ethylene-vinyl acetate copolymer 1985.

12. Meisenheimer, H.; Zens, A. Ethylene Vinylacetate Elastomers. In *Handbook of Specialty Elastomers*; Klingender, R. C., Ed.; CRC Press, 2008.

13. Yatsu, T.; Moriuchi, S.; Fujii, H. Copolymerization of Ethylene with Vinyl Acetate by Trialkylaluminum-Lewis Base-Peroxide Catalyst. *Macromolecules* **1977**, *10*, 249–253.

14. Saegusa, T.; Yatsu, T.; Miyaji, S.; Fujii, H. Dual Site Character of AlEt3-ZnCl2-CCl4 Catalyst in the Copolymerization of Ethylene with Vinyl Acetate. *Polym. J.* **1970**, *1*, 7–12.

15. Henderson, A. M. Ethylene-vinyl acetate (EVA) copolymers: a general review. *IEEE Electr. Insul. Mag.* **1993**, *9*, 30–38.

16. Seeger, A.; Freitag, D.; Freidel, F.; Luft, G. Melting point of polymers under high pressure. *Thermochim. Acta* **2004**, *424*, 175–181.

17. ISO 3795-2, Road vehicles, and tractors and machinery for agriculture and forestry -- Determination of burning behaviour of interior materials. **1989**.

18. EN 13501-2 Fire classification of construction products and building elements. **2007**.

19. ISO 1716, Reaction to fire tests for products - Determination of the gross heat of combustion (calorific value). **2010**.

20. EN 60332-1-2 Tests on electric and optical fibre cables under fire conditions - Part 1-2: Test for vertical flame propagation for a single insulated wire or cable - Procedure for 1 kW pre-mixed flame. **2004**.

21. EN 50399 Common test methods for cables under fire conditions. Heat release and smoke production measurement on cables during flame spread test. Test apparatus, procedures, results. **2011**.

22. Meisenheimer, H. Ethyelene-Vinyl Elastomers (EVM) for Improved Safety in Mass Transit. In *Polymers in Mass Transit Conference*; 2001.

23. Price, D.; Pyrah, K.; Hull, T. R.; Milnes, G. J.; Ebdon, J. R.; Hunt, B. J.; Joseph, P. Flame retardance of poly(methyl methacrylate) modified with phosphorus-containing compounds. *Polym. Degrad. Stab.* **2002**, *77*, 227–233.

24. Wang, H.; Wang, Q.; Huang, Z.; Shi, W. Synthesis and thermal degradation behaviors of hyperbranched polyphosphate. *Polym. Degrad. Stab.* **2007**, *92*, 1788–1794.

25. Weil, E. D.; Levchik, S. V. Flame Retardants in Commercial Use or Development for Polyolefins. *J. Fire Sci.* **2008**, *26*, 5–43.

26. Yang, C.-P.; Chen, W.-T. Effects of brominated flame retardants and crosslinking agents on the flame retardancy of rubbers. *J. Appl. Polym. Sci.* **1988**, *36*, 963–978.

27. Zhang, X.; Guo, F.; Chen, J.; Wang, G.; Liu, H. Investigation of interfacial modification for flame retardant ethylene vinyl acetate copolymer/alumina trihydrate nanocomposites. *Polym. Degrad. Stab.* **2005**, *87*, 411–418.

28. Fernández, A. I.; Haurie, L.; Formosa, J.; Chimenos, J. M.; Antunes, M.; Velasco, J. I. Characterization of poly(ethylene-co-vinyl acetate) (EVA) filled with low grade magnesium hydroxide. *Polym. Degrad. Stab.* **2009**, *94*, 57–60.

29. Huang, G.; Fei, Z.; Chen, X.; Qiu, F.; Wang, X.; Gao, J. Functionalization of layered double hydroxides by intumescent flame retardant: Preparation, characterization, and application in ethylene vinyl acetate copolymer. *Appl. Surf. Sci.* **2012**, *258*, 10115–10122.

30. Zhang, G.; Ding, P.; Zhang, M.; Qu, B. Synergistic effects of layered double hydroxide with hyperfine magnesium hydroxide in halogen-free flame retardant EVA/HFMH/LDH nanocomposites. *Polym. Degrad. Stab.* **2007**, *92*, 1715–1720.

31. Hull, T. R.; Witkowski, A.; Hollingbery, L. Fire retardant action of mineral fillers. *Polym. Degrad. Stab.* **2011**, *96*, 1462–1469.

32. Alongi, J.; Pošković, M.; Frache, A.; Trotta, F. Novel flame retardants containing cyclodextrin nanosponges and phosphorus compounds to enhance EVA combustion properties. *Polym. Degrad. Stab.* **2010**, *95*, 2093–2100.

33. Jiao, C.; Wang, Z.; Chen, X.; Yu, B.; Hu, Y. Irradiation crosslinking and halogen-free flame retardation of EVA using hydrotalcite and red phosphorus. *Radiat. Phys. Chem.* **2006**, *75*, 557–563.

34. Nguyen, C.; Lee, M.; Kim, J. Relationship between structures of phosphorus compounds and flame retardancies of the mixtures with acrylonitrile-butadiene-styrene and ethylene-vinyl acetate copolymer. *Polym. Adv. Technol.* **2011**, *22*, 512–519.

35. Cérin, O.; Duquesne, S.; Fontaine, G.; Roos, A.; Bourbigot, S. Thermal degradation of elastomeric vulcanized poly(ethylene-co-vinyl acetate) (EVM): Chemical and kinetic investigations. *Polym. Degrad. Stab.* **2011**, *96*, 1812–1820.

36. Cérin, O. Development and charaterization of a novel flame retardant EVM-based formulation: investigation and comprehension of the flame retardant mechnisms, University of Lille 1 - Sciences and Technologies, 2010.

37. Zilberman, J.; Hull, T. R.; Price, D.; Milnes, G. J.; Keen, F. Flame retardancy of some ethylene-vinyl acetate copolymer-based formulations. *Fire Mater.* **2000**, *24*, 159–164.

38. Hoffendahl, C.; Fontaine, G.; Duquesne, S.; Taschner, F.; Mezger, M.; Bourbigot, S. The combination of aluminum trihydroxide (ATH) and melamine borate (MB) as fire retardant additives for

elastomeric ethylene vinyl acetate (EVA). *Polym. Degrad. Stab.* **2015**, *115*, 77–88.

39. Basfar, A. A.; Bae, H. J. Influence of Magnesium Hydroxide and Huntite Hydromagnesite on Mechanical Properties of Ethylene Vinyl Acetate Compounds Cross-linked by DiCumyl Peroxide and Ionizing Radiation. *J. Fire Sci.* **2009**, *28*, 161–180.

40. Sabet, M.; Hassan, A.; Ratnam, C. T. Effect of zinc borate on flammability/thermal properties of ethylene vinyl acetate filled with metal hydroxides. *J. Reinf. Plast. Compos.* **2013**, *32*, 1122–1128.

41. Carpentier, F.; Bourbigot, S.; Le Bras, M.; Delobel, R.; Foulon, M. Charring of fire retarded ethylene vinyl acetate copolymer — magnesium hydroxide/zinc borate formulations. *Polym. Degrad. Stab.* **2000**, *69*, 83–92.

42. Fu, M.; Qu, B. Synergistic flame retardant mechanism of fumed silica in ethylene-vinyl acetate/magnesium hydroxide blends. *Polym. Degrad. Stab.* **2004**, *85*, 633–639.

43. Huang, H.; Tian, M.; Liu, L.; He, Z.; Chen, Z.; Zhang, L. Effects of silicon additive as synergists of Mg(OH)2 on the flammability of ethylene vinyl acetate copolymer. *J. Appl. Polym. Sci.* **2006**, *99*, 3203–3209.

44. Ye, L.; Miao, Y.; Yan, H.; Li, Z.; Zhou, Y.; Liu, J.; Liu, H. The synergistic effects of boroxo siloxanes with magnesium hydroxide in halogen-free flame retardant EVA/MH blends. *Polym. Degrad. Stab.* **2013**, *98*, 868–874.

45. Cardelli, A.; Ruggeri, G.; Calderisi, M.; Lednev, O.; Cardelli, C.; Tombari, E. Effects of poly(dimethylsiloxane) and inorganic fillers in halogen free flame retardant poly(ethylene-co-vinyl acetate) compound: A chemometric approach. *Polym. Degrad. Stab.* **2012**, *97*, 2536–2544.

46. Wang, L.; Wang, G.; Jiang, P. Research on the related properties of EVM/Al(OH)3/SiO2 composites applied for halogen-free flame retardant cable insulation and jacket. *J. Appl. Polym. Sci.* **2011**, *120*, 368–378.

47. Ye, L.; Wu, Q.; Qu, B. Synergistic effects and mechanism of multiwalled carbon nanotubes with magnesium hydroxide in halogen-free flame retardant EVA/MH/MWNT nanocomposites. *Polym. Degrad. Stab.* **2009**, *94*, 751–756.

48. Huang, N. H.; Chen, Z. J.; Yi, C. H.; Wang, J. Q. Synergistic flame retardant effects between sepiolite and magnesium hydroxide in ethylene-vinyl acetate (EVA) matrix. *Express Polym. Lett.* **2010**, *4*, 227–233.

49. Durin-France, A.; Ferry, L.; Lopez Cuesta, J.-M.; Crespy, A. Magnesium hydroxide/zinc borate/talc compositions as flame-retardants in EVA copolymer. *Polym. Int.* **2000**, *49*, 1101–1105.

50. Laoutid, F.; Gaudon, P.; Taulemesse, J.-M.; Lopez Cuesta, J.-M.; Velasco, J. I.; Piechaczyk, A. Study of hydromagnesite and magnesium hydroxide based fire retardant systems for ethylene–vinyl acetate containing organo-modified montmorillonite. *Polym. Degrad. Stab.* **2006**, *91*, 3074–3082.

51. Szép, A.; Szabó, A.; Tóth, N.; Anna, P.; Marosi, G. Role of montmorillonite in flame retardancy of ethylene–vinyl acetate copolymer. *Polym. Degrad. Stab.* **2006**, *91*, 593–599.

52. Ahamad, A.; Patil, C. B.; Mahulikar, P. P.; Hundiwale, D. G.; Gite, V. V. Studies on the flame retardant, mechanical and thermal properties of ternary magnesium hydroxide/clay/EVA nanocomposites. *J. Elastomers Plast.* **2011**, *44*, 251–261.

53. Chen, X.; Jiao, C.; Zhang, J. Thermal and combustion behavior of ethylene-vinyl acetate/aluminum trihydroxide/Fe-montmorillonite composites. *Polym. Eng. Sci.* **2012**, *52*, 414–419.

54. Yen, Y.-Y.; Wang, H.-T.; Guo, W.-J. Synergistic flame retardant effect of metal hydroxide and nanoclay in EVA composites. *Polym. Degrad. Stab.* **2012**, *97*, 863–869.

55. Manias, E.; Polizos, G.; Nakajima, H.; Heidecker, M. J. Fundamental of Polymer Nanocomposites Technology. In *Flame Retardant Polymer Nanocomposites*; Wilkie, C. A.; Morgan, A. B., Eds.; John Wiley and Sons, 2007.

56. Tjong, S. C. Structural and mechanical properties of polymer nanocomposites. *Mater. Sci. Eng. R Reports* **2006**, *53*, 73–197.

57. Duquesne, S.; Jama, C.; Le Bras, M.; Delobel, R.; Recourt, P.; Gloaguen, J. M. Elaboration of EVA–nanoclay systems—characterization, thermal behaviour and fire performance. *Compos. Sci. Technol.* **2003**, *63*, 1141–1148.

58. Ramírez-Vargas, E.; Sánchez-Valdes, S.; Parra-Tabla, O.; Castañeda-Gutiérrez, S.; Méndez-Nonell, J.; Francisco Ramos-deValle, L.; López-León, A.; Lujan-Acosta, R. Structural characterization of LDPE/EVA blends containing nanoclay-flame retardant combinations. *J. Appl. Polym. Sci.* **2012**, *123*, 1125–1136.

59. Beyer, G. Flame Retardancy of Nanocomposites - from Research to Technical Products. *J. Fire Sci.* **2005**, *23*, 75–87.

60. Beyer, G. Flame retardant properties of EVA-nanocomposites and improvements by combination of nanofillers with aluminium trihydrate. *Fire Mater.* **2001**, *25*, 193–197.

61. Available from http://serc.carleton.edu/images/NAGTWorkshop/Mineralogy/montmorillonite_structure.jpg.

62. Gilman, J. W.; Jackson, C. L.; Morgan, A. B.; Harris, R. H.; Manias, E.; Giannelis, E. P.; Wuthenow, M.; Hilton, D.; Phillips, S. H. Flammability Properties of Polymer−Layered-Silicate Nanocomposites. Polypropylene and Polystyrene Nanocomposites †. *Chem. Mater.* **2000**, *12*, 1866–1873.

63. Lewin, M. Some comments on the modes of action of nanocomposites in the flame retardancy of polymers. *Fire Mater.* **2003**, *27*, 1–7.

64. Gilman, J. W.; Kashiwagi, T.; Morgan, A. B.; Harris, R. H.; Brassel, L.; Awad, W. H.; Davis, R. D.; Chyall, L.; Sutto, P. C.; Trulove, T.; DeLong, H. Recent advances in flame retardant polymer nanocomposites. In *International SAMPE Symposium and Exhibition*; Long Beach, CA, USA, 2001.

65. Leszczyńska, A.; Njuguna, J.; Pielichowski, K.; Banerjee, J. R. Polymer/montmorillonite nanocomposites with improved thermal properties. *Thermochim. Acta* **2007**, *454*, 75–96.

66. Bouvet, N.; Linteris, G.; Babushok, V.; Takahashi, F.; Katta, V.; Krämer, R. Experimental and numerical investigation of the gas-phase effectiveness of phosphorus compounds. *Fire Mater.* **2015**, n/a–n/a.

67. Takahashi, F.; Katta, V. R.; Linteris, G. T.; Babushok, V. Simulations of gas-phase interactions of phosphorus flame retardants with diffusion flame structure. In *Fire and Materials 2015 - 14th International Conference and Exhibition, Proceedings*; Interscience Communications Ltd, 2015; pp. 499–512.

68. Quintiere, J.; Harkleroad, M. New Concepts for Measuring Flame Spread Properties. In *Fire Safety: Science and Engineering*; Harmathy, T., Ed.; ASTM International: 100 Barr Harbor Drive, PO Box C700, West Conshohocken, PA 19428-2959, 1985.

69. ASTM E1321-13, Standard Test Method for Determining Material Ignition and Flame Spread Properties, ASTM International, West Conshohocken, PA, 2012, www.astm.org.

70. Janssens, M. Piloted Ignition of Wood: *Fire Mater.* **1991**, *15*, 151–167.

71. Janssens, M. Fundamental thermophysical characteristics of wood and their role in enclosure fire

growth, Ghent University, 1991.

72. Dietenbeger, M. Ignitability Analysis Using the Cone Calorimeter and LIFT Apparatus. In *Twenty-Second International Conference on Fire Safety*; Columbus, OH, 1996.

73. Schartel, B.; Hull, T. R. Development of fire-retarded materials—Interpretation of cone calorimeter data. *Fire Mater.* **2007**, *31*, 327–354.

74. Zsako, J. Kinetic analysis of thermogravimetric data. *J. Phys. Chem.* **1968**, *72*, 2406–2411.

75. Bamford, C. H.; Crank, J.; Malan, D. H.; Wilson, A. H. The combustion of wood. Part I. *Math. Proc. Cambridge Philos. Soc.* **1946**, *42*, 166.

76. Kim, E. M.; Dembsey, N. *Engineering Guide for Estimating Material Pyrolysis Properties for Fire Modeling, Worcester Polytechnic Institute, Available at: https://www.wpi.edu/academics/fpe/assets/WPI-Fire-Report-14-III.pdf*; 2012.

77. Stoliarov, S. I.; Safronava, N.; Lyon, R. E. The effect of variation in polymer properties on the rate of burning. *Fire Mater.* **2009**, *33*, 257–271.

78. Stoliarov, S. I.; Crowley, S.; Walters, R. N.; Lyon, R. E. Prediction of the burning rates of charring polymers. *Combust. Flame* **2010**, *157*, 2024–2034.

79. Staggs, J. E. J. Ignition of char-forming polymers at a critical mass flux. *Polym. Degrad. Stab.* **2001**, *74*, 433–439.

80. Li, J.; Gong, J.; Stoliarov, S. I. Development of pyrolysis models for charring polymers. *Polym. Degrad. Stab.* **2015**, *115*, 138–152.

81. Stoliarov, S. I.; Crowley, S.; Lyon, R. E.; Linteris, G. T. Prediction of the burning rates of non-charring polymers. *Combust. Flame* **2009**, *156*, 1068–1083.

82. Li, J.; Gong, J.; Stoliarov, S. I. Gasification experiments for pyrolysis model parameterization and validation. *Int. J. Heat Mass Transf.* **2014**, *77*, 738–744.

83. McKinnon, M. B.; Stoliarov, S. I.; Witkowski, A. Development of a pyrolysis model for corrugated cardboard. *Combust. Flame* **2013**, *160*, 2595–2607.

84. McKinnon, M.; Stoliarov, S. I. Pyrolysis Model Development for a Multilayer Floor Covering. *Materials (Basel).* **2015**, *8*, 6117–6153.

85. Mhike, W.; Ferreira, I. V. W.; Li, J.; Stoliarov, S. I.; Focke, W. W. Flame retarding effect of graphite in rotationally molded polyethylene/graphite composites. *J. Appl. Polym. Sci.* **2015**, *132*, n/a–n/a.

86. Chaos, M.; Khan, M. M.; Krishnamoorthy, N.; De Ris, J. L.; Dorofeev, S. B. Evaluation of optimization schemes and determination of solid fuel properties for CFD fire models using bench-scale pyrolysis tests. *Proc. Combust. Inst.* **2011**, *33*, 2599–2606.

87. *The CRC Handbook of Mechanical Engineering, Second Edition*; CRC Press, 2004.

88. Di Blasi, C. Modeling and simulation of combustion processes of charring and non-charring solid fuels. *Prog. Energy Combust. Sci.* **1993**, *19*, 71–104.

89. Griffin, G. J. Studies on the Effect of Atmospheric Oxygen Content on the Thermal Resistance of Intumescent, Fire-Retardant Coatings. *J. Fire Sci.* **2005**, *23*, 303–328.

90. Patel, P.; Hull, T. R.; Stec, A. A.; Lyon, R. E. Influence of physical properties on polymer flammability in the cone calorimeter. *Polym. Adv. Technol.* **2011**, *22*, 1100–1107.

91. Linteris, G. T. Numerical simulations of polymer pyrolysis rate: Effect of property variations. *Fire Mater.* **2011**, *35*, 463–480.

92. Zhang, F.; Wang, Y.; Li, S.; Zhang, J. Influence of thermophysical properties on burning behavior of intumescent fire-retardant materials. *J. Therm. Anal. Calorim.* **2012**, *113*, 803–810.

93. Rimez, B.; Rahier, H.; Van Assche, G.; Artoos, T.; Biesemans, M.; Van Mele, B. The thermal degradation of poly(vinyl acetate) and poly(ethylene-co-vinyl acetate), Part I: Experimental study of the degradation mechanism. *Polym. Degrad. Stab.* **2008**, *93*, 800–810.

94. McGarry, K.; Zilberman, J.; Woolley, W. D.; Hull, T. R.; David Woolley, W. Decomposition and combustion of EVA and LDPE alone and when fire retarded with ATH. *Polym. Int.* **2000**, *49*, 1193–1198.

95. Soudais, Y.; Moga, L.; Blazek, J.; Lemort, F. Coupled DTA–TGA–FT-IR investigation of pyrolytic decomposition of EVA, PVC and cellulose. *J. Anal. Appl. Pyrolysis* **2007**, *78*, 46–57.

96. Hull, T. R.; Price, D.; Liu, Y.; Wills, C. L.; Brady, J. An investigation into the decomposition and burning behaviour of Ethylene-vinyl acetate copolymer nanocomposite materials. *Polym. Degrad. Stab.* **2003**, *82*, 365–371.

97. Šimon, P. Polymer degradation by elimination of small molecules. *Die Angew. Makromol. Chemie*

1994, *216*, 187–187–203–203.

98. Costache, M. C.; Jiang, D. D.; Wilkie, C. A. Thermal degradation of ethylene–vinyl acetate coplymer nanocomposites. *Polymer (Guildf).* **2005**, *46*, 6947–6958.

99. Costache, M. C.; Heidecker, M. J.; Manias, E.; Camino, G.; Frache, A.; Beyer, G.; Gupta, R. K.; Wilkie, C. A. The influence of carbon nanotubes, organically modified montmorillonites and layered double hydroxides on the thermal degradation and fire retardancy of polyethylene, ethylene–vinyl acetate copolymer and polystyrene. *Polymer (Guildf).* **2007**, *48*, 6532–6545.

100. Rimez, B.; Rahier, H.; Van Assche, G.; Artoos, T.; Van Mele, B. The thermal degradation of poly(vinyl acetate) and poly(ethylene-co-vinyl acetate), Part II: Modelling the degradation kinetics. *Polym. Degrad. Stab.* **2008**, *93*, 1222–1230.

101. Marín, M. L.; Jiménez, A.; López, J.; Vilaplana, J. Thermal degradation of ethylene (vinyl acetate) Kinetic analysis of thermogravimetric data. *J. Therm. Anal.* **1996**, *47*, 247–258.

102. Rychly, J.; Dalinkevich, A. A.; Janigová, I.; Rychlá, L. Nonisothermal thermogravimetry of polymers - IV. Polyethylene and ethylene-vinyl acetate copolymers highly loaded with Al(OH)3 and Mg(OH)2. *J. Therm. Anal.* **1994**, *41*, 115–124.

103. Staggs, J. E. J.; Whiteley, R. H. Modelling the combustion of solid-phase fuels in cone calorimeter experiments. *Fire Mater.* **1999**, *23*, 63–69.

104. Borhani Zarandi, M.; Amrollahi Bioki, H. Thermal and mechanical properties of blends of LDPE and EVA crosslinked by electron beam radiation. *Eur. Phys. J. Appl. Phys.* **2013**, *63*, 21101.

105. Pattanayak, S.; Bhowmick, T. Thermal characteristics of poly(ethylene vinyl acetate) from 80 to 300 K. *Cryogenics (Guildf).* **1990**, *30*, 795–798.

106. Borhani zarandi, M.; Amrollahi Bioki, H.; Mirbagheri, Z. A.; Tabbakh, F.; Mirjalili, G. Effect of crystallinity and irradiation on thermal properties and specific heat capacity of LDPE & LDPE/EVA. *Appl. Radiat. Isot.* **2012**, *70*, 1–5.

107. Ghose, S.; Watson, K. A.; Working, D. C.; Connell, J. W.; Smith, J. G.; Sun, Y. P. Thermal conductivity of ethylene vinyl acetate copolymer/nanofiller blends. *Compos. Sci. Technol.* **2008**, *68*, 1843–1853.

108. Camino, G.; Maffezzoli, A.; Braglia, M.; De Lazzaro, M.; Zammarano, M. Effect of hydroxides and

hydroxycarbonate structure on fire retardant effectiveness and mechanical properties in ethylene-vinyl acetate copolymer. *Polym. Degrad. Stab.* **2001**, *74*, 457–464.

109. Rothon, R.; Hornsby, P. Fire Retardants Fillers for Polymers. In *Polymer Green Flame Retardants*; Elsevier, 2014; pp. 289–321.

110. Witkowski, A.; Stec, A. A.; Hull, T. R.; Richard Hull, T. The influence of metal hydroxide fire retardants and nanoclay on the thermal decomposition of EVA. *Polym. Degrad. Stab.* **2012**, *97*, 2231–2240.

111. Martinez, R. Ketonization of acetic acid on titania-functionalized silica monoliths. *J. Catal.* **2004**, *222*, 404–409.

112. Nicholson, J. W.; Wilson, A. D. The Conversion of Carboxylic Acids to Ketones: A Repeated Discovery. *J. Chem. Educ.* **2004**, *81*, 1362.

113. Pei, Z.-F.; Ponec, V. On the intermediates of the acetic acid reactions on oxides: an IR study. *Appl. Surf. Sci.* **1996**, *103*, 171–182.

114. Pestman, R.; Koster, R. M.; Pieterse, J. A. Z.; Ponec, V. Reactions of Carboxylic Acids on Oxides. *J. Catal.* **1997**, *168*, 255–264.

115. Pestman, R.; Van Duijne, A.; Pieterse, J. A. Z.; Ponec, V. The formation of ketones and aldehydes from carboxylic acids, structure-activity relationship for two competitive reactions. *J. Mol. Catal. A Chem.* **1995**, *103*, 175–180.

116. Ngohang, F.-E.; Fontaine, G.; Gay, L.; Bourbigot, S. Smoke composition using MLC/FTIR/ELPI: Application to flame retarded ethylene vinyl acetate. *Polym. Degrad. Stab.* **2015**, *115*, 89–109.

117. Kondo, S.; Urano, Y.; Tokuhashi, K.; Takahashi, A.; Tanaka, K. Prediction of flammability of gases by using F-number analysis. *J. Hazard. Mater.* **2001**, *82*, 113–128.

118. Chao, J. Thermodynamic properties of key organic oxygen compounds in the carbon range C1 to C4. Part 2. Ideal gas properties. *J. Phys. Chem. Ref. Data* **1986**, 1369–1436.

119. Dembsey, N.; Gillepsie, B.; Long, M.; McMillan, N.; Walde, C. Pyrolysis simulation of fiber reinforced polymer (FRP) composites: challenges of zero-dimensional testing of resin and additive miwtures to measure kinetic parameters. In *15th International Conference Fire and Materials*; 2015; pp. 241–253.

120. Ashton, H. C. Fire Retardants. In *Functional Fillers for Plastics*; Xanthos, M., Ed.; Wiley-VCH, 2005; pp. 285–315.

121. Carson, J. K.; Lovatt, S. J.; Tanner, D. J.; Cleland, A. C. Thermal conductivity bounds for isotropic, porous materials. *Int. J. Heat Mass Transf.* **2005**, *48*, 2150–2158.

122. Florez, J. P. M.; Mantelli, M. B. H.; Nuernberg, G. G. V. Effective thermal conductivity of sintered porous media: Model and experimental validation. *Int. J. Heat Mass Transf.* **2013**, *66*, 868–878.

123. Progelhof, R. C.; Throne, J. L.; Ruetsch, R. R. Methods for predicting the thermal conductivity of composite systems: A review. *Polym. Eng. Sci.* **1976**, *16*, 615–625.

124. Kiliaris, P.; Papaspyrides, C. D. Polymer/layered silicate (clay) nanocomposites: An overview of flame retardancy. *Prog. Polym. Sci.* **2010**, *35*, 902–958.

125. Qin, H.; Zhang, S.; Zhao, C.; Feng, M.; Yang, M.; Shu, Z.; Yang, S. Thermal stability and flammability of polypropylene/montmorillonite composites. *Polym. Degrad. Stab.* **2004**, *85*, 807–813.

126. Riva, A.; Zanetti, M.; Braglia, M.; Camino, G.; Falqui, L. Thermal degradation and rheological behaviour of EVA/montmorillonite nanocomposites. *Polym. Degrad. Stab.* **2002**, *77*, 299–304.

127. De Stefanis, A.; Cafarelli, P.; Gallese, F.; Borsella, E.; Nana, A.; Perez, G. Catalytic pyrolysis of polyethylene: A comparison between pillared and restructured clays. *J. Anal. Appl. Pyrolysis* **2013**, *104*, 479–484.

128. Leszczyńska, A.; Njuguna, J.; Pielichowski, K.; Banerjee, J. R. Polymer/montmorillonite nanocomposites with improved thermal properties. Part II. Thermal stability of montmorillonite nanocomposites based on different polymeric matrixes. *Thermochim. Acta* **2007**, *454*, 1–22.

129. Camino, G.; Sgobbi, R.; Zaopo, A.; Colombier, S.; Scelza, C. Investigation of flame retardancy in EVA. *Fire Mater.* **2000**, *24*, 85–90.

130. Jang, B. N.; Costache, M. C.; Wilkie, C. a. The relationship between thermal degradation behavior of polymer and the fire retardancy of polymer/clay nanocomposites. *Polymer (Guildf).* **2005**, *46*, 10678–10687.

131. Kumar, N.; Dahiya, J. B. Polypropylene-nanoclay composites containing flame retardant additive: Thermal stability and kinetic study in inert atmosphere. *Adv. Mater. Lett.* **2013**, *4*, 708.

132. Bourbigot, S.; Gilman, J. W.; Wilkie, C. a. Kinetic analysis of the thermal degradation of

polystyrene-montmorillonite nanocomposite. *Polym. Degrad. Stab.* **2004**, *84*, 483–492.

133. Liu, H.; Kong, Q.; Cheng, Y.; Cao, G. Thermal Decomposition Kinetics of High Impact Polystyrene/Organo Fe-montmorillonite Nanocomposites. *Chinese J. Chem.* **2012**, *30*, 1594–1600.

134. Lecouvet, B.; Bourbigot, S.; Sclavons, M.; Bailly, C. Kinetics of the thermal and thermo-oxidative degradation of polypropylene/halloysite nanocomposites. *Polym. Degrad. Stab.* **2012**, *97*, 1745–1754.

135. Dabrowski, F.; Bourbigot, S.; Delobel, R.; Le Bras, M. Kinetic modelling of the thermal degradation of polyamide-6 nanocomposite. *Eur. Polym. J.* **2000**, *36*, 273–284.

136. Burnham, A. K.; Braun, R. L. Global Kinetic Analysis of Complex Materials. *Energy & Fuels* **1999**, *13*, 1–22.

137. Shi, L.; Yit Lin Chew, M. A review of fire processes modeling of combustible materials under external heat flux. *Fuel* **2013**, *106*, 30–50.

138. Kaynak, C.; Ibibikcan, E. Contribution of nanoclays to the flame retardancy of polyethylene-based cable insulation materials with aluminum hydroxide and zinc borate. *J. Fire Sci.* **2014**, *32*, 121–144.

139. Li, J.; Stoliarov, S. I. Measurement of kinetics and thermodynamics of the thermal degradation for charring polymers. *Polym. Degrad. Stab.* **2014**, *106*, 2–15.

140. Li, J.; Stoliarov, S. I. Measurement of kinetics and thermodynamics of the thermal degradation for non-charring polymers. *Combust. Flame* **2013**, *160*, 1287–1297.

141. Lyon, R.; Walters, R.; Stoliarov, S. A Thermal Analysis Method for Measuring Polymer Flammability. *J. ASTM Int.* **2006**, *3*, 13895.

142. Lyon, R. E.; Walters, R. N.; Stoliarov, S. I. Thermal analysis of flammability. *J. Therm. Anal. Calorim.* **2007**, *89*, 441–448.

143. Criado, J. M.; Ortega, A.; Gotor, F. Correlation between the shape of controlled-rate thermal analysis curves and the kinetics of solid-state reactions. *Thermochim. Acta* **1990**, *157*, 171–179.

144. ASTM E698-11, Standard Test Method for Arrhenius Kinetic Constants for Thermally Unstable Materials Using Differential Scanning Calorimetry and the Flynn/Wall/Ozawa Method, ASTM International, West Conshohocken, PA, 2012, www.astm.org.

145. Elder, J. P. The general applicability of the Kissinger equation in thermal analysis. *J. Therm. Anal.* **1985**, *30*, 657–669.

146. Kissinger, H. E. Variation of peak temperature with heating rate in differential thermal analysis. *J. Res. Natl. Bur. Stand. (1934).* **1956**, *57*, 217.

147. Ozawa, T. A New Method of Analyzing Thermogravimetric Data. *Bull. Chem. Soc. Jpn.* **1965**, *38*, 1881–1886.

148. Flynn, J. H.; Wall, L. A. A quick, direct method for the determination of activation energy from thermogravimetric data. *J. Polym. Sci. Part B Polym. Lett.* **1966**, *4*, 323–328.

149. Doyle, C. D. Estimating isothermal life from thermogravimetric data. *J. Appl. Polym. Sci.* **1962**, *6*, 639–642.

150. Coats, A. W.; Redfern, J. P. Kinetic Parameters from Thermogravimetric Data. *Nature* **1964**, *201*, 68–69.

151. Friedman, H. L. Kinetics of thermal degradation of char-forming plastics from thermogravimetry. Application to a phenolic plastic. *J. Polym. Sci. Part C Polym. Symp.* **2007**, *6*, 183–195.

152. Snegirev, A. Y. Generalized approach to model pyrolysis of flammable materials. *Thermochim. Acta* **2014**, *590*, 242–250.

153. Gustafsson, S. E. Transient plane source techniques for thermal conductivity and thermal diffusivity measurements of solid materials. *Rev. Sci. Instrum.* **1991**, *62*, 797.

154. Gustavsson, M.; Karawacki, E.; Gustafsson, S. E. Thermal conductivity, thermal diffusivity, and specific heat of thin samples from transient measurements with hot disk sensors. *Rev. Sci. Instrum.* **1994**, *65*, 3856.

155. Suleiman, B. M.; Gustafsson, S. E.; Börjesson, L. A practical cryogenic resistive sensor for thermal conductivity measurements. *Sensors Actuators A Phys.* **1996**, *57*, 15–19.

156. Bohac, V.; Gustavsson, M. K.; Kubicar, L.; Gustafsson, S. E. Parameter estimations for measurements of thermal transport properties with the hot disk thermal constants analyzer. *Rev. Sci. Instrum.* **2000**, *71*, 2452.

157. Gustavsson, M. K.; Gustafsson, S. E. On Power Variation in Self-Heated Thermal Sensors. In *Thermal Conducivity 27*; DEStech Publications, Inc, 2005; pp. 338–346.

158. ISO 22007-2, Plastics - Determination of thermal conductivity and thermal diffusivity - Part 2: Transient plane heat source (hot disc) method. **2008**.

159. Krupa, P.; Malinarič, S. Using the Transient Plane Source Method for Measuring Thermal Parameters of Electroceramics. *World Acad. Sci. Eng. Technol. Int. J. Mech. Mechatronics Eng.* **2014**, *1*.

160. He, Y. Rapid thermal conductivity measurement with a hot disk sensor. *Thermochim. Acta* **2005**, *436*, 122–129.

161. Log, T.; Gustafsson, S. E. Transient plane source (TPS) technique for measuring thermal transport properties of building materials. *Fire Mater.* **1995**, *19*, 43–49.

162. ASTM E1269-11, Standard Test Method for Determining Specific Heat Capacity by Differential Scanning Calorimetry, ASTM International, West Conshohocken, PA, 2012, www.astm.org.

163. ISO 11357-4, Plastics - Differential scanning calorimetry (DSC) - Part 4: Determination of specific heat capacity. **2014**.

164. DIN 51007:1994-06, General principles of differential thermal analysis, Deutsches Institut Fur Normung E.V., 1994.

165. Reading, M. Method and apparatus for spatially resolved modulated differential analysis https://patentscope.wipo.int/search/en/detail.jsf?docId=US38291265&redirectedID=true (accessed Nov 17, 2015).

166. Reading, M. Method and apparatus for gas flow modulated differential scanning calorimetry https://patentscope.wipo.int/search/en/detail.jsf?docId=US38687320&redirectedID=true (accessed Nov 17, 2015).

167. Reading, M.; Hahn, B. K.; Crowe, B. S. Method and apparatus for modulated differential analysis 1992.

168. Menczel, J. D.; Judovits, L.; Prime, R. B.; Bair, H. E.; Reading, M.; Swier, S. 2. Differential Scanning Calorimetry (DSC). In *Thermal Analysis of Polymers: Fundamentals and Applications*; Menczel, J. D.; Prime, R. B., Eds.; John Wiley & Sons, Inc.: Hoboken, NJ, USA, 2009.

169. Reading, M.; Hourston, D. J. *Modulated Temperature Differential Scanning Calorimetry: Theoretical and Practical Applications in Polymer Characterisation*; Springer Science & Business Media, 2006.

170. ASTM E2716-09, Test Method for Determining Specific Heat Capacity by Sinusoïdal Modulated

Temperature Differential Scanning Calorimetry, ASTM International, West Conshohocken, PA, 2012, www.astm.org.

171. Boulet, P.; Parent, G.; Acem, Z.; Collin, A.; Försth, M.; Bal, N.; Rein, G.; Torero, J. Radiation emission from a heating coil or a halogen lamp on a semitransparent sample. *Int. J. Therm. Sci.* **2014**, *77*, 223–232.

172. Försth, M.; Roos, A. Absorptivity and its dependence on heat source temperature and degree of thermal breakdown. *Fire Mater.* **2011**, *35*, 285–301.

173. Boulet, P.; Gérardin, J.; Acem, Z.; Parent, G.; Collin, A.; Pizzo, Y.; Porterie, B. Optical and radiative properties of clear PMMA samples exposed to a radiant heat flux. *Int. J. Therm. Sci.* **2014**, *82*, 1–8.

174. Stull, D. R.; Mayfield, F. D. Heat Capacities of Hydrocarbon Gases. *Ind. Eng. Chem.* **1943**, *35*, 639–645.

175. Domalski, E. S.; Hearing, E. D. Estimation of the Thermodynamic Properties of Hydrocarbons at 298.15 K. *J. Phys. Chem. Ref. Data* **1988**, *17*, 1637.

176. Hakkarainen, T.; Mikkola, E.; Laperre, J.; Gensous, F.; Fardell, P.; Tallec, Y. Le; Baiocchi, C.; Paul, K.; Simonson, M.; Deleu, C.; Metcalfe, E.; Le Tallec, Y.; Baiocchi, C.; Paul, K.; Simonson, M.; Deleu, C.; Metcalfe, E. Smoke gas analysis by Fourier transform infrared spectroscopy - summary of the SAFIR project results. *Fire Mater.* **2000**, *24*, 101–112.

177. ISO 19702, Guidance for sampling and analysis of toxic gases and vapours in fire effluents using Fourier Transform Infrared (FTIR) spectroscopy. **2015**.

178. Haaland, D. M.; Easterling, R. G.; Vopicka, D. A. Multivariate Least-Squares Methods Applied to the Quantitative Spectral Analysis of Multicomponent Samples. *Appl. Spectrosc.* **1985**, *39*, 73–84.

179. Pottel, H. Quantitative Models for Prediction of Toxic Component Concentrations in Smoke Gases from FTIR Spectra. *Fire Mater.* **1996**, *20*, 273–291.

180. ASTM E1582-14, Standard Practice for Calibration of Temperature Scale for Thermogravimetry, ASTM International, West Conshohocken, PA, 2012, www.astm.org.

181. ASTM E967-08, Standard Test Method for Temperature Calibration of Differential Scanning Calorimeters and Differential Thermal Analyzers, ASTM International, West Conshohocken, PA, 2012, www.astm.org.

182. ASTM E968-02, Standard Practice for Heat Flow Calibration of Differential Scanning Calorimeters, ASTM International, West Conshohocken, PA, 2012, www.astm.org.

183. ASTM E793 - 06, Standard Test Method for Enthalpies of Fusion and Crystallization by Differential Scanning Calorimetry, ASTM International, West Conshohocken, PA, 2012, www.astm.org.

184. ISO 13927, Plastics - Simple heat release test using a conical radiant heater and a thermopile detector. **2015**.

185. ASTM E906-14, Standard Test Method for Heat and Visible Smoke Release Rates for Materials and Products Using a Thermopile Method, ASTM International, West Conshohocken, PA, 2012, www.astm.org.

186. Guillaume, E.; Saragoza, L. Application of FTIR analyzers to fire gases-Progress in apparatus and method validation for quantitative analysis. In *Fire and Materials 2015 - 14th International Conference and Exhibition, Proceedings*; Interscience Communications Ltd, 2015; pp. 162–174.

187. NIST Chemistry WebBook, reference database 69, Available at: webbook.nist.gov/ chemistry/ (accessed on 10/10/15).

188. Sánchez-Jiménez, P. E.; Pérez-Maqueda, L. A.; Perejón, A.; Criado, J. M. Nanoclay Nucleation Effect in the Thermal Stabilization of a Polymer Nanocomposite: A Kinetic Mechanism Change. *J. Phys. Chem. C* **2012**, *116*, 11797–11807.

189. Pham, T. N.; Sooknoi, T.; Crossley, S. P.; Resasco, D. E. Ketonization of Carboxylic Acids: Mechanisms, Catalysts, and Implications for Biomass Conversion. *ACS Catal.* **2013**, *3*, 2456–2473.

190. Rajadurai, S. Pathways for Carboxylic Acid Decomposition on Transition Metal Oxides. *Catal. Rev.* **2006**, *36*, 385–403.

191. Kempel, F.; Schartel, B.; Linteris, G. T.; Stoliarov, S. I.; Lyon, R. E.; Walters, R. N.; Hofmann, A. Prediction of the mass loss rate of polymer materials: Impact of residue formation. *Combust. Flame* **2012**, *159*, 2974–2984.

192. Witkowski, A.; Girardin, B.; Försth, M.; Hewitt, F.; Fontaine, G.; Duquesne, S.; Bourbigot, S.; Hull, T. R. Development of an anaerobic pyrolysis model for fire retardant cable sheathing materials. *Polym. Degrad. Stab.* **2015**, *113*, 208–217.

193. Chase, M. W. NIST-JANAF Themochemical Tables, Fourth Edition. *J. Phys. Chem. Ref. Data,*

Monogr. 9 **1998**, *1*, 1951.

194. Ginnings, D. C.; Corruccini, R. J. Enthalpy, specific heat, and entropy of aluminum oxide from 0 degrees to 900 degrees C. *J. Res. Natl. Bur. Stand. (1934).* **1947**, *38*, 593–600.

195. Skauge, A.; Fuller, N.; Hepler, L. G. Specific heats of clay minerals: Sodium and calcium kaolinites, sodium and calcium montmorillonites, illite, and attapulgite. *Thermochim. Acta* **1983**, *61*, 139–145.

196. Luche, J.; Mathis, E.; Rogaume, T.; Richard, F.; Guillaume, E. High-density polyethylene thermal degradation and gaseous compound evolution in a cone calorimeter. *Fire Saf. J.* **2012**, *54*, 24–35.

197. Marquis, D. M.; Guillaume, E.; Camillo, A.; Pavageau, M.; Rogaume, T. Usage of controlled-atmosphere cone calorimeter to provide input data for toxicity modelling. In *Conference Proceedings - Fire and Materials 2011, 12th International Conference and Exhibition*; 2011; pp. 121–134.

198. Marquis, D. M.; Guillaume, É. Effects of under-ventilated conditions on the reaction-to-fire of a polyisocyanurate foam. In *Fire and Materials 2013 - 13th International Conference and Exhibition, Conference Proceedings*; 2013; pp. 103–114.

199. Hermouet, F.; Guillaume, É.; Rogaume, T.; Richard, F.; Ponticq, X. Determination of the fire behaviour of an acrylonitrile butadiene styrene material using a controlled atmosphere cone calorimeter. In *Fire and Materials 2015 - 14th International Conference and Exhibition, Proceedings*; Interscience Communications Ltd, 2015; pp. 776–787.

200. Lemmon, E. W.; McLinden, L. O.; Friend, D. G. Thermophysical Properties of Fluid Systems. NIST Chemistry WebBook, reference database 69, Available at: webbook.nist.gov/ chemistry/ (accessed on 10/10/15).

201. Statler, D. L. J.; Gupta, R. K. A Finite Element Analysis on the Modeling of Heat Release Rate, as Assessed by a Cone Calorimeter of Char Forming Polycarbonate. In *COMSOL Conference, Boston*; 2008.

202. Quintiere, J. G.; Liu, X. Flammability Properties of Clay-Nylon Nanocomposites. **2004**, Federal Aviation Administration, DOT/FAA/AR–07/29.

203. Wasan, S. R.; Rauwoens, P.; Vierendeels, J.; Merci, B. Application of a simple enthalpy-based pyrolysis model in numerical simulations of pyrolysis of charring materials. *Fire Mater.* **2009**, n/a–n/a.

204. Hasan, M. A.; Zaki, M. I.; Pasupulety, L. Oxide-catalyzed conversion of acetic acid into acetone:

an FTIR spectroscopic investigation. *Appl. Catal. A Gen.* **2003**, *243*, 81–92.

205. Choudalakis, G.; Gotsis, A. D. Permeability of polymer/clay nanocomposites: A review. *Eur. Polym. J.* **2009**, *45*, 967–984.

206. Quintiere, J. G.; Lyon, R. E.; Crowley, S. B. An exercise in obtaining flame radiation fraction from the cone calorimeter. *Fire Mater.* **2016**, n/a–n/a.

207. De Ris, J. L. IFE Rasbach Lecture. In *6th FireSeat Symposium*; 2014; pp. 15–16.

208. Tewarson, A. Combustion efficiency and its radiative component. *Fire Saf. J.* **2004**, *39*, 131–141.

209. Tewarson, A. Chapter 4: Generation of Heat and Chemical Compounds in Fires. In *SFPE Handbook of Fire Protection Engineering (3rd edition)*; DiNenno, P. E., Ed.; National Fire Protection Association: Quincy, MA, 2002; pp. 82–162.

210. Zarzecki, M.; Quintiere, J. G.; Lyon, R. E.; Rossmann, T.; Diez, F. J. The effect of pressure and oxygen concentration on the combustion of PMMA. *Combust. Flame* **2013**, *160*, 1519–1530.

211. Atreya, A. Ignition of fires. *Philos. Trans. R. Soc. A Math. Phys. Eng. Sci.* **1998**, *356*, 2787–2813.

212. Rasbash, D. J.; Drysdale, D. D.; Deepak, D. Critical heat and mass transfer at pilot ignition and extinction of a material. *Fire Saf. J.* **1986**, *10*, 1–10.

213. Deepak, D.; Drysdale, D. D. Flammability of solids: An apparatus to measure the critical mass flux at the firepoint. *Fire Saf. J.* **1983**, *5*, 167–169.

214. Drysdale, D. D.; Thomson, H. E. Flammability of plastics II: Critical mass flux at the firepoint. *Fire Saf. J.* **1989**, *14*, 179–188.

215. Staggs, J. E. J.; Nelson, M. I. A critical mass flux model for the flammability of thermoplastics. *Combust. Theory Model.* **2001**, *5*, 399–427.

216. Nelson, M. I.; Brindley, J.; McIntosh, A. C. The dependence of critical heat flux on fuel and additive properties: a critical mass flux model. *Fire Saf. J.* **1995**, *24*, 107–130.

217. Lundström, F. V.; van Hees, P. Challenges in determining critical mass flux for ignition. In *Fire and Materials 2015 - 14th International Conference and Exhibition, Proceedings*; Interscience Communications Ltd, 2015; pp. 198–209.

218. Hoffendahl, C.; Fontaine, G.; Duquesne, S.; Taschner, F.; Mezger, M.; Bourbigot, S. The fire

retardant mechanism of ethylene vinyl acetate elastomer (EVM) containing aluminium trihydroxide and melamine phosphate. *RSC Adv.* **2014**, *4*, 20185.

219. ASTM D7309-13,Standard Test Method for Determining Flammability Characteristics of Plastics and Other Solid Materials Using Microscale Combustion Calorimetry, ASTM International, West Conshohocken, PA, 2012, www.astm.org.

220. European Union, 2011, Regulation (EU) No 305/2011 of the European Parliament and of the Council of 9 March 2011 laying down harmonized conditions for the marketing of construction products and repealing Council Directive 89/106/EEC.

221. OJ No L 88, 04.4.2011. p.5.

222. Grayson, S. J.; van Hees, P.; Vercellotti, U.; Breulet, H.; Green, A. M. *FIPEC, Fire Performance of Electric Cables - new test methods and measurement techniques Final Report on the Europeans Commisision SMT Programme SMT4-CT96-2059*; London, 2000.

223. IEC 60332-3-10 Tests on electric and optical fibre cables under fire conditions - Part 3-10: Test for vertical flame spread of vertically-mounted bunched wires or cables - Apparatus. **2009**.

224. Journeaux, T.; Sundström, B.; Johansson, P.; Försth, M.; Grayson, S. J.; Gregory, S.; Kumar, S.; Breulet, H.; Messa, S.; Lehrer, R.; Kobilsek, M.; Leppert, H.-D.; Mabbott, N. *CEMAC - CE-marking of cables, SP Report 2010:27*; 2010.

225. Sundström, B.; Försth, M.; Johansson, P.; Grayson, S. J.; Journeaux, T. Prediction of fire classification of cables, extended application of test data. In *Interflam conference Proceedings*; 2010; pp. 439–450.

226. EN 13823:2002 Reaction to fire tests for building products - Building products excluding floorings exposed to the thermal attack by a single burning item. **2002**.

227. Tsai, K.-C. Using cone calorimeter data for the prediction of upward flame spread rate. *J. Therm. Anal. Calorim.* **2012**, *112*, 1601–1606.

228. Merryweather, G.; Spearpoint, M. J. Flame spread measurements on wood products using the ASTM E 1321 LIFT apparatus and a reduced scale adaptation of the cone calorimeter. *Fire Mater.* **2009**, *34*, 109–136.

229. ISO 5660-1, Reaction-to-fire tests - Heat release, smoke production and mass loss rate - Part 1: Heat

release rate (cone calorimeter method) and smoke production rate (dynamic measurement). **2015**.

230. Huggett, C. Estimation of rate of heat release by means of oxygen consumption measurements. *Fire Mater.* **1980**, *4*, 61–65.

231. Parker, W. J. Calculations of the Heat Release Rate by Oxygen Consumption for Various Applications. *J. Fire Sci.* **1984**, *2*, 380–395.

232. Janssens, M. L. Measuring rate of heat release by oxygen consumption. *Fire Technol.* **1991**, *27*, 234–249.

233. Babrauskas, V. Development of the cone calorimeter - A bench-scale heat release rate apparatus based on oxygen consumption. *Fire Mater.* **1984**, *8*, 81–95.

234. Guillaume, E.; Marquis, D.; Saragoza, L.; Yardin, C. Uncertainty on heat release rate measurement with cone calorimeter during the combustion of a material. *Rev. française métrologie* **2012**, *3 - n° 31*, 3–11.

235. Babrauskas, V. The Cone Calorimeter. In *The SFPE Handbook of Fire Protection Engineering*; National Fire Protection Association (NFPA)., 2008; pp. 952–980.

236. Gyppaz, F. Flame spread behavior of electric cables: Round-robin characterization of the IEC/EN 60332-1 tests. *J. Fire Sci.* **2012**, *30*, 404–412.

237. IEC 60695-9-2 Fire hazard testing - Part 9-2: Surface spread of flame - Summary and relevance of test methods. **2014**.

238. Försth, M.; Sjöström, J.; Wickström, U.; Andersson, P.; Girardin, B. Characterization of the thermal exposure in the en 50399 cable test apparatus. In *Fire and Materials 2015 - 14th International Conference and Exhibition, Proceedings*; Interscience Communications Ltd, 2015; pp. 23–37.

Appendix 1: EN 50399 FDS model description

Implementation of the EN 50399 cables test apparatus:

The cable test apparatus was implemented according to the requirements in the standard EN 50399. The inner dimensions of the apparatus are 1x2x4 m^3 (width × depth × height) and the walls have a heat transfer coefficient of 0.7 $W/m^2/K$ according to the standard. The inlet air is 0.133 m^3/s injected vertically upward from a 0.8x0.4 m^2 opening in the floor. The outline of the implementation is shown in **Figure 127**. It was found that 50 mm mesh size was an appropriate cell size for the part of the test apparatus where the cable ladder is mounted. There is however a large volume of the test apparatus where there are no flames and where the cell size can be larger. In order to make the simulations more efficient two meshes were used: one 50 mm mesh where the cable ladder is and one 100 mm mesh for the rest of the test apparatus.

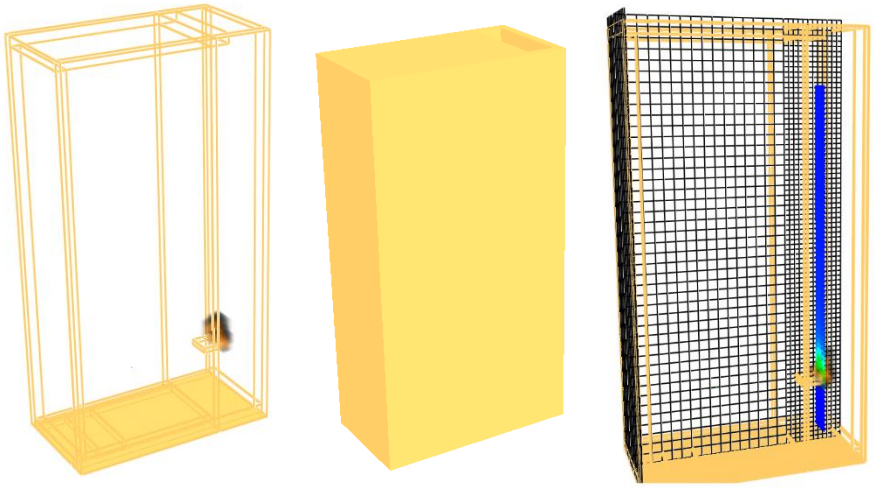

Figure 127: Implementation of the EN 50399 apparatus in FDS

Implementation of the cables:

One of the major limitations of using pyrolysis models in virtual testing is the fact that the meshing should be lower than the modelled objects. In our case, the mesh size should thus be much lower than 12 mm (the diameter of the cables) while a CFD code is used. This implies to have very long computational times. Nonetheless, FDS code introduced the so called fixed cylindrical Lagrangian particle [2]. Using these features, sub-grid modelling of cylindrically symmetric cables can be performed

on a coarser mesh. This allows detailed multi-scale modelling of fine objects, such as cables, in a much larger computational domain as presented in **Figure 128**.

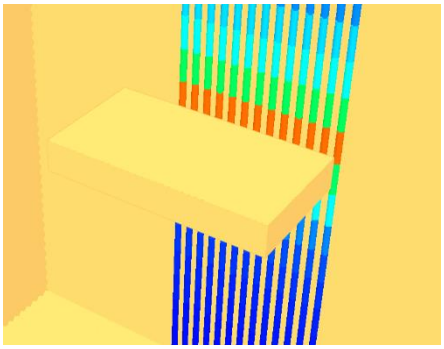

Figure 128: Implementation of the cables as fixed cylindrical Lagrangian particles.

It was shown by Försth *et al.* that the radiative environment in the EN50399 test apparatus is anisotropic [238]. Therefore, we took advantage of the feature in FDS that the Lagrangian particles can be splitted. This means that particles are exposed to the radiation from a specified direction, instead of the average radiation from all directions. In **Figure 129** the cable sees the radiation from four different directions whereas in our implementation eight different directions were used.

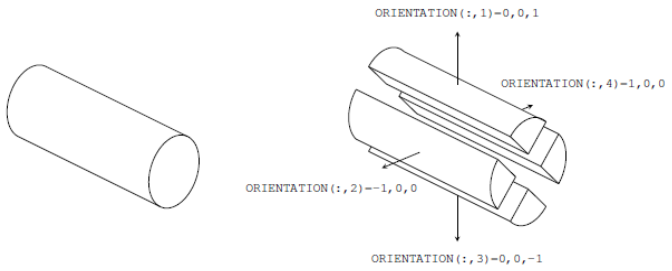

Figure 129: Particle splitting in FDS to correct for a non-isotropic radiative exposure. [2]

Contribution à l'étude du comportement feu de câbles électriques par simulation numérique et par développement d'un banc d'essai à échelle réduite

Résumé: L'objectif de ce travail de thèse est d'étudier le comportement au feu de câbles en développant des méthodes de caractérisation des propriétés des gaines externes de câbles et en modélisant numériquement leurs comportements au feu. Parallèlement, une deuxième approche basée sur le développement d'un banc d'essai original à échelle réduite a été étudiée. La caractérisation poussée des propriétés thermo-physique des matériaux a permis la prédiction de la température et de la perte de masse des matériaux lors d'expériences thermogravimétriques, de gazéification et de combustion. Il a été également montré que la réalisation de test sur de minces échantillons de gaines de câbles dans une enceinte à échelle réduite permettait la prédiction des résultats selon la norme EN 50399 sur des câbles entiers. Ce nouveau test à l'échelle du laboratoire a ensuite été utilisé avec succès pour le développement de nouveaux câbles présentant des propriétés feu améliorées.

Numerical modelling and small scale testing of fire behavior for halogen-free cables

Abstract: The aim of this PhD work is to study the behavior of cables following two approaches: numerical modelling and small scale testing. First, methodologies to characterize the properties of the cables jacket materials were developed to further model their fire behavior. Concurrently, an approach was followed by developing a novel bench-scale fire test. Innovative methodologies using simultaneous thermal analyzer, Hot Disc apparatus were developed and so, the thermo-physical properties of the materials were characterized both as a function of temperature and of the decomposition state. Using these parameters as inputs data for a pyrolysis model, the temperature and mass loss rate were well predicted in case of thermo-gravimetric experiments, gasification and mass loss calorimeter. Moreover, it was shown that testing thin specimen of cables jacket materials in a reduced scaled enclosure of the EN 50399 test allowed the prediction of the results obtained on the large-scale test carried out on whole cables. This new bench scale test was then successfully to develop new material that can be used as jacket for halogen-free electrical cable.